

**Forschungsbericht 2023-01**

# **Coupled Mode Flutter of Turbomachinery Blades**

Matthias Schuff

Deutsches Zentrum für Luft- und Raumfahrt  
Institut für Aeroelastik  
Göttingen



**DLR**

**Deutsches Zentrum  
für Luft- und Raumfahrt**

# **Forschungsbericht 2023-01**

## **Coupled Mode Flutter of Turbomachinery Blades**

Matthias Schuff

Deutsches Zentrum für Luft- und Raumfahrt  
Institut für Aeroelastik  
Göttingen

216 Seiten  
94 Bilder  
11 Tabellen  
100 Literaturstellen



Deutsches Zentrum  
DLR für Luft- und Raumfahrt



*Herausgeber:*

Deutsches Zentrum  
für Luft- und Raumfahrt e. V.  
Wissenschaftliche Information  
Linder Höhe  
D-51147 Köln

ISSN 1434-8454  
ISRN DLR-FB-2023-01  
Erscheinungsjahr 2023

DOI: <https://doi.org/10.57676/k1d4-mk17>

Zugl.: Berlin, Technische Universität, Diss., 2022

### **Erklärung des Herausgebers**

Dieses Werk ist unter einer Creative Commons Lizenz vom Typ Namensnennung 3.0 Deutschland zugänglich.

Um eine Kopie dieser Lizenz einzusehen, konsultieren Sie

<https://creativecommons.org/licenses/by/3.0/de/legalcode> oder wenden Sie sich brieflich an Creative Commons, Postfach 1866, Mountain View, California, 94042, USA.

### **Lizenz**



Creative Commons Lizenz vom Typ Namensnennung 3.0 Deutschland

*Turbomaschinen, Flugtriebwerke, Aeroelastik, Flattern, Modenkopplung*

*(Veröffentlicht in englischer Sprache)*

Matthias SCHUFF

DLR, Institut für Aeroelastik, Göttingen

### ***Flattern durch Modenkopplung von Turbomaschinenbeschaufelungen***

*Dissertation, Technische Universität Berlin*

Neuere Designs von Turbomaschinen, vorallem bei der Fan-Stufe von Flugtriebwerken, senken das Verhältnis von Schaufelmasse zur umliegenden Luft. Bei steigendem Einfluss der aerodynamischen Kräfte im Vergleich zu den Inertialkräften der Struktur kann eine aeroelastische Kopplung nicht mehr ausgeschlossen werden. Üblicherweise werden sogenannte entkoppelte Methoden zur Flatteranalyse verwendet, z.B. die Energiemethode nach Carta, welche allerdings eine nicht-konservative Vorhersage des aeroelastischen Stabilitätslimit liefern.

Das zu betrachtende aeroelastische System zwischen Strukturmechanik und Aerodynamik führt zur aeroelastischen Stabilitätsgleichung, die durch ein generalisiertes Eigenwertproblem abhängig von der aeroelastischen Frequenz beschrieben wird. In der Flatteranalyse von Starrflüglern wurden verschiedene Methoden zur Lösung der Stabilitätsgleichung etabliert. Das heutzutage meistverwendete Verfahren ist die p-k-Methode nach Hassig.

In dieser Arbeit wird die p-k-Methode für Anwendung auf Turbomaschinen angepasst. Dabei wird auf die spezifischen numerischen Aufbauten, insbesondere zyklische Symmetrie und die Veränderung der Struktur-Eigenformen (Modeshapes) und Struktur-Eigenfrequenzen mit der Rotordrehzahl und Drosselungszustand, eingegangen. Unter der Annahme kleiner Auslenkungen beim Einsetzen von Flattern können die Vibrationen mit einem linearisierten Ansatz behandelt werden, der eine Superposition der aerodynamischen Antworten erlaubt. Die instationären aerodynamischen Kräfte durch erzwungene Schwingungen werden deshalb mit einem Frequenzbereichsverfahren ermittelt und können dann für die aeroelastische Frequenz interpoliert werden.

Das Ziel dieser Arbeit ist die Verifikation und Validierung der angepassten p-k-Methode für die Simulation und Untersuchung von Flattern durch Modenkopplung von Turbomaschinen. Die Ergebnisse werden mit Fluid-Struktur-gekoppelten Zeitschrittverfahren verglichen und zeigen gute Übereinstimmungen. Eingängige Untersuchungen der beeinflussenden Parameter, wie z.B. Massenverhältnis, Frequenzabstand und Schaufelabstand, wird durchgeführt. Die Anwendung des hier entstandenen Prozesses auf eine Fan-Schaukel mit niedrigem Massenverhältnis zeigt, dass sich, im Vergleich zur üblicherweise verwendeten Vorhersage per Energiemethode, der flatterfreie Bereich deutlich verkleinert.

*Turbomachinery, aero engines, aeroelasticity, flutter, coupled mode*

Matthias SCHUFF

German Aerospace Center (DLR), Institute of Aeroelasticity, Göttingen

### ***Coupled Mode Flutter of Turbomachinery Blades***

*Doctoral Thesis, Technical University of Berlin*

With new turbomachinery designs, especially for the fan stage of aero engines, the ratio of blade mass to the surrounding air is significantly reduced. As the aerodynamic forces become relevant in relation to the inertial forces of the structure, aeroelastic coupling cannot be neglected anymore. The classically used decoupled methods for flutter analysis, such as Carta's energy method also known as the work-per-cycle approach, yield a non-conservative statement in predicting the aeroelastic stability boundary.

The resulting aeroelastic system of structural dynamics and aerodynamics leads to the aeroelastic stability equation, which itself is a generalized eigenvalue problem depending on an aeroelastic frequency. In fixed-wing analysis, different methods to solve the stability equation were introduced over the decades. The most prominent technique used nowadays is the p-k method as described by Hassig.

Within this thesis, the p-k method is adapted for the usage in turbomachinery with respect to the specific numeric setups, such as cyclic symmetry, or the change of mode shapes and natural frequencies over rotor speed and throttling state. Assuming small perturbations in the vicinity of flutter onset, vibrations can be handled by a linearized approach so that aerodynamic responses are independent of the amplitude and allow a superposition. Thus, the unsteady aerodynamic forces are gained from a set of frequency domain forced motion simulations and interpolated at the aeroelastic frequency.

The goal of this thesis is to verify and validate the adapted p-k method for coupled-mode flutter in turbomachinery. The results are compared against time-marching fluid/structure-coupled simulations and show good agreement. An intensive investigation of the influencing parameters, i.e. mass ratio, frequency separation and solidity, is performed. Applying the herein established process to a low mass ratio fan blade, it is shown that the flutter-free regime is significantly reduced in comparison to the classical energy method approach.

# Coupled Mode Flutter of Turbomachinery Blades

vorgelegt von  
Dipl.-Ing.  
Matthias Schuff  
ORCID: 0000-0003-3276-2539

an der Fakultät V – Verkehrs- und Maschinensysteme  
der Technischen Universität Berlin  
zur Erlangung des akademischen Grades

Doktor der Ingenieurwissenschaften  
- Dr.-Ing. -

genehmigte Dissertation

Promotionsausschuss:

Vorsitzender: Prof. Dr. ir. Maarten Uijt de Haag  
Gutachter: Prof. Dr.-Ing. Dieter Peitsch  
Gutachter: Prof. Dr.-Ing. Lorenz Tichy

Tag der wissenschaftlichen Aussprache: 14. Dezember 2022

Berlin 2023



*“Numerical aeroelasticity is extensive.  
You set up a simulation, and you wait. You go on vacation.  
Then you set up another simulation. You go on vacation.  
That way, you get a lot of vacation.”*

Not his exact words, but in this spirit: Dr. Walter A. Silva, NASA Langley

*“In pieces they stagger”*  
Claudio Sanchez in The Second Stage Turbine Blade’s 33

*“A rapturous verbatim  
Someone said, but who’s to know?”*  
Cedric Bixler-Zavala in Take the Veil Cerpin Text





# Abstract

With new turbomachinery designs, especially for the fan stage of aero engines, the ratio of blade mass to the surrounding air is significantly reduced. As the aerodynamic forces become relevant in relation to the inertial forces of the structure, aeroelastic coupling cannot be neglected anymore. The classically used decoupled methods for flutter analysis, such as CARTA's energy method also known as the work-per-cycle approach, yield a non-conservative statement in predicting the aeroelastic stability boundary.

The resulting aeroelastic system of structural dynamics and aerodynamics leads to the aeroelastic stability equation, which itself is a generalized eigenvalue problem depending on an aeroelastic frequency. In fixed-wing analysis, different methods to solve the stability equation were introduced over the decades. The most prominent technique used nowadays is the p-k method as described by HASSIG.

Within this thesis, the p-k method is adapted for the usage in turbomachinery with respect to the specific numeric setups, such as cyclic symmetry, or the change of mode shapes and natural frequencies over rotor speed and throttling state. Assuming small perturbations in the vicinity of flutter onset, vibrations can be handled by a linearized approach so that aerodynamic responses are independent of the amplitude and allow a superposition. Thus, the unsteady aerodynamic forces are gained from a set of frequency domain forced motion simulations and interpolated at the aeroelastic frequency.

The goal of this thesis is to verify and validate the adapted p-k method for coupled-mode flutter in turbomachinery. The results are compared against time-marching fluid/structure-coupled simulations and show good agreement. An intensive investigation of the influencing parameters, i.e. mass ratio, frequency separation and solidity, is performed. Applying the herein established process to a low mass ratio fan blade, it is shown that the flutter-free regime is significantly reduced in comparison to the classical energy method approach.



# Kurzfassung

Neuere Designs von Turbomaschinen, vorallem bei der Fan-Stufe von Flugtriebwerken, senken das Verhältnis von Schaufelmasse zur umliegenden Luft. Bei steigendem Einfluss der aerodynamischen Kräfte im Vergleich zu den Inertialkräften der Struktur kann eine aeroelastische Kopplung nicht mehr ausgeschlossen werden. Üblicherweise werden sogenannte entkoppelte Methoden zur Flutteranalyse verwendet, z.B. die Energiemethode nach CARTA, welche allerdings eine nicht-konservative Vorhersage des aeroelastischen Stabilitätslimit liefern.

Das zu betrachtende aeroelastische System zwischen Strukturdynamik und Aerodynamik führt zur aeroelastische Stabilitätsgleichung, die durch ein generalisiertes Eigenwertproblem abhängig von der aeroelastischen Frequenz beschrieben wird. In der Flutteranalyse von Starrflüglern wurden verschiedene Methoden zur Lösung der Stabilitätsgleichung etabliert. Das heutzutage meistverwendete Verfahren ist die p-k-Methode nach HASSIG.

In dieser Arbeit wird die p-k-Methode für Anwendung auf Turbomaschinen angepasst. Dabei wird auf die spezifischen numerischen Aufbauten, insbesondere zyklische Symmetrie und die Veränderung der Struktur-Eigenformen (Modeshapes) und Struktur-Eigenfrequenzen mit der Rotordrehzahl und Drosselungszustand, eingegangen. Unter der Annahme kleiner Auslenkungen beim Einsetzen von Flattern können die Vibrationen mit einem linearisierten Ansatz behandelt werden, der eine Superposition der aerodynamische Antworten erlaubt. Die instationären aerodynamischen Kräfte durch erzwungene Schwingungen werden deshalb mit einem Frequenzbereichsverfahren ermittelt und können dann für die aeroelastische Frequenz interpoliert werden.

Das Ziel dieser Arbeit ist die Verifikation und Validierung der angepassten p-k-Methode für die Simulation und Untersuchung von Flattern durch Modenkopplung von Turbomaschinen. Die Ergebnisse werden mit Fluid-Strukturgekoppelten Zeitschrittverfahren verglichen und zeigen gute Übereinstimmungen. Eingängige Untersuchungen der beeinflussenden Parameter, wie z.B. Massenverhältnis, Frequenzabstand und Schaufelabstand, wird durchgeführt. Die Anwendung des hier entstandenen Prozesses auf eine Fan-Schaukel mit niedrigem Massenverhältnis zeigt, dass sich, im Vergleich zur üblicherweise verwendeten Vorhersage per Energiemethode, der flatterfreie Bereich deutlich verkleinert.



# Acknowledgments

The research presented in this thesis resulted from my work as research associate at the Institute of Aeroelasticity of the German Aerospace Center DLR in Göttingen. First of all, I sincerely thank Prof. Dr.-Ing. Dieter Peitsch, Head of the Chair for Aero Engines at the Technical University of Berlin, for being my doctoral supervisor and his strong interest in my research work as well as providing valuable stimuli.

I would like to thank those who enabled me to conduct my research, embedded in challenging project work: Prof. Dr.-Ing. Lorenz Tichy, Head of the Institute of Aeroelasticity, Dr. rer. nat. Holger Mai, Head of the Department of Aeroelastic Experiments, and Dr.-Ing. Joachim Belz, the leader of the group Aeroelasticity of Turbomachinery. I thank Prof. Tichy for being a reviewer to my doctoral thesis, his profound insight, and the link to the airframe and wing theory of aeroelasticity. I also thank Dr. Belz for the (sometimes lengthy) discussions about my thesis topic and beyond, and for his professional advice.

Many thanks are due to Dr.-Ing. Virginie Anne Chenaux for providing new perspectives on many topics, the many fruitful discussions, and also for the many research papers we co-authored together. I like to thank Dr. David Quero Martin, Christoph Kaiser, and Dr. Jan Schwochow for discussions on the p-k method and how to adapt it to turbomachinery usage, which ultimately made it possible to work out the theory for this thesis. For interesting discussions on simulation practices and other aeroelastic topics I like to thank Dr. Markus Ritter. For deepened discussion on aeroelasticity of turbomachinery, I like to thank Michael Blocher, Prof. Dr.-Ing. Holger Hennings, and Prof. Dr.-Ing. Volker Carstens. Special thanks to Dr. Oliver Hach for being the internal mentor for my thesis (although I luckily did not need to counsel as there were no difficult situations with my doctoral committee), but also for providing the software engineering environment. Many thanks to Urte Turlach and Heike Landhäußer for providing and maintaining the IT infrastructure and taking care of a lot of “background stuff” in this matter.

Of course, many thanks are due to Björn Grüber, Harald Schönenborn, and Detlef Korte from MTU Aero Engines in Munich for the collaboration over the past years. I also want to thank the colleagues from the Institute of Propulsion Technology in Cologne, the Department of Numerical Methods for providing the TRACE solver suite, and the Department of Fans and Compressors for providing the CRISPmulti geometry.

A big part of being a successful researcher, in my very humble opinion, is the companionship with co-workers and them being actual friends. Therefore, credit goes to my DLR colleagues at the Institute of Aeroelasticity, the whole DLR campus in Göttingen, and all the DLR sites across Germany. While the paper production industry might be disappointed by this, I cannot name each and every one personally here. However, for companionship, being it in sportive activities, watching American Football *#JedenVerdammtenSonntag*, simple leisure activities or just enjoying a good coffee break, I like to thank Kjell and Katharina Bramsiepe (special thanks for taking care of my apartment and my plants in my absence), Markus Zimmer, Tobias Hecken, Raphael Schöppe, Vega Handojo, Arne Voß, Marc Johan Feldwisch, Dominik Schäfer, Christopher Koch, Martin Tang, Sebastian Helm, Goran Jelicic, Anne Hebler, Jannis Lübker, and Jörn Biedermann.

Most of all, I am very thankful for the unconditional support of my family, my partner Melanie, and the “old-time” friends from and at what-still-feels-like-home, who provided a reliable non-work environment. Thanks for accepting and enduring the times, when I was deeply covered with work and could not meet up. Dear Sebastian, Michael, Patrick, and Julian: I guess, this counts as my last space flight internship. Thanks for constantly reminding me of what my field of study is actually called: “Pilot and Astronaut”.

To satisfy the philosopher within me, here are some thoughts: As with life, writing a doctoral thesis is a constant fight with new challenges. You are presented with an ever growing amount. How to cope with them is personal gusto. If you decide to work on solutions, you will be in constant struggle how to face and integrate new situations. But I believe, this only makes us stronger as the world is in constant change.

*Matthias Schuff, Göttingen, June 2022*

# Contents

<b>Abstract</b>	<b>iii</b>
<b>Kurzfassung</b>	<b>v</b>
<b>Acknowledgments</b>	<b>vii</b>
<b>Table of Contents</b>	<b>ix</b>
<b>List of Figures</b>	<b>xiii</b>
<b>List of Tables</b>	<b>xix</b>
<b>Nomenclature</b>	<b>xxi</b>
<b>1. Introduction</b>	<b>1</b>
1.1. Motivation . . . . .	1
1.2. Aeroelastic Phenomena in Turbomachinery . . . . .	2
1.3. State of the Art . . . . .	4
1.3.1. Aeroelastic Stability Analysis in Turbomachinery . . . . .	4
1.3.2. Previous Investigations on the Limitations of the Energy Method . . . . .	6
1.4. Research Objective . . . . .	8
1.5. Outline of the Thesis . . . . .	10
<b>2. Theory</b>	<b>11</b>
2.1. Free Vibration of the Harmonic Oscillator in the Time Domain . . . . .	11
2.1.1. Damping and Excitation . . . . .	13
2.1.2. Structural Energy . . . . .	14
2.2. Aeroelastic Modeling for Turbomachinery . . . . .	15
2.2.1. Equation of Motion and Forces Acting on Structure . . . . .	15
2.2.2. Prestressed Modal Analysis . . . . .	16
2.2.3. Mechanics of Rotationally Symmetric Structures . . . . .	18
2.2.4. Traveling Waves: The Inter-Blade Phase Angle . . . . .	21
2.2.5. Generalized Aerodynamic Forces . . . . .	22
2.2.6. Reduced Frequency . . . . .	25
2.2.7. Aeroelastic Stability Equation in Modal Form . . . . .	26
2.3. The Energy Method . . . . .	26
2.3.1. Rationale of the Energy Method . . . . .	26
2.3.2. Aerodynamic Work per Cycle . . . . .	27



2.3.3.	Logarithmic Decrement of Aerodynamic Damping . . . . .	28
2.3.4.	Local Excitation . . . . .	30
2.4.	Aerodynamic Coupling of Modeshapes . . . . .	30
2.4.1.	Aeroelastic Eigenvalue Problem . . . . .	31
2.4.2.	Solving the Flutter Equation . . . . .	33
2.4.3.	Physical Representation of Aeroelastic Modeshapes . . . . .	36
2.5.	Parameters in Coupled-Mode Flutter Analysis . . . . .	37
2.5.1.	Mass Ratio . . . . .	37
2.5.2.	Solidity . . . . .	39
2.5.3.	Frequency Separation and Distance . . . . .	40
2.5.4.	Normalized Logarithmic Decrement . . . . .	41
<b>3.</b>	<b>Numerical Approach</b>	<b>43</b>
3.1.	Computational Fluid Dynamics . . . . .	43
3.2.	Computational Structural Mechanics . . . . .	45
3.3.	Aeroelastic Coupling . . . . .	45
3.4.	Aeroelastic Toolchain . . . . .	46
<b>4.</b>	<b>Geometries and Test Cases</b>	<b>51</b>
4.1.	FUTURE-EPFL 2D Linear Cascade . . . . .	51
4.2.	NACA3506 2D Linear Cascade . . . . .	55
4.3.	CRISPmulti Fan Stage . . . . .	58
<b>5.</b>	<b>Verification and Validation of the P-K Method</b>	<b>65</b>
5.1.	General Remarks on Time-Marching Simulations . . . . .	66
5.1.1.	General Observations . . . . .	67
5.1.2.	Post-Processing the Time History of Deflections . . . . .	68
5.1.3.	Disclaimer on Used Non-Reflecting Boundary Conditions . . . . .	70
5.2.	FUTURE-2D-LC . . . . .	70
5.2.1.	GAF Matrix Generation . . . . .	71
5.2.2.	Subsonic Operating Point with Frequency Separation 1:2 . . . . .	73
5.2.3.	Subsonic Single-Mode Flutter vs. Low Frequency Separation . . . . .	79
5.2.4.	Operating Point Transonic I . . . . .	81
5.2.5.	Operating Point Transonic II . . . . .	86
5.3.	NACA3506-2D-LC . . . . .	88
5.3.1.	Subsonic . . . . .	88
5.3.2.	Transonic . . . . .	89
5.4.	CRISPmulti . . . . .	92
5.4.1.	Time-Marching FSC Simulations . . . . .	92
5.4.2.	P-K Analysis . . . . .	93
5.5.	Mode Tracking Strategies . . . . .	98
5.5.1.	Mode Crossing . . . . .	98
5.5.2.	Frequency Coalescence . . . . .	98

5.6. Summary . . . . .	101
<b>6. Aerodynamically Coupled Modeshapes in a Linear Compressor Cascade</b>	<b>103</b>
6.1. General Remarks . . . . .	104
6.2. Subsonic Operating Point . . . . .	104
6.2.1. Influence of Mass Ratio and Frequency Separation . . .	104
6.2.2. Aerodynamic Resonance and Effect on Modal Coupling	109
6.2.3. Influence of Solidity . . . . .	114
6.3. Transonic Operating Point . . . . .	117
6.3.1. Influence of Mass Ratio and Frequency Separation . . .	117
6.3.2. Aerodynamic Resonance and Effect on Modal Coupling	121
6.3.3. Influence of Solidity . . . . .	126
6.4. Summary . . . . .	129
<b>7. Application to Low Mass Ratio Fan Blade</b>	<b>131</b>
7.1. General Remarks . . . . .	131
7.2. Modal Coupling at a Specific Operating Point . . . . .	132
7.2.1. Generalized Aerodynamic Forces . . . . .	132
7.2.2. Energy Method and Coupled-Mode Analysis Compared	135
7.2.3. Modal Participations . . . . .	135
7.2.4. Considering Different Modeshapes in P-K Analysis . . .	139
7.3. Flutter Boundary above Working Line . . . . .	141
7.3.1. Overview . . . . .	141
7.3.2. Subsonic to Transonic Flow at Medium Rotational Speed	142
7.3.3. Transonic Flow at Medium-High Rotational Speed . . .	143
7.3.4. Higher Rotational Speed . . . . .	146
7.4. Mechanism of Modal Coupling . . . . .	149
7.5. Summary and Outlook . . . . .	156
<b>8. Conclusion</b>	<b>157</b>
8.1. Aerodynamic Coupling of Modeshapes in Turbomachinery . . .	157
8.2. Occurrence of Aerodynamically Coupled-Mode Flutter . . . . .	158
8.3. The P-K Method: Verification vs. Validation . . . . .	159
<b>Bibliography</b>	<b>161</b>
<b>A. Appendix</b>	<b>171</b>
A.1. IBPA Patterns . . . . .	171
A.2. Additional Validation for FUTURE-2D-LC Case Transonic I .	173
A.3. Computational Efficiency: Time-Marching Simulation vs. P-K	
Method Analysis . . . . .	177
A.3.1. Natural Frequencies of Modeshapes . . . . .	183

A.4. CRISPMulti: Parameter Changes Throughout the Compressor  
Map . . . . . 185  
A.4.1. Twist-to-Plunge Ratio of Modeshapes . . . . . 185

**Curriculum Vitae** **187**

# List of Figures

1.1.	Schematic of the turbofan engine and its evolution . . . . .	1
1.2.	Typical areas of flutter and where they occur in the compressor map . . . . .	5
2.1.	Sketch of the harmonic oscillator and a cut-free version . . . . .	12
2.2.	Displacement curves . . . . .	13
2.3.	Finite-element model of a simplified bladed disk with ten cyclic symmetric segments . . . . .	20
2.4.	Modal analysis result of full annulus finite-element model of a simplified bladed disk . . . . .	20
2.5.	Definition of inter-blade phase angle $\sigma$ with the example of $\sigma = 90^\circ$	23
2.6.	Flowchart of p-k Method . . . . .	35
2.7.	Example for frequency and damping of the aeroelastic branches over $q_s$ for a system with two structural DOF . . . . .	37
2.8.	Parameters in coupled-mode flutter analysis . . . . .	39
3.1.	Static fluid structure coupling process . . . . .	46
3.2.	Mapping strategies in FSC . . . . .	47
3.3.	Concept of aeroelastic toolchain <i>ATAC</i> . . . . .	48
4.1.	Test case “FUTURE-2D-LC”: 3D model of the non-rotating annular cascade with the position of the extracted midspan slice	53
4.2.	Test case “FUTURE-2D-LC”: CFD mesh of the single passage setup . . . . .	53
4.3.	Structural model of an individual blade in the FUTURE-2D-LC setup . . . . .	54
4.4.	FUTURE-2D-LC, Mach number in steady flowfields of selected operating points . . . . .	54
4.5.	Test case “NACA3506-2D-LC”: CFD mesh of the single passage setup . . . . .	56
4.6.	NACA3506-2D-LC, Mach number in steady flowfields of selected operating points . . . . .	57
4.7.	Illustration of the CRISPMulti fan stage . . . . .	59
4.8.	Compressor map of CRISPMulti with torsion at blade tip of first rotor due to static deformation . . . . .	61
4.9.	Maximum static deformation due to rotational and aerodynamic loads of the CRISPMulti first rotor . . . . .	62
4.10.	Computation meshes of the CRISPMulti fan stage . . . . .	62

4.11. Vacuum modeshapes with frequency $f$ and reduced frequency $k$ of CRISPmulti first rotor at 70% speedline (above WL, close to OP3) . . . . .	63
5.1. Generic time history of blade deflections in fluid/structure-coupled time-marching simulations, evaluation of vibration frequency and logarithmic decrement in harmonic part . . . . .	68
5.2. Detailed time history of physical and modal deflections of a four passage setup . . . . .	69
5.3. FUTURE-2D-LC, case “subsonic”: Generalized aerodynamic forces for selected IBPAs . . . . .	71
5.4. FUTURE-2D-LC, case “transonic I”: Generalized aerodynamic forces for selected IBPAs . . . . .	72
5.5. FUTURE-2D-LC “subsonic”: Random initial deflections and velocities . . . . .	73
5.6. FUTURE-2D-LC “subsonic”: Starting condition equiv. to pitch modeshape displacements with $\sigma = 180^\circ$ . . . . .	76
5.7. FUTURE-2D-LC, case “subsonic”: Structural energy of various time-domain FSC computations, markers: a) random initial deflections, b) initial motion close to final pattern and high initial structural energy, c) no initial motion (“free release”) . . . . .	77
5.8. FUTURE-2D-LC, case “subsonic”: p-k solution history . . . . .	78
5.9. FUTURE-2D-LC, case “subsonic” with $f_{heave} = 500$ Hz and $f_{pitch} = 600$ Hz: p-k solution history at $\sigma = -90^\circ$ . . . . .	80
5.10. FUTURE-2D-LC “transonic I”: Random initial deflections and velocities . . . . .	81
5.11. FUTURE-2D-LC, case “transonic I”: Structural energy of various time-domain FSC computations, markers: a) random initial deflections, b) initial motion close to final pattern and high initial structural energy, c) no initial motion (“free release”), d and e) random initial deflectios at different level than a . . . . .	83
5.12. FUTURE-2D-LC, case “transonic I”: p-k solution history . . . . .	84
5.13. FUTURE-2D-LC, case “transonic I”: p-k solution history . . . . .	85
5.14. FUTURE-2D-LC, case “transonic II”: Structural energy of various time-domain FSC computations, markers: a) random initial deflections, b) initial motion close to final pattern and high initial structural energy, c) no initial motion (“free release”) . . . . .	86
5.15. FUTURE-2D-LC, case “transonic II”: p-k solution history . . . . .	87
5.16. NACA3506-2D-LC, case “subsonic”: Total and individual blade structural energy for same setup with different initial conditions . . . . .	88
5.17. NACA3506-2D-LC, case “subsonic”: p-k solution history . . . . .	90
5.18. NACA3506-2D-LC, case “transonic”: p-k solution history . . . . .	91

5.19. CRISPMulti, $n = 70\%$ above WL: Total and individual blade structural energy for setup with 2 passages, final vibration IBPA is $\sigma = 0^\circ$ in both cases . . . . .	95
5.20. CRISPMulti, $n = 70\%$ above WL: Total and individual blade structural energy for setup with 5 passages . . . . .	95
5.21. CRISPMulti, $n = 70\%$ above WL, 2 passages, $\sigma = 0^\circ$ : p-k solution history . . . . .	96
5.22. CRISPMulti, $n = 70\%$ above WL, 5 passages, $\sigma = 72^\circ$ : p-k solution history . . . . .	97
5.23. Mode tracking via frequency or MAC sort (case: FUTURE-2D-LC, transonic I, $\sigma = -144^\circ$ , $f_{heave} = 300$ Hz, $f_{pitch} = 600$ Hz) . . . . .	99
5.24. Mode tracking strategies with MAC and pw-MAC method (case: FUTURE-2D-LC, transonic I, $\sigma = -108^\circ$ , $f_{heave} = 300$ Hz, $f_{pitch} = 400$ Hz) . . . . .	100
6.1. Frequency separation 1:2, FUTURE-LC-2D, case “subsonic”, solidity $s = 1.22$ : Traveling wave diagram compared between EM and p-k for varying mass ratio . . . . .	106
6.2. Frequency separation 2:3, FUTURE-LC-2D, case “subsonic”, solidity $s = 1.22$ : Traveling wave diagram compared between EM and p-k for varying mass ratio . . . . .	107
6.3. Frequency separation 5:6, FUTURE-LC-2D, case “subsonic”, solidity $s = 1.22$ : Traveling wave diagram compared between EM and p-k for varying mass ratio . . . . .	108
6.4. FUTURE-2D-LC, case “subsonic”, IBPA $\sigma = -54^\circ$ : Generalized aerodynamic forces around resonance condition with different frequency sampling rates . . . . .	109
6.5. FUTURE-2D-LC, case “subsonic”, IBPA $\sigma = -72^\circ$ : Generalized aerodynamic forces around resonance condition with different frequency sampling rates . . . . .	110
6.6. FUTURE-2D-LC, case “subsonic”, IBPA $\sigma = -54^\circ$ : p-k solution histories at two different frequency separations with different frequency sampling rates . . . . .	112
6.7. FUTURE-2D-LC, case “subsonic”, IBPA $\sigma = -72^\circ$ : p-k solution histories at two different frequency separations with different frequency sampling rates (where the orange/purple lines are not visible, they are hidden behind the red/blue lines) . . . . .	113
6.8. FUTURE-LC-2D, case “subsonic”: Normalized aerodamping of second aeroelastic modeshape depending on mass ratio, frequency separation, and solidity . . . . .	115

6.9. FUTURE-LC-2D, case “subsonic”: Normalized aerodamping of second aeroelastic modeshape depending on mass ratio, frequency separation, and solidity . . . . .	116
6.10. Frequency separation 1:2, FUTURE-LC-2D, case “transonic I”, solidity $s = 1.22$ : Traveling wave diagram compared between EM and p-k for varying mass ratio . . . . .	118
6.11. Frequency separation 2:3, FUTURE-LC-2D, case “transonic I”, solidity $s = 1.22$ : Traveling wave diagram compared between EM and p-k for varying mass ratio . . . . .	119
6.12. Frequency separation 5:6, FUTURE-LC-2D, case “transonic I”, solidity $s = 1.22$ : Traveling wave diagram compared between EM and p-k for varying mass ratio . . . . .	120
6.13. FUTURE-2D-LC, case “transonic I”, IBPA $\sigma = -72^\circ$ : Generalized aerodynamic forces around resonance condition with different frequency sampling rates, computed by HB method with one (colored symbols) and five (black dots) harmonics . .	121
6.14. FUTURE-2D-LC, case “transonic I”, IBPA $\sigma = -72^\circ$ : p-k solution histories with different GAF frequency sampling rates for pitch-only system and heave-pitch coupling . . . . .	124
6.15. FUTURE-2D-LC, case “transonic I”, IBPA $\sigma = -72^\circ$ : p-k solution histories for smaller frequency separation between heave and pitch . . . . .	125
6.16. FUTURE-LC-2D, case “transonic I”: Normalized aerodamping (lower value of first or second aeroelastic modeshape) depending on mass ratio, frequency separation, and solidity . . . . .	127
6.17. FUTURE-LC-2D, case “transonic I”: Normalized aerodamping (lower value of first or second aeroelastic modeshape) depending on mass ratio, frequency separation, and solidity . . . . .	128
7.1. Matrix interpolation for the generalized aerodynamic forces of the first three vacuum modeshapes (OP <i>n070b</i> , IBPA $\sigma = 36^\circ$ )	133
7.2. OP <i>n070b</i> : Damping diagram for EM, p-k 1x1, and p-k 6x6 . .	136
7.3. OP <i>n070b</i> : Modal participations of the fundamental aeroelastic modeshapes (AE mode) compared between 3x3 and 6x6 analysis	137
7.4. OP <i>n070b</i> : Modal participations of the higher aeroelastic modeshapes (AE mode) in 6x6 analysis . . . . .	138
7.5. OP <i>n070b</i> : Damping diagram considering different number of higher modeshapes in the p-k analysis . . . . .	139
7.6. Aeroelastic stability above the working line compared between the energy method and different p-k analysis . . . . .	142
7.7. OP <i>n065b</i> : Damping diagram for EM, p-k 3x3, and p-k 3x6 . .	144
7.8. OP <i>n075b</i> : Damping diagram for EM, p-k 3x3, and p-k 3x6 . .	144

7.9. OP <i>n075b</i> : Modal participations of the fundamental aeroelastic modeshapes (AE mode) compared between 3x3 and 6x6 analysis	145
7.10. Comparing the manifestation of the vac. modeshape 1 (1B) at $\omega t = \varphi = 0^\circ$ between OP <i>n070b</i> and <i>n075b</i>	145
7.11. Comparing the manifestation of the vacuum modeshape 3 (1T) and aeroelastic modeshape 3 (from p-k 3x3 and 3x6) between OP <i>n070b</i> and <i>n075b</i>	146
7.12. OP <i>n090b</i> : Damping diagram for EM, p-k 3x3, and p-k 3x6	147
7.13. OP <i>n090b</i> : Modal participations of the fundamental aeroelastic modeshapes (AE mode) compared between 3x3 and 6x6 analysis	147
7.14. OP <i>n090c</i> : Damping diagram for EM, p-k 3x3, and p-k 3x6	148
7.15. OP <i>n100c</i> : Damping diagram for EM, p-k 3x3, and p-k 3x6	148
7.16. Supersonic areas at the blade tip region of rotor 1	149
7.17. OP <i>n070b</i> , $\sigma = 36^\circ$ : Local excitation in the tip region of rotor 1 for different modeshape vibrations	150
7.18. OP <i>n075b</i> , $\sigma = 36^\circ$ : Local excitation in the tip region of rotor 1 for different modeshape vibrations	151
7.19. OP <i>n090b</i> , $\sigma = 36^\circ$ : Local excitation in the tip region of rotor 1 for different modeshape vibrations	154
7.20. OP <i>n090c</i> , $\sigma = 144^\circ$ : Local excitation in the tip region of rotor 1 for different modeshape vibrations	155
A.1. FUTURE-2D-LC, case “subsonic”: Generalized aerodynamic forces for selected IBPAs	174
A.2. FUTURE-2D-LC, case “transonic I”: p-k solution history for two IBPA (left: full view, right: detailed view)	175
A.3. NACA3506-2D-LC, case “subsonic”, $n_{bl} = 4$ , $\mu = 2803$ , only the pitch mode is allowed with natural frequency $f_{vac} = 115$ Hz: Total and individual blade structural energy, and individual blade displacements, unfavorable initial conditions	179
A.4. NACA3506-2D-LC, case “subsonic”, $n_{bl} = 4$ , $\mu = 2803$ , only the pitch mode is allowed with natural frequency $f_{vac} = 115$ Hz: Total and individual blade structural energy, and individual blade displacements, initial conditions close to final vibration pattern	180
A.5. NACA3506-2D-LC, case “subsonic”, $n_{bl} = 4$ , $\mu = 2803$ , only the pitch mode is allowed with natural frequency $f_{vac} = 200$ Hz: Total and individual blade structural energy, and individual blade displacements	181
A.6. Traveling wave damping diagram for pitch mode with different vacuum frequencies, compared between energy method (EM) and as 1x1 system in the p-k analysis (NACA3506-2D-LC, case “subsonic”) at a high mass ratio of $\mu = 2803$	182



A.7. CRISPmulti, rotor 1: Modal frequencies of modes 1 to 4 through- out compressor map . . . . .	183
A.8. CRISPmulti, rotor 1: Modal frequencies of modes 5 to 10 through- out compressor map . . . . .	184
A.9. CRISPmulti, rotor 1: Changes of twist-to-plunge ratio through- out the compressor map . . . . .	186

# List of Tables

1.1. Two Engine Generations in Comparison . . . . .	2
4.1. Parameters of the FUTURE-2D-LC Geometry . . . . .	52
4.2. FUTURE-2D-LC Operating Points . . . . .	52
4.3. FUTURE-2D-LC: Reduced frequency $k$ for selected combinations	52
4.4. Parameters of the NACA3506-2D-LC Geometry . . . . .	55
4.5. NACA3506-2D-LC Operating Points . . . . .	55
4.6. NACA3506-2D-LC: Reduced frequency $k$ for selected combinations	56
4.7. CRISPmulti Design Parameters . . . . .	60
6.1. “Baseline” Configuration of the FUTURE-2D-LC Geometry . .	103
6.2. Solidity Variation of the FUTURE-2D-LC Geometry . . . . .	104
A.1. Phase shift of each blade depending on the IBPA . . . . .	172



# Nomenclature

## Latin Symbols

---

$A$	area
$\mathbf{D}$	damping matrix
$E$	energy
$E_{s,tot}$	total structural energy
$E_0$	total energy
$\tilde{\mathbf{F}}$	matrix of harmonic force perturbations
$\mathbf{K}$	stiffness matrix
$\tilde{\mathbf{K}}$	modal stiffness matrix
$\mathbf{M}$	mass matrix
$\tilde{\mathbf{M}}$	modal mass matrix
$Ma$	Mach number
$N$	number of segments/blades
$\tilde{\mathbf{Q}}$	generalized aerodynamic forces (GAF) matrix
$T$	period (of one oscillation)
$T$	temperature
$T_t$	total temperature
$V$	volume
$W_c$	(aerodynamic) work per cycle
$\hat{a}$	amplitude scaling factors
$c_b$	chordlength of airfoil
$d$	(viscous) damping coefficient
$e$	Euler's number
$f$	force
$\tilde{f}$	harmonic force perturbations
$f$	frequency
$h$	channel height
$i$	index
$j$	imaginary unit, $j^2 = -1$
$k$	index
$k$	reduced frequency
$k$	stiffness
$k_\alpha$	torsional stiffness
$k_h$	longitudinal stiffness
$\tilde{k}$	modal stiffness

---

$l$	length
$m$	mass
$\tilde{m}$	modal mass
$\dot{m}$	mass flow
$n$	rate of rotation
$\vec{n}$	surface normal vector
$n$	multiple of occurrence, e.g. amount of periods
$n_{bl}$	number of blades
$p$	pressure
$p_t$	total pressure
$\tilde{q}_{r,c}$	generalized aerodynamic force (entry in GAF matrix)
$q_s, q_{scale}$	scaling factor in aeroelastic stability eqn.
$\bar{p}$	zeroth harmonic in Fourier series (static pressure)
$\tilde{p}^2(k)$	harmonic pressure coefficient in Fourier series
$s$	solidity
$t$	time
$u$	generalized displacement
$v$	velocity
$v_\infty$	upstream fluid velocity
$x$	coordinate, displacement
$\dot{x}$	velocity
$\ddot{x}$	acceleration
$\vec{x}$	position vector, displacement vector
$\hat{x}$	maximum displacement (reference displacement)
$z$	displacement

## Greek Symbols

---

$\Gamma$	modal participation factor
$\Lambda$	logarithmic decrement
$\Delta\varphi$	phase lag between two vacuum modeshapes in aeroelastic mode
$\Delta\varphi_{h \rightarrow \alpha}$	phase lag of heave in reference to pitch mode
$\Phi$	modeshape matrix
$\alpha$	inflow/outflow angle
$\beta$	stagger angle
$\delta$	decay (or damping) constant
$\epsilon_\eta$	local excitation in surface patch/cell
$\zeta$	damping ratio (acc. to Lehr)
$\eta$	surface patch/cell
$\iota$	modeshape family index
$\lambda$	eigenvalue

$\mu$	mass ratio structure-to-air
$\nu$	nodal diameter
$\pi$	mathematical constant
$\rho$	density (material or fluid)
$\rho_\infty$	upstream fluid density
$\sigma$	inter-blade phase angle
$\tau$	blade-to-blade pitch
$\phi$	amplitude of generalized displacement
$\vec{\phi}$	eigenvector, modeshape
$\varphi$	phase angle
$\chi$	angle
$\psi$	(complex) aeroelastic modeshape
$\omega$	angular frequency
$\omega_0$	undamped (natural) angular frequency

## Subscripts and Indices

---

0	at reference position, at inlet position
blade	of whole blade
cfld	in aero solver
em	calculated by energy method
env	envelope spline
env,l	lower envelope spline
env,u	upper envelope spline
heave	of heave modeshape
kin	kinetic
i	index
j	index
k	index
m	mean value
n	nodal diameter
pitch	of pitch modeshape
pk	calculated by p-k method
pot	potential
ref	reference value
s	structural
raw	raw data point
tot	total
t	total state (of e.g. temperature of pressure)
x	in reference to physical displacement

## Superscripts

---

$H$	Hermetian transpose (conjugate complex) operator
$T$	transpose operator
max	maximum

## Symbols

---

$\text{Re}()$	real part of complex number
$\text{Im}()$	imaginary part of complex number
$\Delta()$	difference value
$\vec{()}$	vector representation
$\dot{()}$	temporal derivative $\frac{d}{dt}$
$\ddot{()}$	second temporal derivative $\frac{d}{dt^2}$
$\hat{()}$	amplitude of displacement, reference displacement length
$\overline{()}$	complex conjugate operator
$\langle \rangle$	mean value in Fourier series (zeroth harmonic)
$\langle \rangle$	modal representation, harmonic variable
$\ $	Euclidian vector norm, modulus of complex number
$\arg()$	argument/phase of complex number
$()^*$	temporary value

## Abbreviations

---

1D	One dimension(al)
2D	Two dimension(al)
3D	Three dimesion(al)
AC	Annular cascade
ADP	Aerodynamic design point
CFD	Computational fluid dynamics
CFL	Curant Friedrich Lewy
CF-PEEK	Carbon fiber polyether ether ketone
CFRP	Carbon fiber reinforced plastics
CPU	Central processing unit
CRISP	Counter-rotating integrated shrouded propfan
CSM	Computational structural dynamics
DLR	Deutsches Zentrum für Luft- und Raumfahrt
DOF	Degree of freedom
EM	Energy method

---

EO	Engine order
EPFL	École Polytechnique Fédérale de Lausanne
FE	Finite element
FEM	Finite element method
FD	Frequency domain
FSC	Fluid/structure coupling
FSI	Fluid/structure interaction
GAF	Generalized aerodynamic force
HB	Harmonic balance
HP	High pressure
IBPA	Inter-blade phase angle
LC	Linear cascade
LCO	Limit cycle oscillation
LE	Leading edge
LES	Linear equation system
LP	Low pressure
MAC	Modal assurance criterion
MTU	Abbr. MTU Aero Engines AG
ND	Nodal diameter
NRBC	Non-reflecting boundary condition
ODE	Ordinary differential equation
OP	Operating point
OP0	Operating point 0
OPX	Operating point X
Q3D	Quasi three-dimensional
TE	Trailing edge
TRACE	Turbomachinery Research Aerodynamics Computational Environment
WL	Working line





# 1

## Introduction

### 1.1. Motivation

*“Current designs in aero-engines have reached their limit in efficiency and new designs are required.” -VAHDATI ET AL [1]*

Aero engine design is driven by the reduction of fuel consumption and noise emission. To increase the efficiency and overall performance, higher bypass ratios and increased fan diameters are consistent trends. Another associated technical requirement is lightweight design, what can be achieved through thinner and slender blades, and also via the usage of composite materials. A more efficient core engine allows for stage reduction, which is also a way to decrease the amount of moving parts, or from a general point of view, a way to downsize the engine core [3]. This evolution is sketched in fig. 1.1. The trends are more graspable when comparing numbers for two generations of turbofan engines in table 1.1. Although the newer generation of fans produce more bypass

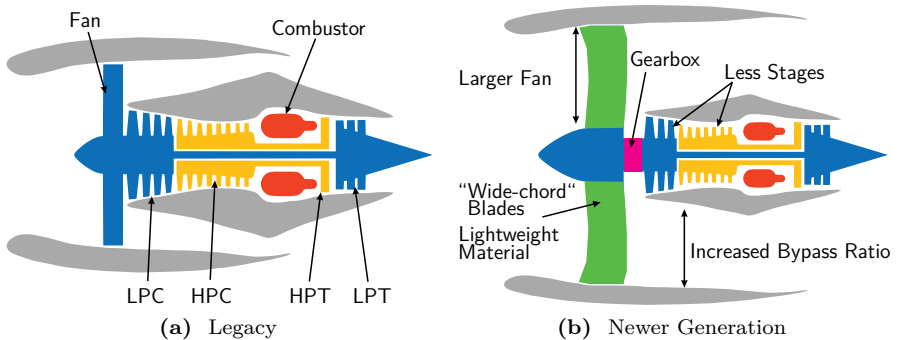


**Figure 1.1.:** Schematic of the turbofan engine and its evolution (adapted from ZHOU ET AL [2])

**Table 1.1.:** Two Engine Generations in Comparison [4, 5, 6]

	CFM-56B4	PW1100-G
Aircraft	A320	A320neo
Fan	36 blades, titanium alloy	20 blades, aluminum alloy, geared
Fan Diameter	1.73m	2.06m
Compressor Stages	4 LP, 9 HP	3 LP, 8 HP
Turbine Stages	1 HP, 4 LP	2 HP, 3 LP
Bypass Ratio	5.7	12.5
Service Entry	1988	2016

ratio at a higher diameter, the number of blades was significantly reduced. As a consequence, the individual blade loading is increased throughout the engine.

If stages in the compressor are reduced but the same overall pressure ratio shall remain, each individual stage has to operate at a higher blade loading. Within this operating range, the angle-of-attack increases and the ultimate limit to the operating range is the stall of one or more rotors. Compressor stall or *surge* is a severe event which leads to rapid destruction due to intermittent reversed flows and the induced vibrations. Before the occurrence of these *aerodynamic* instabilities, compressor and fan blades are prone to *aeroelastic* instabilities, i.e. *flutter*. The accuracy of flutter predictions, not only but especially in this operating regime, is therefore of great importance.

For the scope of this thesis, the major consequence from lightweight design and higher individual blade loadings is the decrease of the mass ratio of structure-to-air. Many analysis methods used in aeroelasticity of turbomachinery are based on the assumption of a high mass ratio.

## 1.2. Aeroelastic Phenomena in Turbomachinery

Any elastic structure will deform under the influence of aerodynamic forces. If the structure is flexible enough, the deformations become significant. In aeroelasticity, these interactions of an elastic structure with the surrounding fluid flow are studied. Lightweight design increases the vulnerability for aeroelastic effects and make the structure prone to negative impacts. A rough division can be made into two major fields. **Static aeroelasticity** is the steady-state response of the structure when exposed to aerodynamic loadings. Deformations induce an additional stress in the material that can cause plastic deformations and even fractures. If the static reaction of the structure reinforces an increase in

torsion or angle-of-attack, **divergence** might occur. **Dynamic aeroelasticity** describes vibrational phenomena, which can further be divided into **external disturbances** (e.g. turbulence or gusts) and self-induced vibrations (**flutter**). While the first type of vibrations are normally damped or at least limited in amplitude, the latter ones will lead to an unbound growth of the amplitude and ultimately to rapid structural failure.

Transferred to turbomachinery, the aeroelastic phenomena are distinguished into:

- **Static deflections** across the operating range are typically considered to be very small and thus neglectable. This assumption is true for most of the turbomachines in usage due to the high stiffness of what is basically a big block of solid metal. It is still true for many of the components nowadays, but with the increase of lightweight design, it has at least to be re-evaluated for newer designs [7, 8].
- **Flutter** is a self-excitation without external forces acting on the blade and thus a stability problem. A positive feedback between the motions of the blade and the fluid responses causes these oscillations to grow exponentially. The influence of adjacent blades of the same rotor play an important role in this context. The amplitudes may be limited due to nonlinearities in the fluid or structure, so that a limit cycle oscillation (LCO) establishes. However, if not rapidly destructing the blades, these vibrations ultimately lead to fatigue. Therefore, methods to predict and evaluate such problems mainly focus on the onset of flutter, which should be avoided at all costs. As the frequencies are not known a priori by simple determination of integer multiples of the fundamental rotation frequency, flutter onset might occur at any point in the operating range. However, the phenomenon is always associated with one of the eigenfrequencies of the system [9, 10].
- **Forced response** describes vibrational influence of one blade row, or in a more broader context by any geometrical feature i.e. vanes or non-uniform inflow disturbances from geometrical features, onto another blade row. The aerodynamic excitation usually comes from the wake of preceding or the potential influence of the following blade rows. The pressure disturbances are periodic in nature: their frequency is an integer multiple, or *engine order* (EO) of the engine rotational speed, and is thus called a *synchronized vibration*. So-called frequency crossings between EOs and the structural eigenfrequencies can be determined in advance and then checked for resonance amplitudes. A typical crossing that is prone for resonance is the blade passing frequency. With the decrease in mass ratio, amplitudes at off-resonance points might also become very high [11].

- **Non-synchronous vibrations** (NSV) describe a phenomenon that cannot be clearly sorted into either of the two previous categories, see KIELB ET AL [12]. *Non-synchronous* means that they do not occur at fixed integer multiples of the engine shaft speed, what is also true for flutter, but the nature of NSV is different. NSV occurs when the frequency of an aerodynamic instability (e.g. tip vortices, trailing edge flow separation, or shock-induced flow separation), or as they are sometimes called ‘fluid vibration modes’ [13, 1], comes close to the structural eigenfrequency. The aerodynamic frequency will then shift to the structural frequency, what is called *lock-in*. These vibrations are even more difficult to predict than the previous categories. In the transonic regime, fluid vibration modes are originating from the decrease of flow stability as stated by GAO AND ZHANG, and that the coupling with the structural modes “causes a misleading of contributing these aeroelastic phenomena to the forced vibration” [14]. In general, this sort of instabilities is similar to the *buffeting* phenomenon in fixed-wing. NITZSCHE ET AL describe the coupling of fluid and structural modes as being “essentially flutter” [15], but more research is still necessary to improve the sorting and understanding of the different phenomena.

The two major areas of research are most certainly flutter and forced response. However, the others are gaining importance as they arise with lower mass ratios and higher aerodynamic loading. Please note, that this thesis focuses on flutter (with some excursions to static deflections), keeping in mind that there are other phenomena which have to be investigated in the design process of turbomachinery.

## 1.3. State of the Art

### 1.3.1. Aeroelastic Stability Analysis in Turbomachinery

While the first turbojet engines of OHAIN or WHITTLE [16] might have been uncritical from an aeroelastic point-of-view as they were built for mechanical stability and suffered from fundamental aerodynamic challenges, subsequent developments were focused on increasing efficiency. Aeroelastic problems were encountered during rig testing or worse, in-flight. Soon, aeroelastic analysis would be included in design studies. As numerical analyses were not yet available and introduced slowly over time, surrogate and reduced order models would be used from early on. The most simple flutter avoidance method was based on analytical thoughts and empirical data, so that the geometry was designed in a way to avoid too low reduced frequencies within the operating range.

Nowadays, typical techniques used for aeroelasticity of turbomachinery are of reduced order, e.g. the principle of **traveling wave modes** by LANE [17] or the **energy method** for flutter analysis by CARTA [18], and have not only “stood the test of time” [19, p. 28], but are also viable from a physical point of view [20, pp. 527-532].

The applied fundamental assumptions of the energy method, which is also known as the work-per-cycle approach, are manifold. In most cases they can be traced back to the high mass ratio of structure to air and its implications. As a consequence, the aerodynamic forces acting on the structure only have an exciting or damping effect on the structure, but do not change the structural response, so that they are comparable to a vacuum behavior with mechanical dampers or exciters. This allows for a massive order reduction of the investigated model and with the benefit of huge savings in computational effort. Unsteady aerodynamic pressure perturbations are integrated to calculate the amount of work exchanged between fluid and structure. A positive energy feed into the structure will lead to flutter.

Over the decades, aeroelastic methods in turbomachinery cascades were reviewed by many researchers, see e.g. the works of MIKOLAJCZAK ET AL, FÖRSCHING, or MARSHALL AND IMREGUN [21, 9, 13]. Typical areas of flutter in compressor stages as illustrated in fig. 1.2 were already identified by MIKOLAJCZAK ET AL and their existence in these regimes can still be found in modern compressors and fans, which indicates a fundamental physical mechanism.

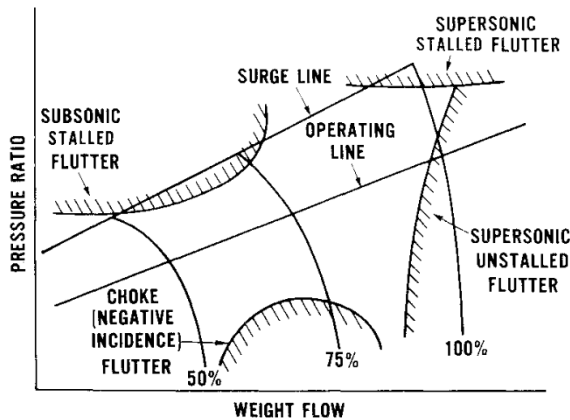


**Figure 1.2.:** Typical areas of flutter and where they occur in the compressor map [21]

### 1.3.2. Previous Investigations on the Limitations of the Energy Method

When it comes to the limitations of the decoupled energy method for flutter analysis of turbomachinery bladings, the literature gets scarce. Flutter in turbomachinery is still considered as a single-mode instability and modal coupling or frequency coalescence is not expected. Frequency neighborhood of natural frequencies, which could lead to frequency coalescence, is often intentionally avoided by design. While the early researchers also use the term “modal coupling”, they usually refer to inertial coupling of bending and torsion degrees of freedom. BENDIKSEN AND FRIEDMANN investigated the bending-torsion flutter in cascades due to structural, aerodynamic and inertial coupling but could not find frequency coalescence associated with aerodynamically coupled-mode flutter as found in fixed-wing aircraft [22, 23]. The review articles by MIKOLAJCZAK ET AL, FÖRSCHING, or MARSHALL AND IMREGUN [21, 9, 13] confirmed the single-mode assumption.

SRIVASTAVA AND REDDY were one of the first to compare single-mode and coupled-mode analysis methods by the means of CFD [24]. The baseline results show that there is a possibility for coupled-mode flutter of fan blades, in contrast to the single-mode analysis which yielded a stable system. Their investigation was limited to subsonic flow conditions and only applied non-viscid CFD based on the Euler equations. For the coupled-mode investigation, a fluid/structure-coupled (FSC) solver and an eigenvalue analysis, similar to the one presented in this thesis, were utilized. The eigenvalue method presented was computationally much more expensive than the time-marching FSC, in stark contrast to the presented results here. However, their proposed method for understanding the flutter characteristics is to use an eigenvalue method.

Investigations with a fluid/structure-coupled solver were performed by CARSTENS AND BELZ on a linear cascade of NACA3506 airfoils [25]. It was shown, that for certain aerodynamic conditions i.e. a choked passage, the decoupled methods could not predict the flutter onset. In this case, the flutter onset was due to alternately rotating blades, also known as *alternate passage divergence*. The blades are slightly increasing or decreasing their stagger angle, which leads to choked and unchoked passages. As a next step, the changed aerodynamic pressure perturbations lead to an instability. The research was extended by SADEGHI AND LIU [26] as they investigated the same effect for different mass ratios of the cascade. They showed that a lower mass ratio increased the alternate staggering effect due to static loading. Aerodynamic coupling of different modeshapes was not investigated in both articles. However, the findings show that decoupled methods can have significant prediction errors for low mass ratio compressor cascades.

CLARK ET AL investigated an open rotor fan blade with a very low mass ratio [27, 28]. They showed that coupled-mode flutter is possible for certain combinations of mass ratio, frequency separation and solidity and that the decision for the use of coupled or decoupled methods is essentially a function of these three parameters. To solve the aeroelastic eigenvalue problem, they implemented a *p-k method* as it will also be used in this thesis. However, they did not include further descriptions of the techniques used to iterate and solve it with the p-k method. Especially some of the major issues and obstacles when adapting and applying the p-k method to turbomachinery – as highlighted throughout this thesis – were not described. Furthermore, their research in coupled-mode flutter was focused on open rotor technology and relied on surrogate models to obtain the aerodynamic responses.

KORTE AND PEITSCH investigated modal coupling for a turbine rotor [29] with different approaches i.e. energy method and different sorts of coupled/uncoupled eigenvalue solvers. The difference in the eigenvalue solvers were the inclusion of changes in aerodynamics due to frequency shifts, the resulting damping of the aerodynamic forces, and the coupling of off-diagonal elements in the eigenvalue solution. The variant including these effects in a full aeroelastic eigenvalue analysis is called the *p-method* that allows to predict true damping values for non-zero damping [30, 31]. The investigation concentrated on intentional mistuning, which is typically considered as a stabilizing contributor in flutter prevention. However, the small frequency separation of the mistuned blades can lead to an aerodynamic coupling within the same modeshape family and thus destabilizes the system. It was shown that for the mistuned rotor, the uncoupled eigenvalue solver had significant prediction errors compared to the more complex approach of solving the coupled eigenvalue problem. As typical for turbine blades, they had a very high mass ratio and coupling between the two investigated mode families could not be observed. Especially the tuned rotor showed no difference between coupled and uncoupled solvers. Similar findings were reported by CORRAL ET AL [32] while investigating vane packing for turbine geometries in comparison to a continuous rig. They report that if the aerodynamic forces become high enough, the stabilizing effect of mistuned packets is lost. Small frequency separation can lead to coupling effects that decrease the stability margin in contrast to the predictions by the energy method.

CHAHINE ET AL compared decoupled and coupled methods for low mass ratio and low stiffness blades in a three-dimensional case [33, 34]. A major finding shows that even without modal coupling the frequency shift due to aeroelastic response of the blade can already lead to a significant change in stability. The most critical case, where flutter onset is observed, was not the lower mass ratio (compared to “conventional” design) but the low stiffness case. This



is not surprising, as lower stiffness leads to lower natural frequencies, which are known to increase the flutter susceptibility due to the effects of a lower reduced frequency. Their research did not include aerodynamic coupling between modeshape families, but the results emphasize the needs to include aeroelastic coupling effects in the analysis of low mass ratio blades.

## 1.4. Research Objective

Legacy, past and many current turbomachinery designs were investigated for flutter using the energy method, e.g. JEFFERS AND MEECE, CLARK ET AL, KORTE AND PEITSCH, or CHAHINE ET AL [35, 27, 29, 33]. Thus, it can be deduced empirically that for current turbomachinery components, flutter caused by aerodynamic modal coupling is most likely not of concern. At least if they are built in the “classical” design as solid metal blocks. For them, the energy method represents an adequate reduced order model for flutter analysis. This is backed up by the theoretical thoughts e.g. from BISPLINGHOFF ET AL, MIKOLAJCZAK ET AL, BENDIKSEN ET AL, FÖRSCHING, MARSHALL AND IMREGUN, or VAHDATI ET AL [20, 21, 22, 23, 9, 13, 1]. However, the previous results found in literature question this approach for newer turbomachinery generations, especially ultra-high bypass ratio fans.

### *Hypotheses*

- A. Turbomachinery blades can experience significant aerodynamic coupling between modeshape families. This results in the so-called coupled-mode flutter phenomenon.*
- B. The energy method is non-conservative in such cases.*
- C. The main driver of the aerodynamic coupling is the design approach resulting in a low structure-to-air mass ratio.*

**On the Modal Coupling Effect** The structural vibrations in the absence of aerodynamic forces (or more precisely in a vacuum) is describable with modeshapes, e.g. bending or torsion. The process to determine these vibrations and its frequencies is known as modal analysis. Introducing aerodynamic forces, a structural response is enforced. If the aerodynamic forces are high enough in comparison to the structural inertia, a coupled system has to be respected. As a consequence, the vibration frequencies will shift under the participation of multiple modeshapes, the so-called *aeroelastic frequency* and *aeroelastic modeshapes*. From a mathematical point-of-view, the resulting aeroelastic system is describable as an eigenvalue problem.

**On the Non-conservative Character of the Energy Method** Using the energy method for flutter analysis, the aerodynamic damping of structural vibrations is determined. The approach is straight forward and relies on a geometry that will only vibrate at the natural frequencies as if being in a vacuum. Superposition of modeshapes is possible as they are not affecting each other. In other words: they are decoupled. The conservative margin is the a priori unknown structural damping, which is always positive and thus stabilizing. If the key assumption of no interference between decoupled modeshapes is not justified anymore, the resulting aeroelastic modeshapes can vary significantly from the energy method – to a good or bad outcome.

**On the Influence of the Mass Ratio** There may not be a universal and absolute value of mass ratio (or other indicators) where to switch to a flutter analysis method that includes aerodynamically coupled modes. However, the mass ratio is a good indicator of the proportion between aerodynamic and structural forces. As a coarse classification, turbine geometries can be as high as  $\mu = O(1000) - O(10\,000)$ , whereas modern hollow titanium or CFRP fan rotors will be in the lower three digits ( $\mu = 100 - 300$ ) or even below that.

**The Treatment of the Aeroelastic Eigenvalue Equation** Time-marching fluid/structure-coupled simulations for sure provide a viable solution to determine the aeroelastic stability at a certain operating condition. On the downside, the approach is neither systematic nor resource-efficient. Coupled-mode flutter can be analyzed via a frequency domain approach that solves the aeroelastic eigenvalue equation. In fixed-wing analysis, the most commonly used method nowadays is the **p-k method** as introduced by HASSIG [36], see the thesis works of e.g. SCHWOCHOW, VAN ROOIJ, or FEHRS [31, 37, 38].

Using the p-k method is a logical and viable evolution of the flutter analysis process for future turbomachinery as it increases the complexity or order of the analysis by “just one step”<sup>1</sup>.

The goal of this thesis is to establish a process that suffices as instrument for aerodynamically coupled-mode flutter analysis. Therefore, the **p-k method** is adapted to turbomachinery usage.

---

<sup>1</sup>A very large step, metaphorically spoken. But as shown in this thesis, all the required ingredients and capabilities of the numerical fluid and mechanics solvers are already available when the energy method in its frequency domain implementation is currently used. They just have to be applied to a wider group of parameter combinations. The major “magic” is performed by incorporating them into a LES, namely the aeroelastic stability equation, and solving it numerically.

## 1.5. Outline of the Thesis

The thesis is organized in the following way to introduce the p-k method for turbomachinery application:

- **Chapter 2** explains the theoretical background of the structural mechanics and how they are combined with harmonic aerodynamic forces to form the aeroelastic stability equation. The transfer of the the p-k method to turbomachinery flutter analysis is derived. Furthermore, the numerical tools/solvers and integration into a toolchain is presented in **Chapter 3**.
- **Chapter 4** presents and describes the test cases and setups used.
- In **Chapter 5**, the p-k method is extensively compared to time-marching fluid/structure coupled simulations. The results show good agreement in predicting the flutter onset.
- **Chapter 6** studies variation of key parameters that have an influence onto the flutter susceptibility of the system, e.g. mass ratio, frequency separation and solidity. Also, the effects of aerodynamic resonances onto the interpolation of the aerodynamic responses via pre-computed frequency domain results is discussed.
- In **Chapter 7**, the p-k method is applied to a low mass ratio fan blade and is compared to the energy method. The non-conservative results of the energy method are demonstrated above the working line over a wide range of rotational speeds. The influence of using so-called “higher modeshapes” in the analysis process is discussed.
- Finally, **Chapter 8** summarizes the results of the work presented and puts them into perspective for future design approaches.

# 2

## Theory

*The fundamental equations of structural dynamics analysis and the specific concept of rotationally symmetric structures with a segment-wise description, as used for modeling turbomachinery components, is introduced. Aerodynamic responses to structural motions are characterized as generalized aerodynamic forces. Using these ingredients for aeroelastic stability analysis, the energy method and its fundamental assumptions are described. To incorporate aerodynamic coupling between modeshape families, the aeroelastic eigenvalue problem is solved by the p-k method.*

### 2.1. Free Vibration of the Harmonic Oscillator in the Time Domain

Considering the simple harmonic oscillator as in fig. 2.1, the equation of motion is

$$m\ddot{x}(t) + d\dot{x}(t) + kx(t) = f(t) \quad (2.1)$$

with the deflections  $x(t)$ , the mass  $m$ , the spring constant  $k$  and the viscous damping coefficient  $d$ . The external force  $f(t)$  can be any arbitrary function. The decay constant  $\delta$ , the damping ratio  $\zeta$ , the undamped angular frequency  $\omega_0$

and the *damped angular frequency*  $\omega$  are known from classical mechanics with the following relations:

$$\delta = \frac{d}{2m} \quad (2.2)$$

$$\zeta = \frac{d}{2\sqrt{km}} = \frac{d}{2m\omega_0} \quad (2.3)$$

$$\omega_0 = \sqrt{\frac{k}{m}} \quad (2.4)$$

$$\omega = \sqrt{\omega_0^2 - \delta^2} \quad (2.5)$$

If  $d = 0$  and  $f(t) = 0$ , the oscillator will perform sinusoidal oscillations around the equilibrium point with constant amplitude  $\hat{x}$  and the angular frequency  $\omega_0$ . For a structural system alone, only positive damping is possible and any value of  $d > 0$  decreases the amplitude over time.

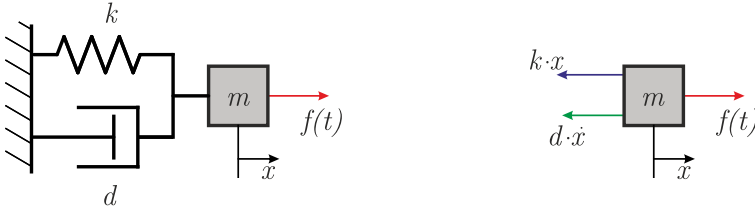


**Figure 2.1.:** Sketch of the harmonic oscillator and a cut-free version

As this thesis deals with flutter, which is a self-excited phenomenon without any external forces, the homogenous part of the ODE as sinusoidal motion is stated by

$$x(t) = \hat{x} e^{(-\delta + j\omega)t}. \quad (2.6)$$

Note that the starting condition here at  $t = 0$  is the initial deflection  $\hat{x}$ . For a more general expression,  $\hat{x}$  may be expressed as complex number and only the real part of  $x(t)$  will be the physical displacement. Furthermore, the initial deflection may also include an offset. Nevertheless, the following explanations avoid such detailed statements for the sake of simplicity, but without the loss of generality.

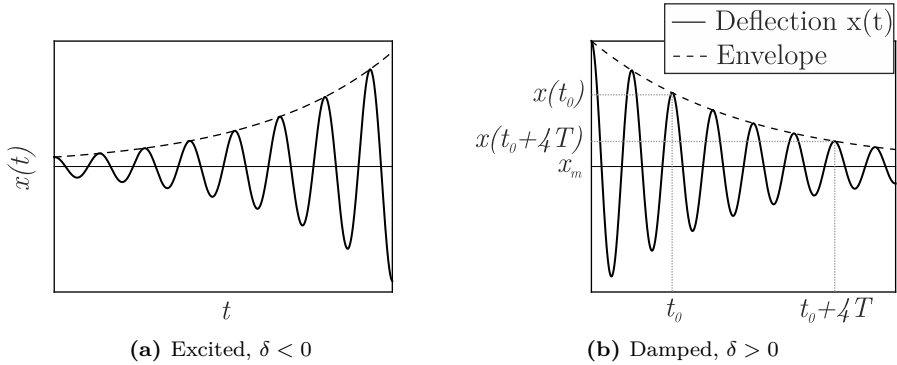


**Figure 2.2.:** Displacement curves

In a more general context, the physical displacement  $x(t)$  can be expressed by a generalized displacement  $u(t)$  that relates to  $x(t)$ :

$$x(t) = \text{Re}(\phi u(t)) \quad (2.7)$$

$$\dot{x}(t) = \text{Re}(\phi \dot{u}(t)) \quad (2.8)$$

where  $\phi$  is a reference amplitude, which can also be a vector and will later also be called *modeshape*. For a harmonic oscillation with angular frequency  $\omega$  and no damping, the generalized displacement and its derivative become

$$u(t) = e^{j\omega t} \quad (2.9)$$

$$\dot{u}(t) = j\omega e^{j\omega t} \quad (2.10)$$

### 2.1.1. Damping and Excitation

As stated above, the decay ratio for a purely structural system is always positive. As shown later, self-excitation is possible if aerodynamic forces are considered. If  $\delta$  becomes negative as seen in fig. 2.2a, the amplitudes of the oscillations grow.

Figure 2.2b marks the amplitudes for two instants in time. In general, comparing the amplitudes for the times  $t$  and  $t + nT$  with the period  $T = 2\pi/\omega$  and an integer-multiple  $n$ , the ratio of the oscillation amplitudes

$$\frac{x(t)}{x(t + nT)} = \frac{e^{(-\delta + j\omega)t}}{e^{(-\delta + j\omega)(t + nT)}} = e^{\delta nT} \quad (2.11)$$

can be reformulated for the *logarithmic decrement* under the premise of an underdamped system  $\zeta \ll 1$ :

$$\Lambda = \frac{1}{n} \ln \left( \frac{x(t)}{x(t+nT)} \right) = \delta T = \frac{2\pi\delta}{\omega} \quad (2.12)$$

Please note that the oscillations might occur around a mean value of  $x_m$  that is not equal to zero. This becomes of importance when dealing with time domain data from either experimental or numerical sources. The mean value  $x_m$  must therefore be eliminated before entering in (2.11). As this is not always a trivial task and dependent on the individual circumstances, it will be discussed once needed.

### 2.1.2. Structural Energy

A deeper insight into the aeroelastic behavior can be given by the total structural energy provided by the sum of kinetic and potential energy [25]. The structural energy  $E_{s,tot}$  increases, if the aeroelastic system is unstable.

The *kinetic energy*  $E_{kin}(t)$  describes the energy due to masses in motion, the *potential energy*  $E_{pot}$  is the energy stored in the spring. From classical mechanics of the one degree-of-freedom (DOF) oscillator, it is known that

$$E_{kin} = \frac{1}{2} m \dot{x}^2(t) \quad (2.13)$$

$$E_{pot} = \frac{1}{2} k x^2(t) \quad (2.14)$$

which sum up to the structural energy

$$E_{s,tot} = E_{kin}(t) + E_{pot}(t) = \frac{1}{2} m \dot{x}^2(t) + \frac{1}{2} k x^2(t). \quad (2.15)$$

The structural energy may also be expressed in a modal form using the generalized coordinate  $u(t)$  from (2.9) and (2.10). As detailed later and fully introduced in section 2.2.2 below, the modal mass and modal stiffness are  $\tilde{m} = \phi m \phi$  and  $\tilde{k} = \phi k \phi$ . By replacing the modal mass respectively modal stiffness and the generalized coordinate with these definitions, the equivalence of physical  $E$  and modal notation  $\tilde{E}$  is shown:

$$\tilde{E}_{kin}(t) = \frac{1}{2} \tilde{m} \dot{u}^2(t) = \frac{1}{2} \phi m \phi \left( \frac{\dot{x}}{\phi} \right)^2(t) = \frac{1}{2} m \dot{x}^2(t) = E_{kin}(t) \quad (2.16)$$

$$\tilde{E}_{pot}(t) = \frac{1}{2} \tilde{k} u^2(t) = \frac{1}{2} \phi k \phi \left( \frac{x}{\phi} \right)^2(t) = \frac{1}{2} k x^2(t) = E_{pot}(t) \quad (2.17)$$

The usage of the modal form is especially useful, if the structural vibrations are approximated by the superposition of a sufficient set of modeshapes.

By extension, the energy equation also applies for a system with many DOFs and is a simple summation over all elements  $i = 1, 2, \dots, n$ :

$$E_{s,\text{tot}} = \sum_{i=1}^n \left( \frac{1}{2} m_i \dot{x}_i^2 + \frac{1}{2} k_i x_i^2 \right) \quad (2.18)$$

## 2.2. Aeroelastic Modeling for Turbomachinery

### 2.2.1. Equation of Motion and Forces Acting on Structure

In a general form, the equation of motion in physical coordinates for a system with  $m$  degrees-of-freedom can be expressed as

$$\mathbf{M}_x \ddot{\vec{x}}(t) + \mathbf{D}_x \dot{\vec{x}}(t) + \mathbf{K}_x \vec{x}(t) = \vec{f}(t) \quad (2.19)$$

where the left side is implied as the structural part with  $\mathbf{M}_x, \mathbf{D}_x, \mathbf{K}_x \in \mathbb{R}^{m \times m}$  as the mass, damping and stiffness matrices, respectively and the displacement vector  $\vec{x} \in \mathbb{C}^m$ . The right side of the system includes any forces  $\vec{f}(t) \in \mathbb{C}^m$  acting on the structure and can be split into:

$$\vec{f}(t) = \vec{f}_{\text{motion}}(x, \dot{x}, \ddot{x}) + \vec{f}_{\text{external}}(t) \quad (2.20)$$

This is a major distinction in which way the aeroelastic system will be viewed and treated:

- **External forces**  $\vec{f}_{\text{external}}$  are an excitation of the system and cause a structural response. Classical examples are gust loads of wings or transient loads from maneuvers. More commonly found in turbomachinery are periodic loads at a fixed frequency, i.e. the wake of an upstream blade row or the potential field of downstream blades. This leads to the investigation of **forced response** that is, from a general point of view, a driven harmonic oscillator.
- **Motion-induced forces**  $\vec{f}_{\text{motion}}$  are the reaction of the fluid to structural movements and thus depending on the deflection and its time derivatives. In the forced response case, the motion-induced forces act as a damping factor and limit the amplitude of the structural reaction. **Flutter** occurs when the motion-induced forces alone feed energy from the fluid into the structure.



This thesis only deals with the flutter phenomenon that excludes external forces, so that  $\vec{f}_{\text{external}} = 0$ .

Aeroelastic stability is a dynamic problem and a good approximation of the oscillations is the assumption of sinusoidal motions. Thus, the harmonic structural deflections and its time-derivative become:

$$\vec{x}(t) = \hat{x} e^{\lambda t} \quad (2.21a)$$

$$\dot{\vec{x}}(t) = \lambda \hat{x} e^{\lambda t} \quad (2.21b)$$

$$\ddot{\vec{x}}(t) = \lambda^2 \hat{x} e^{\lambda t} \quad (2.21c)$$

with the amplitude  $\hat{x}$  and  $\lambda \in \mathbb{C}$  that contains the damping  $\delta$  and the angular frequency  $\omega$ , so that

$$\lambda = -\delta + j\omega. \quad (2.22)$$

If no external forces are acting on the structure, the remaining part on the right side is the motion-induced aerodynamic response. As stated by SADEGHI ET AL [39], the notation of these forces on the right side is common practice in aeroelastic texts, but may lead to the impression of them being a forcing function and deny their character as being strictly motion-dependent and not directly time-dependent. Flutter is not a forced response problem, but an inherent instability of the aeroelastic system. Considering this, putting (2.20) with  $\vec{f}_{\text{external}} = 0$  and (2.21) into (2.19), the equation of motion for the aeroelastic stability analysis should be written as

$$\mathbf{M}_x \lambda^2 \hat{x} + \mathbf{D}_x \lambda \hat{x} + \mathbf{K}_x \hat{x} - \vec{f}_{\text{motion}}(\hat{x}, \lambda) = 0. \quad (2.23)$$

In this form, the stability of the system is not time-dependent anymore. The damping  $\delta$ , which indicates the stability of the system, is an implicit feature and is not easy to deduce, as it is depending on the amplitudes in  $\hat{x}$  and the angular frequency  $\omega$ . Furthermore, the chosen discretization for investigation would need to be the same on the structure and aerodynamic models in the solution process. As this may be impractical in numerical analysis, there are certain ways to reduce the complexity of this system.

## 2.2.2. Prestressed Modal Analysis

From a purely structural point of view, the behavior of a structure can be described by the equation of motion in (2.19). If only time-invariant forces are applied, i.e. centrifugal and static pressure loads, the system will reach a new equilibrium state at a deflected position. This is very important in turbomachinery modeling, as rotational speeds, and to some extent also the

static aerodynamic loads, have a large impact on the dynamical behavior of the system. The stiffness matrix consists of different parts (cf. [40, 19]):

$$\mathbf{K}_x = \mathbf{K}_{\text{linear}} + \mathbf{K}_{\text{centrifugal}} + \mathbf{K}_{\text{geometrical}} \quad (2.24)$$

The unloaded system has the linear-elastic stiffness matrix  $\mathbf{K}_{\text{linear}}$ . Under constant rotational speed, the changes of centrifugal forces when moving are included in  $\mathbf{K}_{\text{centrifugal}}$ . Centrifugal forces and static pressure distribution cause the model to deform and geometrical stiffening is added in  $\mathbf{K}_{\text{geometrical}}$ .

This allows the investigation of the now operational system under the static loads. Any dynamical loads are neglected for the moment. Only small perturbations from the static position are assumed and thus, as it is common practice, the structural damping can also be neglected. The equation of motion can be simplified to

$$\mathbf{M}_x \ddot{\vec{x}}(t) + \mathbf{K}_x \vec{x}(t) = 0. \quad (2.25)$$

This leaves only the homogeneous part of  $\vec{x}(t)$  and assuming a harmonic motion, the ansatz writes

$$\vec{x}(t) = \vec{\phi} e^{\lambda t}. \quad (2.26)$$

Analogous to (2.21) and with (2.26) in (2.25), a prestressed normal mode analysis, or modal analysis, is performed via the generalized resulting eigenvalue problem:

$$\lambda^2 \mathbf{M}_x \vec{\phi} e^{\lambda t} + \mathbf{K}_x \vec{\phi} e^{\lambda t} = 0 \quad (2.27a)$$

$$(\lambda^2 \mathbf{M}_x + \mathbf{K}_x) \vec{\phi} = 0 \quad (2.27b)$$

This leads to the eigenvalues  $\lambda_i^2$  for  $i = 1 \dots n$  roots of the LES, where  $n$  is specified by the number of modes of interest. In general, the ansatz (2.26) yields  $\lambda = -\delta + j\omega$  as in (2.22). As no damping is present, the equation can be simplified to  $\lambda = j\omega$ .

With the eigenvalue  $\lambda_i^2$  from (2.27), the undamped angular velocity  $\omega_i$  can be obtained via

$$\lambda^2 = (j\omega_i)^2 = -\omega_i^2. \quad (2.28)$$

Each eigenvalue has a linear uncorrelated eigenvector  $\phi_i \in \mathbb{C}^m$ , which is also called a *vacuum modeshape*<sup>2</sup>. The physical interpretation is that – under the

---

<sup>2</sup>Though *vacuum modeshape* is not technically correct, as the static aerodynamic load has an influence on the static deformation of the system and thus the prestressing. However, this becomes only relevant for highly flexible structures. From a practical point of view, only the dynamic pressure perturbations will be of interest later on and the source or root cause of the prestiffened structure is de-facto not relevant. Whether static deformations come from rotational loads alone or include a static aerodynamic distribution, has the same effect on the dynamic behavior of the system.

assumption of a linear behavior for small perturbations – any dynamical motion of the system can be described by a combination of the  $n$  modeshapes with individual amplitude  $\hat{u}_i$ :

$$\vec{x}(t) = \sum_{i=1}^n \vec{\phi}_i \hat{u}_i e^{\lambda_i t} \quad (2.29)$$

The individual modeshapes are combined in the modeshape matrix  $\Phi \in \mathbb{C}^{m \times n}$ :

$$\Phi = \begin{bmatrix} \vec{\phi}_1 & \vec{\phi}_2 & \dots & \vec{\phi}_n \end{bmatrix} \quad (2.30)$$

and the generalized displacement vector  $\vec{u} \in \mathbb{C}^n$  is introduced:

$$\vec{x} = \Phi \vec{u} \quad (2.31)$$

Using (2.30) and (2.31) in (2.25) and, the equation of motion in modal form is derived by multiplying  $\Phi^H$  in front:

$$\underbrace{\Phi^H \mathbf{M}_x \Phi}_{\widetilde{\mathbf{M}}} \ddot{\vec{u}} + \underbrace{\Phi^H \mathbf{K}_x \Phi}_{\widetilde{\mathbf{K}}} \vec{u} = 0 \quad (2.32)$$

where  $\widetilde{\mathbf{M}}, \widetilde{\mathbf{K}} \in \mathbb{R}^{n \times n}$  contain the modal masses  $\tilde{m}_i$  respectively the modal stiffnesses  $\tilde{k}_i$  in the diagonals.

$$\widetilde{\mathbf{M}} = \begin{bmatrix} \ddots & & & \\ & \tilde{m}_i & & \\ & & \ddots & \\ & & & \ddots \end{bmatrix} \quad \text{and} \quad \widetilde{\mathbf{K}} = \begin{bmatrix} \ddots & & & \\ & \tilde{k}_i & & \\ & & \ddots & \\ & & & \ddots \end{bmatrix} \quad (2.33)$$

As a common practice, the eigenvectors  $\vec{\phi}_i$  are scaled so that the modal mass for each modeshape becomes  $\tilde{m}_i = 1 \text{ kg m}^2$ . As a result, the modal stiffnesses are equivalent to the eigenvalues, so that  $\tilde{k}_i = -\omega_i^2$ . The modeshapes are the degrees of freedom of the system described in the modal space and represent a drastically reduced order of the model.

### 2.2.3. Mechanics of Rotationally Symmetric Structures

In comparison to the above introduced concept, the extension to a realistic model of turbomachinery bladings is not straight forward. The obstacles are:

- Modern turbomachinery bladings are more and more manufactured from one single part as an integrally bladed disk (blisk). The structural damping of those is negligible and even small aerodynamic forces can have a large impact on aeroelastic stability.

- As a fundamental feature of rotor dynamics, the eigenfrequency and modeshape appearance can change significantly depending on the nodal diameter. Most of the time, those modeshapes are not real-valued, but complex and need thorough interpretation.
- Modeling the full setup of a blade row, the number of degrees of freedom will increase drastically and require high computational resources. To face this challenge, one can make use of the rotational symmetry of the structure and only simulate a segment of the rotor. The interpretation for the full annulus rotor are not trivial and again, need thorough evaluation.
- Despite being neglected in the previous sections, the structural damping is not zero. In practical terms, it can be neglected for modal analysis and be considered as a safety margin. Moreover, in numerical flutter analysis, the onset of flutter at very small amplitudes is sought, so that damping or excitation of the structural motions is solely attributed to aerodynamic forces.
- As already explained, the rotational speed of turbomachines has a stiffening effect that impacts especially on the eigenfrequencies. Although the theory is briefly described above, the practical implementation into finite-element solvers can present a challenge.

The whole structural mechanics theory would be worth a full textbook alone, but it is only used as a tool in the context of this thesis. A focus shall be put on the concept of traveling waves as first described by LANE [17] and later extended as well as mathematically verified by CRAWLEY in the “AGARD Manual on Aeroelasticity in Axial-Flow Turbomachinery”, edited by PLATZER and CARTA [41, 42]. A very picturesque explanation and distinguished description of the traveling wave concept can be found in the thesis of MAY [19]. A full mathematical derivation on how to physically interpret complex modal analysis towards traveling wave modes can be found in a technical report by the author [43], going from full annulus to segment-wise analysis.

Considering the full annulus FE model (e.g. fig. 2.3a), the returned modeshapes are real deformations and standing waves. In general, the modeshapes can be grouped into their physical appearance form  $\iota$  (e.g. bending, torsion)<sup>3</sup>, so that there are eigenvalues  $\lambda_n^{(\iota)}$  with corresponding eigenvectors  $\vec{\phi}_n^{(\iota)}$  where  $n$  is the index in this group. One group is also called a *modeshape family*.

---

<sup>3</sup>These names are easy to declare in the simple example given here. More complex 3-dimensional geometries might be harder to categorize only by visual aspects. Sometimes the frequency range is an indicator.

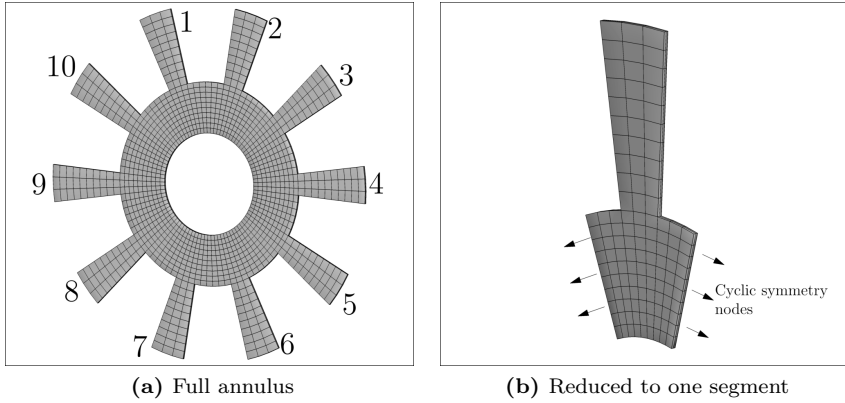


**Figure 2.3.:** Finite-element model of a simplified bladed disk with ten cyclic symmetric segments [43]

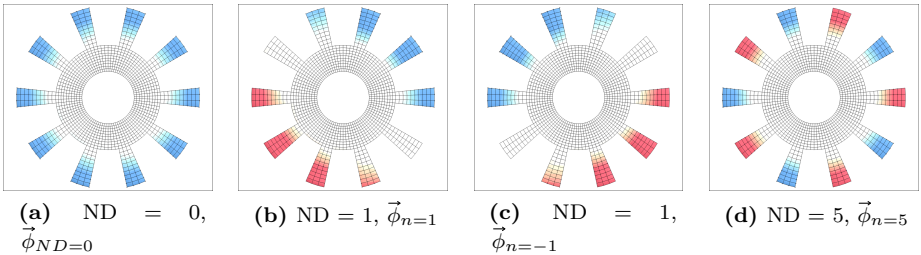


**Figure 2.4.:** Modal analysis result of full annulus finite-element model of a simplified bladed disk (blue is eigenvector into plane, red is out of plane) [43]

For each modeshape family, the eigenvalues appear in a certain systematic [19, p. 18 ff.] where  $N$  is the number of cyclic symmetric segments, with  $n = 0, \dots, N/2$  (for an even  $N$ ) resp.  $n = 0, \dots, N/2 - 1$  (for an odd  $N$ ):

- A single eigenvalue  $\lambda_0^{(\iota)}$  where every blade (or better: each cyclic symmetric segment) has the same deformation (meaning they are “in phase”), e.g. fig. 2.4a. This manifestation of the modeshape is a standing wave.
- If there is an even number of cyclic segments, a single eigenvalue  $\lambda_{N/2}^{(\iota)}$  is found where the adjacent segments move in the opposite direction with a phase shift of  $180^\circ$ , e.g. fig. 2.4d. This also manifests as a standing wave.

- All remaining eigenvalues appear in pairs  $\lambda_n^{(i)} = \lambda_{N-n}^{(i)}$ . The two modes appear as in figs. 2.4b and 2.4c as a pair of standing waves with a rotation of the eigenvectors' deformation of half the angle between the nodal diameters. These two forms can be referred to as real part  $\vec{\phi}_{Re}^{(i)}$  and imaginary part  $\vec{\phi}_{Im}^{(i)}$ , or more picturesque as cosine and sine form. A linear combination of two eigenvectors with equal eigenvalues is also an eigenvector, so that two combinations are possible:

$$\vec{\phi}_n^{(i)} = \vec{\phi}_{Re}^{(i)} + j\vec{\phi}_{Im}^{(i)} \quad (2.34a)$$

$$\vec{\phi}_{-n}^{(i)} = \vec{\phi}_{Re}^{(i)} - j\vec{\phi}_{Im}^{(i)} \quad (2.34b)$$

The nodal diameter now rotates around the annulus and the manifestation is a *traveling wave*.

This fundamental characteristic of turbomachinery vibration was first introduced by LANE [17]. It even applies if almost no structural coupling due to the disk is present, i.e. clamped composite blades in some rig tests (e.g. the *CRISPmulti* geometry). Thus, if structural coupling is negligible the modal analysis can be performed for an isolated blade and the modeshapes are the same for all possible IBPA-ND combination. Note that for mistuned structures or more complicated cases such as lateral motion of the rotor, LANE's assumption may no longer hold true.

Although there is a typical distinction between *modeshape family* and *traveling wave modes*, it is to mention that each of those combinations represents an orthogonal eigenvector of the system.

### 2.2.4. Traveling Waves: The Inter-Blade Phase Angle

An equivalent description for the nodal diameter is the inter-blade phase angle  $\sigma_i$  (IBPA) that is depending on the number of segments respectively blades  $N$ :

$$\sigma_i = 2\pi \frac{i}{N} \quad \text{with} \quad i = 0, 1, \dots, N-1 \quad (2.35)$$

Nodal diameters are sign-less from a mathematical or structural dynamicist's point of view. The sign only becomes important when transforming the deflection into time domain. A definition is made, that *positive* nodal diameters correspond

to *positive* IBPA and vice versa. Thus, the nodal diameter  $\nu$  and IBPA  $\sigma$  can be derived from each other with the number of segments  $N$ :

$$\sigma = 2\pi \frac{\nu}{N} \quad (2.36)$$

$$\nu = \frac{\sigma N}{2\pi} \quad (2.37)$$

Multiple modeshape families and IBPA-ND combinations can vibrate at the same time and be linearly superimposed. For a specific mode family  $\iota$  and IBPA, each blade  $k = 1, 2, \dots, N$  oscillates harmonically at the same frequency  $\omega = 2\pi f$  and modeshape  $\vec{\phi}_i^{(\iota)}$ , but with a constant phase shift of  $\sigma_i$ . The deflection  $x_k$  at a point in time  $t$  is

$$\begin{aligned} \vec{x}_k(t) &= \text{Re} \left( \vec{\phi}_i^{(\iota)} (\cos \chi + j \sin \chi) \right) \quad \text{with} \quad \chi = \omega t + (k-1)\sigma_i \\ &= \text{Re} \left[ \left[ \text{Re} \left( \vec{\phi}_i^{(\iota)} \right) + j \text{Im} \left( \vec{\phi}_i^{(\iota)} \right) \right] (\cos \chi + j \sin \chi) \right] \\ &= \text{Re} \left( \vec{\phi}_i^{(\iota)} \right) \cos \chi - \text{Im} \left( \vec{\phi}_i^{(\iota)} \right) \sin \chi. \end{aligned} \quad (2.38)$$

Normalizing  $\sigma_i$  into the range of  $(-\pi, \pi]$ , a *forward* or *backward* traveling wave can be defined in geometrical terms by looking at the sign of  $\sigma_i$ . The positive direction used in this thesis uses a positive blade counting in the (suggested) rotational direction, as depicted in fig. 2.5.

### 2.2.5. Generalized Aerodynamic Forces

The motion-induced aerodynamic forces in (2.23) are in general dependent on the amplitude  $\hat{x}$ , angular frequency  $\omega$  and damping  $\delta$  of the oscillation. Assuming a sinusoidal motion, the unsteady pressure acting on a surface patch  $\eta$  can be expressed by a harmonic Fourier series of length  $n_k$ , where the static pressure (or zeroth harmonic) is  $\bar{p}_\eta \in \mathbb{R}$  and the harmonic coefficients  $\hat{p}_\eta^{(k)} \in \mathbb{C}$  with  $k = 1, 2, \dots, n_k$ .

For small perturbations, the harmonic aerodynamic response is considered as linear to the amplitude. Furthermore, let assume that changes in amplitude are only small, so that  $\lambda \approx j\omega$ . The unsteady aerodynamic force for an individual surface patch  $\eta$  is

$$\vec{f}_{\eta, \text{motion}}(t) = \sum_{k=1}^{n_k} \left( \hat{p}_\eta^{(k)} \vec{n}_\eta + \bar{p}_\eta \hat{\vec{n}}_\eta^{(k)} \right) A_\eta e^{jk\omega t} \quad (2.39)$$

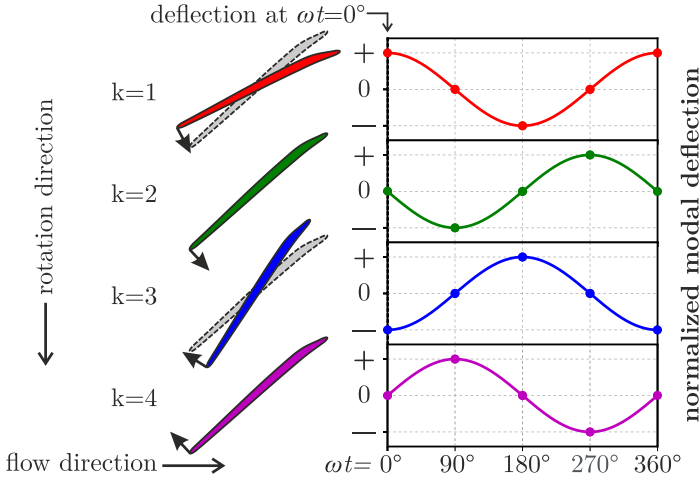


**Figure 2.5.:** Definition of inter-blade phase angle  $\sigma$  with the example of  $\sigma = 90^\circ$  (cascade stagger and dimensions not to scale) [44, 45]

where  $\vec{n}_\eta$  is the outward unit surface normal vector and  $\hat{n}_\eta^{(k)}$  are its variations in Fourier harmonics.  $A_\eta$  is the area of the surface patch at rest. The steady pressure  $\bar{p}_\eta \in \mathbb{R}$  contributes to the unsteady aerodynamics through the change in surface area, according to [19] up to 10% of the total value. The harmonic parts of the force fluctuations can be summed up into a frequency-dependent part  $\tilde{\vec{f}}_{\text{motion}}(\omega)^{(k)} \in \mathbb{C}^3$ :

$$\vec{f}_{\eta,\text{motion}}(t) = \sum_{k=1}^{n_k} \tilde{\vec{f}}_{\eta,\text{motion}}(\omega)^{(k)} e^{jk\omega t} \quad (2.40)$$

To evaluate the damping or excitation characteristic, only the first harmonic of the Fourier series will be of interest as the forces coming from higher harmonics cancel out over one period in a sinusoidal motion, so that the harmonic part becomes

$$\tilde{\vec{f}}_{\eta,\text{motion}}(\omega) \approx \left( \tilde{p}_\eta \vec{n}_\eta + \bar{p}_\eta \hat{n}_\eta \right) A_\eta, \quad (2.41)$$

which is inserted into (2.39):

$$\vec{f}_{\eta,\text{motion}}(t) \approx \tilde{\vec{f}}_{\eta,\text{motion}}(\omega) e^{j\omega t}. \quad (2.42)$$



Please note, that in numerical analysis the grid resolution for structural and aerodynamic solvers is mostly not the same. The aerodynamic forces or the modeshape displacement have to be projected from one to the other resolution. Typically, the surface displacements of the modeshape are interpolated onto the aerodynamic surface.

Based on the principle of superposition, the unsteady aerodynamics can be computed for each vibration mode individually. Extending (2.42) to all surface points, the unsteady aerodynamic forces at a specific vibration frequency  $\omega$  are gathered for all modeshapes. Using the generalized displacement vector  $\vec{u} \in \mathbb{C}^n$  again, the forces matrix  $\tilde{\mathbf{F}} \in \mathbb{C}^{m \times n}$  where  $m$  is the number of degrees of freedom and  $n$  the number of modeshapes of interest, is used to express the motion-induced forces acting on the surface (some subscripts are dropped for better readability):

$$\vec{f}(\omega) = \tilde{\mathbf{F}}(\omega) \vec{u} = \begin{bmatrix} \vec{f}_1(\omega) & \vec{f}_2(\omega) & \dots & \vec{f}_n(\omega) \end{bmatrix} \vec{u} \quad (2.43)$$

The *generalized aerodynamic force* (GAF) is the product of a (complex conjugate) modeshape displacement  $\vec{\phi}_r^H$  and a harmonic aerodynamic response  $\vec{f}_c$ :

$$\vec{q}_{r,c} = \vec{\phi}_r^H \cdot \vec{f}_c = \vec{\phi}_r \cdot \vec{f}_c \quad (2.44)$$

Thus, at any given frequency  $\omega$ , the harmonic aerodynamic forces acting on the structure due to modeshape vibrations as described in (2.43) can be combined into the GAF matrix  $\tilde{\mathbf{Q}} \in \mathbb{C}^{n \times n}$  with  $n$  modeshapes of interest.

$$\begin{aligned} \tilde{\mathbf{Q}}(\omega) &= \begin{bmatrix} \tilde{q}_{1,1} & \tilde{q}_{1,2} & \dots & \tilde{q}_{1,n} \\ \tilde{q}_{2,1} & \tilde{q}_{2,2} & \dots & \tilde{q}_{2,n} \\ \vdots & \vdots & \ddots & \vdots \\ \tilde{q}_{n,1} & \tilde{q}_{n,2} & \dots & \tilde{q}_{n,n} \end{bmatrix} \\ &= \Phi^H \tilde{\mathbf{F}}(\omega) = \begin{bmatrix} \vec{\phi}_1^H \cdot \vec{f}_1(\omega) & \vec{\phi}_1^H \cdot \vec{f}_2(\omega) & \dots & \vec{\phi}_1^H \cdot \vec{f}_n(\omega) \\ \vec{\phi}_2^H \cdot \vec{f}_1(\omega) & \vec{\phi}_2^H \cdot \vec{f}_2(\omega) & \dots & \vec{\phi}_2^H \cdot \vec{f}_n(\omega) \\ \vdots & \vdots & \ddots & \vdots \\ \vec{\phi}_n^H \cdot \vec{f}_1(\omega) & \vec{\phi}_n^H \cdot \vec{f}_2(\omega) & \dots & \vec{\phi}_n^H \cdot \vec{f}_n(\omega) \end{bmatrix} \end{aligned} \quad (2.45)$$

Care has to be taken about the scaling of the first harmonic  $\hat{p}_\eta$  and for the flutter equation later to be physically correct, the entries in the GAF matrix have to refer to the correct modal mass. When using CFD to obtain the harmonic pressure perturbations and to assess small amplitudes, the modeshape

is commonly scaled by an amplitude factor  $\hat{a}$ . As this is common practice, it is assumed that the deflection amplitudes in the reference modeshape are scaled so that  $\tilde{m} = 1$ , so the relations are:

$$\tilde{m}_{\text{cfd}} = \hat{a}^2 \tilde{m} = \hat{a}^2 \quad (2.46)$$

$$\vec{\phi}_{\text{cfd}} = \hat{a} \vec{\phi}_{\tilde{m}=1} \quad (2.47)$$

$$\vec{f}_{\text{cfd}} = \hat{a} \vec{f}_{\tilde{m}=1} \quad (2.48)$$

Thus, the  $\vec{f}_{\text{cfd}}$  from CFD is inserted in the GAF matrix as

$$\tilde{\mathbf{q}}_{r,c}(\omega) = \frac{1}{\hat{a}^2} \vec{\phi}_{r,\text{cfd}}^H \vec{f}_{c,\text{cfd}}(\omega). \quad (2.49)$$

### 2.2.6. Reduced Frequency

The angular frequency of the vibration  $\omega$  can be transformed into the non-dimensional reduced frequency  $k$ :

$$k = \frac{\omega l_{\text{ref}}}{v_{\infty}} = \frac{\omega c_b}{2 v_0} \quad (2.50)$$

with the upstream flow velocity  $v_{\infty}$  and a reference length  $l_{\text{ref}}$ . Typically the half of the chordlength  $c_b$  is used for further definitions [20]. In turbomachinery, the upstream flow velocity may be hard to determine if there are upstream stator blades or other geometric features, which limit the (computational) domain of the investigated blade row. As a surrogate, the flow velocity  $v_0$  at the inlet boundary will be used instead. The value of the reduced frequency characterizes the level of unsteadiness in the vibration. This level of unsteadiness can be divided into subgroups as described by e.g. LEISHMAN [46]. The flow is steady for  $k = 0$  and quasi-steady for  $k < 0.05$ , so that unsteady effects are small. In the range of  $0.05 < k < 0.2$ , the unsteady effects cannot be neglected anymore, and for  $k > 0.2$ , the flow is highly unsteady. As further defined by SCHWOCHOW [31], if the reduced frequency becomes  $k > 1$ , the unsteadiness is likely to not induce a flutter phenomenon anymore.

While it is easy to define the upstream flow velocity  $v_{\infty}$  for free flying wings, the flow velocity increases with the radius for rotating machinery. Especially for large fans, there is a significantly higher velocity towards the tip than at the hub. For aircrafts, the reference chordlength is often averaged over the whole wing, whereas turbomachinery bladings typically have fewer variation of the chordlength over the radius. In this thesis, the flow velocity  $v_0$  and

chordlength  $c_n$  will be measured at 90 % of the channelheight. In this area, the most significant unsteady aerodynamic effects take place.

### 2.2.7. Aeroelastic Stability Equation in Modal Form

After deciding about the relevant modeshapes for the flutter analysis – which is not necessarily a trivial task, but not discussed at the moment – the flutter equation can be set up in the modal form. Placing (2.31) and (2.43) into (2.23) and multiplying  $\Phi^H$  in front and neglecting structural damping, the flutter equation in modal form reads

$$\begin{aligned} \Phi^H \mathbf{M}_x \Phi \ddot{\vec{u}} + \Phi^H \mathbf{K}_x \Phi \vec{u} - \Phi^H \tilde{\mathbf{F}}(\omega) \vec{u} &= 0 \\ \tilde{\mathbf{M}} \ddot{\vec{u}} + \tilde{\mathbf{K}} \vec{u} - \tilde{\mathbf{Q}}(\omega) \vec{u} &= 0. \end{aligned} \quad (2.51)$$

The equation is only depending on the frequency of the oscillation. The generalized displacement vector  $\vec{u} \in \mathbb{C}^n$  is the modal participation factor of each modeshape with the total number of  $n$  modeshapes.

## 2.3. The Energy Method

The energy method (EM) or *work-per-cycle* method as described by CARTA [18], and later confirmed by MIKOLAJCZAK ET AL [21], is the classical approach for numerical flutter analysis in turbomachinery. For small deflections inducing a linear flow response, the onset of flutter is determined by the forced motion approach obtaining the pressure or force perturbations for an individual modeshape at a fixed amplitude and fixed frequency.

### 2.3.1. Rationale of the Energy Method

The basic assumption is that aerodynamic forces have a neglectable influence on the structural properties and eigenfrequencies. Looking at (2.51), if the entries in  $\tilde{\mathbf{Q}}$  are very small compared to  $\tilde{\mathbf{K}}$ , an eigenanalysis will always result in the trivial solution of the corresponding vacuum frequencies and proper eigenvectors  $\vec{u}$  are isolated vacuum modeshapes. As a consequence, the structure is effectively vibrating in vacuum [20, pp. 527-532]. The pressure fluctuations due to the vibrations produce aerodynamic work that is transferring energy from the structure into the fluid or vice versa. The stability is therefore assumed as independent of the modal mass or respectively, the mass ratio of structure-to-air. This neglects any aerodynamic coupling effects and the energy method is thus sometimes also called an uncoupled or decoupled approach.

### 2.3.2. Aerodynamic Work per Cycle

The aerodynamic work exerted per cycle period  $T$  at a surface patch  $\eta$  is

$$W_{c,\eta} = \int_0^T \dot{\vec{x}}(t) \cdot \vec{f}(t) dt. \quad (2.52)$$

The physical displacement and its time-derivative is analogous to (2.29) and the real part is resolved with the help of  $\text{Re}(z) = \frac{1}{2}(z + \bar{z})$  [47], so that for a sinusoidal motion:

$$\vec{x}(t) = \text{Re}(\vec{\phi} e^{j\omega t}) = \frac{1}{2} \left( \vec{\phi} e^{j\omega t} - \bar{\vec{\phi}} e^{-j\omega t} \right) \quad \text{and} \quad (2.53)$$

$$\dot{\vec{x}}(t) = \text{Re}(j\omega \vec{\phi} e^{j\omega t}) = \frac{1}{2} j\omega \left( \vec{\phi} e^{j\omega t} - \bar{\vec{\phi}} e^{-j\omega t} \right). \quad (2.54)$$

The aerodynamic forces are also assumed to be harmonic, so that

$$\vec{f}(t) = \tilde{\vec{f}} e^{j\omega t}. \quad (2.55)$$

With  $\vec{\phi}, \tilde{\vec{f}} \in \mathbb{C}^3$ , (2.54) and (2.55) are introduced to (2.52):

$$\begin{aligned} W_{c,\eta} &= \int_0^T \text{Re} \left( j\omega \vec{\phi} e^{j\omega t} \right) \cdot \left( \tilde{\vec{f}} e^{j\omega t} \right) dt \\ &= \int_0^T \frac{1}{2} j\omega \left( \vec{\phi} e^{j\omega t} - \bar{\vec{\phi}} e^{-j\omega t} \right) \cdot \left( \tilde{\vec{f}} e^{j\omega t} \right) dt \\ &= \frac{1}{2} j\omega \int_0^T \vec{\phi} \cdot \tilde{\vec{f}} e^{j2\omega t} - \bar{\vec{\phi}} \cdot \tilde{\vec{f}} dt \\ &= -j\pi \left( \vec{\phi} \cdot \tilde{\vec{f}} \right) = -j\pi \vec{\phi}^H \tilde{\vec{f}} \end{aligned} \quad (2.56)$$

and summed up to the global work over all surface cells:

$$W_c = - \sum_{\eta} W_{c,\eta} = -j\pi \sum_{\eta} \vec{\phi}_{\eta}^H \tilde{\vec{f}}_{\eta}. \quad (2.57)$$

In analogy to power considerations in electrical engineering, the exerted work over one period can be split in the real and reactive (imaginary) component [19]. Thus, the actual work exerted between structure and fluid is expressed in the real part. The imaginary part is the energy shuffling over one period without an effective outcome. A positive work entry ( $\text{Re}(W_c) > 0$ ) indicates that energy is transferred from the fluid into the structure and exciting the blade. Vice versa ( $\text{Re}(W_c) < 0$ ) the blade releases energy so that vibrations are damped.

Note that the sum consists of the generalized aerodynamic force of the individual surface cells, for detailed derivation see e.g. the work of MAY [19]. Therefore, the energy method is effectively a subset of the GAF matrix in (2.45), being one of the diagonal entries for the specified modeshape and frequency.

### 2.3.3. Logarithmic Decrement of Aerodynamic Damping

For a constant amplitude oscillation, the principle of energy conservation (section 2.1.2) yields a constant shuffling between potential and kinetic energy,  $E_{pot}$  and  $E_{kin}$  respectively, that is quadratically proportional to the amplitude:

$$E_{kin}(t) + E_{pot}(t) = \frac{1}{2}m\dot{x}^2(t) + \frac{1}{2}kx^2(t) = E_{s,tot} = const. \quad (2.58)$$

The total structural energy  $E_{s,tot}$  is equal to the maximum kinetic energy (at the zero deflection point). This statement also holds true for the modal form of the energy equation which is a practical way to express the structural energy in this case. The maximum energy can be derived from (2.16) for a harmonic motion with the generalized velocity as in (2.10).

$$\begin{aligned} E_{kin}^{max} &= \max \left[ \frac{1}{2} \tilde{m} \operatorname{Re} (\dot{u}^2(t)) \right] = \frac{1}{2} \tilde{m} \max \left[ \operatorname{Re} \left( (j\omega e^{j\omega t})^2 \right) \right] \\ &= \frac{1}{2} \tilde{m} \max \left[ \operatorname{Re} \left( (j\omega (\cos \omega t + j \sin \omega t))^2 \right) \right] \\ &= \frac{1}{2} \tilde{m} \max \left[ -\omega^2 \sin^2 \omega t \right] = \frac{1}{2} \tilde{m} \omega^2 \end{aligned} \quad (2.59)$$

Let the modal mass  $\tilde{m}_0$  be given at a reference amplitude  $\hat{x}_0$  (typically so that  $\tilde{m}_0 = 1 \text{ kg m}^2$ ). The amplitude of the current oscillation has the ratio of  $\hat{a}$  towards to the reference. Thus, the modal mass of the current oscillation is  $\tilde{m} = \hat{a}^2 \tilde{m}_0$  (cf. (2.46)).

$$E_{s,tot} = E_{kin}^{max} = \frac{1}{2} \tilde{m} \omega^2 = \frac{1}{2} \tilde{m}_0 \hat{a}^2 \omega^2 \quad (2.60)$$

The real part of the aerodynamic work per cycle  $\operatorname{Re}(W_c)$  is draining or feeding energy into the structure, thus changing the total structural energy  $E_{s,tot}$ . Thus,

the structural energy is changed by the amount of aerodynamic work  $\text{Re}(W_c)$  exerted over one period  $T$ . Its amplitude changes from

$$x(t) = \hat{a}_1 \hat{x}_0 \quad \text{to} \quad (2.61)$$

$$x(t+T) = \hat{a}_2 \hat{x}_0. \quad (2.62)$$

and the relation of the two amplitudes is

$$\frac{x(t)}{x(t+T)} = \frac{\hat{a}_1 \hat{x}_0}{\hat{a}_2 \hat{x}_0} = \frac{\hat{a}_1}{\hat{a}_2}. \quad (2.63)$$

Expressing the ratio of structural energy between the two instances in time as

$$\frac{E_{s,tot}}{E_{s,tot} + \text{Re}(W_c)} = \frac{\frac{1}{2} \tilde{m}_0 \hat{a}_1^2 \omega^2}{\frac{1}{2} \tilde{m}_0 \hat{a}_2^2 \omega^2} = \left( \frac{\hat{a}_1}{\hat{a}_2} \right)^2, \quad (2.64)$$

it can replace the amplitude ratio in (2.12):

$$A = \ln \frac{x(t)}{x(t+T)} = \ln \frac{\hat{a}_1}{\hat{a}_2} = \ln \sqrt{\frac{E_{s,tot}}{E_{s,tot} + \text{Re}(W_c)}} = \frac{1}{2} \ln \left( \frac{E_{s,tot}}{E_{s,tot} + \text{Re}(W_c)} \right) \quad (2.65)$$

Let assume, that the amount of aerodynamic work exerted is much smaller than the structural energy  $\text{Re}(W_c) \ll E_0$  and a linearization of the natural logarithm is possible, so that

$$\begin{aligned} \ln \frac{E_{s,tot}}{E_{s,tot} + \text{Re}(W_c)} &= -\ln \frac{E_{s,tot} + \text{Re}(W_c)}{E_{s,tot}} \\ &= -\ln \left( 1 + \frac{\text{Re}(W_c)}{E_{s,tot}} \right) \approx -\frac{\text{Re}(W_c)}{E_{s,tot}}. \end{aligned} \quad (2.66)$$

Finally, the *logarithmic decrement of aerodynamic damping* can be approximated by entering (2.66) in (2.65):

$$A \approx -\frac{1}{2} \frac{\text{Re}(W_c)}{E_{kin}^{max}} = \frac{\text{Re}(W_c)}{\tilde{m} \omega^2}. \quad (2.67)$$

This definition of damping will be referred to in this thesis if not otherwise noted.

Though the physical interpretation of the logarithmic decrement is not sound when the initial assumption of  $\text{Re}(W_c) \ll E_0$  is not met, it is a simple way to non-dimensionalize the aerodynamic work and make it comparable. Thus, will also be applied if the initial assumption is not true anymore.

### 2.3.4. Local Excitation

In analogy to the definition of the global aerodynamic damping in (2.67), a local equivalent can be given for each surface cell  $\eta$  by the local excitation

$$\epsilon_\eta = \frac{\operatorname{Re}(W_{c,\eta})}{2E_{kin}^{max} A_\eta}. \quad (2.68)$$

The local excitation is given per unit area and accounts for the size of the surface cell  $A_\eta$ . Note the sign change compared to the global damping. Positive values mean that the corresponding part of the blade feeds energy into the structure over one vibration period, thus supporting the motion and contributing to an instability. Vice versa, negative values indicate areas where the motion is suppressed. The local excitation may be useful from a designer's point of view or to understand the flutter mechanism.

By summing up all the local contributions, the global value of the aerodynamic damping is given again:

$$\Lambda = - \sum_{\eta} \epsilon_\eta A_\eta. \quad (2.69)$$

## 2.4. Aerodynamic Coupling of Modeshapes

If the aerodynamic forces in (2.51) cannot be neglected, the flutter equation can be treated as an aeroelastic eigenvalue problem. By using a frequency domain method, the structural and aerodynamic parts can be treated separately and combined later. Different methods exist that solve the linear flutter problem, i.e. the “ $k$  method”, “ $p$  method”, “ $p$ - $k$  method” or “ $g$  method” [20, 36, 48, 49, 31]. Each method has its own advantage/disadvantage and complexity in terms of numerical implementation, or representation respectively approximation of the physics. The chosen method for this thesis is the  $p$ - $k$  method, that is the most commonly used in today's aircraft flutter analysis.

This section deals with the adaptation of the “classical”  $p$ - $k$  method used in fixed wings to turbomachinery usage. The name  $p$ - $k$  method stems from the definition of the eigenvalue  $p$  and the dependence of the GAF matrix on the reduced frequency  $k$  [36]. However, a different definition will be followed in this thesis. For the sake of convenience/form, it is still called the “ $p$ - $k$  method” throughout the remainder of the thesis, as the fundamental assumptions and approach is the same.

### 2.4.1. Aeroelastic Eigenvalue Problem

#### Stability Equation

The flutter equation in modal form – without damping as in (2.51) and introducing the generalized displacement  $\vec{u}$  analogous to section 2.2.2 – becomes

$$\lambda^2 \widetilde{\mathbf{M}} \vec{u} + \widetilde{\mathbf{K}} \vec{u} - \widetilde{\mathbf{Q}}(\lambda) \vec{u} = 0. \quad (2.70)$$

The aerodynamic responses are in general dependent on the eigenvalue  $\lambda$ . For low damping, HASSIG demonstrated that a good approximation of  $\widetilde{\mathbf{Q}}$  can be achieved if it is only depending on the reduced frequency [36]. As a consequence, the p-k method in general is only valid for the special case of zero damping and therefore in the vicinity of flutter onset. For highly damped or excited systems, when strong flow nonlinearities are likely and higher vibration amplitudes occur, an error has to be expected which can yield misleading results [30]. However, at the point of zero damping, the p-k method is exact and can therefore be used to predict a stability boundary. Thus,  $\widetilde{\mathbf{Q}} \approx \widetilde{\mathbf{Q}}(\omega)$  and by reformulating (2.70), so that

$$-\lambda^2 \widetilde{\mathbf{M}} \vec{u} = \left( \widetilde{\mathbf{K}} - \widetilde{\mathbf{Q}}(\omega) \right) \vec{u}, \quad (2.71)$$

the flutter equation is a general eigenvalue problem depending on the (angular) frequency  $\omega$  of the vibration, that yields a set of  $\lambda_i^2 = (-\delta_i + j\omega_i)^2$ . As  $\omega$  changes with the eigenvalue, but influences the  $\widetilde{\mathbf{Q}}(\omega)$ , an iterative solution process is required. The corresponding eigenvectors  $\vec{u}_i$  are the *modal participation factors* of the considered vacuum modeshapes and describe the *aeroelastic modeshape* (combination of vacuum modes).

In aeroelasticity of turbomachinery, the *logarithmic decrement*  $\Lambda$  is more commonly used to describe the damping characteristics. The stability equation (2.70) yields the damping constant  $\delta$ . As already described in section 2.3.3, the definitions are only physical for underdamped systems. Nevertheless, they represent a non-dimensionalized form of the damping or excitation and can be used for comparison even if the system is not strictly underdamped. The logarithmic decrement is converted from the damping constant with the relation found in (2.12):

$$\Lambda = \delta \frac{2\pi}{\omega} \quad (2.72)$$

#### Root of Eigenvalue to Extract Damping and Frequency

Beware that  $\lambda_i^2$  yields an ambiguous solution for the frequency as the square root has to be extracted. With *de Moivre's theorem* [47] of  $\sqrt[n]{z} = \sqrt[n]{|z|} e^{j(\varphi/n+2k\pi/n)}$



where  $k = 0, \dots, n - 1$ , the square root of the eigenvalue  $\lambda^2 = r e^{j\varphi}$  with  $r, \varphi \in \mathbb{R}$  is taken by

$$\sqrt{\lambda_i^2} = \begin{cases} \sqrt{r} e^{j\varphi/2} \\ \sqrt{r} e^{j(\varphi/2+\pi)} \end{cases} \quad (2.73)$$

and thus

$$\lambda_{i,\pm} = \sqrt{(-\delta_i + j\omega_i)^2} = \begin{cases} \lambda_{i,+} = -\delta_i + j\omega_i \\ \lambda_{i,-} = \delta_i - j\omega_i \end{cases} . \quad (2.74)$$

Only the square root with a positive imaginary part  $\text{Im} \left( \sqrt{(-\delta_i + j\omega_i)^2} \right) > 0$  is the one with a physical reason.

### Physical Interpretation

The system's degrees of freedom are the modeshapes with properties of the modal mass  $\tilde{m}_i$  and the modal stiffness  $\tilde{k}_{i,\pm}$  included in the diagonal matrices  $\tilde{\mathbf{M}}$  and  $\tilde{\mathbf{K}}$ , respectively. The GAF matrix  $\tilde{\mathbf{Q}}$  is fully populated. The diagonals are the influence of each modeshape on itself. The off-diagonal terms are the coupling terms of unsteady aerodynamic forces.

To get a better grasp of this, let us perform a thought experiment. One vacuum modeshape starts to vibrate at its vacuum frequency and thus produces unsteady aerodynamic forces which fills one column of  $\tilde{\mathbf{Q}}$ . The other degrees of freedom now see an excitation and respond with an individual amplitude. This amplitude is majorly influenced by the (modal) mass of the responding oscillator. As the stiffnesses combine, the frequency of the vibration is also changed. This will induce a change in the unsteady aerodynamic forces from the first modeshape and in return also a change in the amplitude of the responding modeshapes. The lower the mass to be excited, the higher the responses are. For now, the other modeshapes do not produce unsteady aerodynamic forces. So this example continues, until a new equilibrium of frequency and amplitudes is achieved. If we now allow aerodynamics for the other modes, they will also produce entries in  $\tilde{\mathbf{Q}}$  and perform an excitation of the original and other modeshapes, becoming a coupled system.

This interplay is included in the off-diagonals of  $\tilde{\mathbf{Q}}(\omega)$ . It also becomes apparent, that very small numbers in comparison to  $\tilde{\mathbf{K}}$  will have a neglectable outcome on the eigenanalysis which is the rationale of the energy method described in section 2.3.

### 2.4.2. Solving the Flutter Equation

The variable  $q_s$  is introduced into (2.71) as a scaling factor of the GAF matrix for the purpose of mode tracking and as a convergence technique.

$$-\lambda^2 \tilde{\mathbf{M}} \tilde{\mathbf{u}} = \left( \tilde{\mathbf{K}} - q_s \tilde{\mathbf{Q}}(\sigma, \omega) \right) \tilde{\mathbf{u}} \quad (2.75)$$

In line with the linear theorem in LANE's theory, it is assumed that modal coupling only happens within the same inter-blade phase angle (resp. nodal diameter). In the linear and harmonic system, forces exchanged between IBPAs cancel out over one period and are therefore neglected. For clarity of this, the IBPA has been added to the dependency of  $\tilde{\mathbf{Q}}$ .

#### Differences Between Fixed Wing and Rotating Machinery

In the classical fixed wing analysis, the natural frequencies and modeshapes of the structure remain unchanged throughout the flight envelope and independent of the load case, although that might not be true anymore for highly flexible wings [50, 51] (*M. Zimmer, personal communication, DLR-Institute of Aeroelasticity, 2018-2019 ongoing discussion*). The wing will ultimately start to flutter when the flight speed becomes high enough. The strategy to solve the flutter equation is straight forward by successively increasing the flight speed (and thus the dynamic pressure) until flutter occurs. Depending on the flow condition, the GAF matrix may be determined by (semi-)analytical equations [52] or via CFD, the latter one especially if Mach and Reynolds number effects in compressible flow play an important role [37, 38].

In turbomachinery, natural frequencies and modeshapes vary largely with rotational speed (and sometimes also with the throttling state), so the physical rationale in solving the flutter equation is a little different. As a consequence, for each operating point the flutter equation needs to be solved individually.

The solution is only of interest, if the right proportion of modal mass, modal stiffness and generalized aerodynamic forces is met. The process in getting there may be achieved in such a way that implausible physics are used, as it is only done for mode tracking purpose. From a mathematical point of view, simply running  $q_s = 0 \dots 1$  is justified. Technically, the mass ratio is reduced with increasing the factor  $q_s$ , starting with infinite mass ratio at  $q_s = 0$ , as only vacuum modeshapes result. At  $q_s = 1$  the mass ratio used to calculate the GAFs is matched.

**Definition: Naming of the  $p$ - $k$  method in this thesis.** The eigenvalue in HASSIG's paper has the sign  $p$ , in this thesis it is  $\lambda$  to avoid confusion with the

variable for pressure. The reduced frequency  $k$  is not part of the GAF matrix dependency for practical reasons. Thus, the formal name of the used method here would need to be called  $\lambda$ - $\omega$  *method*. CFD solvers in turbomachinery will require the angular frequency as an input in some form and the evaluation for  $k$  is a mere pre-/post-processing step. Note that the flutter equation can be expressed in order to depend on the reduced frequency if needed.

## Mode Tracking

The solution of the flutter equation is an iterative process with an initial guess for  $\omega$ . The eigenanalysis yields  $n$  roots for the system, each contains a new  $\omega$  but only one of them is physically reasonable. The task will be to find, or *track*, the “right” modeshape for the next iteration. For each mode to be tracked, the iterative process is started from the beginning.

To decide which eigenvalue is selected, different methods exist. The simplest way is to sort the eigenvalues by frequency and choose the index which corresponds to the index of the tracked mode. In lightly coupled cases where frequencies of the aeroelastic system are close to the in-vacuo structural frequencies, this works very good. For strongly coupled systems with frequency coalescence or frequency crossing, a modal assurance criterion (MAC) can be applied to sort the resulting eigenvectors  $\vec{u}$  compared to the previous iteration.

The *complex MAC* value when comparing two complex vectors  $\vec{u}_1$  and  $\vec{u}_2$  is defined by [53]

$$MAC(\vec{u}_1, \vec{u}_2) = \frac{|\vec{u}_1^H \vec{u}_2|^2}{(\vec{u}_1^H \vec{u}_1) (\vec{u}_2^H \vec{u}_2)}. \quad (2.76)$$

If not explicitly stated otherwise, this criterion is used for mode tracking.

In special cases, it might not be sufficient enough as MAC values are close together. A *pole-weighted MAC* value containing also the complex eigenvalues  $\lambda_1, \lambda_2$  can improve the identification [54]:

$$pw-MAC(\lambda_1, \vec{u}_1, \lambda_2, \vec{u}_2) = \frac{\left( \frac{|\vec{u}_1^H \vec{u}_2|}{|\lambda_1 + \lambda_2|} + \frac{|\vec{u}_1^T \vec{u}_2|}{|\lambda_1 + \lambda_2|} \right)^2}{\left( \frac{\vec{u}_1^H \vec{u}_1}{2|\operatorname{Re} \lambda_1|} + \frac{|\vec{u}_1^T \vec{u}_1|}{2|\lambda_1|} \right) \left( \frac{\vec{u}_2^H \vec{u}_2}{2|\operatorname{Re} \lambda_2|} + \frac{|\vec{u}_2^T \vec{u}_2|}{2|\lambda_2|} \right)} \quad (2.77)$$

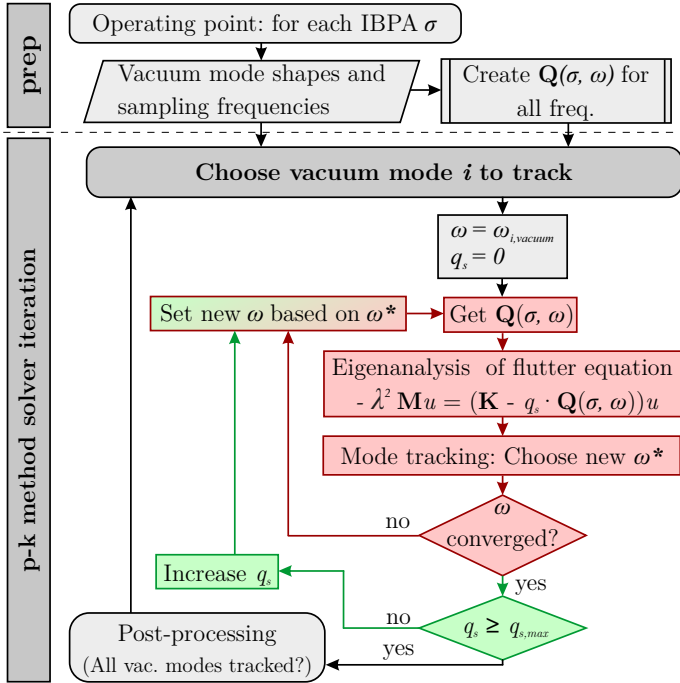


Figure 2.6.: Flowchart of p-k Method (adapted from [44, 45])

**Definition: Aeroelastic Modeshape.** The eigenvector  $\vec{u} \in \mathbb{C}^n$  combines the  $n$  vacuum modeshapes of interest for a specific eigenvalue of the flutter equation. The aeroelastic modeshape is thus a combination of amplitude and phase shift between the fundamental degrees of freedom. Especially if only light coupling between modeshape families occur, the associated vacuum modeshape is the dominating contributor.

**Definition: Aeroelastic Branch.** An aeroelastic branch is the track of an aeroelastic modeshape throughout the iterative solution. As the starting vacuum modeshape is associated with the branch, the branch can be named accordingly, e.g. “pitch branch” or “bending branch”.

## Workflow and Convergence Iteration of P-K Method

The procedure is depicted in fig. 2.6: We start with an initial guess of  $\omega$  (preferably the vacuum frequency of a modeshape) at  $q_{s,j=0} = 0$  with the trivial solution (vacuum modeshapes) and successively increase  $q_s$  in an outer loop  $j$ :

$$q_{s,j+1} = q_{s,j} + \Delta q_s \quad (2.78)$$

$\Delta q_s$  is a user choice, but will mostly depend on the gradient of

$$\frac{\omega(q_{s,j+1}) - \omega(q_{s,j})}{\Delta q_s}. \quad (2.79)$$

The loop is carried out until  $q_{s,max} = 1$ , where the right proportion of structural and aerodynamic forces is reached. A certain *under-* or *overscaling* (running  $q_s$  to a value other than 1) can be utilized for mass ratio effects as demonstrated later.

In an inner loop  $k$  at each  $q_{s,j}$  the equation (2.75) is solved iteratively: First, the eigenvalue analysis is performed and next, the mode tracking procedure is applied. The corresponding eigenvalue's frequency is retrieved as  $\omega_{k+1}^*$ :

$$\omega_{k+1} = \omega_k + \epsilon(\omega_{k+1}^* - \omega_k) \quad (2.80)$$

Relaxation of  $\omega_{k+1}^*$  with a simple damping factor of  $\epsilon = 0.7$  proved to be sufficient for most cases in order to stabilize the numerical solution. If not otherwise noted, this factor is used throughout the thesis. The next inner loop step  $k + 1$  is now carried out with the new  $\omega_{k+1}$  until convergence of  $\omega$ , before returning to the outer loop and further iterating  $q_s$ .

These outer loop has to be applied for all aeroelastic branches  $i$  that should be tracked, as depicted in fig. 2.7.

### 2.4.3. Physical Representation of Aeroelastic Modeshapes

The aeroelastic mode of an aeroelastic branch is the combination of structural modeshapes. The elements  $i$  of the complex eigenvector  $\vec{u} = (u_1, \dots, u_i, \dots, u_n)^T$  from (2.75) contain the modal participation factor  $\Gamma_i$  and

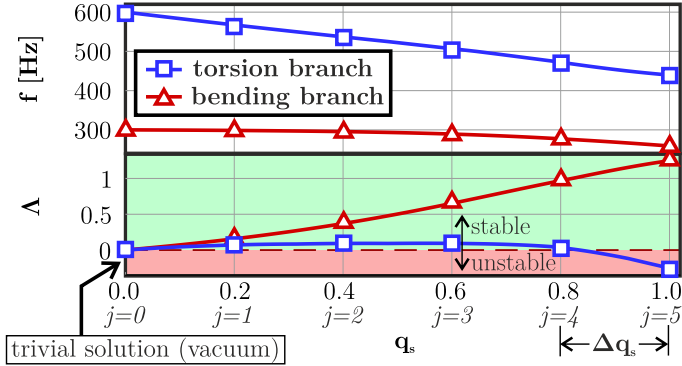


**Figure 2.7.:** Example for frequency and damping of the aeroelastic branches over  $q_s$  for a system with two structural DOF (adapted from [44, 45])

the phase  $\varphi_i$ . Analogous to (2.31), the aeroelastic modeshape  $\vec{\psi} \in \mathbb{C}^m$  is the sum of all participating structural modeshapes.

$$u_i = \Gamma_i (\cos \varphi_i + j \sin \varphi_i) \quad (2.81)$$

$$\vec{\psi} = \Phi \vec{u} = \sum_{i=1}^n \vec{\phi}_i \Gamma_i (\cos \varphi_i + j \sin \varphi_i) \quad (2.82)$$

The physical deflection at a given time is then the real part:

$$\vec{x}(t) = \text{Re} \left( \vec{\psi} (\cos \omega t + j \sin \omega t) \right) \quad (2.83)$$

## 2.5. Parameters in Coupled-Mode Flutter Analysis

### 2.5.1. Mass Ratio

The mass ratio  $\mu$  is defined as

$$\mu = \frac{m_{\text{blade}}}{\rho_{\infty} \pi (c_b/2)^2 h} \quad (2.84)$$

with  $m_{\text{blade}}$  as the mass of the blade without the root or disk, the upstream fluid density  $\rho_{\infty}$ , the chord length  $c_b$  (in case of 3D blades, a reference chord length) and the channel height  $h$ , see fig. 2.8a.

The scaling factor  $q_s$  in the flutter equation has a physical interpretation under the premise, that changing the mass ratio  $\mu$  does not change the vacuum frequencies and modeshapes<sup>4</sup>.

Considering the existing  $\tilde{\mathbf{Q}}$  at a mass ratio of  $\mu_0$  with  $\tilde{m}_0$ , analogous to (2.46), changing the mass ratio to  $\mu_1$ , the modal mass changes to  $\tilde{m}_1^*$ , with the relation

$$\tilde{m}_1^* = \hat{a}^2 \tilde{m}_0 \quad (2.85)$$

This means that, analogous to the relations in (2.46) and (2.47), the amplitude of the modeshape would have to be scaled by  $1/\hat{a}$  to get a modal mass of 1 for the new mass ratio  $\mu_1$ . However, the absolute amplitude and thus the modeshape  $\vec{\phi}_0$  is the same on both sides of (2.85). The fundamental definition of the modal mass for a single DOF oscillation with the mass  $m$ , the material density  $\rho$  and the volume  $V$  is

$$\tilde{m} = \vec{\phi}^H m \vec{\phi} = \vec{\phi}^H \rho V \vec{\phi}. \quad (2.86)$$

Replacing the modal masses in (2.85) by this definition, it now reads

$$\vec{\phi}_0^H \rho_1 V_{\text{blade}} \vec{\phi}_0 = \hat{a}^2 \vec{\phi}_0^H \rho_0 V_{\text{blade}} \vec{\phi}_0. \quad (2.87)$$

Eliminating left and right hand side equivalents, it can be derived:

$$\rho_1 = \hat{a}^2 \rho_0 \quad (2.88)$$

The reduction to a single mass point is done for better understanding and clarity. Note that this operation can be easily written for a system with multiple mass points, resp. DOFs, as in a typical CSM model and still lead to the same outcome. Setting the number of the mass points to  $k$ , the modal mass is the sum of all individual elements  $i$ . Each element has the local displacements  $\vec{\phi}_i$  of the considered modeshape, the mass  $m_i$ , and the cell volume  $V_i$ , so that

$$\tilde{m} = \sum_{i=1}^k \vec{\phi}_i^H m_i \vec{\phi}_i = \vec{\phi}_i^H \rho_i V_i \vec{\phi}_i. \quad (2.89)$$

which can be put into (2.85) on both sides and the equivalents are eliminated in the same manner, so that (2.88) results.

---

<sup>4</sup>Although this is not realistic in terms of actual structural dynamics, as changing the mass has a direct influence on frequencies. For the sake of the purpose here – to demonstrate the influence of aerodynamic modal coupling – it is usable as a technique.

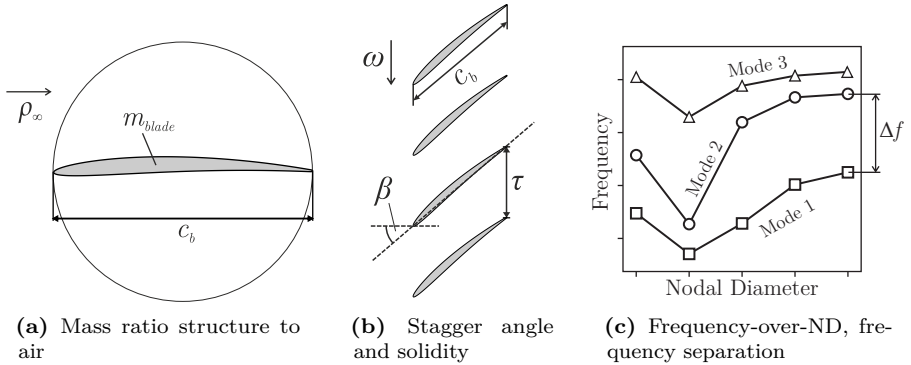


**Figure 2.8.:** Parameters in coupled-mode flutter analysis

The two mass ratios  $\mu_0$  and  $\mu_1$  are put in relation and then expanded with (2.84). The blade mass is replaced by the definition  $m_{\text{blade}} = \rho V_{\text{blade}}$ . The relation becomes

$$\frac{\mu_0}{\mu_1} = \frac{m_{\text{blade},0}/m_{\text{air}}}{m_{\text{blade},1}/m_{\text{air}}} = \frac{\rho_0}{\rho_1}. \quad (2.90)$$

To scale the GAFs for the new  $\mu_1$ , the relation in (2.49) can be utilized. Comparing it with (2.88) and (2.90),  $q_s$  is the “ratio of mass ratio” or the quadratic inverse of the scaling factor  $\hat{a}$ :

$$\tilde{\mathbf{Q}} \Big|_{\mu_1} = \frac{1}{\hat{a}^2} \tilde{\mathbf{Q}} \Big|_{\mu_0} = q_s \tilde{\mathbf{Q}} \Big|_{\mu_0} \quad (2.91)$$

$$q_s = \frac{\mu_0}{\mu_1} = \frac{\rho_0}{\rho_1} = \frac{1}{\hat{a}^2} \quad (2.92)$$

The  $\tilde{\mathbf{Q}}$  for a certain motion only has to be computed once (the reference modal mass or mass ratio) and can then be transcribed to a certain  $q_s$  (the target mass ratio). From a physical perspective, the p-k iterations are running from infinite mass of the blade until the target mass ratio is reached.

## 2.5.2. Solidity

The solidity  $s$  is a dimensionless description of the distance between two blades:

$$s = \frac{c_b}{\tau} \quad (2.93)$$



with the chordlength  $c_b$  and the blade pitch  $\tau$ . As seen in fig. 2.8b, it does not fully describe the spatial distance between two blades. A high stagger angle  $\beta$  will cause the leading edge and trailing edge of two adjacent blades to be close together. Nevertheless, the solidity leads to an impression about the ratio of structure to air volume in the channel. A higher solidity causes stronger aerodynamic disturbances on the adjacent blades.

From a designer's point of view, lowering the solidity happens when the number of blades in one stage is reduced but the same design space (inner/outer diameters) is kept. Of course reducing the number of blades per stage is not a trivial design aspect and also comes with a higher individual blade loading when the same amount of pressure ratio shall be reached.

### 2.5.3. Frequency Separation and Distance

The frequency separation or frequency distance between modeshapes  $i$  and  $j$  is only of interest within the same nodal diameter, as coupling can only happen within a certain nodal diameter vibration pattern. Frequency separation in absolute values alone is not a good indicator or suitable for comparison in coupled-mode flutter analysis. The ratio of the involved structural modeshapes' frequencies, e.g.  $f_i$  and  $f_j$  (where  $f_i < f_j$ ) is also important:

$$f_{\text{ratio,separation}} = \frac{f_j}{f_i} \quad (2.94)$$

The closer the ratio is to 1, the higher the probabilities are for an aerodynamic coupling. In literature, sometimes the relative frequency separation is used:

$$f_{\text{rel,separation}} = \frac{\Delta f_{i,j}}{f_i} = \frac{f_j - f_i}{f_i} \quad (2.95)$$

For this ratio, the value needs to be close to 0 for higher probabilities of aerodynamic coupling. Both ratios represent to same principle, but represent different aspects.

A generic diagram of frequency over nodal diameter for three different modeshape families is given in fig. 2.8c. In the given generic example, the second mode has a low frequency distance towards the first mode for the lower nodal diameters and with the third mode in the higher nodal diameters. However, close frequencies are neither a necessary nor a sufficient condition for aerodynamic modal coupling to take place. The GAF resulting from the vibration also need to meet the right excitation patterns. Most likely to couple are modeshape combinations with one bending and one torsional dominated mode (so-called bending-torsion flutter).

### 2.5.4. Normalized Logarithmic Decrement

To compare the energy method and p-k method for different mass ratios, the logarithmic decrement at a mass ratio  $\mu_i$  is normalized with the ratio of mass ratio  $\mu_i/\mu_0$ , analogous to (2.92), so that the energy method results retain the value of the reference mass ratio  $\mu_0$ . This is done in order to show that a drift away from the energy method results. When lowering the mass ratio, the material density gets smaller. If the same physical amplitude of the mode shapes is retained, the work per cycle stays the same in (2.67), but the modal mass decreases. As a result, the absolute value of the logarithmic decrement increases. To avoid this misleading impression of the system becoming more stable, the damping values are normalized. Note that in the diagrams of the aeroelastic branches, the logarithmic decrement is not normalized by this factor.



# 3

## Numerical Approach

*The numerical solvers and the fundamental concepts for coupling between them is presented. As the different tools are exchanging information and rely on information of the others, a numerical toolchain for the aeroelastic computations has been implemented and is briefly introduced.*

### 3.1. Computational Fluid Dynamics

The TRACE (Turbomachinery Research Aerodynamic Computational Environment) code is a solver suite for internal flows especially in turbomachinery and consists not only of a fluid solver but also integrates a great variety of pre- and post-processing tools. It is developed and maintained at the DLR-Institute of Propulsion Technology [55, 56] and used at several German universities as well as MTU Aero Engines and Siemens. The version 9.1. of TRACE is used for all computations shown in this thesis.

TRACE solves the compressible three-dimensional Navier-Stokes equations in a rotating frame of reference [56] for multistage and multipassage setups in hybrid-grid (structured/unstructured) setups, but also has efficient implementations of reduced order setups. Unsteady simulations can be run via a nonlinear time-marching solver, either with rigid, prescribed motion, or freely vibrating blades. Fluid/structure coupling (FSC) resp. fluid/structure interaction (FSI) is available via a modal approach [57, 58]. The modal dynamic equations are integrated in time with a Newmark scheme and solved with the Newton method. The coupling of flow and structure is performed with a serial Gauss-Seidel scheme [59]. For reduced computational effort, frequency domain (FD) methods included in TRACE are a time-linearized and a nonlinear harmonic balance (HB) solver in the [60, 61, 62]. The time-linearized solver bases on a frozen eddy viscosity approach, which is not sufficient in the transonic regime, when e.g.

shock-induced flow separation occurs [63, 64]. Due to the mathematical basis of the harmonic balance method, the unsteady perturbations of the turbulence are included in the simulation if not explicitly deactivated. All presented results from FD use the HB module, considering only the fundamental harmonic (1st) with nine sampling points, a constant CFL number of 5 and the 0th harmonic corresponding to mean flow coupling is activated.

TRACE implements a variety of turbulence models. All computations in this thesis are carried out with the Wilcox  $k-\omega$  turbulence model [65, 66]. Periodic boundary conditions can be applied in the circumferential direction, so that only one blade passage per rotor is needed in steady-state simulations. Only the averaged values are exchanged at interfaces between two adjacent rows with a mixing plane implementation. In contrast, unsteady computations require the time-dependent exchange of physical variables. Thus, phase-lag boundary conditions are available in TRACE which allow the setup to be restricted only the one passage again [56].

At inlet and outlet boundaries, non-reflecting boundary conditions (NRBC) in the formulations according to Giles can be applied [67]. There are mainly two formulations (one-dimensional and two-dimensional), both of them are used in this thesis for different purposes [68, 69, 70, 71, 72]: NRBC are strictly only analytically defined in the frequency domain, but there are efforts to translate the formulations into the time domain. The 1D variation neglects some of the critical wave propagation, which reduces the physical validity in some cases, if the inlet or outlet boundary is too close to the blades. However, it is computationally cheap, which makes it attractive especially for time domain simulations. The 2D formulation in the time domain is implemented via a Fourier decomposition and relies on the knowledge of the fundamental frequencies in the fluid flow. Otherwise, the solver has to assume the fundamental frequency, but this task is not trivial and can quickly lead to unphysical behavior. This can be circumvented by a preceding spectral analysis. On the downside of this, if no fixed frequency is set in the simulation (as it is the case for a free vibration with no a priori determinable vibration frequency), the computational effort is extremely high because all possible frequencies down to the Nyquist frequency have to be considered. For applications where actual statements of the aerodynamics need to be made, it is almost paramount to use the 2D formulation. In the course of this thesis, the frequency domain results shall be verified against time domain simulations. In this special case, it is acceptable to use the 1D variation in order to have the same physical interpretation of the flow field in both domains. Once this verification is achieved and only frequency domain methods are used thereafter for the validation, the 2D formulation is applied.

## 3.2. Computational Structural Mechanics

NASTRAN, an acronym for *NASA Structural Analysis*, is a finite element analysis program originally developed for NASA and has since been integrated into a number of different software packages, the most prominent by MSC Software [73] is used in this thesis in the release version of 2017.

NASTRAN integrates many different structural analysis steps, internally called “sequences”, including nonlinear static deformation and prestressed normal mode analysis. Also included is a cyclic symmetry modal analysis as described in section 2.2.3. The finite element mesh in Nastran is capable of handling hybrid-grids containing shell and volume elements with varying number of nodes (e.g. triangle, quadrilateral, tetrahedron, or hexahedron) and also a variety of non-volumetric elements (e.g. beams or rigid body elements) [74].

## 3.3. Aeroelastic Coupling

Aerodynamic loads and static deformations are a coupled problem and both disciplines, aerodynamics and structural mechanics, have to be executed individually. In the most usual case, the meshes in CFD and CSM do not share the same nodes or cell surfaces, so when information between both solver has to be exchanged, a mapping between the different meshes is needed.

Figure 3.1 shows the schematic of a static fluid/structure coupled process. The loop starts with a CFD run and the surface loads are then mapped onto the CSM mesh. The static structural deflections are applied to the CFD surfaces and a mesh morphing algorithm is utilized to deform the volume mesh of CFD. The loop starts again with a new CFD computation and is iterated until convergence of static deformations and aerodynamics is reached.

In turbomachinery analysis, the CFD mesh is typically generated for an aerodynamic design point (“OP 0”), whereas the structural mesh has to be the unloaded, or “cold”, geometry<sup>5</sup>. Thus, the CSM deflections  $\Delta x_{c \rightarrow X}$  from the “cold” to the investigated “OP X” cannot be directly applied onto the CFD surfaces. The offset  $\Delta x_{c \rightarrow 0}$  of each CSM node between the “cold” and “OP0” geometry has to be known. One way to address this, is the so-called “hot-to-cold” transformation (as will be described below). As illustrated in fig. 3.2a, the deflections  $\Delta x_{0 \rightarrow X}$ , that are to be mapped onto the CFD surface, are

$$\Delta x_{0 \rightarrow X} = \Delta x_{c \rightarrow X} - \Delta x_{c \rightarrow 0}. \quad (3.1)$$

---

<sup>5</sup>Unlike in fixed-wing analysis, where both meshes are typically generated from a so called “jig-shape”, i.e. the manufacturing geometry from CAD data.

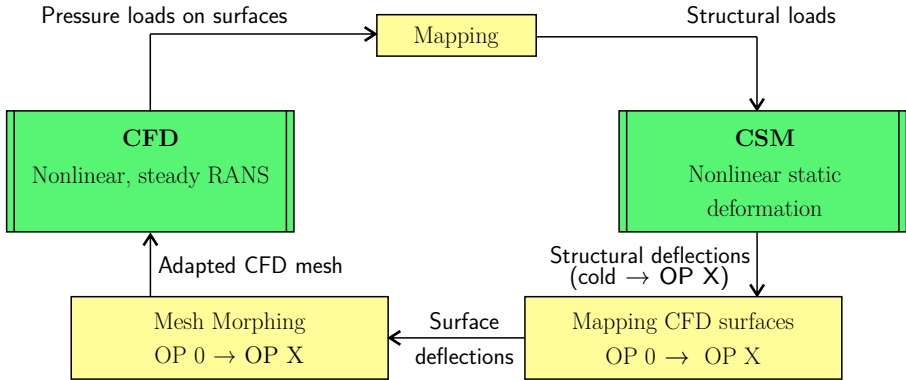


**Figure 3.1.:** Static fluid structure coupling process

The actual transfer of the variables is performed by the surface mapping algorithm in the *TRACE suite* [75].

For the mapping of the pressure loads onto the CSM mesh, the mapping assignments have to be generated in the same deflection state of both meshes, what can be done once at the “OP0” (where the CSM mesh is typically generated from the CFD surfaces) and reused for all following coupled simulations. The strategy is to find all overlapping CFD surface cells of each individual CSM surface cell, see fig. 3.2b, and weighting factors are calculated on the overlap percentage. This scheme works for both shell and volume elements on the FE side. With this strategy, the same pressure distribution is transferred from CFD to CSM, circumventing issues with cutting loads and moments as long as sufficient mesh resolution is present on both sides.

The mesh morphing algorithm used in this thesis is based on radial basis function interpolation [76, 77]. The tool *RaBaDz* implements the algorithm with specifics for turbomachinery application [78].

### 3.4. Aeroelastic Toolchain

The required steps when running an aeroelastic analysis consist of a long line of different tools, programs and heavy data processing in-between. To facilitate all those steps, a toolchain called *ATAC* (*A Toolchain for turbomachinery Aeroelasticity Computations*) was implemented [79]. *ATAC* incorporates the complete steps from setup to computations and post-processing and analysis in a unified environment. It is intended to control almost all computation steps

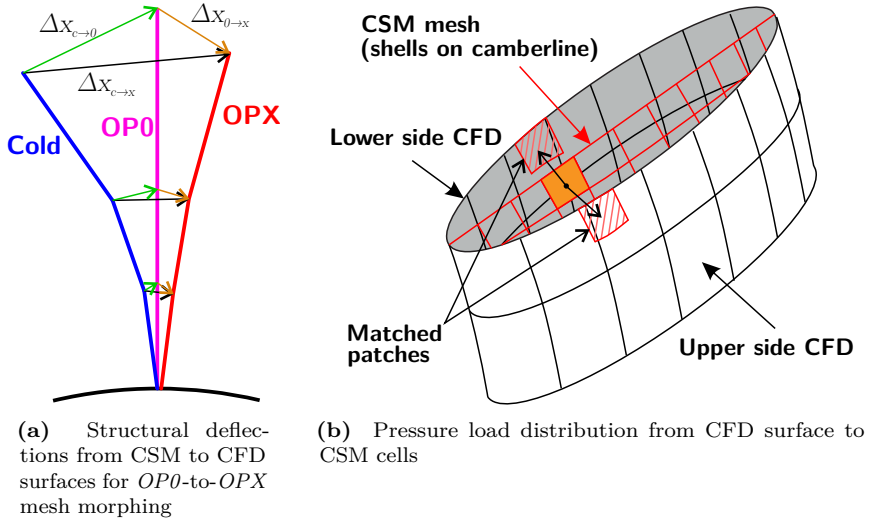


**Figure 3.2.:** Mapping strategies in FSC

with text-based input files and command line executes and removes the necessity for the user to change and add program code.

The concept of the toolchain is presented in fig. 3.3. The common database represents the geometry information and provides all the meshes, as well as the coupling and mapping data. To initialize the toolchain, the user has to provide data in a standardized input format. The basic CFD and CSM meshes are first provided in a certain “running” shape, typically the peak efficiency or aerodynamic design point (ADP). With this information, the so-called “unrunning” or “hot-to-cold” procedure can be performed. It results in the manufacturing or “cold” structural geometry [13, 80], which will be used in later analysis. The mapping information as described in section 3.3 is gained based on both running shapes and remains the same for all operating points.

Each steady-state operating point is saved in a standardized format and further computations are triggered by the user as required or requested. The basic workflow represents the typical aeroelastic analysis step by step:

1. Steady CFD/FSC: Based on the definition of an operating point, given by inlet conditions, the rotational speed and outlet conditions, i.e. back pressure or mass flow, the steady-state fluid solution is obtained. In case a fluid/structure coupling is activated, the iteration process described in



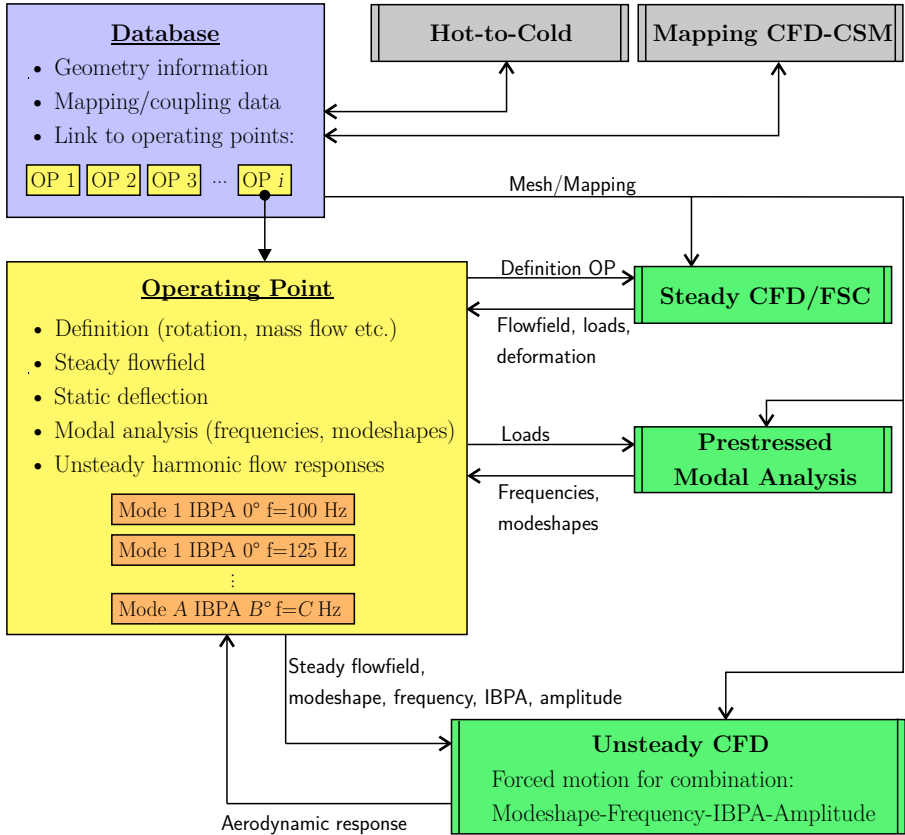


**Figure 3.3.:** Concept of aeroelastic toolchain ATAC

section 3.3 is run. As a result, the steady flowfield and the structural deformations are stored in the database.

2. Modal analysis: The structural modeshapes and their corresponding eigenfrequencies are obtained by prestressed normal mode analysis.
3. Flutter analysis:
  - The flutter analysis (energy method or p-k method) requires a set of unsteady CFD computations with forced motion.
  - Each computation is based on a specific modeshape, frequency, IBPA, and amplitude combination. The appropriate set of unsteady computations is generated from user input, either by using global values for

a desired range (which is likely used in the first round of the analysis) or by explicitly stating the parameters in a list (which is useful for a more detailed study if necessary).

- All unsteady computations are stored in the database for further evaluation.

All steps require the database to provide the aforementioned coupling and mapping data for quick exchange of state variables (pressure, deflections, etc.) on the boundary surfaces. Once the simulation part is done, both methods (energy method and p-k method) are post-processing steps in terms of the whole workflow. The post-processing tools are also integrated in the toolchain and rely on the standardized storage which the simulation part produced.

In general, the solvers for fluid and structure are exchangeable as the whole toolchain is object-oriented. For the results shown in this thesis, the solvers described above – namely *TRACE* and *NASTRAN* – were fully integrated and used.



# 4

## Geometries and Test Cases

### 4.1. FUTURE-EPFL 2D Linear Cascade

The *FUTURE-EPFL* airfoil is taken from a rig setup of an existing non-rotating annular compressor cascade, which was previously investigated experimentally as well as numerically [81, 82, 83]. The geometry is sliced at mid-span (fig. 4.1) and arranged as a linear cascade in a Q3D mesh (fig. 4.2), and will be called “FUTURE-2D-LC”.

The structured CFD grid is wall-resolved with  $y^+ < 1$  and contains roughly 26 000 volume cells per passage. In the generic structural model as shown in fig. 4.3, the elastic axis (E.A.) and the center of gravity (C.G.) are at the same physical coordinates of 50% chord length. Thus, heave and pitch motions are structurally decoupled and any coupling is solely aerodynamic. The spring constants  $k_h, k_\alpha$ , in combination with the mass and mass moment of inertia of the blade, are trimmed to achieve desired natural frequencies and mass ratio of structure-to-air.

Three flow conditions will be used later on, one subsonic and two transonic. For all operating points, the total pressure and total temperature is identical, only the inflow angle  $\alpha_0$  and static back pressure is varied as listed in table 4.2 to achieve the flow conditions which are shown in fig. 4.4. The transonic points have a higher angle-of-attack than the subsonic point and both have a strong shock on the suction side. The supersonic bubble is larger for the second transonic case and the comparison between these two cases can be used for sensitivity analysis regarding the non-linearity of the shock area. To get an impression about the non-dimensional reduced frequencies, a selection is listed in table 4.3.

**Table 4.1.:** Parameters of the FUTURE-2D-LC Geometry

Airfoil	FUTURE-EPFL annular compressor
Blades	$N = 20$ (in full wheel)
Chord length	$c_b = 69$ mm
Stagger angle LE-TE	$\beta_S = 60^\circ$
Pitch	$\tau = 56.55$ mm
Solidity	$s = c_b/\tau = 1.22$

**Table 4.2.:** FUTURE-2D-LC Operating Points

	Subsonic	Transonic I	Transonic II
$T_{t,0}$ [K]	313.15	313.15	313.15
$p_{t,0}$ [kPa]	170	170	170
$\rho_0$ [kg m <sup>-3</sup> ]	1.646	1.352	1.295
$\alpha_0$	62.2°	65.2°	65.2°
$Ma_0$	0.534	0.847	0.905
$v_0$ [m s <sup>-1</sup> ]	184.2	281.0	297.6
$p_1$ [kPa]	145	131	128
$\alpha_1$	59.2°	60.3°	60.4°
$Ma_1$	0.472	0.601	0.624

**Table 4.3.:** FUTURE-2D-LC: Reduced frequency  $k$  for selected combinations

Vibration frequency $f$	Subsonic	Transonic I	Transonic II
300 Hz	0.35	0.23	0.22
400 Hz	0.47	0.31	0.29
500 Hz	0.59	0.39	0.36
600 Hz	0.71	0.46	0.44

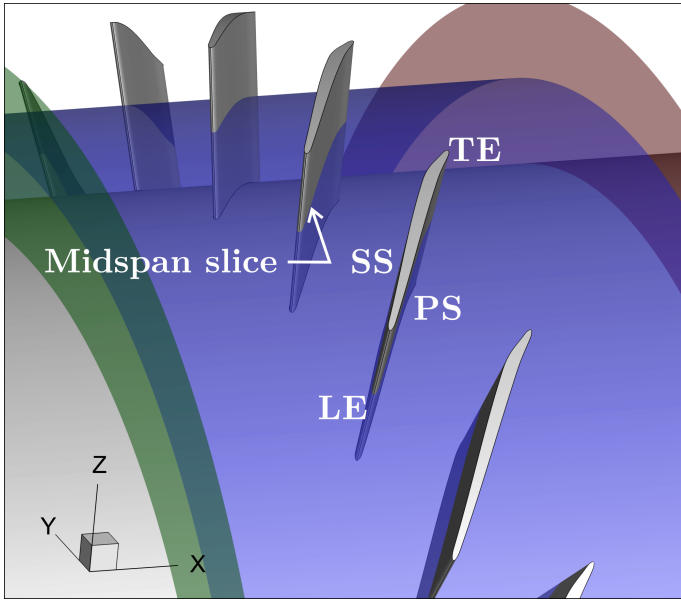


**Figure 4.1.:** Test case “FUTURE-2D-LC”: 3D model of the non-rotating annular cascade with the position of the extracted midspan slice

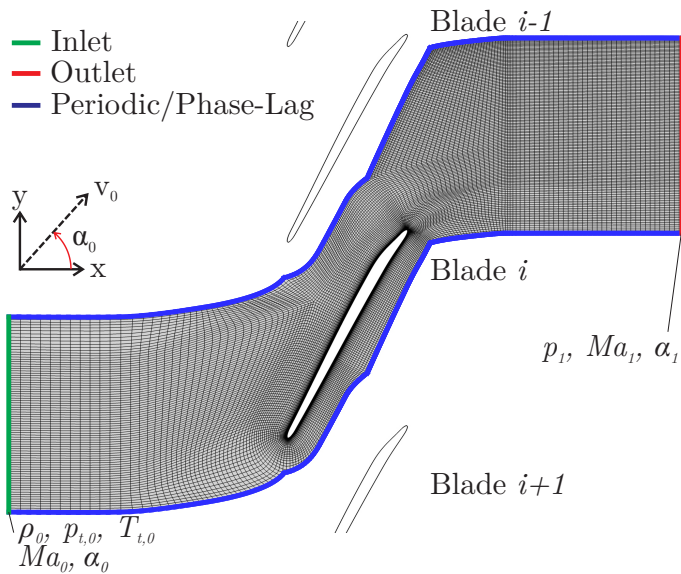


**Figure 4.2.:** Test case “FUTURE-2D-LC”: CFD mesh of the single passage setup

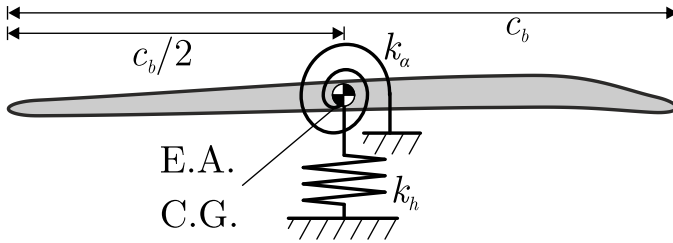
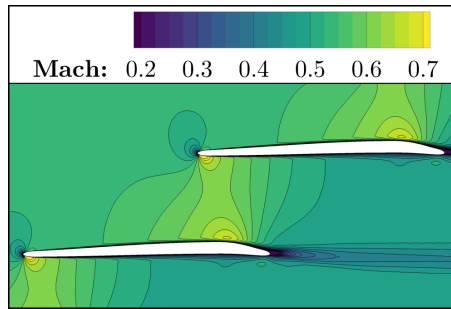
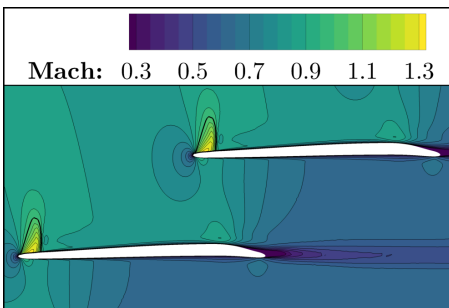


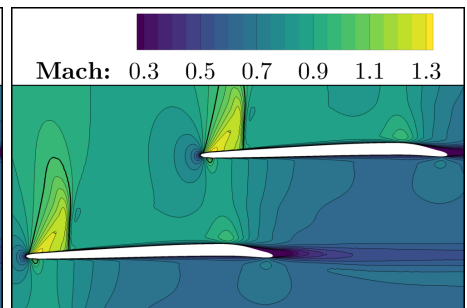
**Figure 4.3.:** Structural model of an individual blade in the FUTURE-2D-LC setup [44, 45]



(a) Subsonic



(b) Transonic I



(c) Transonic II

**Figure 4.4.:** FUTURE-2D-LC, Mach number in steady flowfields of selected operating points (adapted from [44, 45])

## 4.2. NACA3506 2D Linear Cascade

The *NACA3506* linear cascade is also based on the existing non-rotating annular compressor cascade described for the *FUTURE-2D-LC* but with a different blade geometry. The same procedure of extracting a mid-span slice is applied and it will be referenced to as “NACA3506-2D-LC”. General parameters are listed in table 4.4 and the geometry is equal to previous publications, see [25, 26, 84].

The structured CFD grid shown in fig. 4.5 is wall-resolved with  $y^+ < 1$  and contains roughly 26 000 volume cells per passage. The same generic structural model as in fig. 4.3 is used, only using another airfoil for the application of forces and moments. Refer to the description in the previous section for the implications on the spring constants and mass ratios.

Two flow conditions are chosen as shown in fig. 4.6, the total conditions at the inlet are unchanged and the inflow angle and back pressure is varied to adjust to the current flow condition. A listing of the flow conditions is given in table 4.5, a selection of the reduced frequencies is listed in table 4.6.

**Table 4.4.:** Parameters of the NACA3506-2D-LC Geometry

Airfoil	NACA3506 with rounded TE
Blades	$N = 20$ (in full wheel)
Chord length	$c_b = 77$ mm
Stagger angle LE-TE	$\beta_S = 40^\circ$
Pitch	$\tau = 56.55$ mm
Solidity	$s = c_b/\tau = 1.362$

**Table 4.5.:** NACA3506-2D-LC Operating Points

	Subsonic	Transonic
$T_{t,0}$ [K]	313.15	313.15
$p_{t,0}$ [kPa]	170	170
$\rho_0$ [kg m <sup>-3</sup> ]	1.583	1.302
$\alpha_0$	48.3°	51.3°
$Ma_0$	0.608	0.898
$v_0$ [m s <sup>-1</sup> ]	208.1	295.6
$p_1$ [kPa]	145	135
$\alpha_1$	38.0°	38.6°
$Ma_1$	0.472	0.561



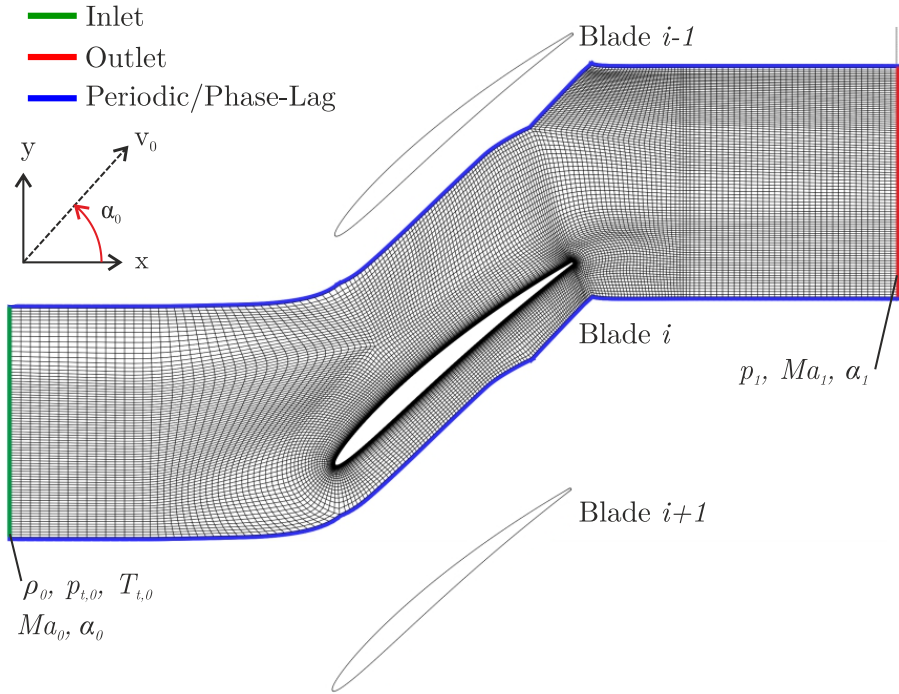


**Figure 4.5.:** Test case “NACA3506-2D-LC”: CFD mesh of the single passage setup (adapted from [85])

**Table 4.6.:** NACA3506-2D-LC: Reduced frequency  $k$  for selected combinations

Vibration frequency $f$	Subsonic	Transonic
100 Hz	0.07	0.05
150 Hz	0.11	0.08
200 Hz	0.14	0.10

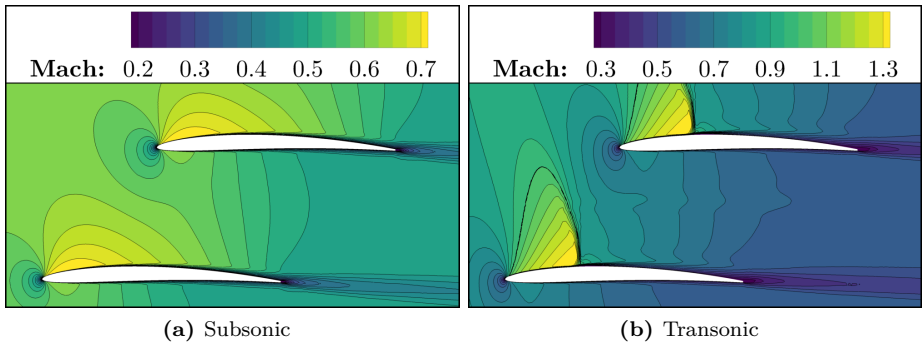


**Figure 4.6.:** NACA3506-2D-LC, Mach number in steady flowfields of selected operating points (adapted from [86])

### 4.3. CRISPMulti Fan Stage

The main objective in the future engine development is to reduce the noise and to improve the efficiency. The most promising fan concepts are the geared turbofan based on the significant noise reduction and the counter-rotating open rotor due to the high propulsive efficiency. A possible compromise between these both concepts could be a counter-rotating ducted fan, which merges the advantages of both concepts. In the 90s, a common MTU-DLR research project “CRISP” was dealing with the experimental investigation of a counter-rotating integrated shrouded propfan [87, 57]. The project “CRISPMulti”, as illustrated in fig. 4.7, is a multi-disciplinary effort to develop a highly efficient fan stage regarding every participating discipline based on the initial results from the earlier project [88, 89, 90]. Main design parameters are listed in table 4.7.

Besides the main goals of increased aerodynamic efficiency, reduced noise emissions, and overall weight reduction, the design involved a new manufacturing technique. Different from classical “onion skin configuration”, the blades are stacked up in a flat plate, shaped by a hot press and the final aerodynamic surface is milled [80]. The material used is a carbon fiber reinforced PEEK (Polyether Ether Ketone) and very flexible compared to conventional geometries, resulting in large static deformations across the compressor map [78], depicted in figs. 4.8 and 4.9. These large static deformations lead to significant changes in the aerodynamic flowfield when compared to a classical turbomachinery assumption of rigid blades which do not deflect under rotational and aerodynamic loads. As a consequence, the static deformation cannot be neglected any more and needs to be included in the numerical analysis of the aerodynamic, structural mechanics and aeroelastic characteristics [78, 91].

The meshes used in numerical analysis are illustrated in fig. 4.10. In CFD, one blade passage of one rotor consists of approx. 400 000 cells, with wall functions used on every surface. The CSM mesh is a shell element configuration of 16 560 quad cells per blade which represent the local camberline with the respective thickness of the local blade geometry. Due to their clamping, the blades are structurally decoupled, thus nodal diameter influences on vibration frequencies and modeshape appearances are neglectable. The CSM mesh has single-point constraints on their mounting at the hub. The relevant properties for flutter analysis were found to be in good accordance with more complex setups, i.e. volume meshes and structural coupling between blades. The static deflections of both rotors at each individual OP are gained through the iterative steady FSC process described in section 3.4. Structural modeshapes are plotted in fig. 4.11 for a selected OP. Their general appearance stays the same for all OPs, especially the low integer bending and torsion allocation (1. bending, 2. bending, 1. torsion etc.). As a complex three-dimensional and twisted geometry, there

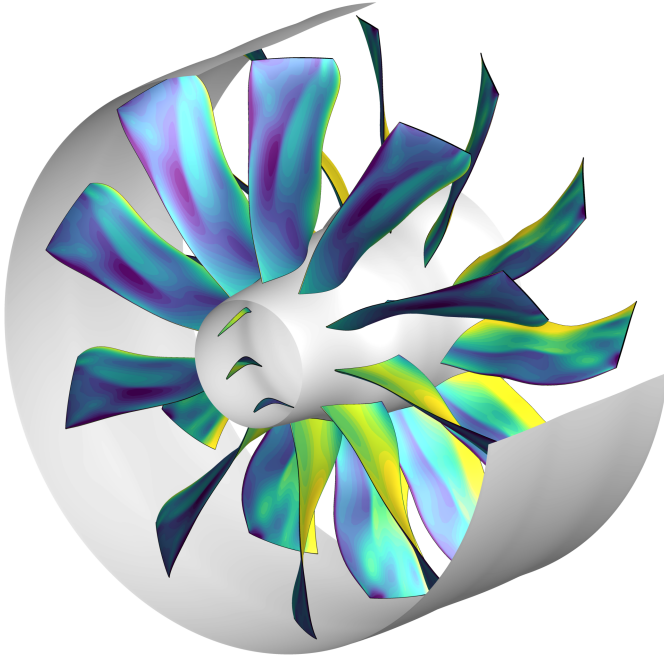


**Figure 4.7.:** Illustration of the CRISPMulti fan stage

are no pure bending or torsion modeshapes. Throughout the compressor map, this proportion of bending and torsion shifts for each individual modeshape, see appendix A.4.1. The natural frequencies are affected by the rotational speed and also, to a lesser extent, by the aerodynamic loading, see appendix A.3.1.

**Table 4.7.:** CRISPMulti Design Parameters

Material	CF-PEEK
Blades R1/R2*	10/12
Diameter	1 m
Total pressure ratio <sup>†</sup>	1.3
Corr. mass flow <sup>†</sup>	159 kg
Rotational speed <sup>†</sup> R1/R2	-5044 <sup>‡</sup> / 3982 min <sup>-1</sup>
Abs. inlet Mach number <sup>†</sup>	0.69 at tip
Rel. inlet Mach number <sup>†</sup>	1.06 at tip
Mass ratio $\mu$ of R1	between 50 and 70
Chordlength $c_b$ of R1	0.156 m at 90% channelheight

\* R1: first rotor, R2: second rotor

<sup>†</sup> At aerodynamic design point (ADP)

<sup>‡</sup> Negative number indicates counter-clockwise rotation  
(viewed from front)

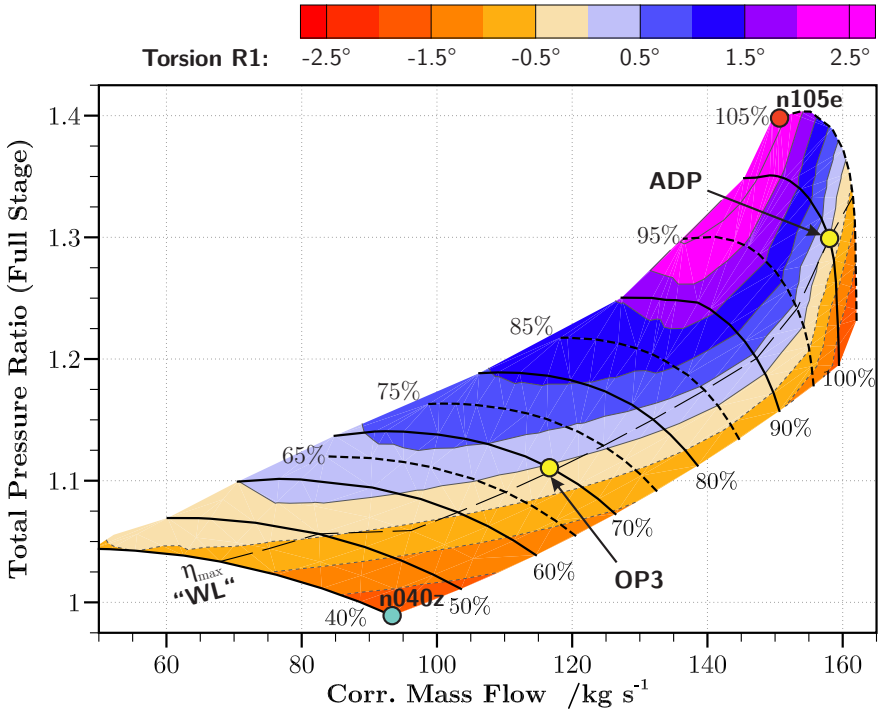


**Figure 4.8.:** Compressor map of CRISPMulti with torsion at blade tip of first rotor due to static deformation (relative to ADP); selected operating points are marked with a circle

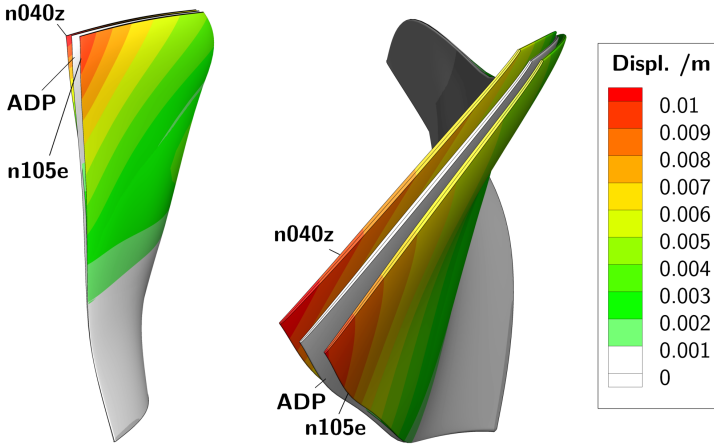


**Figure 4.9.:** Maximum static deformation due to rotational and aerodynamic loads of the CRISPmulti first rotor (relative to ADP)

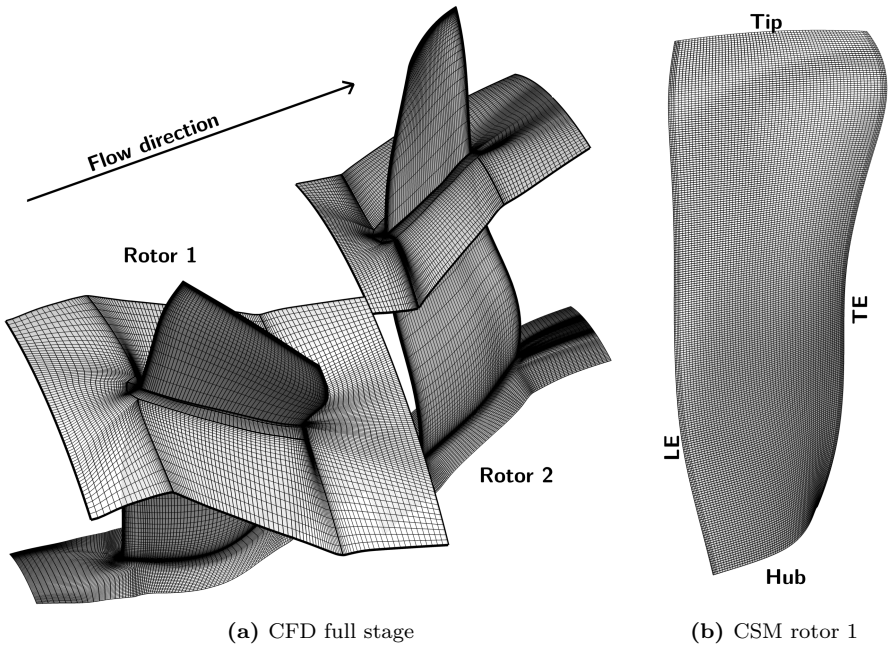


**Figure 4.10.:** Computation meshes of the CRISPmulti fan stage

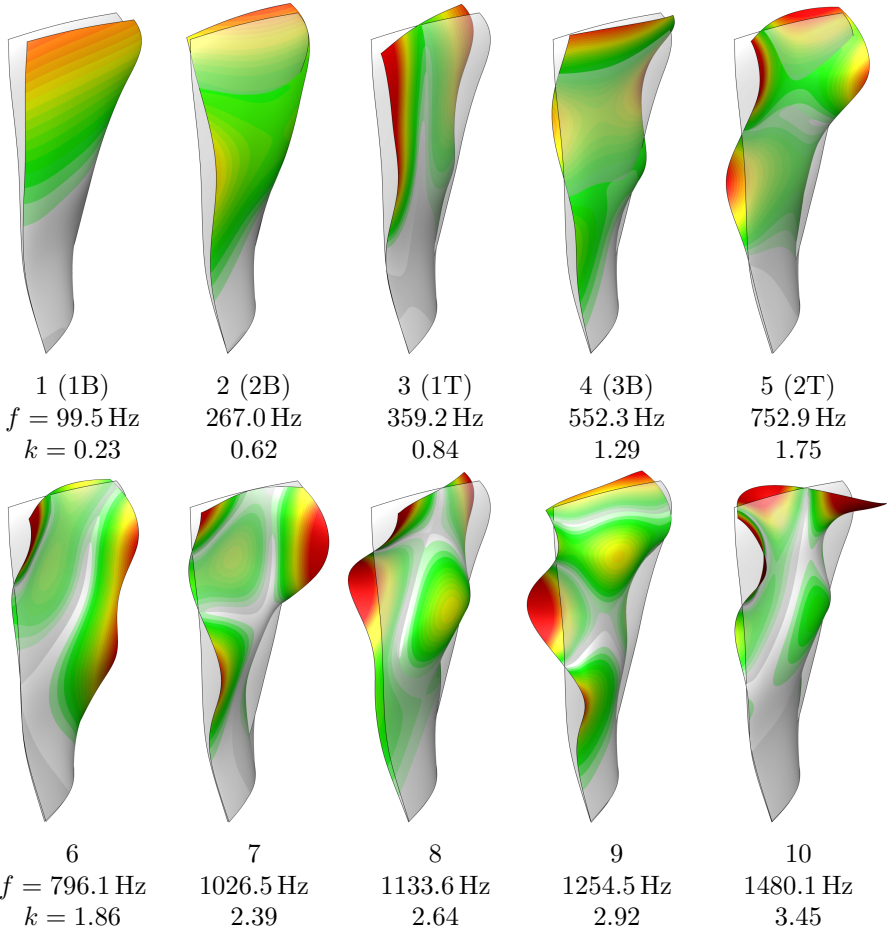


**Figure 4.11.:** Vacuum modeshapes with frequency  $f$  and reduced frequency  $k$  of CRISPMulti first rotor at 70% speedline (above WL, close to OP3)





# 5

## Verification and Validation of the P-K Method

*Time-marching simulations with fluid/structure-coupling (FSC) are performed for the two-dimensional cases FUTURE-2D-LC and NACA3506-2D-AC, and for the 3D geometry of the CRISP-multi rotor. Preliminary results of this investigation were already published by the author [86, 44, 45]. The results are compared to frequency domain results with the energy method and the p-k method. It is shown, that the p-k method is able to predict the modal participation and damping/excitation due to aerodynamic coupling as evaluated from time domain.*

*Experimental data for the presented cases was not available, thus a more thorough analysis with time-marching CFD is performed. The focus of this chapter is to verify and validate the results of the p-k method at different flow conditions and geometries. An interpretation from a physical point-of-view and extension of parameters is part of the next chapter.*

A distinction between *verification* and *validation* can be found in the “PMBOK Guide” [92]:

- “**Verification.** The evaluation of whether or not a product, service, or system complies with a regulation, requirement, specification, or imposed condition. It is often an internal process. Contrast with *validation*.”
- “**Validation.** The assurance that a product, service, or system meets the needs of the customer and other identified stakeholders. It often

involves acceptance and suitability with external customers. Contrast with *verification*.”

In the context of this thesis and especially of this chapter, this separation of two aspects is important to keep in mind. It is often narrowed down into two questions:

- **Verification:** “Are you building it right?”
- **Validation:** “Are you building the right thing?”

Transferred to the context of this thesis, the first question translates to whether the mathematical concepts are implemented correctly and represent the physical rationale. The second question is the applicability to the use case, i.e. turbomachinery aeroelasticity.

## 5.1. General Remarks on Time-Marching Simulations

*The majority of this section has been previously published by the author [86]. More detailed equations are added and some additions for more background have been made.*

Time-marching simulations with freely vibrating blades are carried out for the different geometry test cases. The flow field is initialized by the steady-state RANS solution. Structural degrees of freedom are the given modeshapes, which differ with the investigated geometry. The appropriate stiffnesses are applied to achieve the vacuum eigenfrequency of the respective modeshape. With this given information, the modal FSI module of TRACE (cf. section 3.1) can be started.

Various computations with different starting conditions of the structural mechanics have been computed separately. The chosen starting conditions vary in the initial displacement and the initial velocity of the blades. Compared to the steady-state solution, where all blades are fixed to the same deflection, this approach adds an artificial discontinuity of the blade motions, which is desired to introduce an unsteadiness into the flow field. In some of the early simulations with no initial displacement or velocity a very large number of timesteps was needed until enough structural energy was in the vibrating system so that the displacements were clearly distinguishable from numerical noise or numerical

artifacts<sup>6</sup>. As shown later, this approach will introduce enough structural energy so that a physical vibration is observable right away. Furthermore, by forcing the blades into certain vibration patterns (e.g. IBPA, small or larger amplitudes of all blades, or random starting conditions) the transition from a stable towards an unstable IBPA can be observed.

The blades vibrate in the given modeshapes as degrees of freedom. Each modeshape has an individual so-called “modal displacement”. The logged time history of modal displacements is used to extract the physical displacement at any blade surface node. The physical displacement  $z_{LE}(t)$  presented in the studies is the distance of the leading edge at a given time  $t$  compared to the resting position.

### 5.1.1. General Observations

A generic time history of physical displacements is given in fig. 5.1 with two degrees of freedom, heave and pitch. This behavior is representative for all performed computations: Depending on the starting condition (i.e. initial deflection and/or velocity), some blades have a significantly higher energy level. Especially if the blades are excited randomly, there is an initial phase with a transient behavior of the blades, which is due to an uneven distribution of energy in the cascade. The cascade shuffles energy in the cascade to achieve an equilibrium energy distribution. During this process a distinct IBPA pattern is formed. After this transient phase, a periodic phase sets in, where the blades are vibrating harmonically in damped or excited oscillations.

Furthermore, the mean displacement of the blades are not equal to the resting position as indicated by the envelopes and mean displacement. This phenomenon can be separated from the coupled-mode flutter as described later and may be attributed to a slight difference in the treatment of static loading when going from steady to unsteady flow simulation and thus, not physical. The effect is not investigated further, as it is not influencing the flutter investigation (which occur at much higher frequencies). Nevertheless, the local mean displacement has to be removed from any further evaluations to separate low and high frequency oscillations.

---

<sup>6</sup>“Law” of very small fluid forces that cause very small displacement as a reaction. The change in field variables can initially be so small that the numbers are too small even with standard double precision, so it is merely distinguishable from numerical noise. However, after very many timesteps the blades will start to vibrate in a physical pattern.

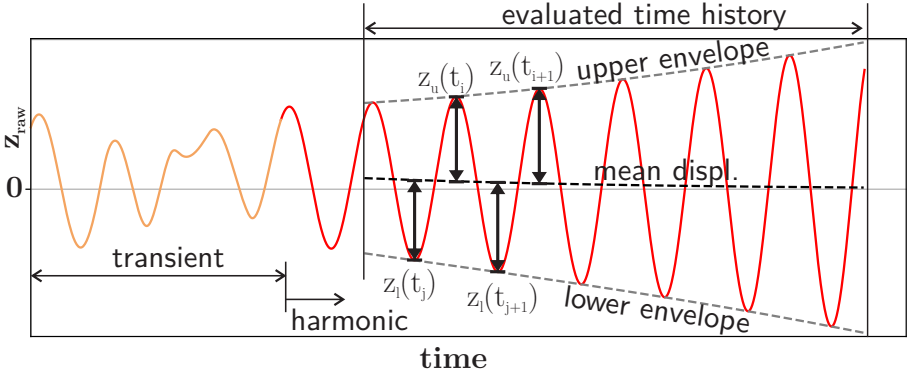


**Figure 5.1.:** Generic time history of blade deflections in fluid/structure-coupled time-marching simulations, evaluation of vibration frequency and logarithmic decrement in harmonic part (adapted from [86])

### 5.1.2. Post-Processing the Time History of Deflections

From the peaks in the time history two splines are created, representing the envelope limits in fig. 5.1 as a lower  $z_{env,l}$  and upper  $z_{env,u}$ , respectively. The mean displacement is the average of both envelope splines. To get the to-be-evaluated displacement  $z$  at a vibration peak time  $t_i$  the envelopes are utilized:

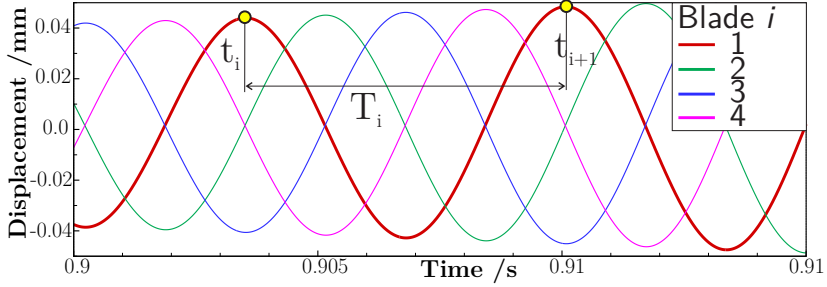
$$z(t_i) = z_{raw}(t_i) - (z_{env,l}(t_i) + z_{env,u}(t_i)) / 2 \quad (5.1)$$

More sophisticated signal processing tools like high or low pass filters might be used, but the described procedure is straight forward and turns out to deliver reasonable data. The technique is applied on modal and physical displacements before any further processing.

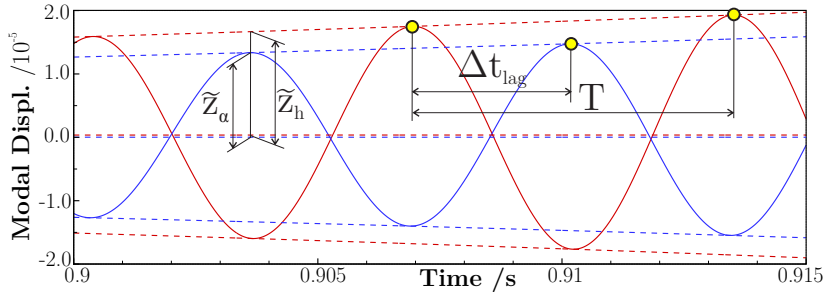
In the time history of blade displacements and once the excited system is established (after the initial transient phase), the physical displacements  $z(t)$  of each blade can be probed for the vibrational frequency from the period  $T$  between two peaks at  $t_i$  and  $t_{i+1}$ . The logarithmic decrement between the two peaks is defined as

$$\Lambda = \ln \left( z(t_i) / z(t_{i+1}) \right). \quad (5.2)$$

The IBPA needs to be interpreted with the help of fig. 2.5 (order of peaks from different blades). In the given example in fig. 5.2, the IBPA of  $-90^\circ$  is identified. The modal displacements show a participation of heave and pitch in the resulting vibration pattern.



(a) Physical displacement at leading edge for all blades



(b) Modal displacements of blade 1

**Figure 5.2.:** Detailed time history of physical and modal deflections of a four passage setup (adapted from [86])

In addition, the envelope of the modal displacements  $\tilde{z}(t)$  are used in accordance with (2.81) to calculate the modal participation factors  $\Gamma$  (confer to the example in fig. 5.2):

$$\Gamma_h = \tilde{z}_h / (\tilde{z}_h + \tilde{z}_\alpha) \quad (5.3)$$

$$\Gamma_\alpha = \tilde{z}_\alpha / (\tilde{z}_h + \tilde{z}_\alpha) \quad (5.4)$$

The phase difference or phase lag between pitch and heave is evaluated from the peaks of the modal displacements

$$\Delta\varphi_{h \rightarrow \alpha} = \frac{\Delta t_{lag}}{T} 360^\circ \quad (5.5)$$

$$\Delta\varphi_{\alpha \rightarrow h} = \frac{(T - \Delta t_{lag})}{T} 360^\circ = 360^\circ \left( 1 - \frac{\Delta t_{lag}}{T} \right) \quad (5.6)$$

so that it can be compared to the p-k results that are build via:

$$\Delta\varphi_{h\rightarrow\alpha} = \varphi_\alpha - \varphi_h \quad (5.7)$$

$$\Delta\varphi_{\alpha\rightarrow h} = \varphi_h - \varphi_\alpha \quad (5.8)$$

As there are many vibration periods within the evaluation time, the average is build and a standard deviation can be calculated.

By rule, the phase lag can be converted accordingly:

$$\Delta\varphi_{h\rightarrow\alpha} = 360^\circ - \Delta\varphi_{\alpha\rightarrow h} \quad (5.9)$$

$$\Delta\varphi_{\alpha\rightarrow h} = 360^\circ - \Delta\varphi_{h\rightarrow\alpha} \quad (5.10)$$

### 5.1.3. Disclaimer on Used Non-Reflecting Boundary Conditions

Throughout this chapter, the unsteady non-reflecting boundary condition in the one-dimensional formulation (NRBC-1D) is used. It is known to the author that there are deficiencies in the representation of physical effects (cf. section 3.1). Considering computational effort vs. physical representation and the premise of this chapter, only the NRBC-1D allows for a direct comparability of results from frequency and time domain computations on the same grid, where the frequencies in the fluid flow cannot be determined in advances (non-synchronous vibration with a free vibration frequency). The p-k method will be compared with the time-marching simulations both using the NRBC-1D, the task in this chapter is to verify that the frequency domain computations coupled with a eigenvalue solution will deliver the same result as a comparable time domain simulation.

## 5.2. FUTURE-2D-LC

The FUTURE-2D-LC is investigated at different operating conditions and with different mass ratios. If not specifically noted otherwise, the vacuum frequencies of the modeshapes are set to a heave frequency  $f_h = 300$  Hz and a pitch frequency  $f_\alpha = 600$  Hz.

*Some of the results in this section are previously published by the author [44, 45]. More detailed investigations and a wider parameter range is given here.*

### 5.2.1. GAF Matrix Generation

For all operating points, the GAF matrices  $\tilde{\mathbf{Q}}(\sigma, \omega)$  as introduced in (2.45) are generated for heave  $\vec{\phi}_1$  and pitch  $\vec{\phi}_2$  for each individual IBPA. Aerodynamic responses  $\vec{f}_1$  and  $\vec{f}_2$  for both mode shape vibrations are computed in the frequency domain at a fixed amplitude of approx. 0.01% chord length, and for a set of discrete frequencies in the range from 250Hz up to 650Hz with an increment of 25Hz.

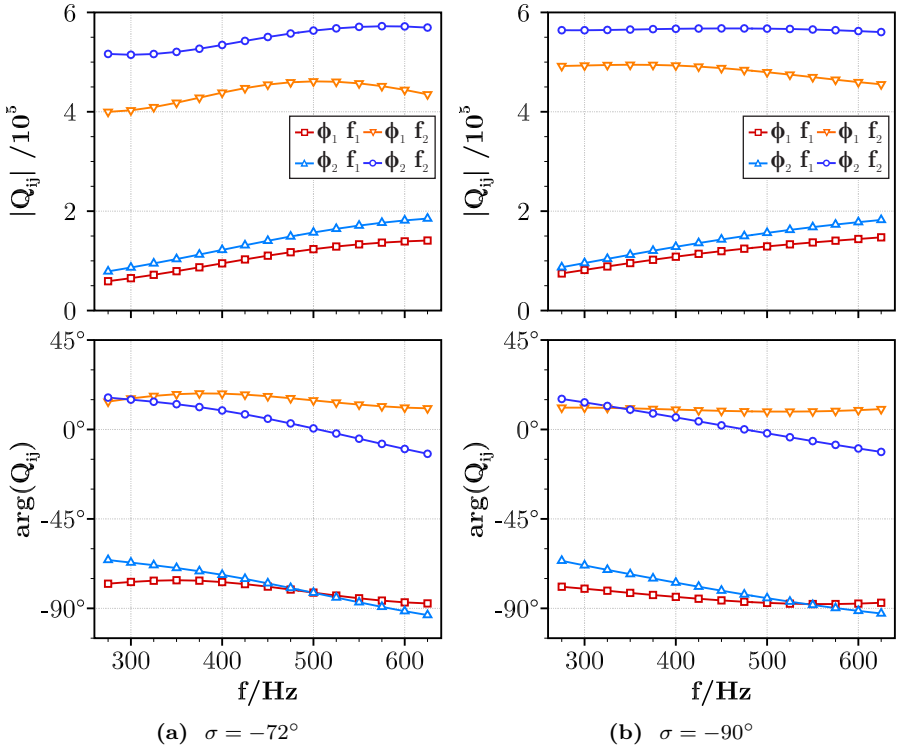


**Figure 5.3.:** FUTURE-2D-LC, case “subsonic”: Generalized aerodynamic forces for selected IBPAs

As an example, the resulting GAF matrix entries at the discrete frequencies and their interpolation are plotted for two IBPAs of the operating condition *subsonic* and two IBPAs of *transonic I* in figs. 5.3 and 5.4. It is noticeable, that magnitude and phase of the GAFs are depending in the frequency as well as the IBPA.



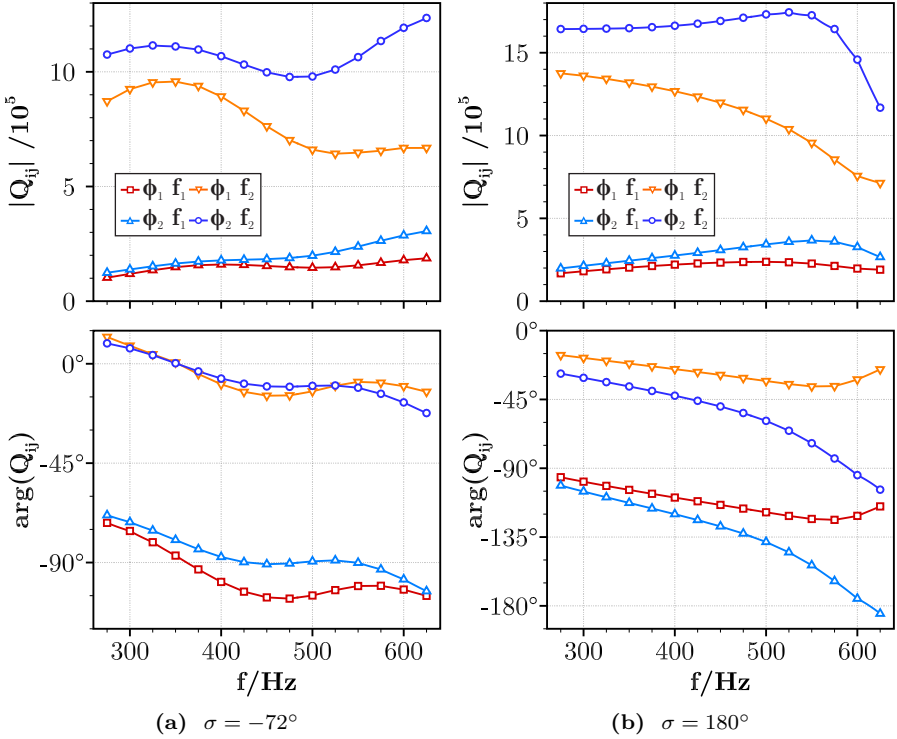


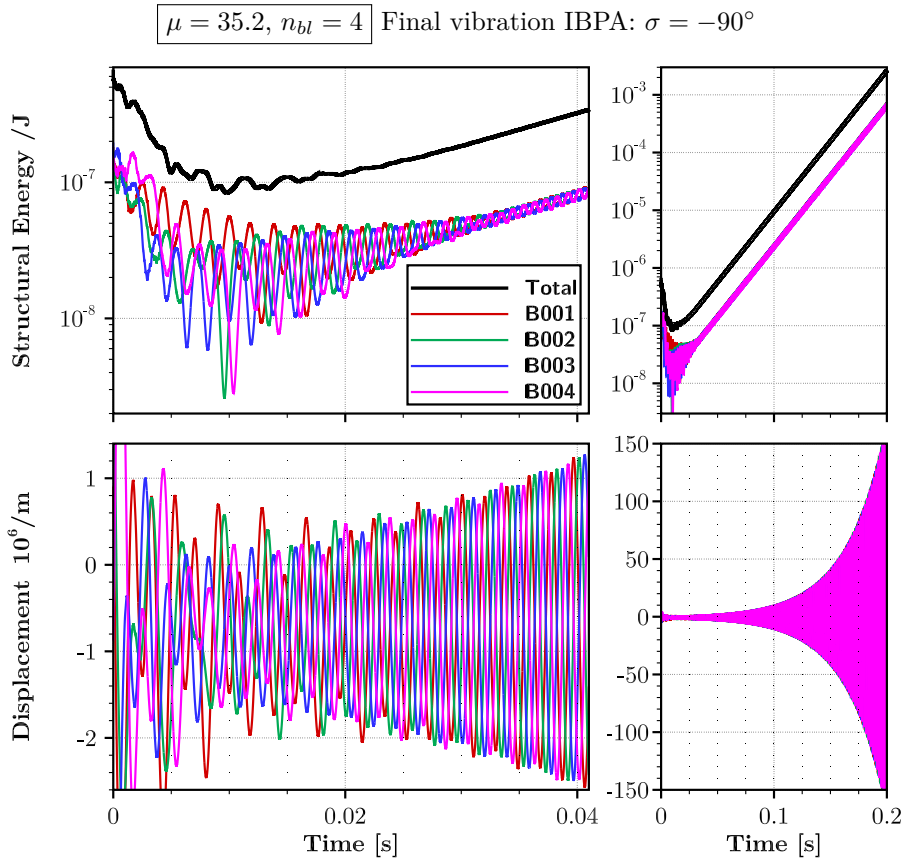
**Figure 5.4.:** FUTURE-2D-LC, case “transonic I”: Generalized aerodynamic forces for selected IBPAs

No obvious conclusion about modal coupling can be deduced from the behavior in this type of graph, but the quality of the interpolation method for the GAF matrix can be assessed quickly. In this case, the number of sampling points for a smooth spline appears to be high enough, even a higher increment for the frequency samples might have been possible. However, as the setup is rather small, a higher-than-necessary number of CFD computations is acceptable. The determination of an optimal number of frequency samples is an interesting aspect and needs to be addressed for computationally more expensive setups.

## 5.2.2. Subsonic Operating Point with Frequency Separation 1:2

### Time-Marching FSI

A four passage setup of the FUTURE-2D-LC geometry at subsonic flow with a mass ratio of structure-to-air  $\mu = 35.2$  is investigated with time-marching FSI. The blades are excited with small random initial deflections and velocities. The structural energy and physical displacements are plotted in fig. 5.5.



*Physical displacements are measured at LE to resting position.*

**Figure 5.5.:** FUTURE-2D-LC “subsonic”: Random initial deflections and velocities

In the initial phase, the energy decreases as the cascade transients from the random starting conditions to a harmonic motion. During this phase, the

structural energy decreases until a harmonic vibration sets in. At around  $t = 0.01$  s, the final vibration IBPA is already established, but the energy levels of the blades are still not in equilibrium and large amounts of energy are shuffled between the blades. During this phase, the structural energy in the cascade reaches a plateau. At around  $t = 0.025$  s, the total energy of all blades is rising linearly already, but the blades itself still shuffle a larger but steadily decreasing amount of energy between each other. After  $t = 0.04$  s, the energy is almost evenly distributed between the blades and all blades perform the same motion just with a time-lag. A small variation around the linear increasing energy level of each blade is visible, which can be compared to a nutation-like motion. This behavior is typical for the time-marching FSI and may be attributed to small nonlinearities in the flow. They have a negligible effect on the overall outcome of the frequency, logarithmic decrement or modal participation factors. The amplitudes continue to grow until finally reaching the capability of the mesh deformation process and the simulation is aborted.

The blades do not move around the zero displacement axis as described in the general remarks section 5.1, especially visible in the initial phase ( $t < 0.1$  s). This effect, which can be attributed to a small difference in load calculation between steady and unsteady FSC algorithms and is thus a numerical artifact, is also negligible as seen when amplitudes get bigger ( $t > 0.1$  s).

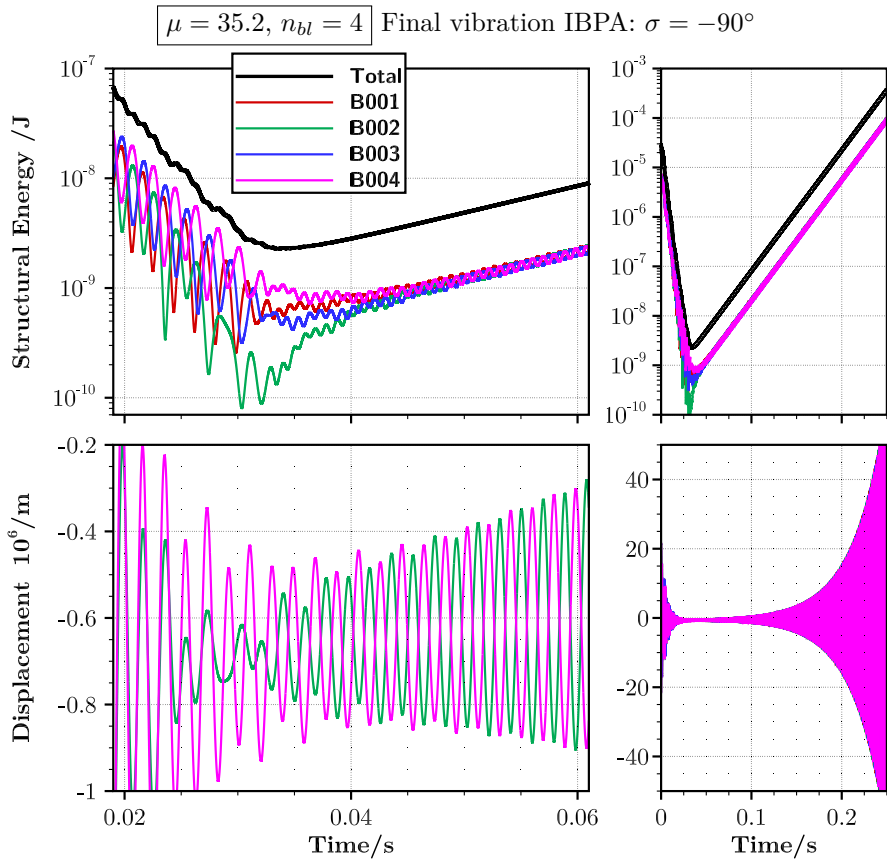
Figure 5.6 shows the same setup, but the initial motion of the blades is set to a specific IBPA of  $\sigma = 180^\circ$ . In the initial phase, the cascades vibrates with this IBPA until around  $t = 0.03$  s, the phase of the second blade is shifted. At this point, the cascade transitions from a stable to an unstable IBPA. This behavior is also typical for cascades vibrating in a stable IBPA, but another IBPA is aerodynamically excited. The final vibration pattern is equivalent to the first simulation, only that more wall time is required for the computation.

More computations with four and five blade passages are performed. The mass ratio is varied and the structural model is always set a heave frequency  $f_h = 300$  Hz and a pitch frequency  $f_\alpha = 600$  Hz. In fig. 5.7, the computations with the marker “a” are randomly excited starting conditions and the “b”-marked computations have the final vibration IBPA as initial motion. Besides the different initial transient phase, the final vibration is always the same for the same model parameters. The four passage setup always vibrates with an IBPA  $\sigma = -90^\circ$ , the five passages have an IBPA  $\sigma = -72^\circ$ . The marker “c” are computations with no initial vibration set (“free release”) and the transient phase is much longer. In the end, those computations establish the same excited vibration pattern as the previous ones. The dependency of coupled-mode flutter on the mass ratio is represented already in this diagram: the lower the mass ratio, the higher the excitation becomes. Vice versa, the system is stable at higher mass ratios.

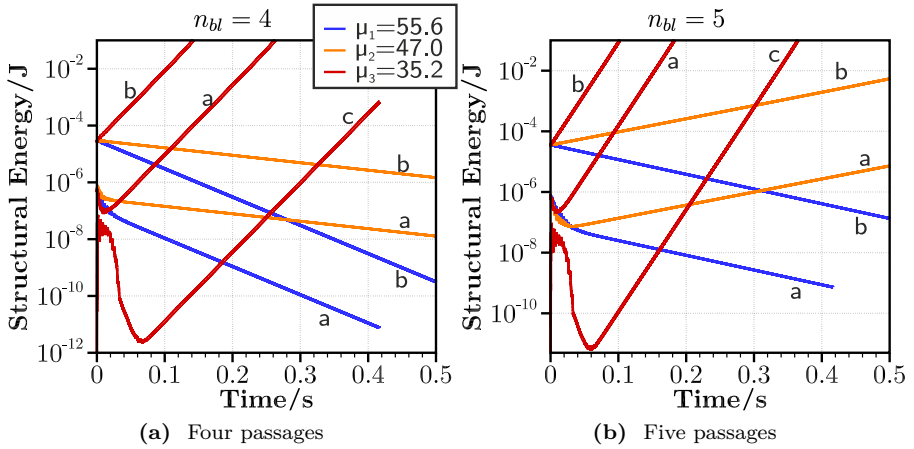
### Comparison of Time-Marching FSI and P-K Method

Figure 5.8 plots various information of the p-k method solution process over the scaling factor  $q_{scale}$  (that can be translated to a certain mass ratio as demonstrated in section 2.5.1) for the two IBPA of interest. The results from the coupled simulations in time domain are plotted at the  $q_{scale}$  corresponding to the mass ratio.

Frequency and logarithmic decrement of the coupled-mode match very good. Especially the transition from stable to unstable, depending on the mass ratio, is in a very good agreement. The lower two graphs give information about the shape of the coupled-mode system in terms of modal participation  $\Gamma$  and the phase lag  $\Delta\varphi_{h \rightarrow \alpha}$  between the pitch and heave mode. Only for the damped case of four passages ( $\sigma = -90^\circ$ ) the phase shift has a high standard deviation. This is attributed to the fact that the coupled-mode vibration is not fully established (as seen in fig. 5.5 between  $0.01 \text{ s} < t < 0.03 \text{ s}$ ) before the amplitudes become to low and vanish into noise.



**Figure 5.6.:** FUTURE-2D-LC “subsonic”: Starting condition equiv. to pitch modeshape displacements with  $\sigma = 180^\circ$



**Figure 5.7.:** FUTURE-2D-LC, case “subsonic”: Structural energy of various time-domain FSC computations, markers: a) random initial deflections, b) initial motion close to final pattern and high initial structural energy, c) no initial motion (“free release”)

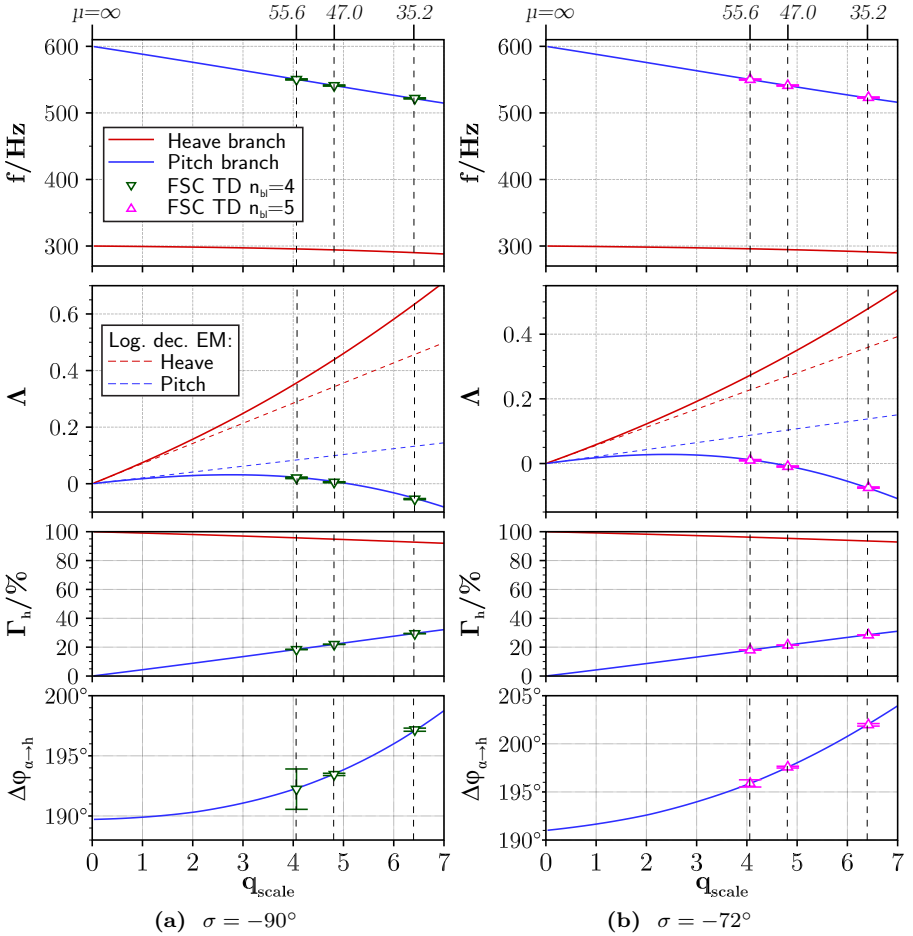


Figure 5.8.: FUTURE-2D-LC, case "subsonic": p-k solution history

### 5.2.3. Subsonic Single-Mode Flutter vs. Low Frequency Separation

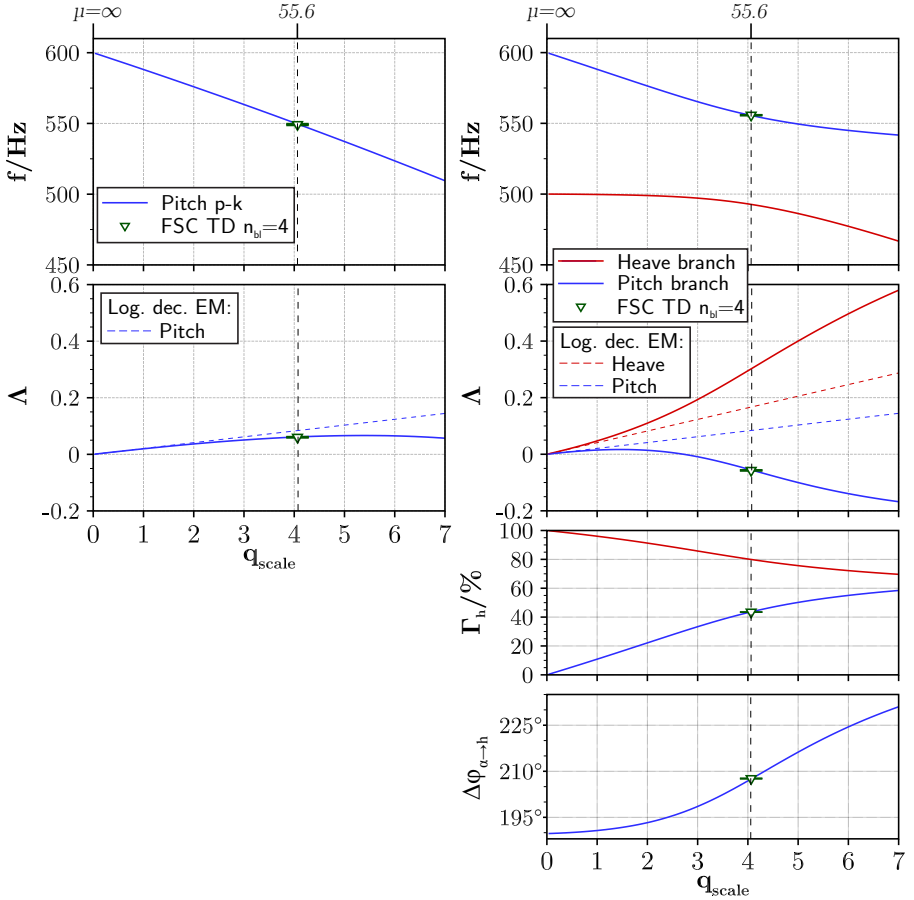
If the p-k method is used considering only one modeshape, frequency changes due to the added mass and damping effects are allowed, but only a single-mode flutter case is considered. This is a sort of intermediate approach between full modal coupling and the energy method. For this example, the frequency separation is changed, by increasing the vacuum frequency of the heave mode to 500Hz. The results are supported by time-marching FSC simulations at one specific mass ratio.

The comparison between a single-mode analysis with frequency change and a modal coupling analysis is shown in fig. 5.9. If only the pitch mode is considered, the vibration frequency decreases with a lower mass ratio. However, in the regime shown here, no flutter onset is observed. One could imagine, that the frequency will decrease further for higher values of  $q_{scale}$  (or: even lower mass ratios) until finally the zero damping line is reached.

Considering modal coupling with the heave mode, the aeroelastic branch of the pitch mode gets unstable much sooner than the single-mode analysis would yield. It is interesting to mention, that the vibration frequency at flutter onset of the coupled system is higher than the single-mode system.

This case points out, that the energy method is potentially non-conservative in comparison to the a single-mode analysis with allowed frequency change, which is non-conservative to a coupled-mode method.





(a) Considering only the pitch mode in a  $1 \times 1$  matrix (only frequency shift allowed, no modal coupling)

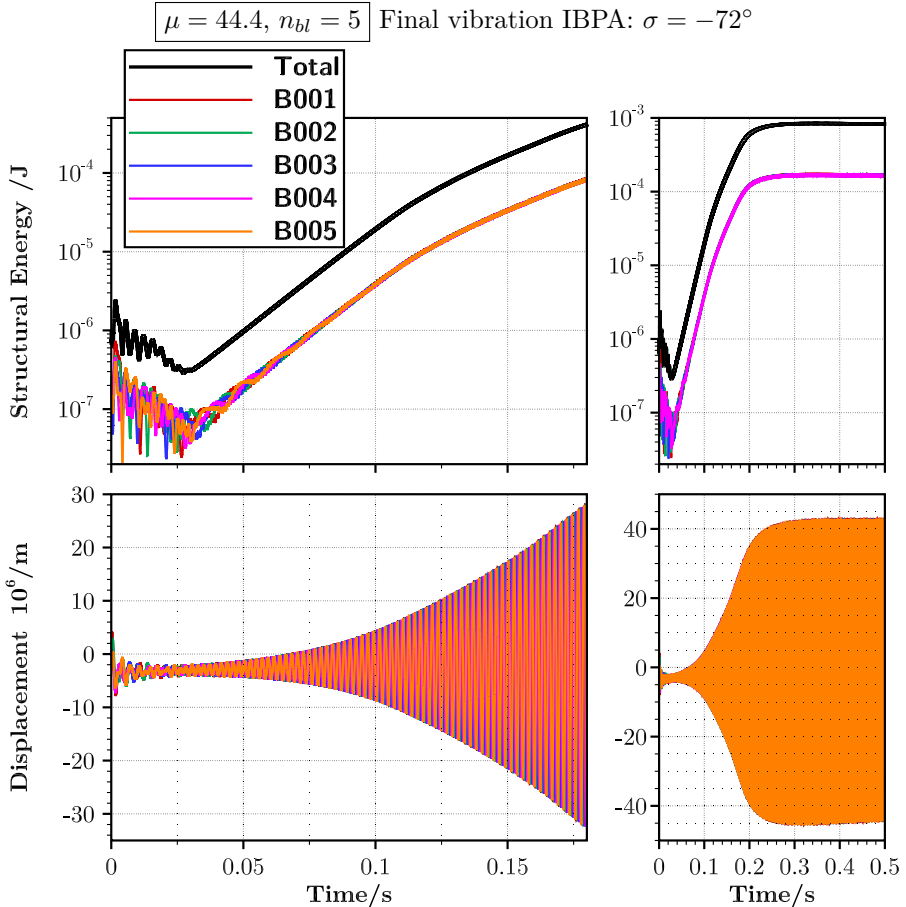
(b) Considering modal coupling

**Figure 5.9.:** FUTURE-2D-LC, case “subsonic” with  $f_{\text{heave}} = 500$  Hz and  $f_{\text{pitch}} = 600$  Hz: p-k solution history at  $\sigma = -90^\circ$

## 5.2.4. Operating Point Transonic I

### Time-Marching FSI

A five passage setup with a mass ratio of structure to air  $\mu = 44.4$  is investigated with time-marching FSI, the blades are excited with small random initial deflections and velocities. The structural energy and physical displacements are plotted in fig. 5.10.



*Physical displacements are measured at LE to resting position.*

**Figure 5.10.:** FUTURE-2D-LC “transonic I”: Random initial deflections and velocities

There is a transient phase at the beginning, comparable to the subsonic case. Once the excited system is established ( $t \approx 0.025$  s), the amplitudes grow in a linear fashion but the individual blades still shuffle energy between each other until around  $t \approx 0.075$  s. The overall logarithmic decrement is steady (linear line in logarithmic plot) until  $t \approx 0.1$  s and decreases thereafter. This is an amplitude-dependent behavior. At around  $t = 0.2$  s, the vibration turns into a limit cycle oscillation. Thus, when comparing to the p-k method, the amplitude in the frequency domain solver needs to be respected. The amplitudes set in the FD solver to compute the entries of the GAF table are in the order that is comparable to the time frame between  $0.1 \text{ s} < t < 0.2 \text{ s}$ .

In fig. 5.11, more simulations with different mass ratios and number of passages are depicted. The marker “a” indicates the random initial motion, marker “b” starts with the now known IBPA pattern and “c” marks the computations without initial excitation of the blades. As with the subsonic case, the influence of mass ratio is directly visible: the lower the mass ratio, the higher the excitation. Also comparable is the wobbling of the structural energy in a nutation-like manor as described above (on this scale only implicitly visible because some of the lines in fig. 5.11 are much broader than the reference line thickness in the legend). Especially visible is the amplitude-dependent behavior for the five passages setup at the lowest mass ratio  $\mu = 42.9$ . The four passage setup always vibrate with an IBPA  $\sigma = 180^\circ$ , the five passages have an IBPA  $\sigma = -72^\circ$ .

A special case is the five passage setup for  $\mu = 45.9$ . The initial amplitudes at the marker “b” are above the limit cycle level. The amplitudes decrease until reaching the level of “a”. Computations with marker “d” and “e” show random initial motions with a different level of structural energy. They all establish the same pattern as already seen from “a”.

### Comparison of Time-Marching FSI and P-K Method

Figures 5.12 and 5.13 plot the p-k method convergence over the scaling factor  $q_{scale}$  for the two IBPA of interest. The results from the coupled simulations in time domain are plotted at the  $q_{scale}$  corresponding to the mass ratio.

The modal parameters (frequency, logarithmic decrement, modal participation, phase lag) differ slightly and are not meeting the p-k solution perfectly like in the subsonic case. This can be expected as the transonic flow likely has small nonlinearities not covered by the p-k method. Still, they are a very close match. The transition from stable to unstable depending on the mass ratio is met very good.

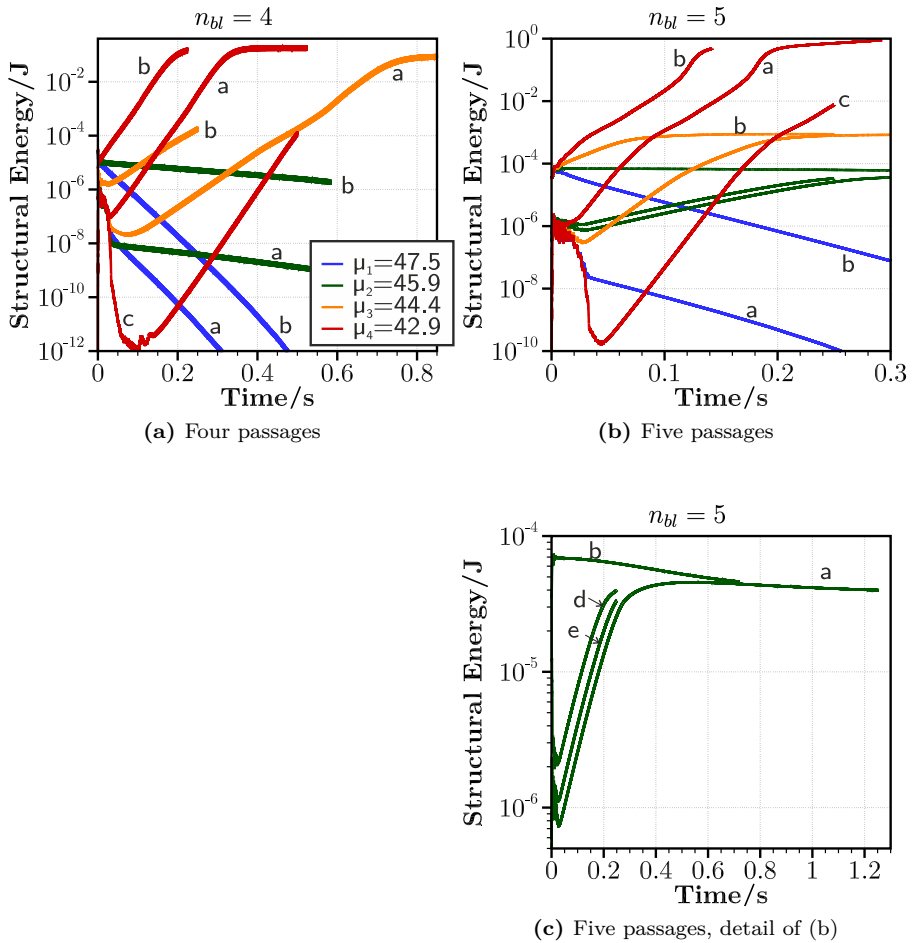


**Figure 5.11.:** FUTURE-2D-LC, case “transonic I”: Structural energy of various time-domain FSC computations, markers: a) random initial deflections, b) initial motion close to final pattern and high initial structural energy, c) no initial motion (“free release”), d and e) random initial deflections at different level than a

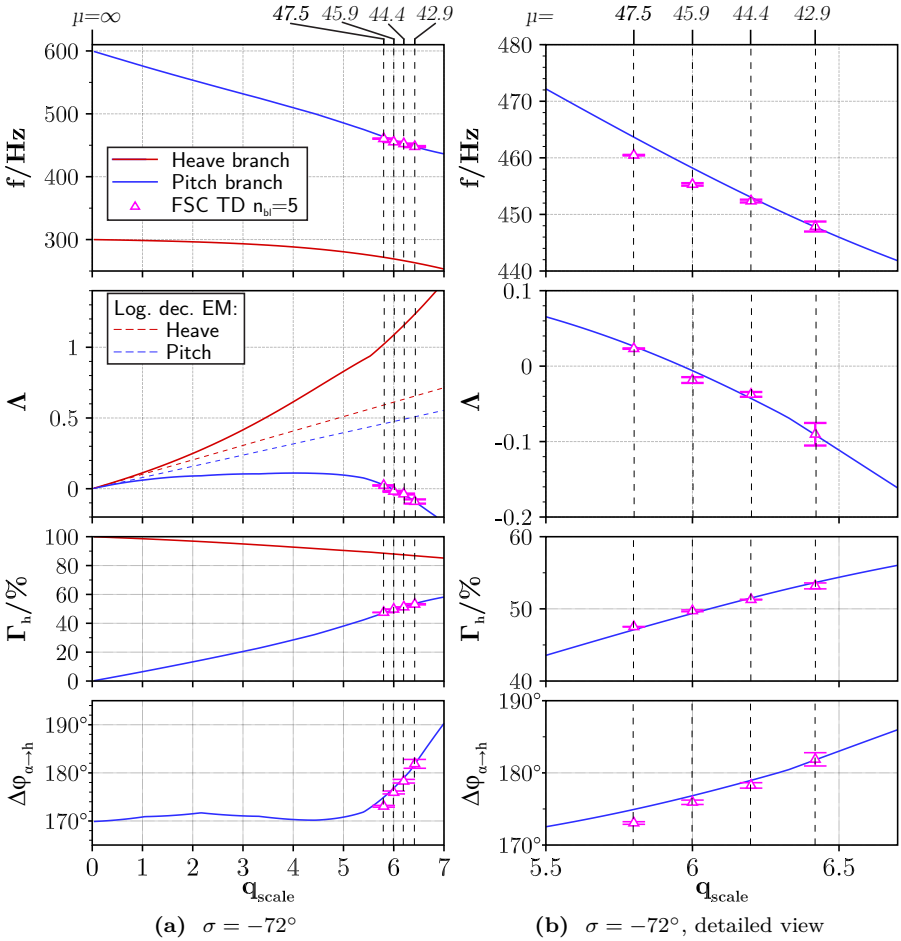


Figure 5.12.: FUTURE-2D-LC, case "transonic I": p-k solution history

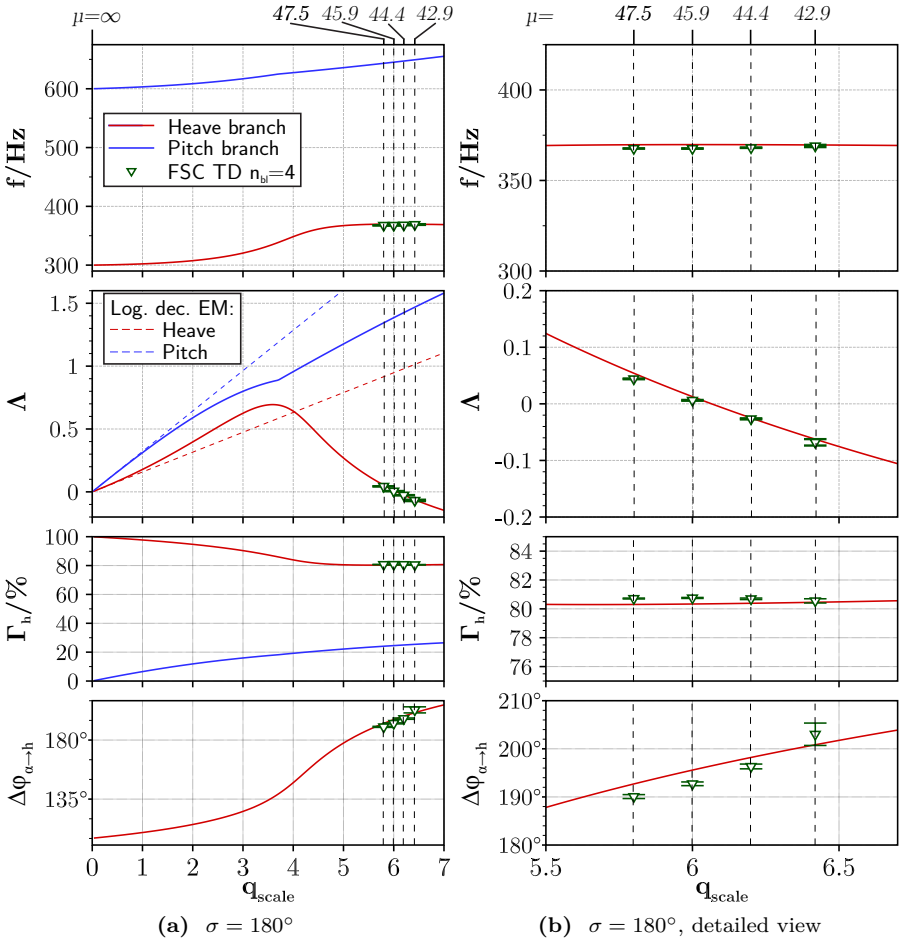
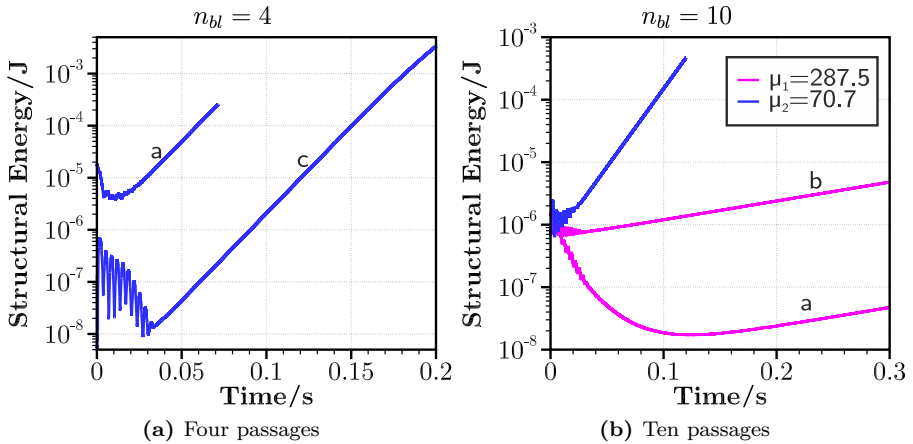


Figure 5.13.: FUTURE-2D-LC, case “transonic I”: p-k solution history

### 5.2.5. Operating Point Transonic II



**Figure 5.14.:** FUTURE-2D-LC, case “transonic II”: Structural energy of various time-domain FSC computations, markers: a) random initial deflections, b) initial motion close to final pattern and high initial structural energy, c) no initial motion (“free release”)

Four and ten passage setups are investigated, even for a much higher mass ratio than above. The structural energy and physical displacements are plotted in fig. 5.14.

Markers “a”, “b” and “c” are again the random initial excitation, excitation in final IBPA and no excitation at all, respectively. The results are of the same quality as before. The ten passage setup falls to the IBPA  $\sigma = -108^\circ$  and has an aerodynamically excited coupled-mode at a significantly higher mass ratio  $\mu = 287.5$  than known from the previous cases. For the mass ratio of  $\mu = 70.7$ , the excited system has the IBPA  $\sigma = -108^\circ$ .

Figure 5.15 compares the time-marching FSI and p-k method solution. In the same quality as for the OP “transonic I”, the results do not perfectly match but are still in good agreement.

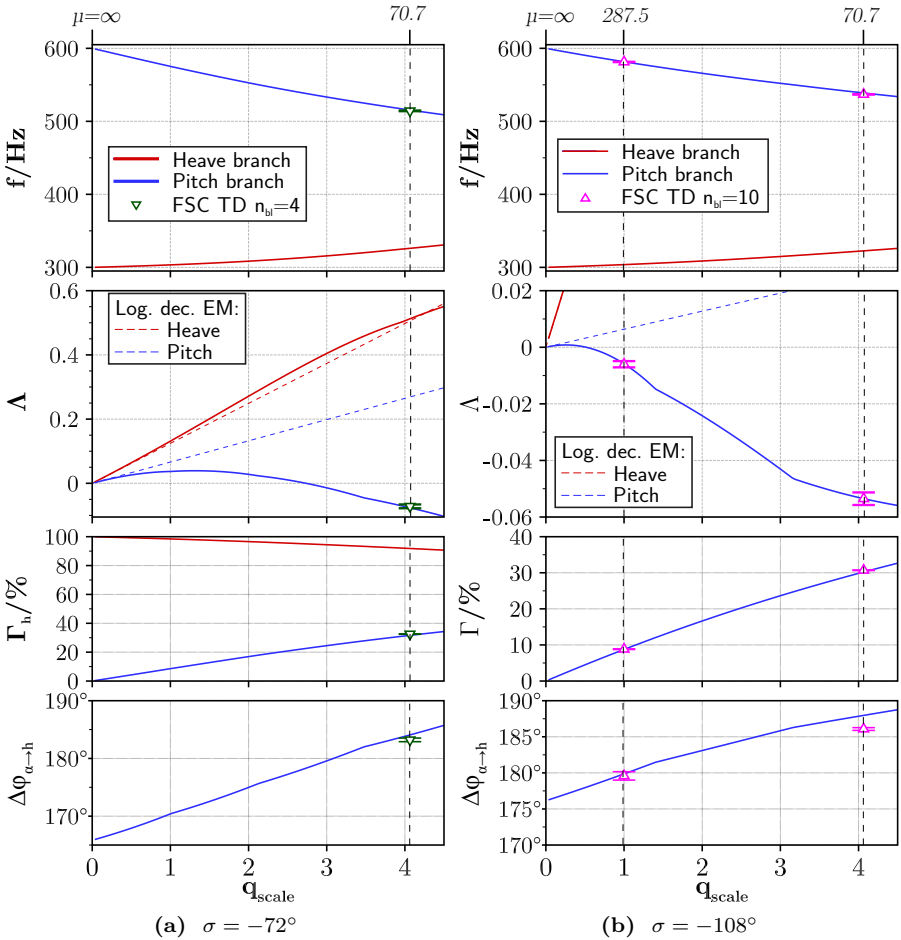


Figure 5.15.: FUTURE-2D-LC, case “transonic II”: p-k solution history



### 5.3. NACA3506-2D-LC

The NACA3506 linear cascade is used to check geometry-dependent features of the verification and validation process. This case is not as extensively investigated as the FUTURE-EPFL geometry above, but leads to the same conclusion when comparing time-marching FSC simulations with the p-k method.

*The results of the time-marching FSC simulations are previously published by the author [86]. In the article, it is shown that only the multi-mode coupled system leads to flutter for the investigated parameters. In the scope of this thesis, only the validation and verification between time-marching FSC simulations and the p-k method is performed.*

#### 5.3.1. Subsonic

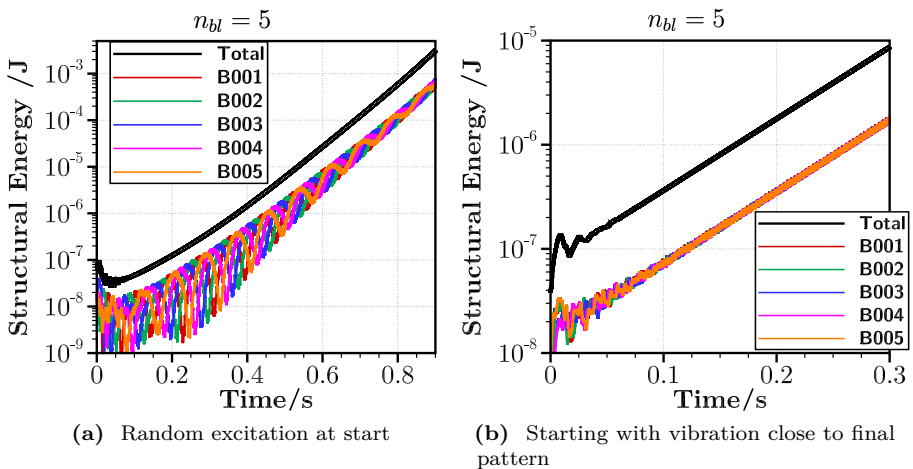


**Figure 5.16.:** NACA3506-2D-LC, case “subsonic”: Total and individual blade structural energy for same setup with different initial conditions

The blades have a much higher mass ratio than the FUTURE-2D-LC case. The effect of this leads to longer time periods until the energy is evenly distributed in the cascade and all blades perform the same vibrational pattern. This can be seen in fig. 5.16. If initial deflections are chosen randomly, the cascade starts to increase the structural energy relatively fast, but the individual blades have a high deviation. If the starting conditions are chosen very close to the expected result, the time until a uniform vibration pattern is formed is relatively

short. The initial transient phase is virtually non-existent and amplitudes grow right away with the already established vibration pattern. This reflects in the standard deviation of the modal parameters.

The four passage blade setup results in the IBPA  $\sigma = -90^\circ$  and the five passage setup with the IBPA  $\sigma = -72^\circ$ . The comparison is in fig. 5.17 plots the p-k solution convergence of these IBPAs and the results agree very good. The high standard deviation of the randomly excited case is visible, but also that the averaged value is already in good agreement with the p-k method.

### 5.3.2. Transonic

The four passage blade setup results in the IBPA  $\sigma = 180^\circ$  and the five passage setup with the IBPA  $\sigma = -72^\circ$ . The comparison is fig. 5.18 plots the p-k solution convergence of these IBPAs. As for the FUTURE-2D-LC case, there are slight differences between time-marching simulations and the p-k method, especially in the phase-shift between heave and pitch mode. Still, the results are very close agreement and predict the excited cases correctly.

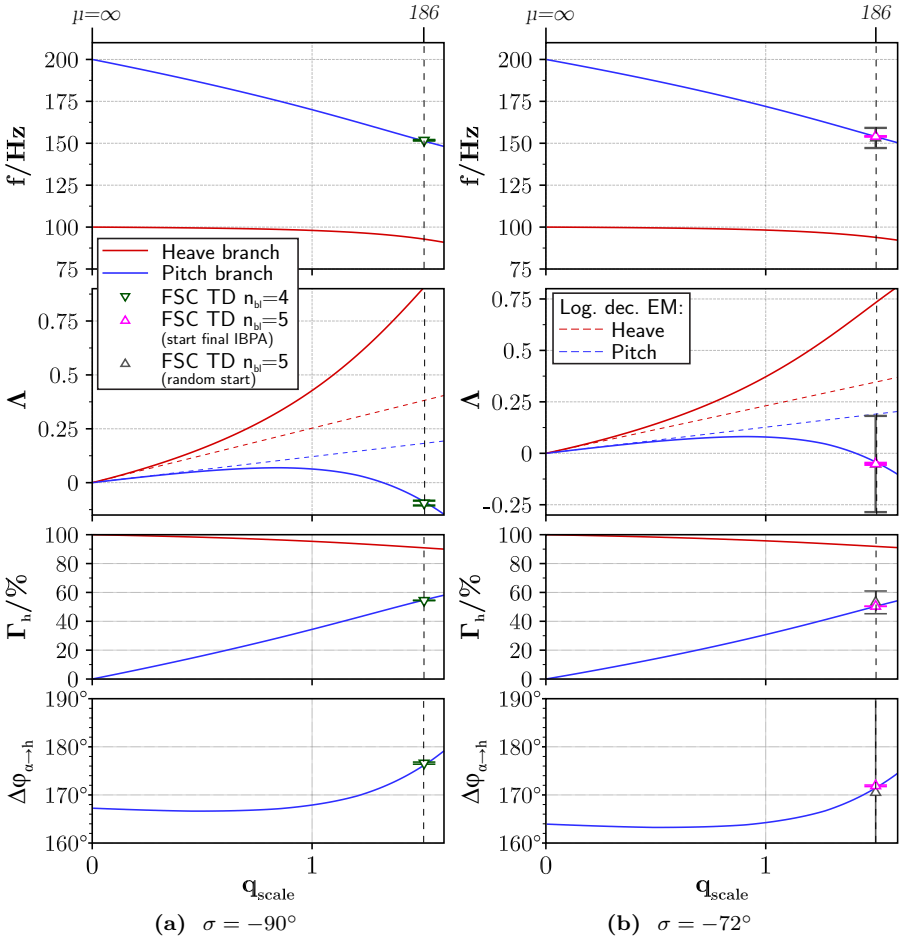


Figure 5.17.: NACA3506-2D-LC, case “subsonic”: p-k solution history

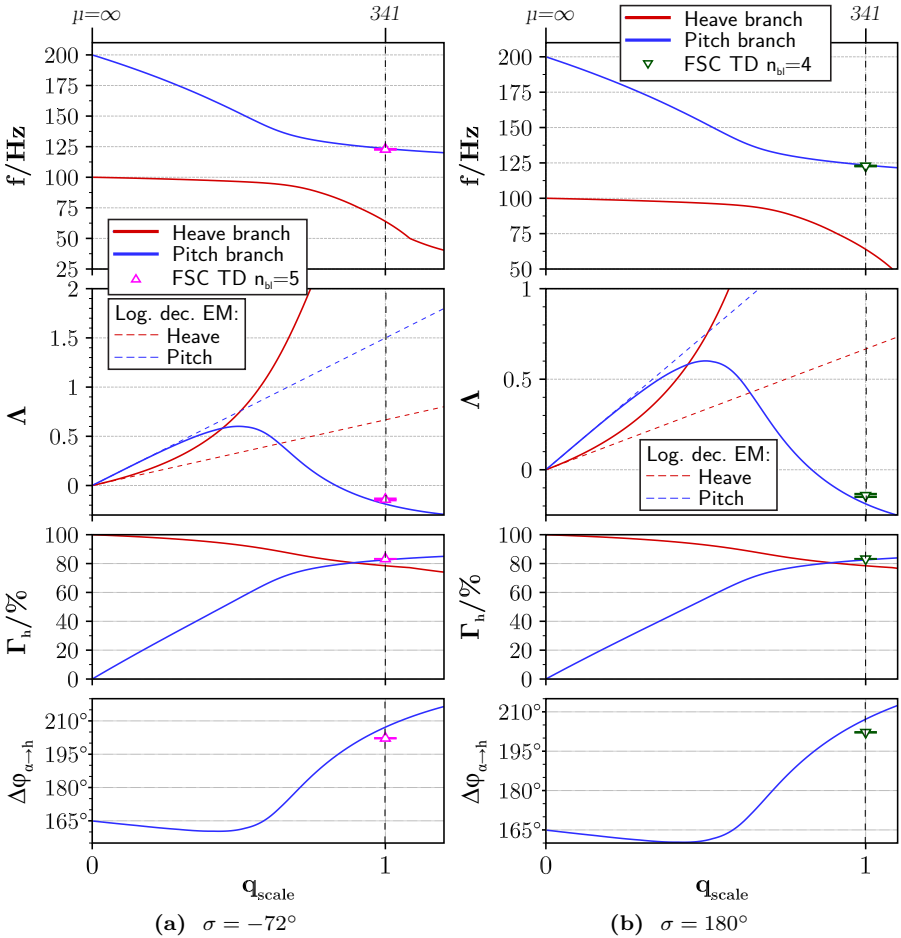


Figure 5.18.: NACA3506-2D-LC, case “transonic”: p-k solution history

## 5.4. CRISPMulti

The CRISPMulti geometry is subject to a deeper analysis later. In the context of this chapter, time-marching FSC simulations for the isolated first rotor are compared to results from the p-k method. As a full 3D setup, especially the time-marching computations are much more demanding in terms of CPU time. Therefore, only one particular operating point at the 70% speedline above the working line (WL) is investigated. As will be shown later, this OP is predicted to be stable with the energy method, but the p-k analysis shows a flutter onset. This behavior is verified with the time-marching FSC simulations.

The phase difference in the modal participation is build in analogy to section 5.1.2, where  $\Delta t_{\text{lag}}$  is the time between the peaks of modeshape  $i$  and modeshape  $j$ :

$$\Delta\varphi_{i \rightarrow j} = \frac{\Delta t_{\text{lag}}}{T} 360^\circ \quad (5.11)$$

$$\Delta\varphi_{j \rightarrow i} = \frac{(T - \Delta t_{\text{lag}})}{T} 360^\circ = 360^\circ \left(1 - \frac{\Delta t_{\text{lag}}}{T}\right) \quad (5.12)$$

and also in analogy are the p-k results build via:

$$\Delta\varphi_{i \rightarrow j} = \varphi_j - \varphi_i \quad (5.13)$$

$$\Delta\varphi_{j \rightarrow i} = \varphi_i - \varphi_j \quad (5.14)$$

and the conversion is accordingly:

$$\Delta\varphi_{i \rightarrow j} = 360^\circ - \Delta\varphi_{j \rightarrow i} \quad (5.15)$$

$$\Delta\varphi_{j \rightarrow i} = 360^\circ - \Delta\varphi_{i \rightarrow j} \quad (5.16)$$

### 5.4.1. Time-Marching FSC Simulations

For the selected OP, two different setups are chosen. Both setups include the three modeshapes with the lowest frequency: first bending (1B), second bending (2B), and first torsion (1T), as depicted in fig. 4.11. The first setup consists of two passages allowing the two IBPAs  $0^\circ$  and  $180^\circ$ . The second setup has five passages, allowing the five IBPAs  $0^\circ$ ,  $\pm 72^\circ$ , and  $\pm 144^\circ$ .

#### Two Passages

The two passage setup is started with no initial structural deflections (fig. 5.19a). As the steady flowfield is released to unsteady simulations, there is a small but relevant flow disturbance. It stems from small unsteadiness, which was not

fully resolvable in the steady CFD. While this could be artificially damped in the numerics, it is useful to get some initial energy into the system. Due to this artifact, the mean modal force changes a little bit, what then causes both blades to adjust their static deflection slightly. Interestingly, the two blades perform different deflections in reaction to this, visible through the different energy level for  $t < 0.2$  s. After that initial phase, both blades transition to a harmonic vibration and at around  $t \approx 0.3$  s the final vibration IBPA  $\sigma = 0^\circ$  is reached. The structure then continues to increase amplitudes with a stable logarithmic decrement.

The simulations are restarted with higher, but random initial deflections (fig. 5.19b). The small flow disturbance when going from steady to unsteady is now not significant anymore. The cascade transitions relatively fast to the final vibration pattern known from the first simulation. At high amplitudes around  $t \approx 1.2$  s, a limit cycle oscillation (LCO) is reached.

### Five Passages

The first computation of the five passage setup is started with the first torsion (1T) at an IBPA  $\sigma = 0^\circ$  (fig. 5.20a). The vibration couples with the other modeshapes but stays at this IBPA and increases amplitudes (starting at  $t \approx 0.05$  s). At  $t \approx 0.2$  s, the IBPA pattern transitions to  $\sigma = 72^\circ$ , which causes the blades to have largely differing amplitudes. The computation was stopped at around  $t \approx 0.9$  s because of large and unfavorable deflections which could not be handled by the mesh deformation algorithm anymore. Thus, a shift to a fully established pattern of  $\sigma = 72^\circ$  cannot be observed.

The second simulation is now started with the initial IBPA changed to  $\sigma = 72^\circ$  (fig. 5.20b). Opposing to the two passages setup, the system does not just rapidly transition into a harmonic vibration pattern. The cause to this behavior is not really obvious, but might be due suddenly introduced unsteadiness when the initial deflections disturb the flowfield. The blades now equalize the energy distribution between them, but cannot reach a strict harmonic pattern as for the two passage setup. Nevertheless, the sum of the individual blade structural energy grows exponentially as in a linearly excited system. This will be the cause for a high standard deviation in the next section.

### 5.4.2. P-K Analysis

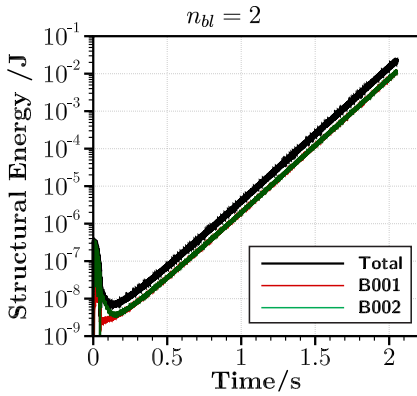
The p-k convergence plot for both IBPAs, which resulted in the time-marching FSC computations, are plotted in figs. 5.21 and 5.22. The vibration characteristics (frequency, damping, modal participation) is marked by the triangles in the respective plot. The phase shift between the modeshapes is relative to the

dominant vacuum modeshape 1T (phase angle of the respective modeshape, when 1T is at  $0^\circ$ ).

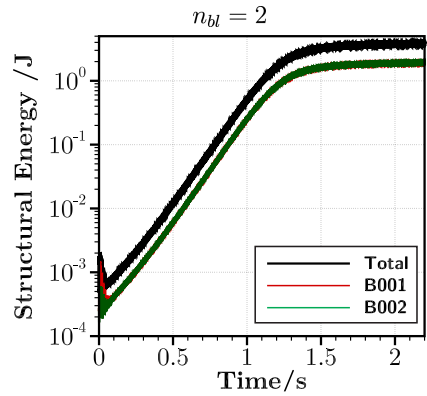
For the two passage setup, the resulting IBPA  $\sigma = 0^\circ$  shows good agreement in the prediction of the frequency and modal participation of the dominant vacuum modeshapes 1T (major) and 1B (minor). The participation of 2B has some errors in the phase shift, but looking at it globally, the values are not that far off. A similar observation can be made for the IBPA  $\sigma = 72^\circ$ .

The logarithmic decrement  $A$  is not predicted exactly. This is not concerning, as the p-k method is only accurate at the zero damping line. A little below or above, the frequency domain (p-k) values can thus differ from the time-marching (FSC) simulations. The important part is that the flutter onset is captured.

The five passage setup allows for both unstable IBPAs shown here, with  $\sigma = 72^\circ$  having a slightly higher excitation. The behavior shown in fig. 5.20a actually shows, that the structure will tend to vibrate in the IBPA with this higher excitation.

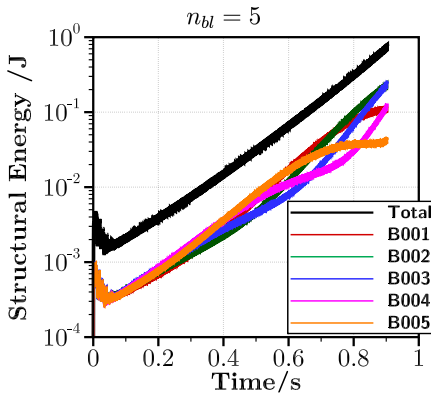


(a) Low initial structural energy, simulation terminated by choice before reaching LCO

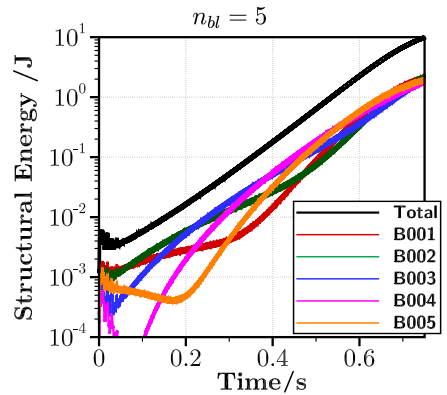


(b) High initial structural energy, cascade runs into LCO

**Figure 5.19.:** CRISPMulti,  $n = 70\%$  above WL: Total and individual blade structural energy for setup with 2 passages, final vibration IBPA is  $\sigma = 0^\circ$  in both cases



(a) Initial deflections close to IBPA  $\sigma = 0^\circ$ , cascade transitions to  $\sigma = 72^\circ$



(b) Initial deflections close to final IBPA pattern  $\sigma = 72^\circ$

**Figure 5.20.:** CRISPMulti,  $n = 70\%$  above WL: Total and individual blade structural energy for setup with 5 passages



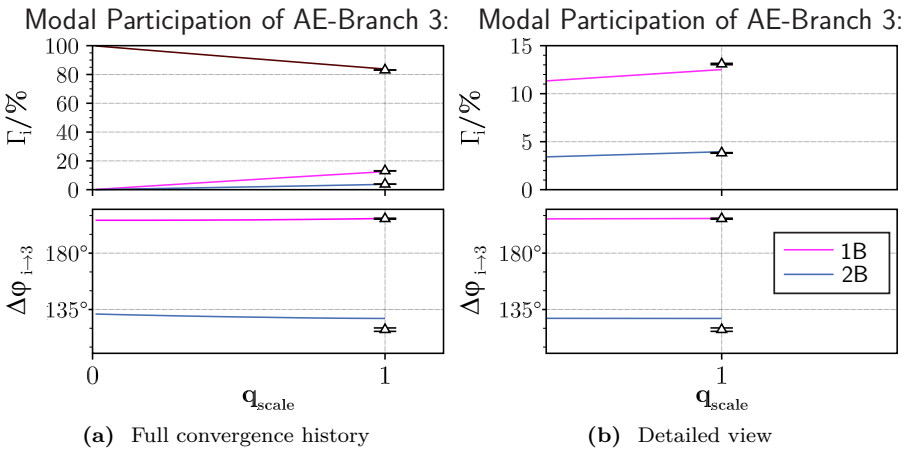
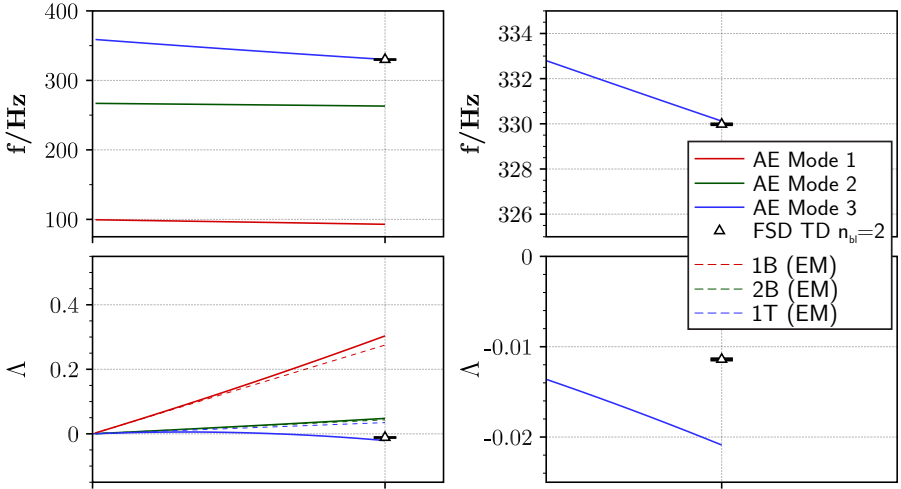


**Figure 5.21.:** CRISPmulti,  $n = 70\%$  above WL, 2 passages,  $\sigma = 0^\circ$ : p-k solution history

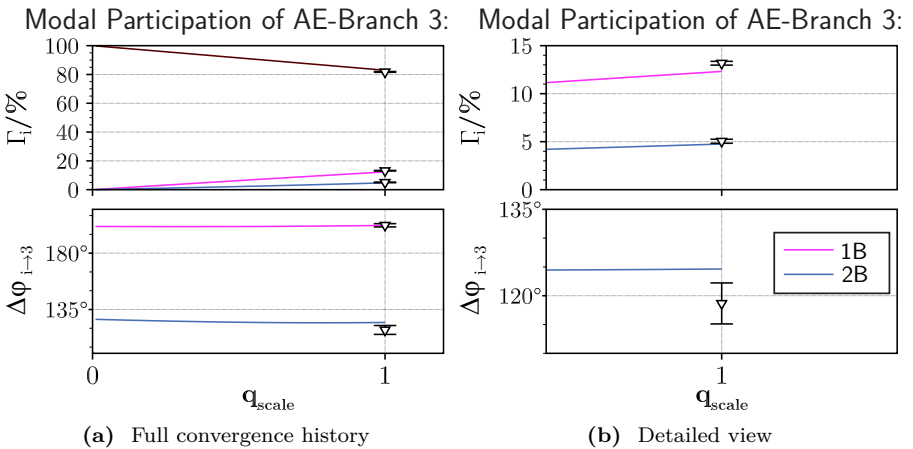
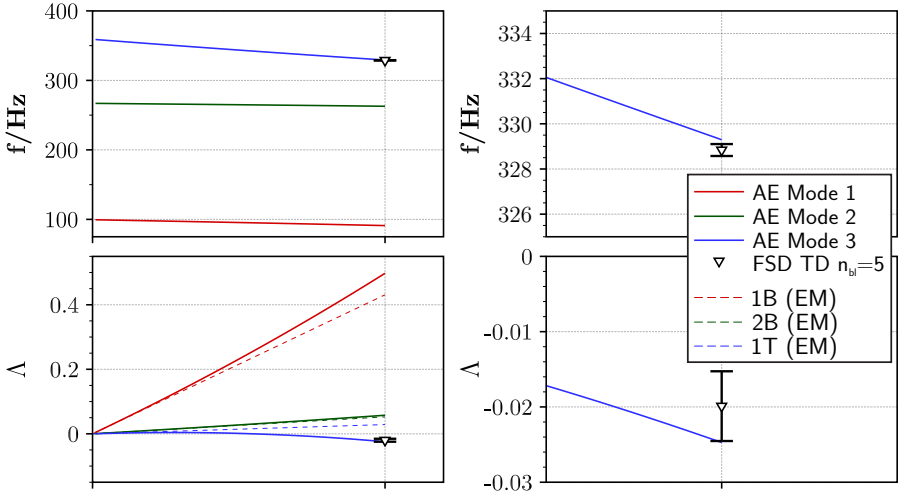


**Figure 5.22.:** CRISPMulti,  $n = 70\%$  above WL, 5 passages,  $\sigma = 72^\circ$ : p-k solution history

## 5.5. Mode Tracking Strategies

### 5.5.1. Mode Crossing

The eigenvalue analysis of the flutter equation requires the identification of the physically reasonable eigenvalue and eigenvector results of the aeroelastic branch (cf. section 2.4.2). As mentioned, the mode identification can be done with simple frequency sorting and assignment in lightly coupled cases. However, neglecting the path of the aeroelastic branch along the  $q_{scale}$ -axis of the p-k solution can lead to misleading results.

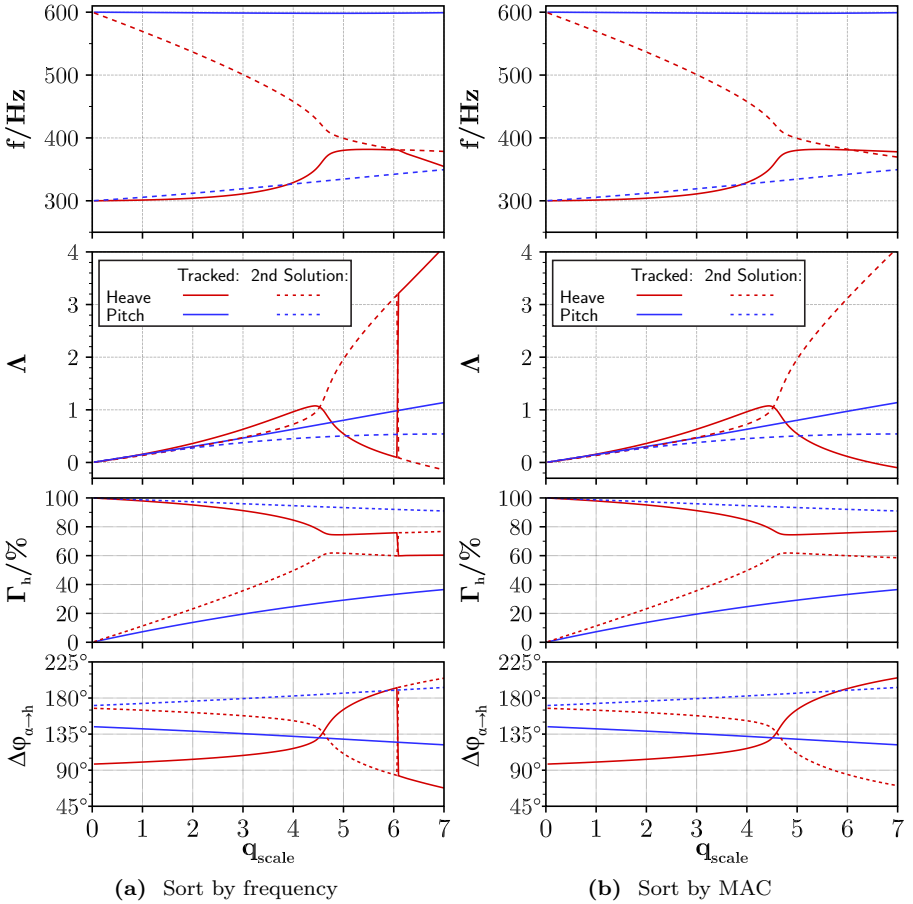
In fig. 5.23, the tracking via frequency sorting and via MAC matching is compared. Starting at the vacuum frequencies  $f_{heave} = 300$  Hz and  $f_{pitch} = 600$  Hz, each branch yields two solutions of the eigenanalysis, marked by the same color. The solid lines mark the tracked mode, the dashed lines are the unphysical solution that is discarded based on the tracking. For values of  $q_{scale} < 4$ , one solution is the obvious physical solution as it is close to the vacuum frequency. Slightly over  $q_{scale} = 6$ , a kind of bifurcation occurs. The frequency tracking will lead to a jump in the damping and modal participation for  $q_{scale} > 6$ . In contrast, when MAC tracking is applied, these values continue smoothly on their previous track.

This behavior can be called “mode crossing” and is easily trackable by the MAC value as shown. Important to note is that the switch to a unphysical track results in a very high damping value as opposed to the MAC tracking, which will predict a flutter onset at  $q_{scale} \approx 6.5$ . Furthermore, the tracks of the heave mode (red) after the bifurcation are not simply swapped when frequency tracking is used. Almost not visible, they differ very slightly. This happens because the eigenanalysis depends on the GAFs corresponding to the given vibration frequency.

### 5.5.2. Frequency Coalescence

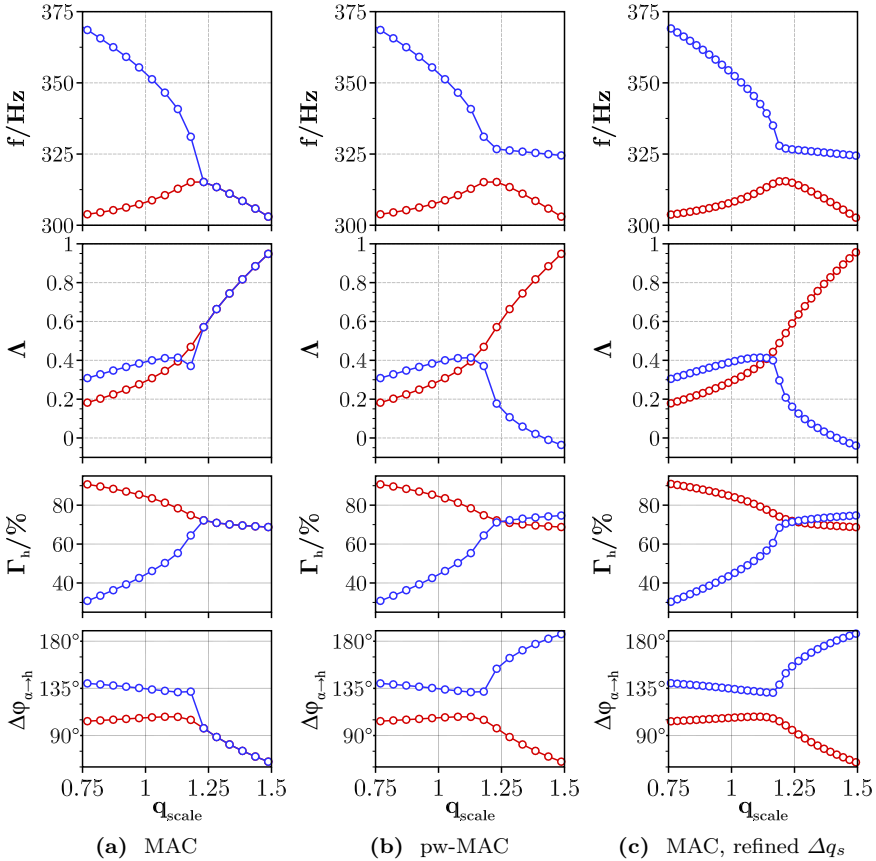
Jumping between mode tracks of the aeroelastic branches may occur in the case of *frequency coalescence*, when two (or more) aeroelastic branches are converging their frequency. At the same time, the eigenvectors (or modal participation) also converge to each other.

Figure 5.24a shows the MAC tracking strategy only yields one result for  $q_{scale} > 1.25$ . This happens because the modal participation factor is nearly the same, showing the disadvantages of a criterion that only compares the eigenvectors for sorting and assigning. The pw-MAC (cf. section 2.4.2) allows a correct tracking of the two aeroelastic branches even when eigenvectors are very similar and hard to distinguish: in fig. 5.24b, the vibration frequency are coalescing without



**Figure 5.23.:** Mode tracking via frequency or MAC sort (case: FUTURE-2D-LC, transonic I,  $\sigma = -144^\circ$ ,  $f_{heave} = 300$  Hz,  $f_{pitch} = 600$  Hz)

converging and separate afterward. The tracks of the two aeroelastic branches appear much smoother from a visual and physical interpretation. As with the previous case, the jump is unfavorable since it discards the flutter onset that occurs at  $q_{scale} \approx 1.4$  if the lower path would be tracked.



**Figure 5.24.:** Mode tracking strategies with MAC and pw-MAC method (case: FUTURE-2D-LC, transonic I,  $\sigma = -108^\circ$ ,  $f_{heave} = 300$  Hz,  $f_{pitch} = 400$  Hz)

The behavior of the MAC tracking in this case depends on the increment  $\Delta q_{scale}$ . If the increment is smaller as shown in fig. 5.24c, the MAC tracking yields the same result as the pw-MAC tracking. The disadvantage of this method is the higher computational effort. An adaptive increment size would improve on this matter and is part of the future extension plans for the p-k solver toolchain.

## 5.6. Summary

For all time-marching fluid/structure-coupled simulations with growing amplitudes, it can be observed that once the excited system is established, the amplitudes increase until either the mesh deformation process cannot handle the large deflections anymore or an amplitude-dependent aerodynamic response occurs and a limit cycle oscillations is formed. As no fixed IBPA is set in the simulations, the phase shift between the blades is of natural occurrence in the coupled system.

Regardless of the initial condition, i.e. modal displacements and velocities of the cascade at  $t = 0$ , if an unstable combination of modeshape and IBPA is present in the system, the cascade will ultimately vibrate in this pattern. Furthermore, the system vibrates in one dominant IBPA pattern, even if multiple IBPAs have an aeroelastically coupled instability. Ultimately, the dominant IBPA is the one with the highest excitation, as can be observed e.g. in fig. 5.22. This shows from a practical point of view, that the coupled-mode analysis per individual IBPA is justified.



# 6

## Aerodynamically Coupled Modeshapes in a Linear Compressor Cascade

*A deeper analysis with varying key parameters is performed for the FUTURE-2D-LC cascade. The influence of the mass ratio is already shown in the previous chapter, but will now be discussed in detail. Furthermore, the frequency separation and solidity changes are discussed. In the validation chapter, only selected IBPA-combinations were looked at. In this chapter, the survey is extended to the full spectrum of IBPAs and analyzed as a whole.*

*Flutter is a geometry-dependent phenomenon and discrete values for mass ratio or other key parameters are always connected to the investigated geometry. Nevertheless, the tendencies might be the same for similar structures (i.e. turbomachinery blades), but specific numbers may vary a lot.*

*The fundamental findings from preliminary research were already published by the author [93]. More detailed and deeper analyses are performed in the scope of this thesis.*

**Table 6.1.:** “Baseline” Configuration of the FUTURE-2D-LC Geometry

Vacuum Frequency Heave	$f_{\text{heave}} =$	300 Hz
Vacuum Frequency Pitch	$f_{\text{pitch}} =$	600 Hz
Rotation Axis	50% chordlength	
Pitch	$\tau =$	56.55 mm
Solidity	$s = c_b/\tau =$	1.22



**Table 6.2.:** Solidity Variation of the FUTURE-2D-LC Geometry

Variation	+20 %	baseline	-20 %	-40 %
Solidity $s = c_b/\tau =$	1.36	1.22	1.02	0.87
Pitch $\tau =$	50.90 mm	56.55 mm	67.86 mm	79.17 mm

## 6.1. General Remarks

The CFD simulations in this chapter are now only carried out in the frequency domain using the harmonic balance solver. In contrast to the validation section, the two-dimensional unsteady non-reflecting boundary conditions are applied. The “baseline” is listed in table 6.1, the variations in solidity in table 6.2.

With the energy method, the aeroelastic behavior is not affected qualitatively when changing the mass ratio as described in section 2.5.4. To avoid misleading results in the energy method due to mass ratio effects, the aerodynamic damping in the traveling wave mode diagrams (damping-over-IBPA) in this chapter is normalized using the mass ratio. As a consequence, the normalized logarithmic decrement is independent of mass ratio and only plotted once for the energy method results.

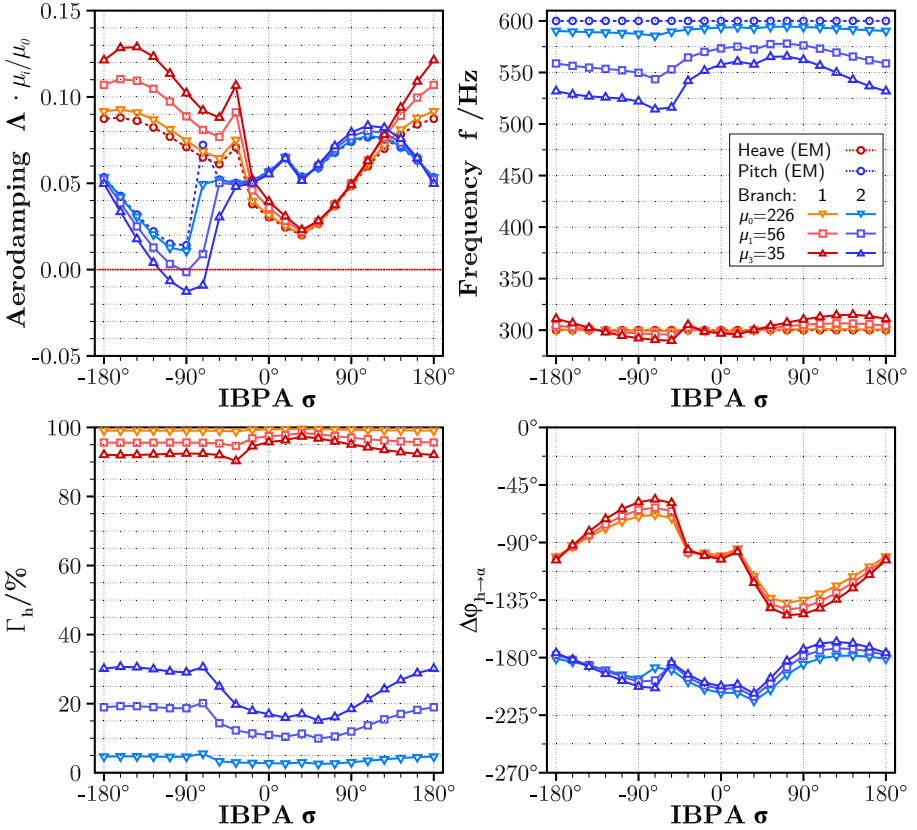
## 6.2. Subsonic Operating Point

### 6.2.1. Influence of Mass Ratio and Frequency Separation

For the “baseline” configuration, the damping diagram comparing EM and p-k method at different mass ratios is plotted in fig. 6.1. At the highest shown mass ratio  $\mu_0 = 226$ , the damping according to the p-k method stays close to the EM results, although a slight frequency shift is already visible for the second aeroelastic branch. An outlier is the IBPA  $\sigma = -72^\circ$  of this second aeroelastic branch, which will be discussed later. Lowering the mass ratios increases the coupling effects and lead to a drift away from the EM for both branches. Some IBPAs are affected stronger than others. Again, the IBPA  $\sigma = -72^\circ$  strikes out with a big shift in damping from a very stable point to almost becoming the point with the highest excitation at the lowest mass ratio. Interestingly, the IBPAs with the lowest damping values in the EM are the ones that become unstable (branch 2 at negative IBPAs), while in contrast the highest damped values become more stable (branch 1 at negative IBPAs and branch 2 at positive IBPAs). The aeroelastic modeshape for this case changes mainly in terms of the modal participation while the phase lag between heave and pitch stays almost unaffected by the mass ratio.

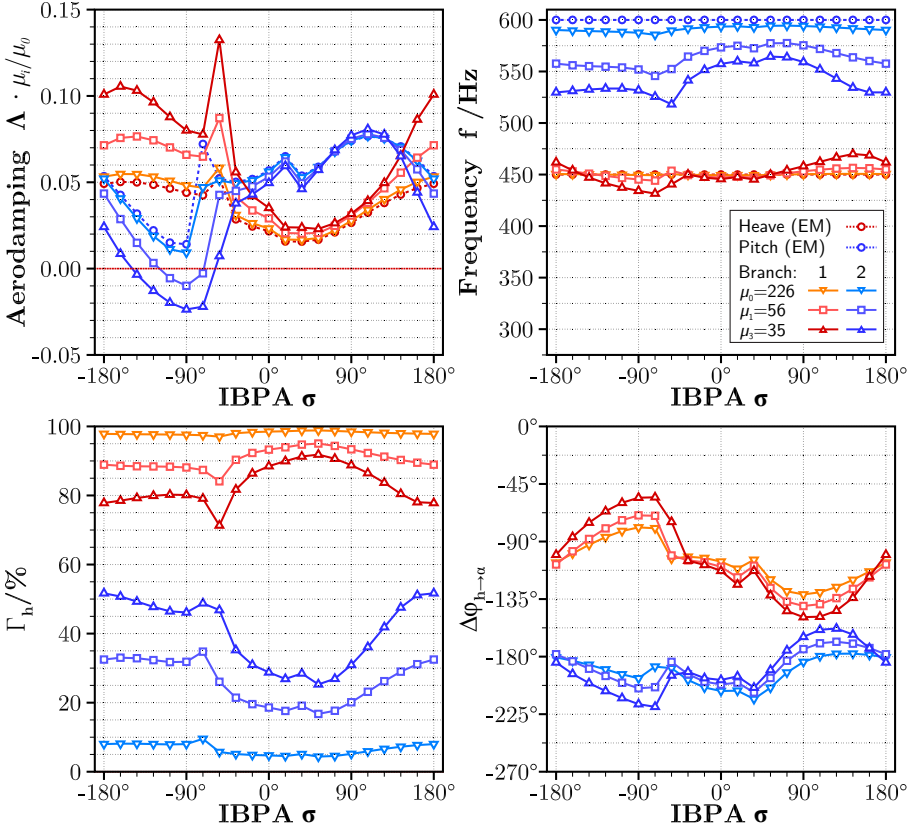
By moving the vacuum frequency of the heave motion closer to the frequency of the pitch, the destabilization effect due to a lowered mass ratio increases as shown in fig. 6.2. More IBPAs become unstable at a higher mass ratio now, even if the aeroelastic frequencies are not shifted in the same significance. Figure 6.3 has an even lower frequency separation and the trend continues. In this case, there is also a frequency coalescence of both branches at the IBPA  $\sigma = 126^\circ$ , but the two branches have different aerodampings. Between this and the next higher IBPA  $\sigma = 144^\circ$ , a crossover of the aerodamping occurs. While the aeroelastic frequencies of the branches diverge again, the aerodampings might be interpreted as wrongly sorted. However, as the IBPAs are periodic, this would connect the branches to the opponent in the negative IBPA range. The coalescence character of the high modal coupling becomes also apparent when looking at the manifestation of both aeroelastic modeshapes. For the mentioned IBPAs, both modeshapes have almost the same modal participation and a similar picture as with the aerodamping can be found for the phase lag. Most important is the correct tracking of the physical aeroelastic modeshapes along the  $q_{\text{scale}}$  convergence iterations.

$$f_{\text{heave}} = 300 \text{ Hz}, f_{\text{pitch}} = 600 \text{ Hz}$$



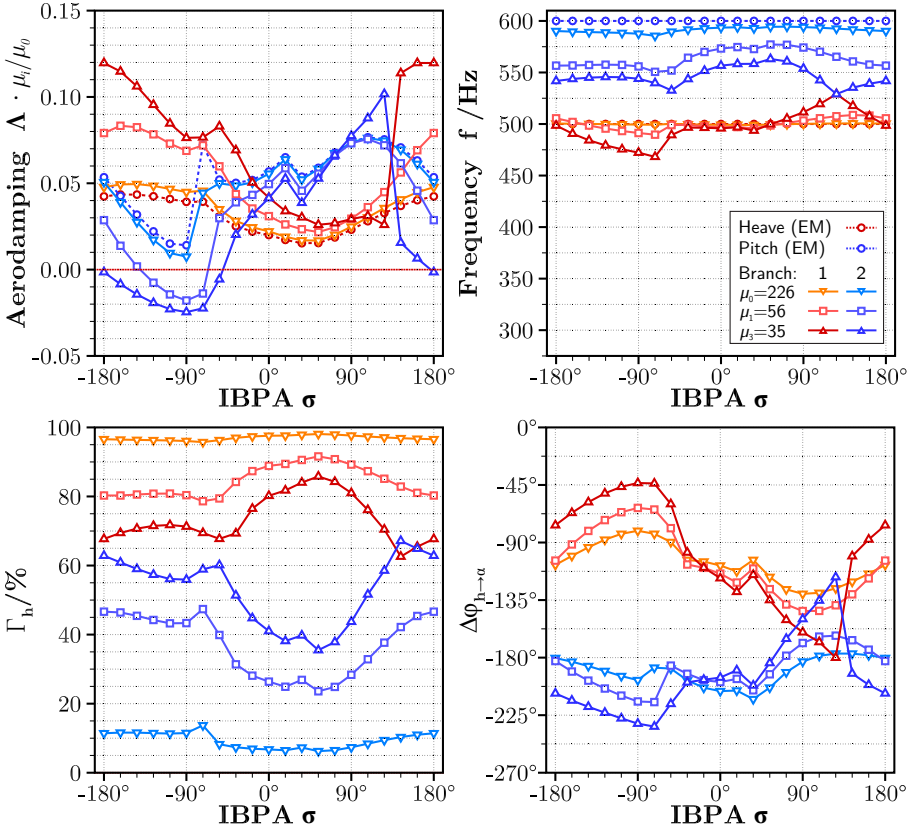
**Figure 6.1.:** Frequency separation 1:2, FUTURE-LC-2D, case “subsonic”, solidity  $s = 1.22$ : Traveling wave diagram compared between EM and p-k for varying mass ratio

$$f_{\text{heave}} = 450 \text{ Hz}, f_{\text{pitch}} = 600 \text{ Hz}$$



**Figure 6.2.:** Frequency separation 2:3, FUTURE-LC-2D, case “subsonic”, solidity  $s = 1.22$ : Traveling wave diagram compared between EM and p-k for varying mass ratio

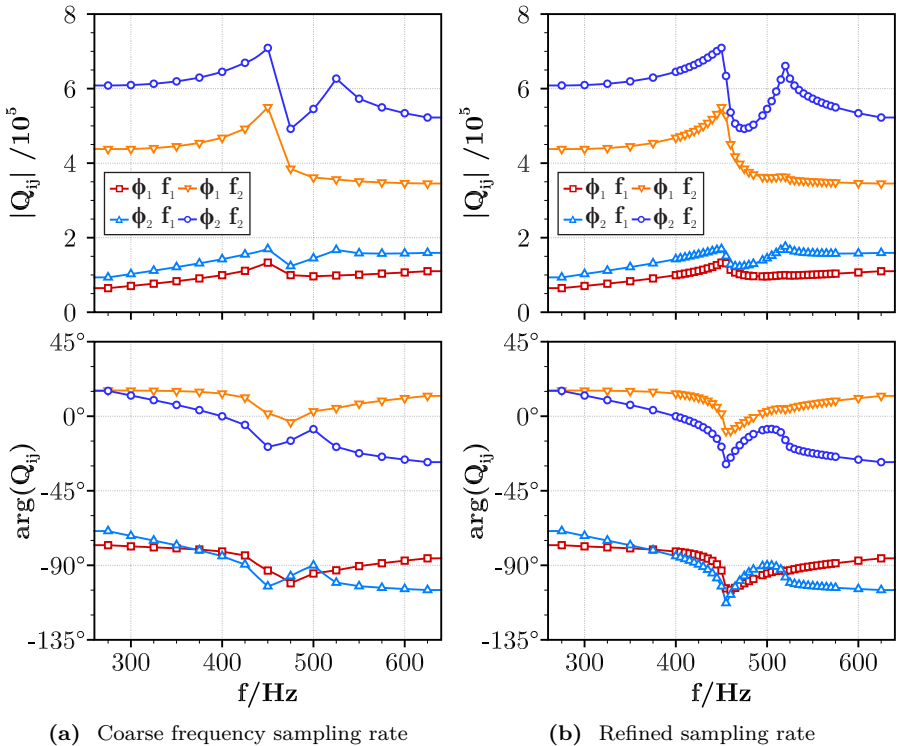
$$f_{\text{heave}} = 500 \text{ Hz}, f_{\text{pitch}} = 600 \text{ Hz}$$



**Figure 6.3.:** Frequency separation 5:6, FUTURE-LC-2D, case “subsonic”, solidity  $s = 1.22$ : Traveling wave diagram compared between EM and p-k for varying mass ratio

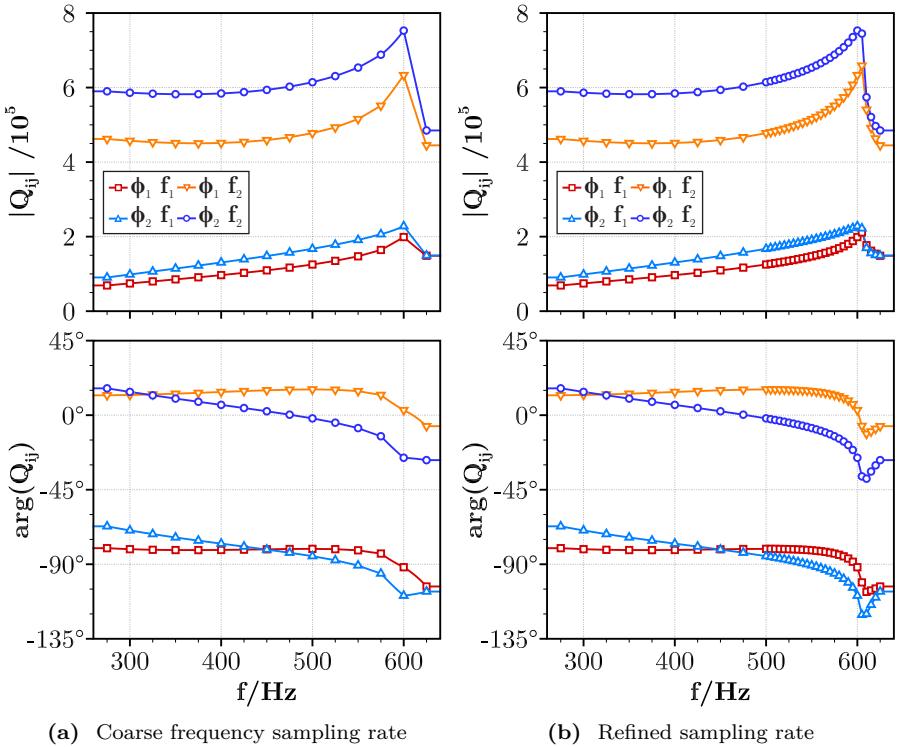
### 6.2.2. Aerodynamic Resonance and Effect on Modal Coupling

Figure 6.4a plots the generalized aerodynamic forces over the frequency with the default sampling rate. Apparently, there are some sort of aerodynamic resonance phenomena around  $f \approx 450$  Hz and  $f \approx 525$  Hz. When using a refined sampling rate around these two points, fig. 6.4b shows a much smoother track. A similar phenomenon is visible at another IBPA in fig. 6.5. Other IBPAs have a more smooth curve and do not show such large resonance points. Some of these refinements will have a huge impact on the outcome of the p-k analysis.



**Figure 6.4.:** FUTURE-2D-LC, case “subsonic”, IBPA  $\sigma = -54^\circ$ : Generalized aerodynamic forces around resonance condition with different frequency sampling rates

Figure 6.6a shows the larger frequency separation, where the natural frequency of the heave mode is far away from the resonance points and only the pitch branch is affected by the different sampling rates. If only the coarse frequency



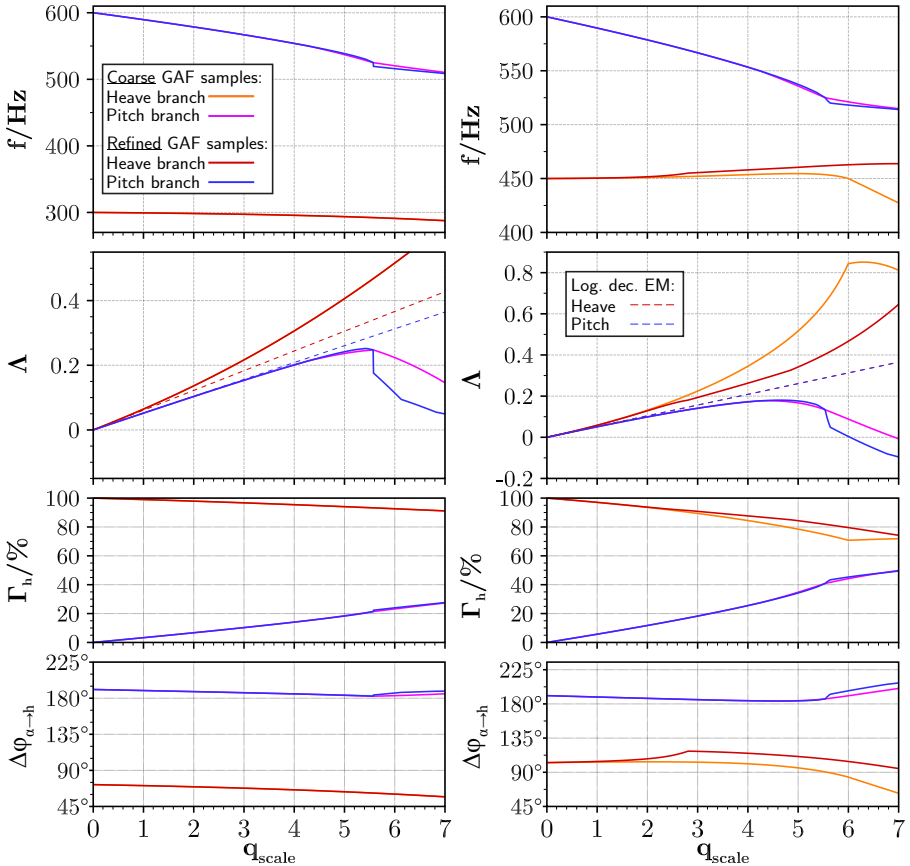
**Figure 6.5.:** FUTURE-2D-LC, case “subsonic”, IBPA  $\sigma = -72^\circ$ : Generalized aerodynamic forces around resonance condition with different frequency sampling rates

sampling rate is used, the pitch branch has a smooth track along the  $q_{\text{scale}}$ . With the better resolved aerodynamic resonance, a frequency and damping jump occurs at  $q_{\text{scale}} \approx 5.5$ . This unsteadiness is not an artifact of the p-k method convergence but also happens if the  $\Delta q_{\text{scale}}$  is refined. It occurs in close vicinity to the resonance’s peak frequency. Once the modal coupling shifts the aeroelastic frequency from one side to other of this peak, a sudden change in aeroelastic behavior results. Even before that, minor differences are already visible. The result is a non-conservative damping prediction for a coarser resolution of the GAFs. However, the damping in the investigated range does not drop below zero.

A more severe impact can be seen in fig. 6.6b, where the natural frequency of the heave mode is very close to one of the resonance points. Due to the lower frequency separation, the pitch branch gets unstable earlier. A similar behavior of the pitch branch as discussed above is observed when the refined GAFs are used. In this case, the pitch branch becomes unstable at  $q_{\text{scale}} \approx 6$ , compared to the coarse resolution where the zero damping is reached at  $q_{\text{scale}} \approx 7$ . The heave branch diverges between coarse and refined frequency sampling already at around  $q_{\text{scale}} \approx 2$  and finally a huge difference in its character occurs at  $q_{\text{scale}} \approx 6$ .

For the IBPA  $\sigma = -72^\circ$ , the peak of the resonance is almost at the vacuum frequency of the pitch modeshape. As the aeroelastic frequency is always lower than the vacuum frequency, there is no transition from one side to the other of this peak and thus, no unsteadiness in the p-k solution. Some minor difference can be seen in fig. 6.5 for the low  $q_s$  values. However, the impact on the aeroelastic frequency and aerodamping is neglectable.





(a) Heave natural frequency far from resonance ( $f_{\text{heave}} = 300$  Hz,  $f_{\text{pitch}} = 600$  Hz)

(b) Heave natural frequency close to resonance ( $f_{\text{heave}} = 450$  Hz,  $f_{\text{pitch}} = 600$  Hz), closeness of heave and pitch damping in EM is just a coincidence.

**Figure 6.6.:** FUTURE-2D-LC, case “subsonic”, IBPA  $\sigma = -54^\circ$ : p-k solution histories at two different frequency separations with different frequency sampling rates

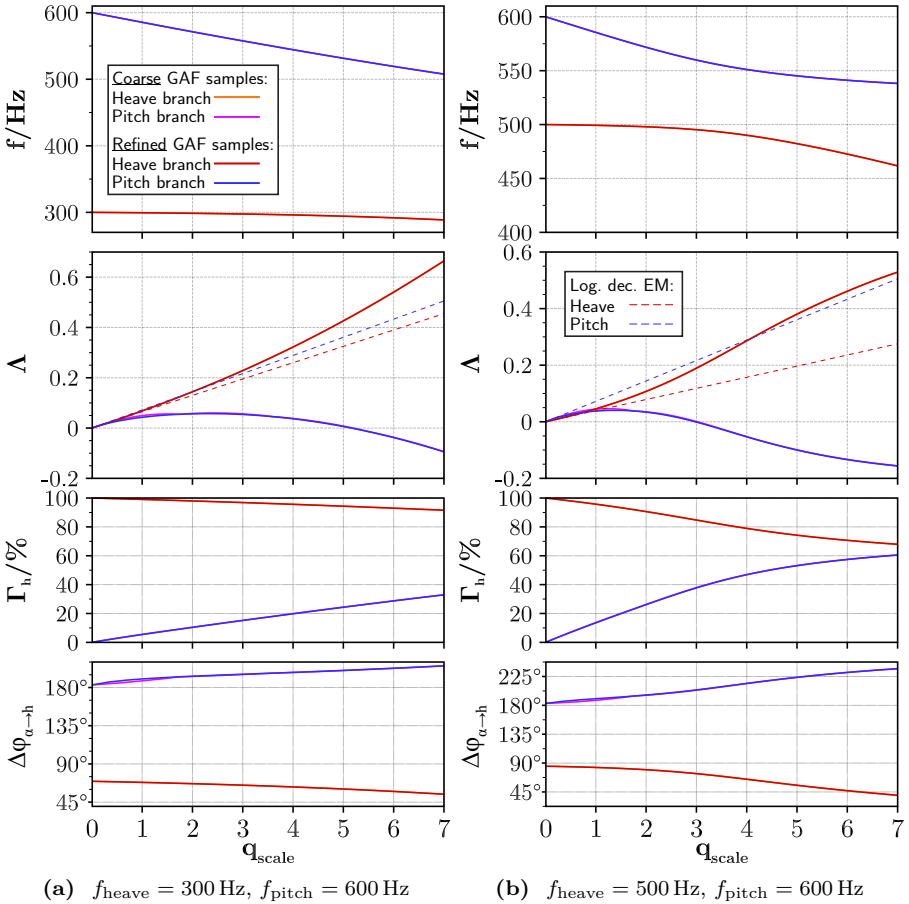


**Figure 6.7.:** FUTURE-2D-LC, case “subsonic”, IBPA  $\sigma = -72^\circ$ : p-k solution histories at two different frequency separations with different frequency sampling rates (where the orange/purple lines are not visible, they are hidden behind the red/blue lines)

### 6.2.3. Influence of Solidity

The extension of section 6.2.1 is the application to different blade-to-blade distances. The solidity is the inverted non-dimensional blade-to-blade distance and thus a higher solidity means, that the blades are closer together. This increases the impact of blade-to-blade effects, which are most pronounced at IBPAs unequal to zero.

Figures 6.8 and 6.9 shows the incremental change of the solidity and frequency separation listed in table 6.2. At first glance, increasing the solidity leads to flutter at higher mass ratios. The highest mass ratios are indeed almost equivalent to the energy method. At higher solidities, the previously observed trend is confirmed: the least stable IBPAs become unstable, and in contrast, the most stable IBPAs are increased in stability. Very clearly visible is an outlier at  $s = 0.87$  and IBPA  $\sigma = 36^\circ$  with a very high damping compared to the surrounding IBPAs. This is also due to an aerodynamic resonance point like shown above. The vacuum frequency is very close to the resonance peak. In contrast to the previously presented case, this resonance is acting as a dampening factor, producing the spike in aerodamping. The aeroelastic frequency is shifted away from this resonance point at lower mass ratios. Therefore, the impact is more pronounced (happening at higher mass ratios) for the higher modal coupling strength at lower frequency separations.

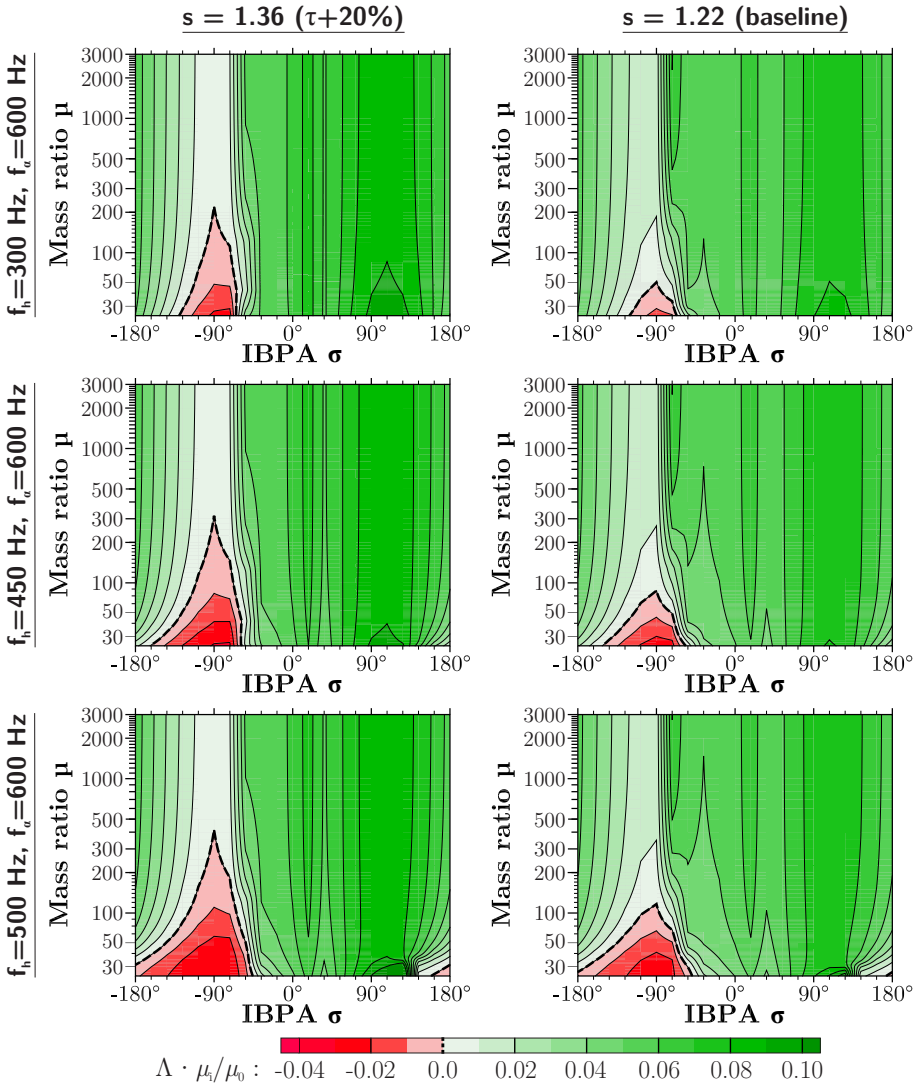


**Figure 6.8.:** FUTURE-LC-2D, case “subsonic”: Normalized aerodamping of second aeroelastic modeshape depending on mass ratio, frequency separation, and solidity

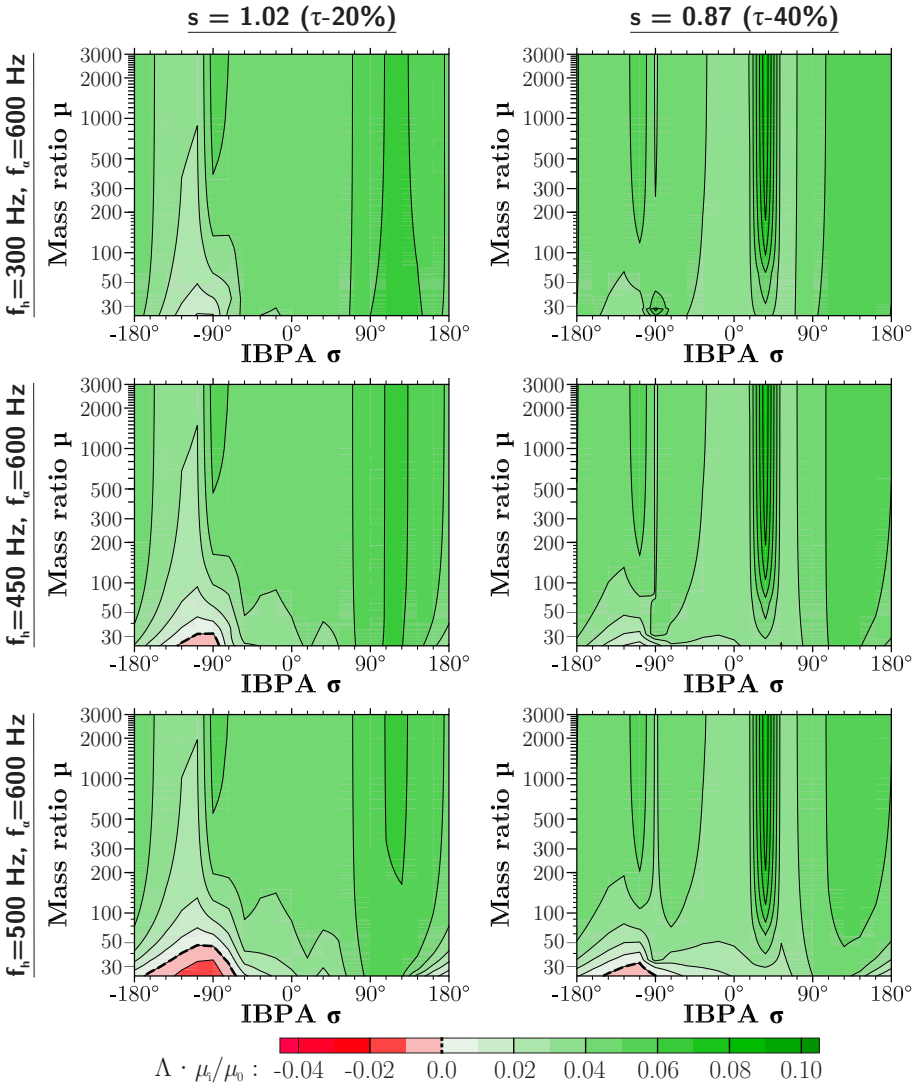


**Figure 6.9.:** FUTURE-LC-2D, case “subsonic”: Normalized aerodamping of second aeroelastic modeshape depending on mass ratio, frequency separation, and solidity

## 6.3. Transonic Operating Point

### 6.3.1. Influence of Mass Ratio and Frequency Separation

Going from high to lower frequency separation in figs. 6.10 to 6.12, a lower mass ratio or a lower frequency separation leads to a higher coupling strength when looking at the modal participation factor. So far, this finding is in line with the subsonic operating point. At the same frequency separation, with a lower mass ratio, the drift away from the energy method's results is also in line with the above results. Between different frequency separations and for the high positive and negative IBPAs, the damping values of the intermediate mass ratio of  $\mu = 68$  see a higher drift for lower separations. This is especially good visible for the heave branch at the positive IBPAs. To some extent, this is also true for the lower IBPAs, but the situation gets more complicate here.

A closer look actually reveals a lower level of excitation in the critical IBPAs with a lower frequency separation. While the highest damping of the pitch branch around the IBPA  $\sigma = 126^\circ$  is almost unaffected by the change of the heave vacuum frequency, the area of highest excitation around the IBPA  $\sigma = -72^\circ$  shifts upwards in the diagram with lower frequency separation. For the lowest separation, the most excited IBPA shifts to  $\sigma = -90^\circ$ . Lowering the frequency separation for  $\sigma = -90^\circ$  also results in a higher excitation, so this is again in line with the findings from the subsonic operating point. The effect seen for the IBPA  $\sigma = -72^\circ$  can be attributed to the two factors: the mode and frequency coalescence and the occurrence of an aerodynamic resonance. This will be addressed in the next subsection.

$$f_{\text{heave}} = 300 \text{ Hz}, f_{\text{pitch}} = 600 \text{ Hz}$$

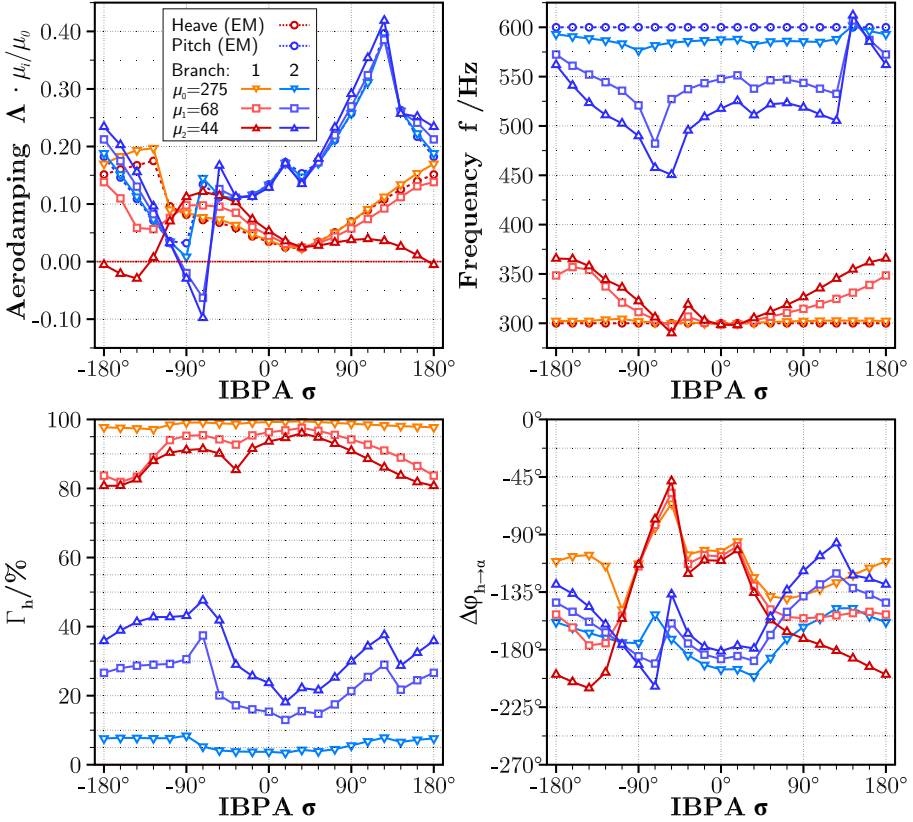


**Figure 6.10.:** Frequency separation 1:2, FUTURE-LC-2D, case “transonic I”, solidity  $s = 1.22$ : Traveling wave diagram compared between EM and p-k for varying mass ratio

$$f_{\text{heave}} = 450 \text{ Hz}, f_{\text{pitch}} = 600 \text{ Hz}$$

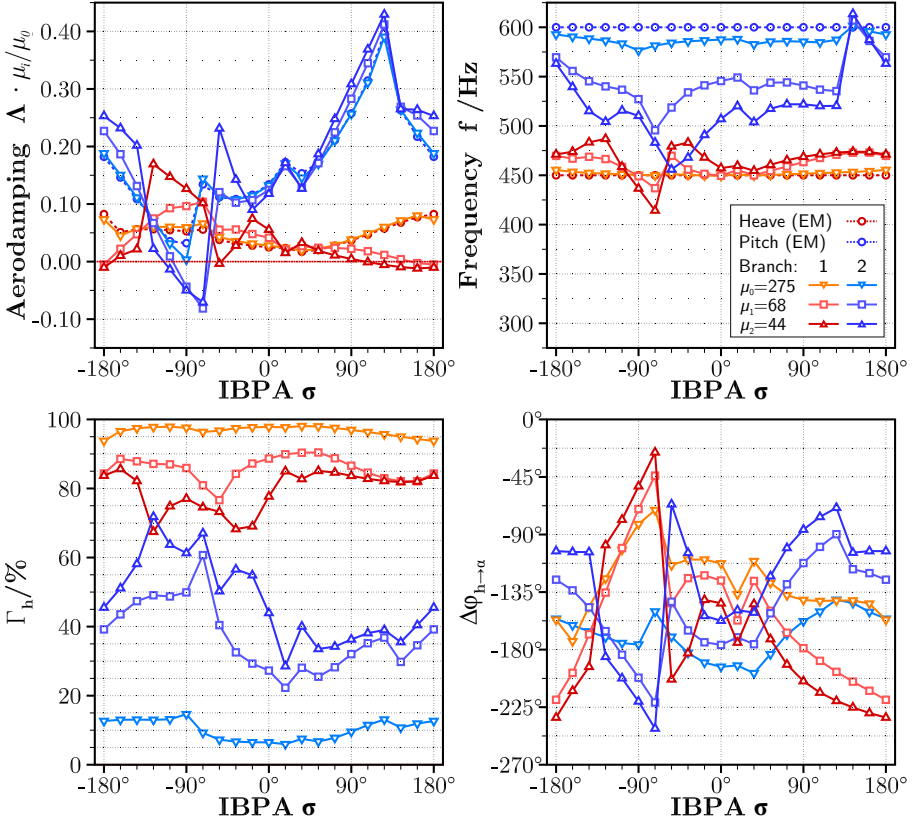


**Figure 6.11.:** Frequency separation 2:3, FUTURE-LC-2D, case “transonic I”, solidity  $s = 1.22$ : Traveling wave diagram compared between EM and p-k for varying mass ratio



$$f_{\text{heave}} = 500 \text{ Hz}, f_{\text{pitch}} = 600 \text{ Hz}$$

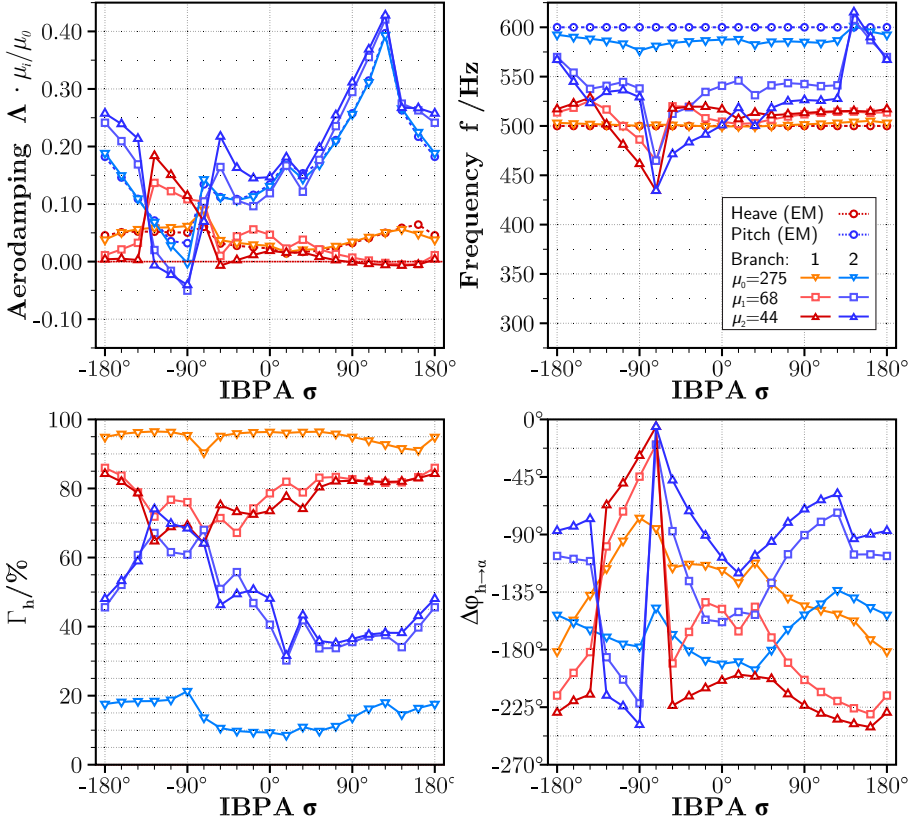


**Figure 6.12.:** Frequency separation 5:6, FUTURE-LC-2D, case “transonic I”, solidity  $s = 1.22$ : Traveling wave diagram compared between EM and p-k for varying mass ratio

### 6.3.2. Aerodynamic Resonance and Effect on Modal Coupling

Figure 6.13 depicts the GAFs for a specific IBPA with different sampling rates in the vicinity of the resonance peak. To exclude nonlinear effects that would not be resolved by the harmonic balance method using only the first harmonic [94], simulations with five harmonics were performed and the result added to the plot. No notable changes between the two harmonic sets are observed. As in the previous section, the GAFs with a higher sampling rate provide a better resolution of the resonance.

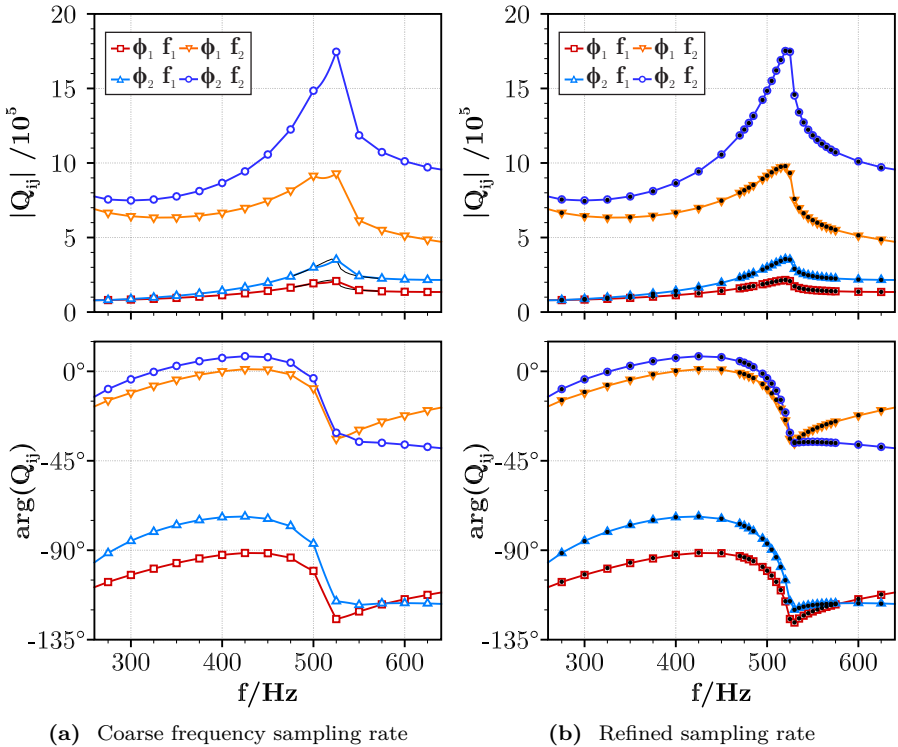


**Figure 6.13.:** FUTURE-2D-LC, case “transonic I”, IBPA  $\sigma = -72^\circ$ : Generalized aerodynamic forces around resonance condition with different frequency sampling rates, computed by HB method with one (colored symbols) and five (black dots) harmonics

First, the one degree-of-freedom system with only the pitch mode is investigated. Figure 6.14a plots the results for the two GAF samplings schemes. At first, the

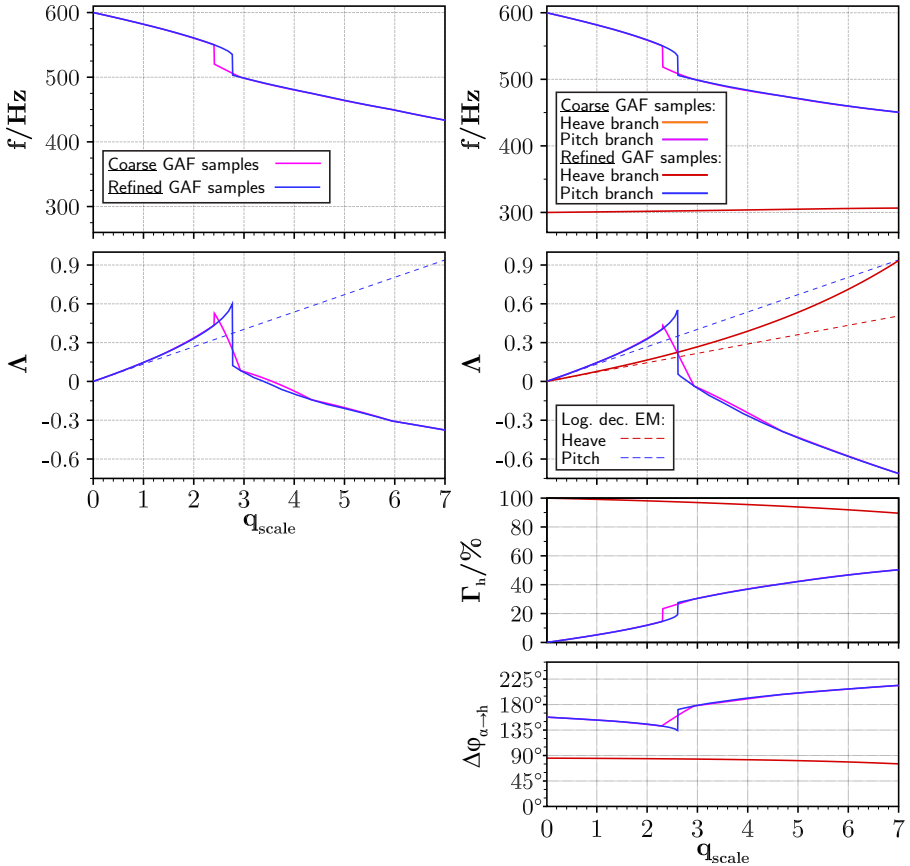
aeroelastic frequency changes due to the mass ratio effect. The aerodamping also drifts away from the energy method's results as a result of the frequency change. At around  $q_s \approx 2.5$ , the aeroelastic frequency comes close and coincides with the resonance's frequency. In the same manner as shown in the previous section, the aeroelastic behavior has a sudden change. With the finer GAF sampling in this frequency range, a non-continuous drop in aerodamping can be observed. Using only the coarser GAF samplings, the drop is smeared over a broader range of  $q_s$  (these are not two data points, there are actually many intermediate solution steps). The same behavior can be observed for the two degree-of-freedom system in fig. 6.14b, only that now the same drop also applies to the modal participation and phase lag in the pitch branch. This effect already explains the large shift of the aerodamping between the energy method and the coupled-mode system, visible in fig. 6.10.

Figure 6.15 shows smaller frequency separations. In fig. 6.15a, the effect is more pronounced compared to fig. 6.14b, what is in line with the theorem that the smaller frequency separation leads to stronger modal coupling effects. Going to higher  $q_s$ , the aerodamping of the pitch branch has a smaller gradient over  $q_s$  for the lower frequency separation, what appears to be contradicting the previous findings. Actually, another effect comes into play: When two modeshapes are coalescing (in terms of frequency and modal participation), increasing the coupling strength through a lower mass ratio will cause a divergence of the two coalescing branches after their closest approach. One branch becomes unstable and the other more stable. This is well-known for fixed-wing structures. The shallower gradient of the aerodynamic excitation compared to the higher frequency separation is due to the smaller frequency shift here. The frequency shift of the pitch mode is the main contributor towards destabilization, as depicted in the pitch-only plot.

Figure 6.15b depicts a case where coalescence of the modes can be observed. As the two branches are coalescing towards each other, coming close to the frequency of the aerodynamic resonance, the pitch branch performs the above already observed drop in frequency. In this case, the pitch branch hits the frequency of the heave branch. At this point, the pitch branch gets united with the heave branch. A full mode coalescence is performed. In this case, the now unified branches are stable. This explains the absence of an excitation in the IBPA  $-72^\circ$  of fig. 6.12. However, from a mathematical point of view, the pitch branch can be forced to take another track, e.g. by sorting the eigenvalues only by frequency. This "alternate" tracking can be seen as a green line. The track is more reminiscent of the previous shown track for a higher frequency separation. It may be possible that there are three solutions in this case: similar effects are described for the occurrence of fluid modes and their coalescence or crossing with the structural/aeroelastic modeshapes [95, 96, 15]. If a fluid mode is to

---

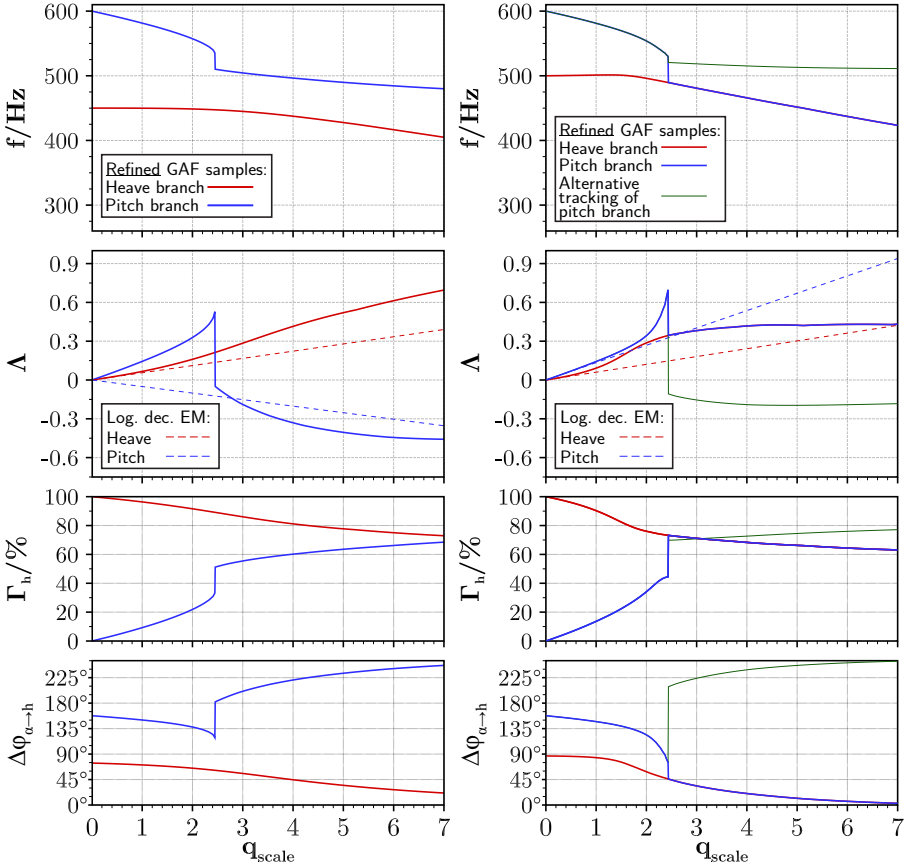
be taken into account, the aeroelastic stability equation has to be extended to this extra degree-of-freedom. Behavior of the generalized aerodynamic forces for non-zero damping and also nonlinear effects may have to be considered. The coupling with fluid modes and how to incorporate them into the flutter analysis is an active research topic in the aeroelasticity community. Method development for such cases is part of this research [14, 97].



(a) Pitch-only system

(b) Heave-pitch coupling ( $f_{heave} = 300$  Hz,  $f_{pitch} = 600$  Hz), heave branch of coarser GAF sampling rate with orange line hidden behind blue line of finer sampling rate

**Figure 6.14.:** FUTURE-2D-LC, case “transonic I”, IBPA  $\sigma = -72^\circ$ : p-k solution histories with different GAF frequency sampling rates for pitch-only system and heave-pitch coupling



(a) Heave-pitch coupling ( $f_{\text{heave}} = 450$  Hz,  $f_{\text{pitch}} = 600$  Hz) (b) Heave-pitch coupling ( $f_{\text{heave}} = 500$  Hz,  $f_{\text{pitch}} = 600$  Hz) with alternative tracking strategy for pitch branch

**Figure 6.15.:** FUTURE-2D-LC, case “transonic I”, IBPA  $\sigma = -72^\circ$ : p-k solution histories for smaller frequency separation between heave and pitch

### 6.3.3. Influence of Solidity

Different blade-to-blade distances are investigated as in the previous section. Figures 6.16 and 6.17 shows the incremental change of the solidity and frequency separation listed in table 6.2. While at the subsonic operating point the pitch branch is always the critical mode to become unstable, at the transonic operating point either branch can become unstable, depending on the IBPA. Therefore, at each IBPA-mass ratio combination, the value with the lower aerodynamic damping (or higher aerodynamic excitation respectively) is taken.

The resulting image is very similar to the subsonic condition. Lowering the frequency separation or increasing the solidity shifts the flutter boundary to higher mass ratios. The effect described in section 6.3.2 for the baseline solidity at the IBPA  $\sigma = -72^\circ$  is an outlier: at the lowest frequency separation, the highly excited area shown in red is broken up by a dark green area of high damping. At the other solidities, this effect is not visible.

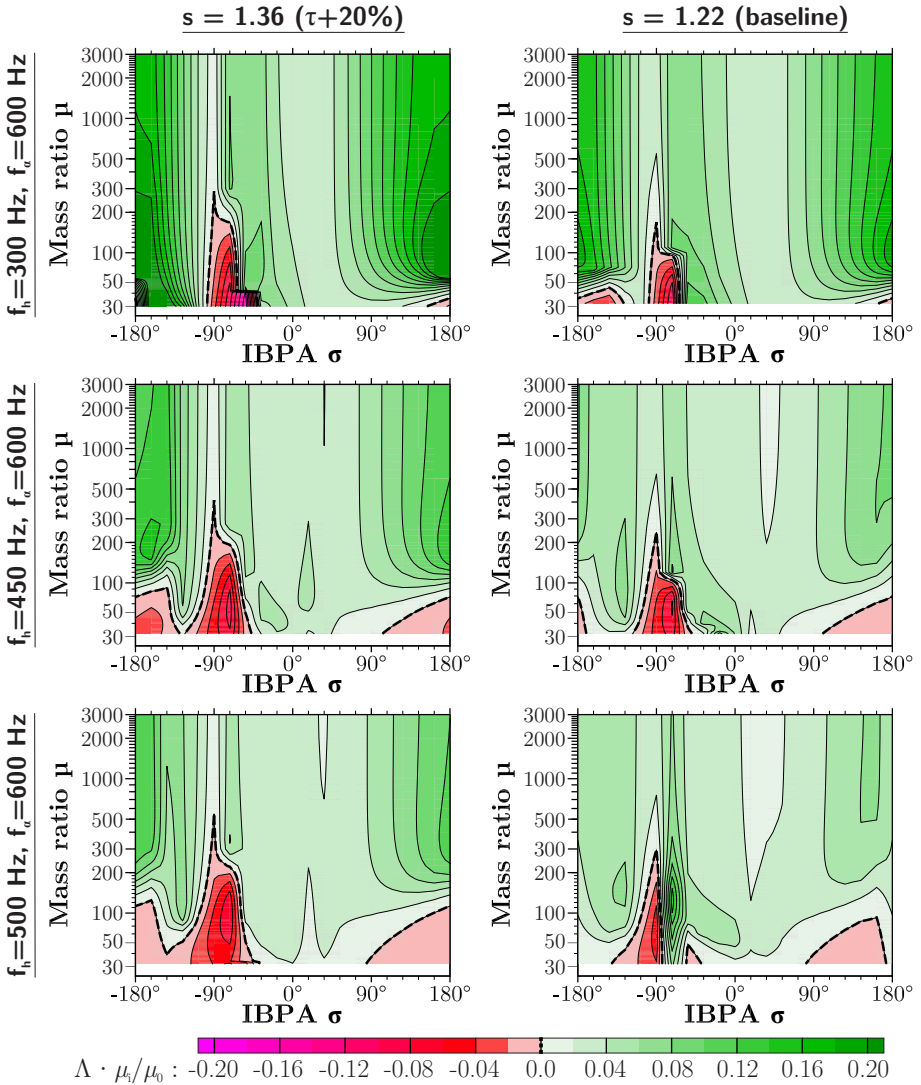


**Figure 6.16.:** FUTURE-LC-2D, case “transonic I”: Normalized aerodamping (lower value of first or second aeroelastic modeshape) depending on mass ratio  $\sigma$ , frequency separation, and solidity



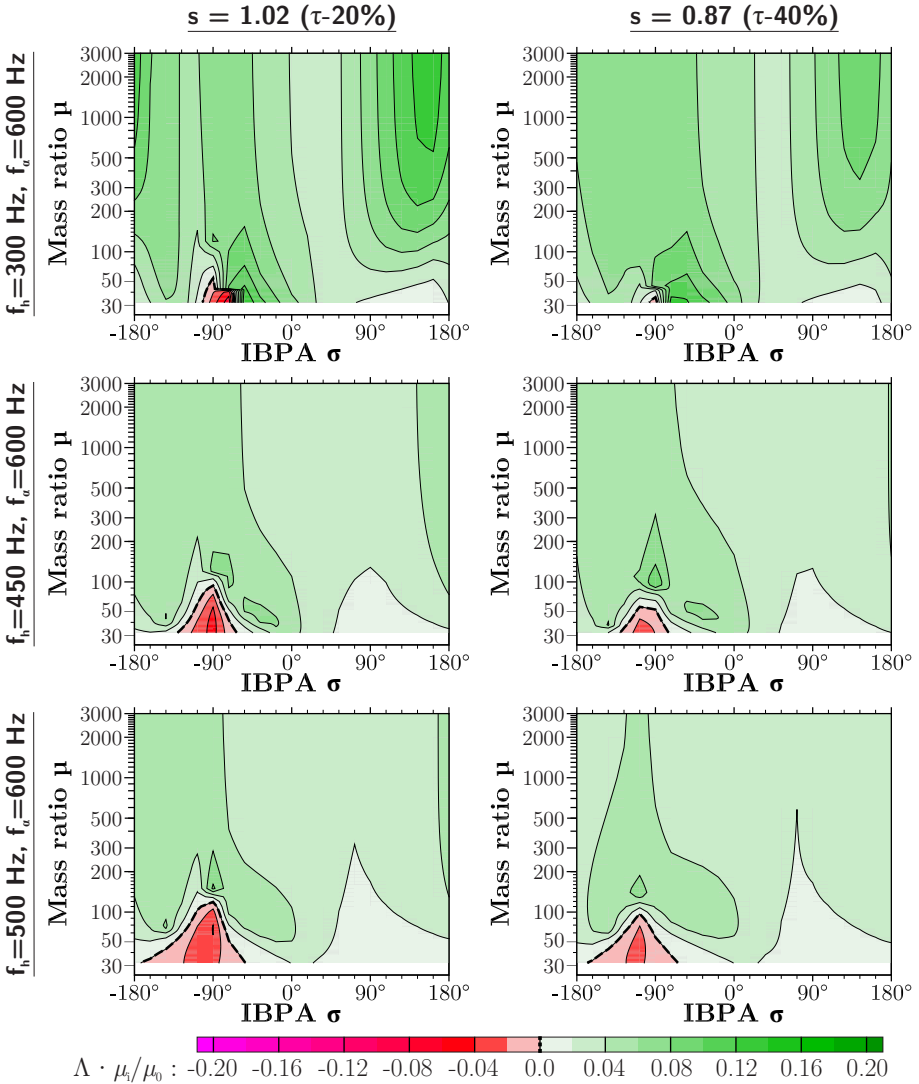


**Figure 6.17.:** FUTURE-LC-2D, case “transonic I”: Normalized aerodamping (lower value of first or second aeroelastic modeshape) depending on mass ratio  $\sigma$ , frequency separation, and solidity

## 6.4. Summary

As already indicated in the previous chapter: the lower the mass ratio, the more likely a significant aerodynamic coupling between vacuum modeshapes occurs. From the observations, an empirical assumption can be made that a high enough modal coupling strength will lead to destabilizing effects that cause coupled-mode flutter. Furthermore, the higher the coupling strength, the higher the drift away from energy method predictions will become.

The three factors that will ultimately lead to flutter due to aerodynamic coupling of the modeshapes are:

- a low mass ratio
- a low frequency separation
- a high solidity

All these factors contribute towards stronger aerodynamic forces in relation to the structural inertia forces. As postulated from the beginning of this thesis, once the aerodynamic forces become high enough, modal coupling cannot be neglected in flutter analysis and the energy method becomes a non-conservative approach.

Strictly by definition, the p-k method is only valid for the zero damping case. As shown before, the p-k method is still usable to predict aeroelastic modeshapes and their aerodynamic damping or excitation around the zero damping line. For cases with very strong coalescence of structural and aerodynamic frequencies, the limit of this prediction method is most likely reached. How to incorporate or facilitate those effects is an ongoing research topic in the aeroelasticity community [95, 96, 15, 14, 97].



# 7

## Application to Low Mass Ratio Fan Blade

*The p-k method is applied to the first rotor of the CRISPmulti fan. It is shown that the near-stall flutter boundary in part speed is significantly closer to the working line when compared to conventional energy method results. For selected operating points, the influence of so-called higher structural modeshapes on the p-k analysis is investigated.*

*The fundamental findings from preliminary research were already published by the author [44, 45]. More detailed and deeper analyses are performed in the scope of this thesis. Furthermore, the discussion is majorly extended.*

### 7.1. General Remarks

**Definition: Operating Point Names.** The operating points addressed in this chapter are named by the convention  $n000a$ . The digits are replaced by the rate of rotation in percent. The last character refers to specific marker in the compressor map diagram as shown in fig. 7.6, e.g.  $n070b$  means the OP at the 70% speedline marked with a “b”.

**Definition: p-k Analysis Names.** The coupled-mode analyses with the p-k method are shown for various numbers and constellations of considered modeshapes. The naming convention is  $AxB$ , where A means the number of the aeroelastic branches that are investigated. B shows how many vacuum modeshapes are considered and always means the first B modeshapes from the ascending order of their respective frequency. Thus, a 3x6 descriptor translates

to a coupled analysis where three branches (associated to the three modeshapes with the lowest frequency) are obtained at and the vacuum modeshapes 1 to 6 are included as degrees-of-freedom of the system. In the special case of a 1x1 system, only one vacuum modeshape is considered in the matrices as a single-mode analysis with an allowed frequency shift.

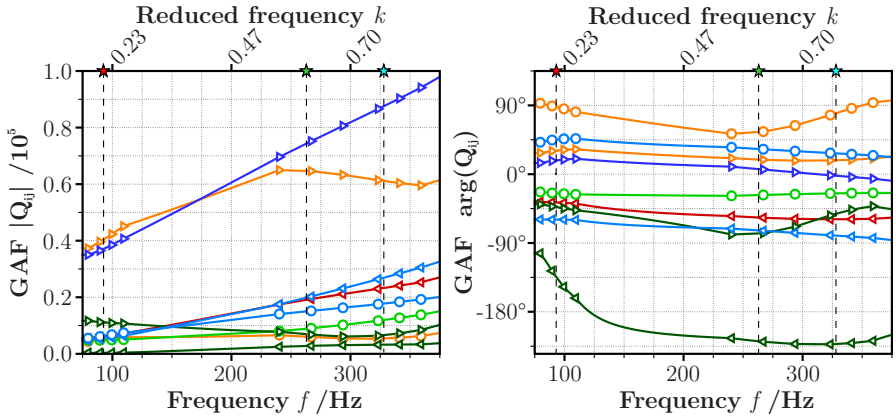
## 7.2. Modal Coupling at a Specific Operating Point

The operating point *n070b* is subject to a detailed analysis how vacuum modeshapes influence the aeroelastic branches. Modal coupling might occur for all modeshapes but may have a critical influence only on the lowest frequencies. Thus, the influence of the first six aeroelastic branches (in ascending order of their fundamental modeshape's frequency) is investigated. As shown here, evaluating only the first three branches is justified for the rest of similar operating points above the working line. This information is critical for the number of required sampling points that need to be computed with CFD.

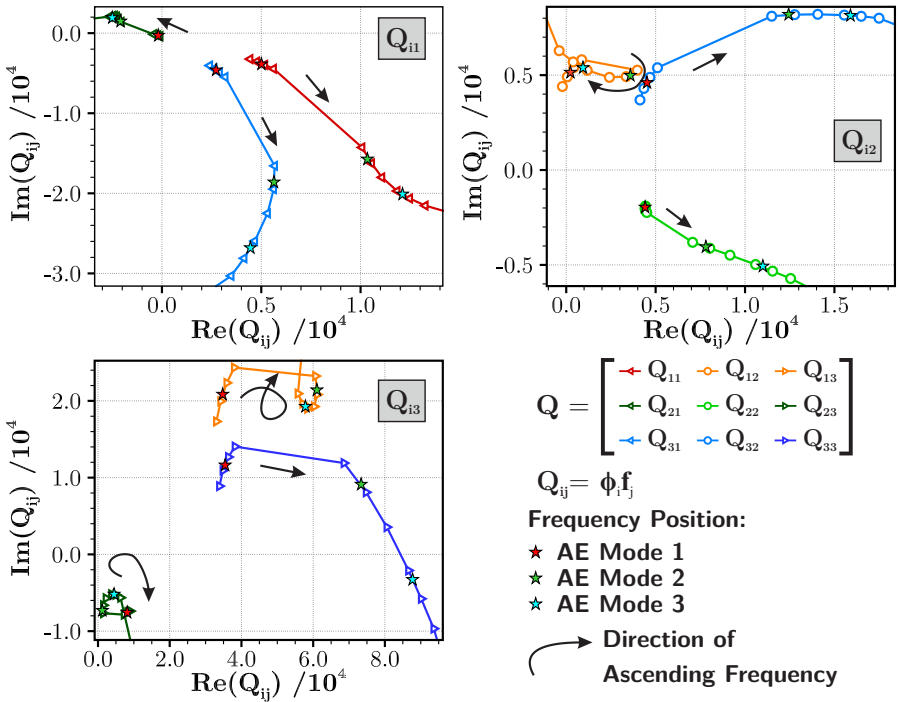
### 7.2.1. Generalized Aerodynamic Forces

In general, if modal coupling only slightly shifts the frequencies, it is a good start to take three sampling points around the natural frequencies of the vacuum modeshapes (one below, one above and one at the natural frequency). If there is no phenomenon that causes strong spikes in the aerodynamic responses like acoustic resonances within this interval, this approach will allow for an adequate interpolation of the aerodynamic forces.

From preliminary investigations, the expected frequency ranges of the aeroelastic branches were already known. The approach as described above for frequency sampling is used with some exceptions: Around the modeshape 1B an additional lower frequency is added. The third aeroelastic branch (belonging to 1T) will only have lower frequencies than the respective vacuum frequency and thus, only samples below this frequency are taken. The sampling scheme listed in table 7.1 is applied to all operating points. Depending on how many aeroelastic branches are investigated, only the frequencies around the fundamental natural frequency is selected, i.e. for a *3xB* scheme only the first three rows and for a *6xB* all rows accordingly. At each frequency sampling point, the aerodynamic responses to the considered vacuum modeshapes are computed for a fixed amplitude and all IBPAs. With that information, the matrix of generalized aerodynamic forces (GAF)  $\tilde{\mathbf{Q}}$  can be generated.



(a) Magnitude and phase over frequency



(b) Complex plane

**Figure 7.1.:** Matrix interpolation for the generalized aerodynamic forces of the first three vacuum modeshapes (OP *n070b*, IBPA  $\sigma = 36^\circ$ )

**Table 7.1.:** Frequency sampling scheme for the CRISPmulti geometry

Vac. modeshape	Percentage deviation from natural frequency			
1 (1B)	-20 %	-10 %	0 %	+10 %
2 (2B)		-10 %	0 %	+10 %
3 (1T)		-10 %	-5 %	0 %
4		-10 %	0 %	+10 %
5		-10 %	0 %	+10 %
6		-10 %	0 %	+10 %

Some entries of  $\tilde{\mathbf{Q}}$  are plotted in fig. 7.1 for the lower frequency regime, showing only the entries of the upper left  $3 \times 3$  system. The other entries are also relevant, but would make the plot very confusing. Thus, only a selection is shown here. Of course, the basic evaluation of the GAF sampling and interpolation needs to be applied to all entries and possible frequency regimes.

The scattered points are the discrete points at which GAFs are computed, the lines show the interpolated data. The interpolation scheme chosen has two decisions that need to be made:

1. The entries are complex values, thus the values can be interpolated for magnitude and phase or for real and imaginary part, both having advantages and disadvantages. The real/imaginary option is chosen here.
2. The values in between the discrete sampling points can then be interpolated with a linear or higher order approach (e.g. splines with quadratic, cubic etc. ansatz). A linear interpolation is chosen here.

The consequences of those decisions are visible in the GAF plot. The GAFs can be plotted in two different ways, each visualizing different aspects. When looking at magnitude and phase over frequency, the computed frequencies appear as *clusters*, that can be attributed to a certain natural frequency of the vacuum modeshape<sup>7</sup>. As long as the aeroelastic frequencies are within a respective “cluster” of frequency samples, there is not much difference between the two choices of interpolation and both will deliver a sufficient result. In contrast, the plot in the complex plane shows the difficulties for large gaps in frequency sampling. In general, the GAFs follow a track through the complex plane, although the frequency affiliation is not immediately visible anymore. The linear interpolation delivers reasonable results within the clusters, but have more or less deficiencies outside.  $Q_{11}$  and  $Q_{31}$  might be accepted as “close enough”,

<sup>7</sup>Although the two clusters of the modes 2B around  $f \approx 270$  Hz and 1T around  $f \approx 360$  Hz are not as distinct from the others as the cluster at 1B around  $f \approx 99$  Hz.

but the track of  $Q_{33}$  already shows an unreasonable “shortcut” that might look much more curve-like with a higher order spline. Even more critical are tracks like  $Q_{12}$  or  $Q_{13}$ . This loop-like behavior is typical for GAFs throughout the complex plane and the reason why the resulting aeroelastic frequencies need to be inside a cluster. Furthermore, the behavior of the GAFs inside the cluster is crucial: if large GAF variations were found, a higher sampling would have been needed.

### 7.2.2. Energy Method and Coupled-Mode Analysis Compared

Figure 7.2 compares the energy method with the p-k method for the first six modeshapes of the OP *n070b*. In a single-mode analysis with a variable frequency ( $1x1$ ), the vacuum modeshapes are not coupling with each other, but a frequency shift is already allowed. This frequency change might be a strong contributor to the aerodynamic response already [34]. The flutter-critical aeroelastic modeshape in all analyses is number 3, which is associated to the first torsion as the dominant participant. For the  $1x1$  systems, the aeroelastic frequencies shift away from the vacuum frequencies, especially for the flutter-critical mode, and damping is reduced significantly, although the operating point is evaluated as stable. When allowing modal coupling in the  $6x6$  system, the critical aeroelastic mode 3 does not significantly change the frequency compared to the  $1x1$  analysis, but the aerodamping is now below zero for three IBPAs.

For the aeroelastic mode 6, the  $1x1$  analysis has a larger frequency shift than the  $6x6$  system, but the aerodamping is not much affected in the  $1x1$  system, whereas the  $6x6$  analysis yields a clear reduction in aerodamping. It is to mention, that the damping of the mode 6 is in the magnitude of the mode 2. Mode 5 and 6 have a low frequency distance, which is a contributor to the strength of the modal coupling. Although it does not get unstable in this scenario, the clear reduction of aerodamping due to modal coupling, mainly between mode 5 and 6, shows that not only the fundamental modes (“first bending”, “first torsion”) can participate in a coupled-mode flutter scenario.

### 7.2.3. Modal Participations

A deeper insight into the mechanisms that are at work is delivered by the modal participation of the aeroelastic modeshape. As introduced in section 2.4, the modal participations can be extracted from the eigenvectors of the flutter equation. Figures 7.3 and 7.4 plot those factors for each aeroelastic modeshapes, comparing the  $3x3$  and  $6x6$  results. For the unstable aeroelastic mode 3, a high participation of the first bending is visible. When the higher modes are considered in  $6x6$ , the percentage of the first bending stays almost unchanged,



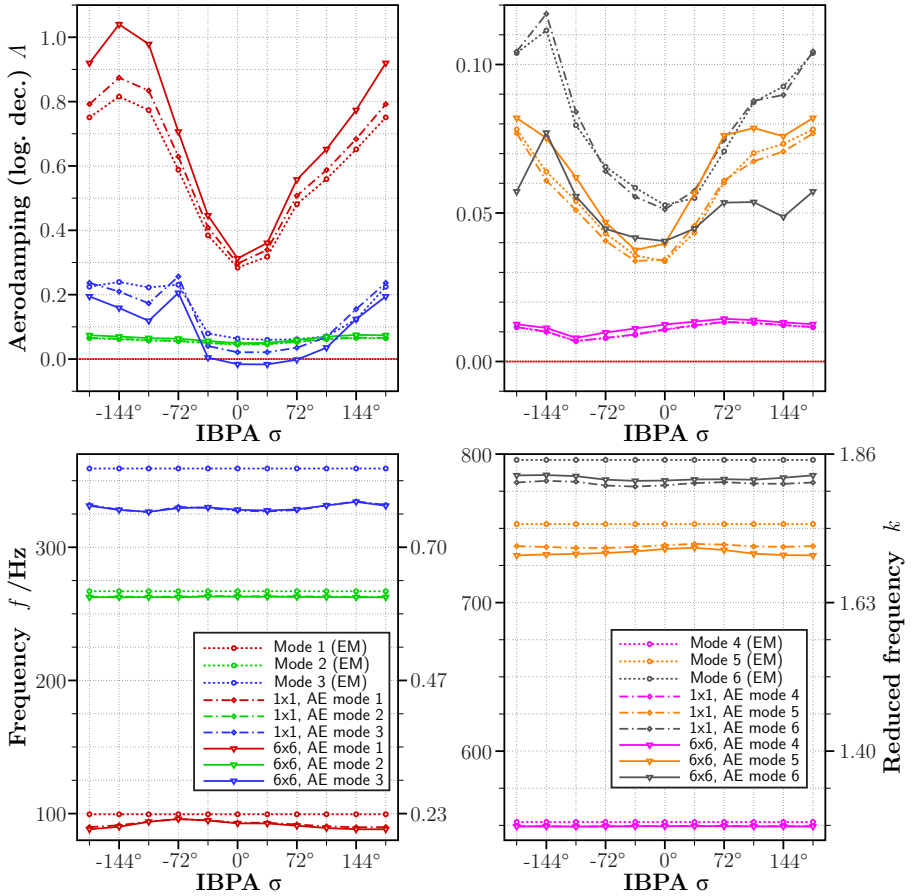
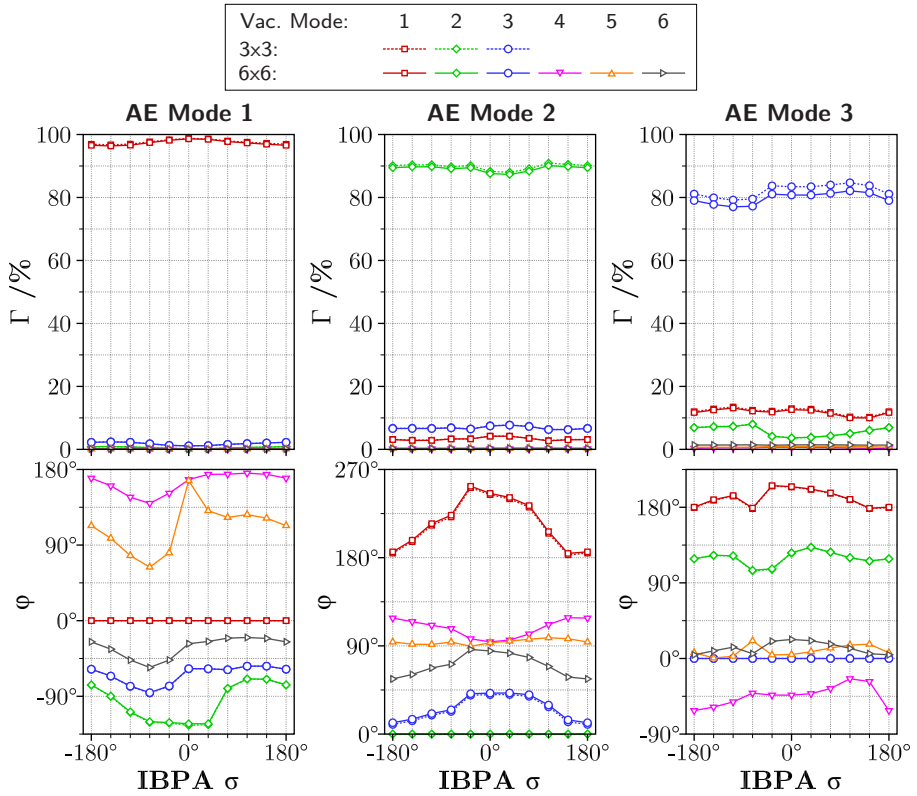
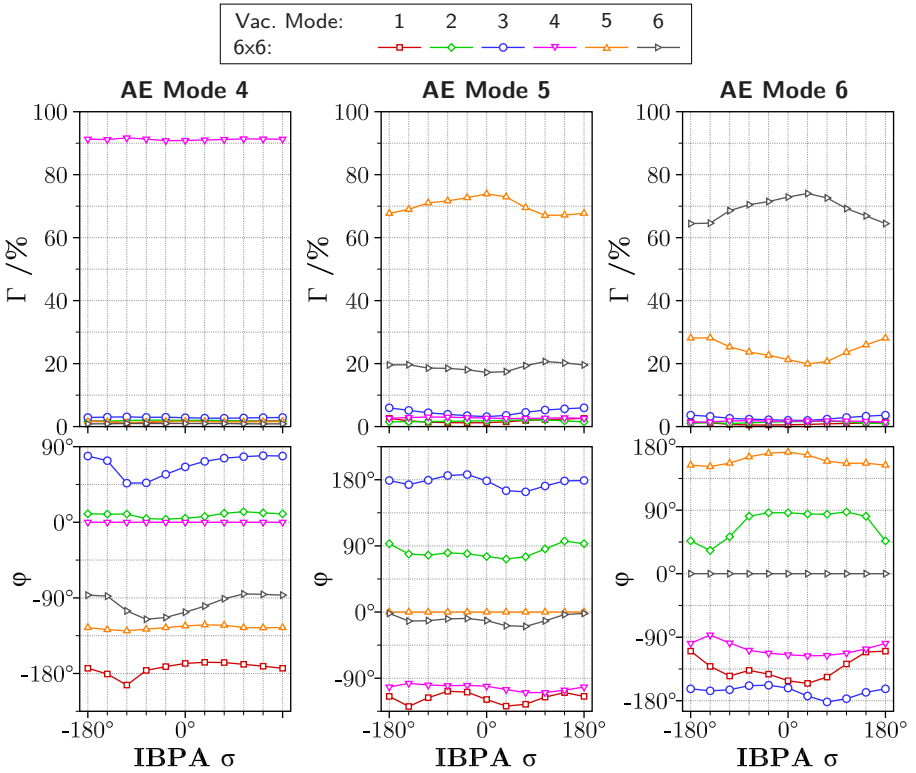


Figure 7.2.: OP *n070b*: Damping diagram for EM, p-k 1x1, and p-k 6x6



**Figure 7.3.:** OP *n070b*: Modal participations of the fundamental aeroelastic modeshapes (AE mode) compared between 3x3 and 6x6 analysis



**Figure 7.4.:** OP *n070b*: Modal participations of the higher aeroelastic modes (AE mode) in 6x6 analysis

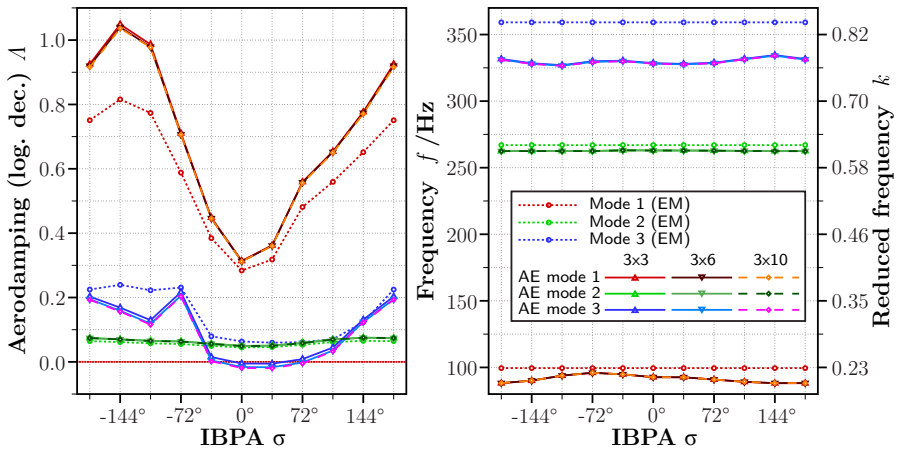


**Figure 7.5.:** OP *n070b*: Damping diagram considering different number of higher modes in the p-k analysis

but the participation of the added modes gradually decrease the dominance of the dominant first torsion.

A clear sign for strong coupling, or coalescence, between two modes is the behavior in aeroelastic mode 5 and 6: both aeroelastic modes are clearly dominated by their associated vacuum modes, but also have a high participation of the frequency-wise close neighboring vacuum mode. The coalescence of these two modes can also be observed in the damping diagram above (fig. 7.2), where one branch gets more stable and the other more unstable. This behavior is characteristic for coupled-mode flutter. Looking at the aeroelastic modes which get destabilized compared to the single-mode energy method approach, there is always a “partner” aeroelastic mode which becomes more stable (aeroelastic modes 1 and 3, aeroelastic modes 5 and 6). Both partnering aeroelastic modes will have a strong participation of the associated vacuum mode.

#### 7.2.4. Considering Different Modes in P-K Analysis

Figure 7.5 depicts the result of a different number of considered vacuum modes in the p-k analysis. The  $3 \times 6$  results are the same as in the previous subsection with the  $6 \times 6$  system and used as a reference. When the three modes with the highest frequency are dropped in the analysis, the  $3 \times 3$  system results. In general, the results with the  $3 \times 3$  system are very close to the  $3 \times 6$  system already with slightly less excitation especially for the critical IBPA. The  $3 \times 10$  system considers more higher frequency vacuum modes, but

almost no impact is found  $3x6$ . Nevertheless, the more vacuum modes shapes are considered, the more unstable the system becomes. As expected, the influence decreases with the frequency distance.

Summing up, the  $3x3$  system delivers already a very good impression, the  $3x6$  system appears to be the best compromise in the regime where the fan is transitioning from stable to unstable. The influence on the position of the flutter boundary is discussed in the next section.

## 7.3. Flutter Boundary above Working Line

### 7.3.1. Overview

The flutter analysis with the different methods EM, p-k  $3x3$ , and p-k  $3x6$ , is performed for many OPs above the working line (WL). For each OP, the lowest aerodamping of all modes and IBPAs in the damping diagram is extracted per analysis method and plotted in the compressor map in fig. 7.6. The stability limit is interpolated and drawn for all three methods.

At first glance, the EM delivers a non-conservative result. Considering modal coupling, the stability limit moves much closer into the compressor map. As already found for one specific OP, the inclusion of more vacuum modeshapes into the analysis slightly decreases the stability. This is especially visible for OPs like  $n065b$ ,  $n080b$ , and  $n085b$ , where the difference between  $3x3$  and  $3x6$  is decisive whether some aeroelastic modeshapes are evaluated with positive or negative damping. Although the shift of flutter boundary position is nearly marginal, considering less modeshapes is non-conservative.

The OPs at higher rotational speeds (above 90%) appear very stable in this kind of plotting. This is a result of the color maps choice in the particular figure and also the information that is plotted (lowest overall damping). Indeed, a destabilization of the flutter-critical modeshapes can be observed as shown later, but flutter does not occur before reaching the surge line.

The reduction or loss in stability margin are extracted and put into table 7.2. The margin is calculated as percentage of the relation between  $\dot{m}_{\text{flutter}}$  as the highest mass flow at the speedline where flutter is predicted, and  $\dot{m}_{\eta_{\text{max}}}$  as the mass flow at the working line, so that

$$\text{Margin} = \left( 1 - \frac{\dot{m}_{\text{flutter}}}{\dot{m}_{\eta_{\text{max}}}} \right) \cdot 100 \% . \quad (7.1)$$

It gives an idea how far the mass flow can be reduced at a respective speedline before reaching the possible flutter onset.

The absolute loss is the direct subtraction of both margin percentages (the reduced distance to the WL)

$$\text{Abs. Loss} = \text{Margin}_{\text{pk}} - \text{Margin}_{\text{em}} = \frac{\dot{m}_{\text{flutter,em}} - \dot{m}_{\text{flutter,pk}}}{\dot{m}_{\eta_{\text{max}}}} \cdot 100 \% \quad (7.2)$$

and the relative loss (decrease of stability margin compared to the EM)

$$\text{Rel. Loss} = \frac{\text{Abs. Loss}}{\text{Margin}_{\text{em}}} = \frac{\dot{m}_{\text{flutter,em}} - \dot{m}_{\text{flutter,pk}}}{\dot{m}_{\eta_{\text{max}}} - \dot{m}_{\text{flutter,em}}} \cdot 100 \% . \quad (7.3)$$

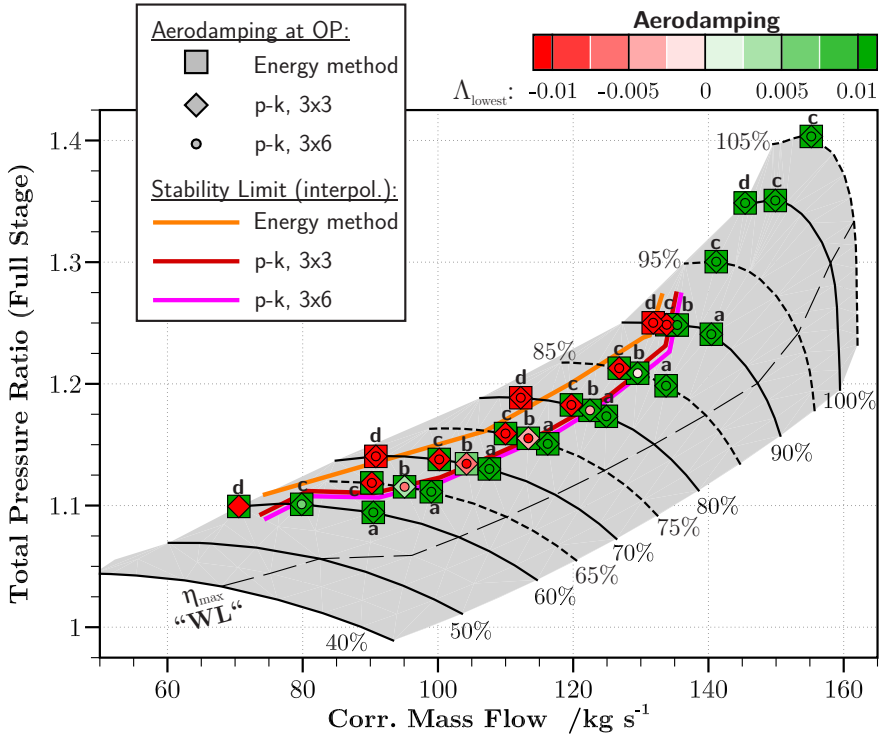


**Figure 7.6.:** Aeroelastic stability (lowest damping of all modeshapes and IBPAs) above the working line compared between the energy method and different p-k analyses. The interpolated stability limit is generated using 2D triangulation and subsequent contour plotting for the zero value line in Tecplot [98, ch. 20-10]

The highest impact is found for the lower rotational speeds around 65% to 70%, where a mild flutter onset is found. For medium-high speeds around 90% a more abrupt onset is predicted. As the stability margin is quite low already here, small changes in absolute loss have a high impact on the relative loss.

### 7.3.2. Subsonic to Transonic Flow at Medium Rotational Speed

The two OPs *n065b* and *n075b* in figs. 7.7 and 7.8 appear very similar to the extensively investigated *n070b*. The main conclusion is confirmed: the modeshapes at higher frequencies have a slight influence on the aerodamping especially for the flutter-critical aeroelastic modeshape. The *3x3* analysis is

**Table 7.2.:** Loss of Aeroelastic Stability Margin at Best Efficiency Line

RoR	$\dot{m}_{\eta_{\max}}$	Margin <sub>EM</sub>	Margin <sub>pk,3x6</sub>	Abs. Loss	Rel. Loss
60 %	103	31 %	23 %	-8 %	-25 %
65 %	110	24 %	13 %	-11 %	-46 %
70 %	117	20 %	10 %	-10 %	-48 %
75 %	124	15 %	8 %	-7 %	-44 %
80 %	132	12 %	7 %	-5 %	-43 %
85 %	139	11 %	6 %	-5 %	-40 %
90 %	147	10 %	8 %	-2 %	-20 %

already quite sufficient but it becomes clear again, that lesser considered vacuum modeshapes offers a non-conservative approach.

The general shape of the damping curve over IBPA changes a little bit: for *n065b*, the lowest damping is at the IBPA  $\sigma = 0^\circ$  and shifts to the IBPA  $\sigma = 36^\circ$  for *n075b*. The change in aerodynamic excitation is progressive, but the modal participation *appears* to shift abruptly. The phase lag of the first bending in the third aeroelastic mode is shifted by about  $180^\circ$ , see fig. 7.3 vs. fig. 7.9, now being almost in phase with the torsional mode. This is a deception: Looking at the manifestation of the first bending at both OPs in fig. 7.10, the vectors of displacement are flipped by  $180^\circ$  between *n070b* and *n075b* (with some minor changes to due different centrifugal stresses). As eigenvectors of a system remain linearly independent eigenvectors, even when multiplied with a negative scalar, the physical output of the displacement vectors depends on the normalization in the CSM tool. Small changes in the static deformation, and thus prestressing, lead to the flipped modeshape. The physical influence of the modal coupling is thus the same, as the manifestation of the third aeroelastic mode is almost identical comparing *n070b* and *n075b* in fig. 7.11.

### 7.3.3. Transonic Flow at Medium-High Rotational Speed

At the 90% speedline, the EM already delivers an interesting damping curve. The OP *n090b* in fig. 7.12 has the lowest damping of the third mode (1T) at the IBPA  $\sigma = 180^\circ$ . This is due to a strong transonic effect, where the flowchannel is periodically increasing and decreasing the convergent-divergent geometry. Apparently, the lowest aerodamping values at this OP are found for the second mode (2B).

When looking at the coupled-mode analysis, the second aeroelastic mode gets stabilized compared to the associated mode (2B) in the energy method. This



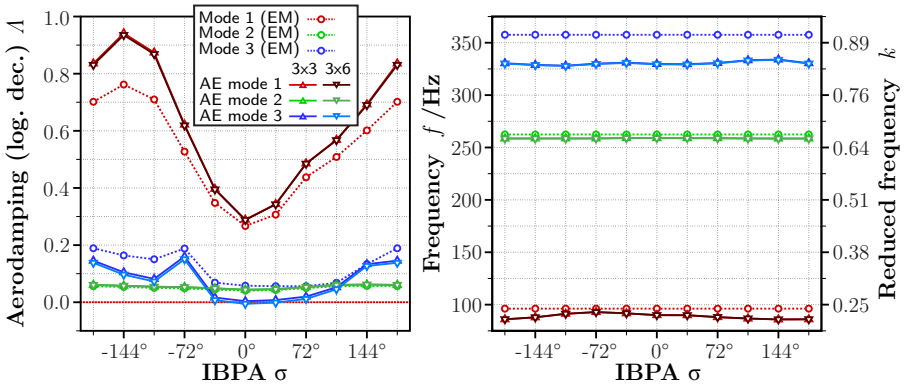


Figure 7.7.: OP *n065b*: Damping diagram for EM, p-k 3x3, and p-k 3x6

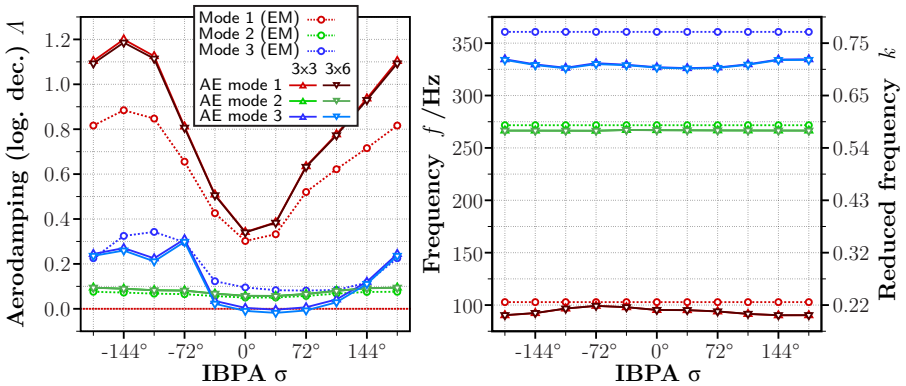
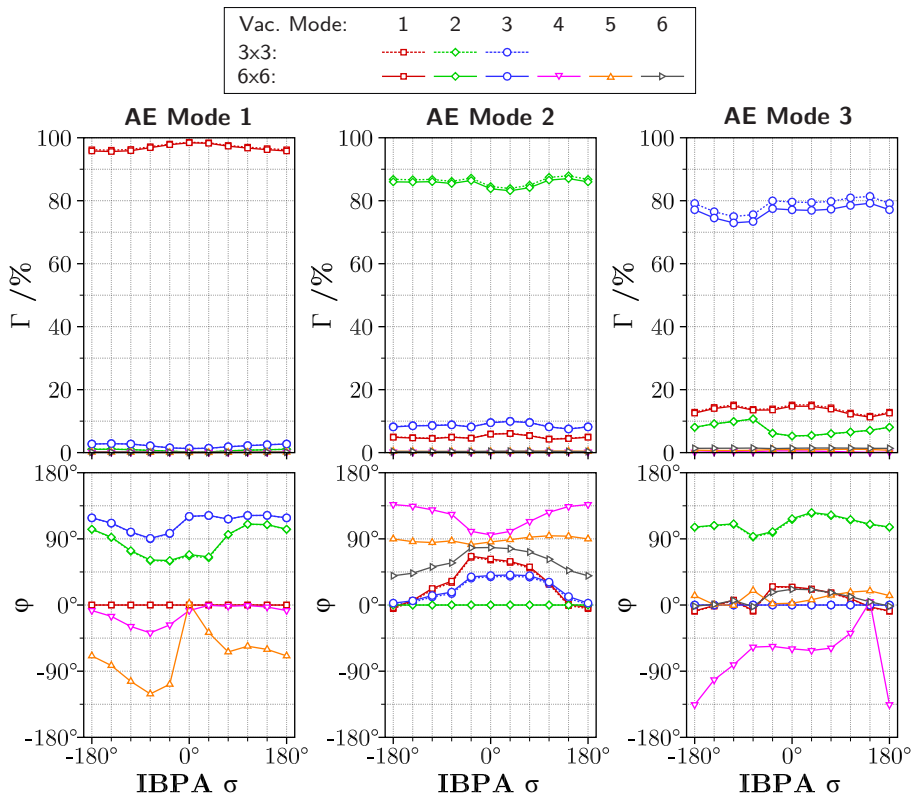
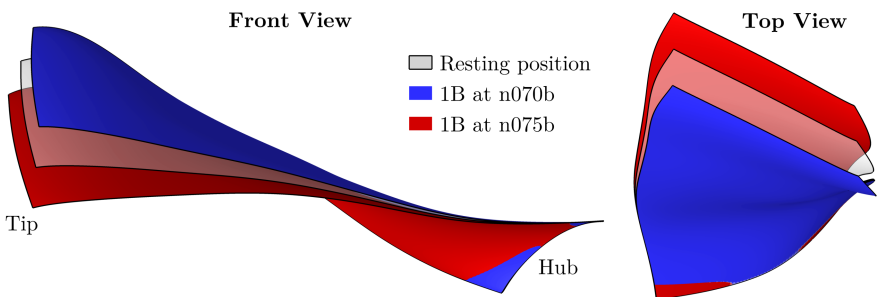


Figure 7.8.: OP *n075b*: Damping diagram for EM, p-k 3x3, and p-k 3x6



**Figure 7.9.:** OP *n075b*: Modal participations of the fundamental aeroelastic modeshapes (AE mode) compared between 3x3 and 6x6 analysis



**Figure 7.10.:** Comparing the manifestation of the vac. modeshape 1 (1B) at  $\omega t = \varphi = 0^\circ$  between OP *n070b* and *n075b*

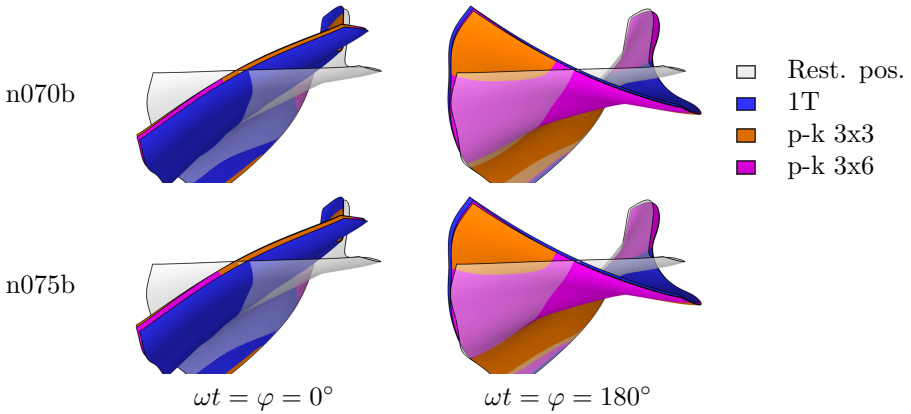


**Figure 7.11.:** Comparing the manifestation of the vacuum modeshape 3 (1T) and aeroelastic modeshape 3 (from p-k 3x3 and 3x6) between OP *n070b* and *n075b*

behavior was also found for the previously investigated OPs. The third aeroelastic mode is destabilizing due to the modal coupling influence as also seen before. However, the aerodamping values are still higher than the second aeroelastic mode. For the overview in the compressor map (fig. 7.6), only the lowest aerodamping overall was selected, which is now coming from the second aeroelastic mode (instead of the third aeroelastic mode below the 90% speedline). When only considering such a global value as criterion, the impression might arise that the rotor gets stabilized by the modal coupling in this flow regime. But this would be a false conclusion or deception. Actually, the third aeroelastic mode already shows clear tendency towards excitation.

Some similarity to the *n075b* are found in fig. 7.13. In the third aeroelastic mode, the first vacuum modeshape (1B) is almost in phase with the third (1T). In contrast, the sixth vacuum modeshape has jumped by approximately 180°, a behavior by the modal analysis in the opposite direction than it was found for 1B when comparing *n070b* to *n075b*.

At the OP *n090c*, the third aeroelastic mode is now finally destabilized, see fig. 7.14. Also the analysis including more vacuum modeshapes in particular leads to a higher excitation in the unstable IBPAs.

### 7.3.4. Higher Rotational Speed

At the highest rotational speeds, the rotor appears to be unaffected by the modal coupling effects when looking at the compressor map in fig. 7.6. As pointed

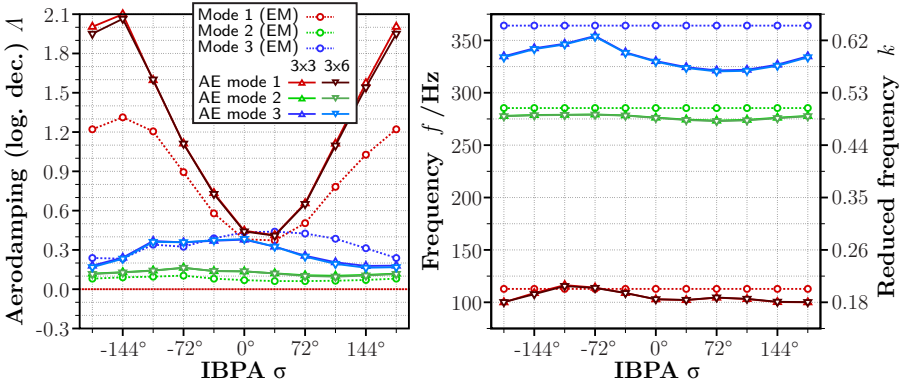


Figure 7.12.: OP *n090b*: Damping diagram for EM, p-k 3x3, and p-k 3x6

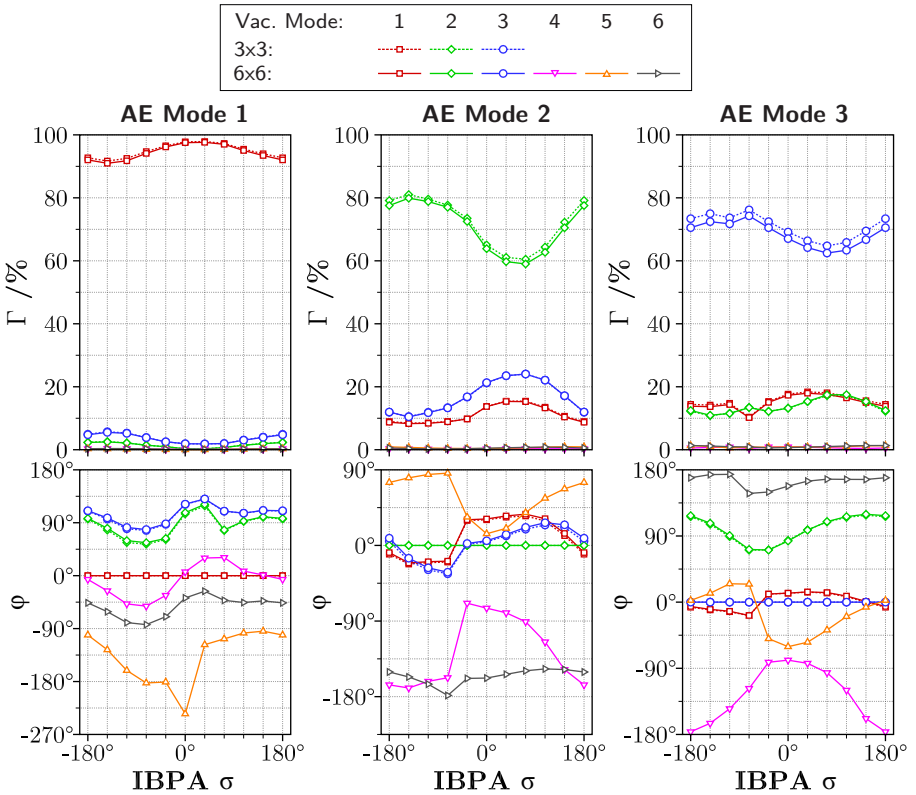


Figure 7.13.: OP *n090b*: Modal participations of the fundamental aeroelastic modeshapes (AE mode) compared between 3x3 and 6x6 analysis

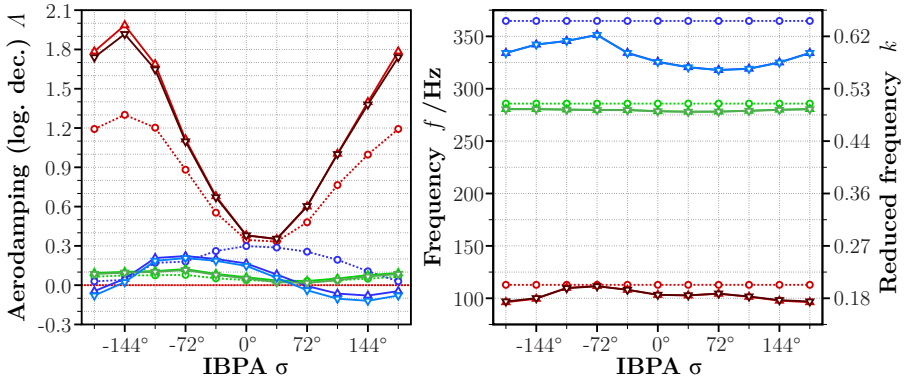


Figure 7.14.: OP *n090c*: Damping diagram for EM, p-k 3x3, and p-k 3x6

out in the previous subsection, this conclusion may be a deception. Figure 7.15 clearly points out, that the third aeroelastic mode is destabilized by the modal coupling, but the second aeroelastic mode still has the lower aerodamping over all. A very same picture is also found at *n095c* and *n105c*: Until reaching the surpline, the destabilization is not strong enough to impact the aeroelastic stability of the rotor for this particular geometry. Those examples point out, that such a behavior has to be tracked and no false conclusion is drawn from preliminary results.

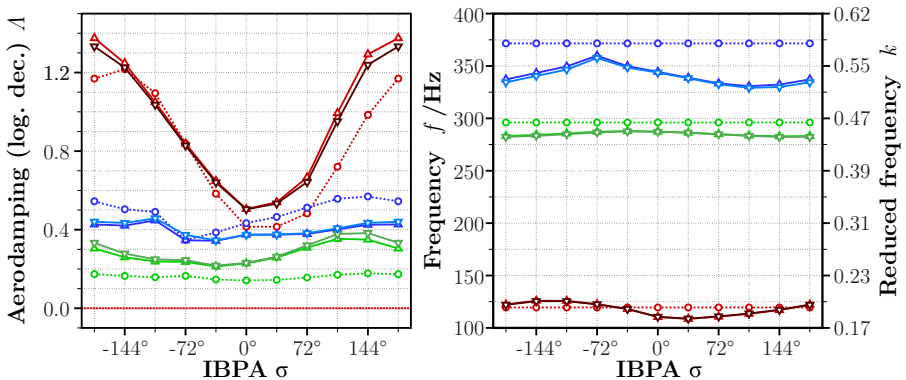
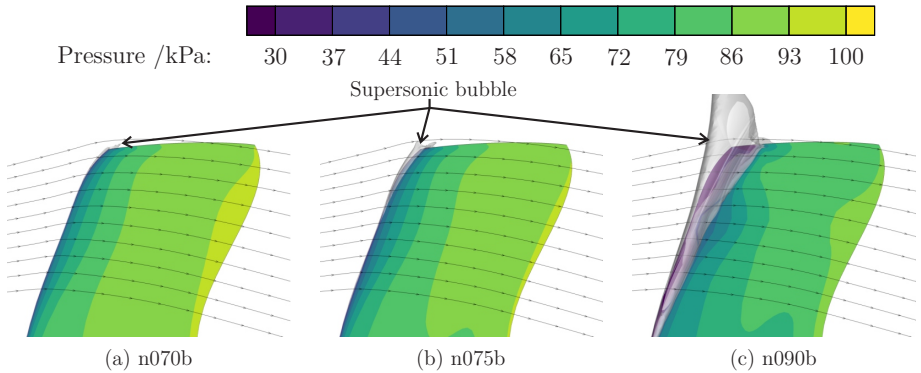


Figure 7.15.: OP *n100c*: Damping diagram for EM, p-k 3x3, and p-k 3x6



**Figure 7.16.:** Supersonic areas at the blade tip region of rotor 1

## 7.4. Mechanism of Modal Coupling

In the previous section, the effects on the aerodamping due to modal coupling, as well as the modal participation factors, were observed. Now, the mechanism which leads to destabilization of the vibrating system is investigated.

By looking at the steady flowfields in fig. 7.16, an evolving supersonic system can be seen. At *n070b*, the flowfield already has a very small bow shock at the tip leading edge, but aside from the tip region, the rest of the blade does not see supersonic flow and shocks along the flow path. In contrast, a supersonic bubble appears at the leading edge from tip to around the half-span for the *n075b*. A full transonic region is established at *n090b*, with a strong shock located around 10% to 20% of the chordlength.

When looking at the damping diagrams in figs. 7.2 and 7.5 comparing the EM with p-k in 1x1, 3x3, 3x6, and 3x10, an evolving pattern can be observed: going from EM to 1x1, the third modeshape starts to destabilize which is further increased as more vacuum modeshapes are coupled in. The same pattern is visible for the other OPs as shown (figs. 7.7, 7.8 and 7.12).

The local excitations of selected cases in fig. 7.16 are analyzed in the following. For the EM results, the unsteady aerodynamic pressures are directly taken from the CFD computations. The p-k results are interpolated for each vacuum modeshape at the respective frequency and assembled according to the modal participation factors and phase lag as determined by the p-k solver. The combination of modeshape and unsteady pressure leads to the local excitation as in equation (2.69).

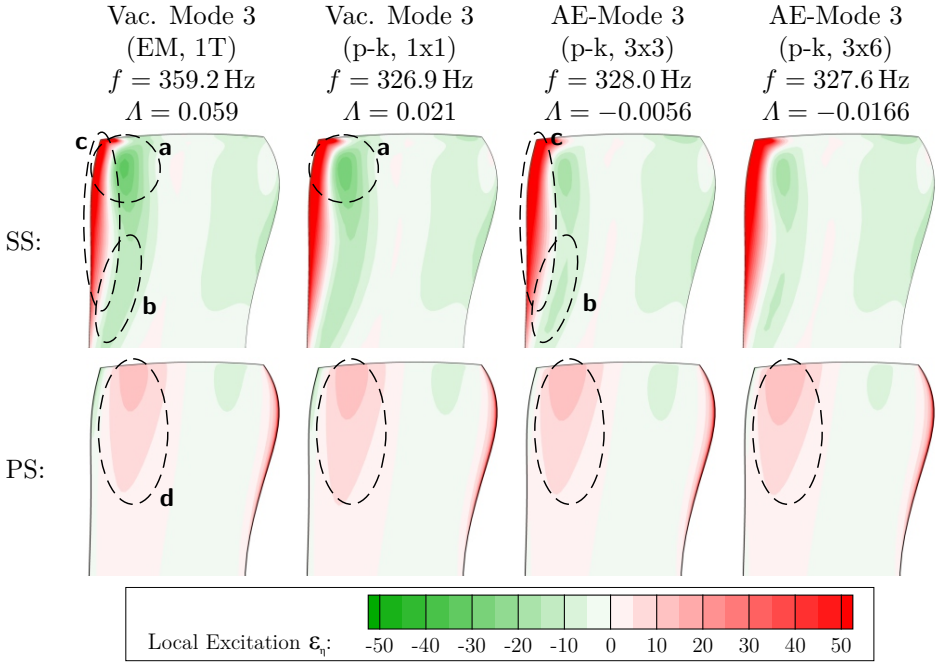


**Figure 7.17.:** OP *n070b*,  $\sigma = 36^\circ$ : Local excitation in the tip region of rotor 1 for different modeshape vibrations

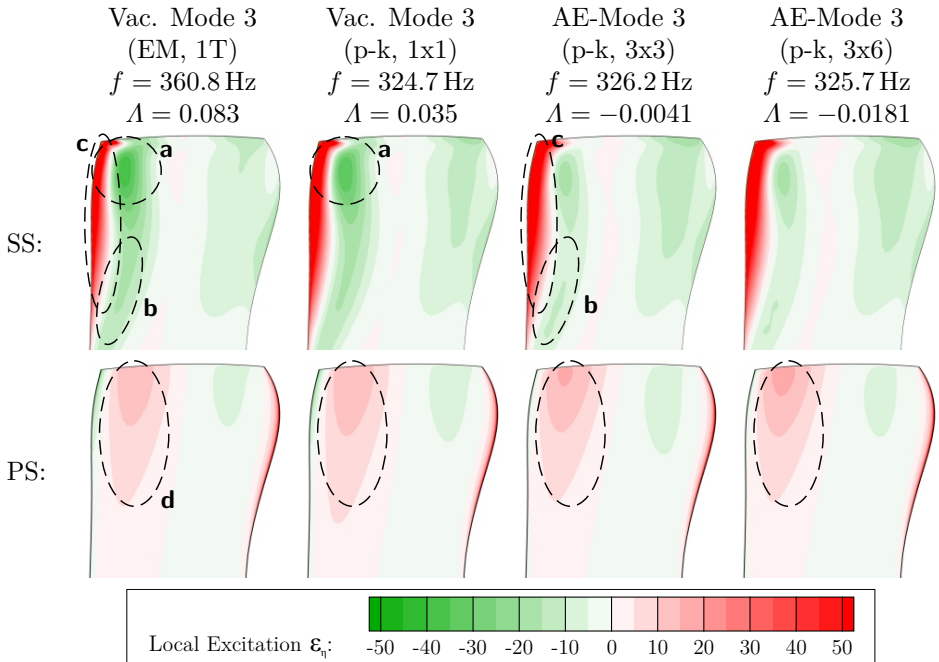


**Figure 7.18.:** OP  $n075b$ ,  $\sigma = 36^\circ$ : Local excitation in the tip region of rotor 1 for different modeshape vibrations



For the OP *n070b*, the local excitations in fig. 7.17 already experience minor changes between EM and p-k 1x1 as only the vibration frequency is changed. Especially the locally damped area on the suction side (SS) marked by “a” is slightly less intensive. Once other vacuum modeshapes are coupled in, this region has an even lower intensity. The marker “b” indicates an additional area where the stabilizing forces are reduced. Furthermore, the already strongly excited area at the leading edge marked by “c” becomes a little larger. On the pressure side (PS), the locally excited area marked by “d” in the front part increases. Looking at the manifestation of the aeroelastic modeshape (fig. 7.11), the elastic axis is shifted towards the leading edge due to the modal coupling. As a consequence, the coupled modeshape has a lower amplitude in the front part, which effectively decreases the aerodynamic work done by the pressure fluctuations. The aeroelastic mode which includes six vacuum modeshapes has almost the same elastic axis position, but especially in the leading edge region of the blade, the amplitude is slightly higher than the aeroelastic mode with only three vacuum modeshapes. The sixth vacuum modeshape contributes to this behavior what can be observed by looking at its appearance (fig. 4.11). This particular region has high pressure amplitudes and because of the high excitation resulting from this, their contribution by integration to the global excitation of the blade has a large impact. A very similar mechanism with minor local differences is acting for the OP *n075b*, see fig. 7.18.

Generally, the fully transonic OP *n090b* shifts the unstable IBPAs towards higher angles. Figure 7.19 does not show similarity to the above discussed mechanisms and also the IBPA  $\sigma = 36^\circ$  is damped, even when modal coupling is considered. The strong shock location is very much visible, leading to a locally very highly damped trench, marked by “a”. However, once modal coupling is included, this trench appears less strong and additionally, behind the shock location an excited area marked by “b” is now contributing to the destabilization of the blade. The marker “c” on the pressure side (PS) shows small contributions when respecting more vacuum modeshapes to the aeroelastic system. On contrary, the pressure side (PS) has a slight stabilization effect marked by “d”.

The aerodynamically excited IBPA  $\sigma = 144^\circ$  of the OP *n090c* is shown in fig. 7.20. For this case, the front part of the blade remains almost unaffected by the modal coupling. With a lowered aeroelastic frequency of the vacuum modeshape alone, at around 50% of the chordlength and towards the trailing edge marked by “a”, the large damped area is removed. The aeroelastic modeshape contribute to destabilizing this particular area even further. A similar effect is shown by the marker “b”. The marker “c” and “d” show a similar behavior as already reported for *n090b* above.

In this way, small contributions in either direction are possible. They may big differences in the analysis methods when drastic flowfield changes are distinct.

However, even small changes over a large surface are, as small as they may be, can influence to overall outcome due to their sum after integration over the whole surface.

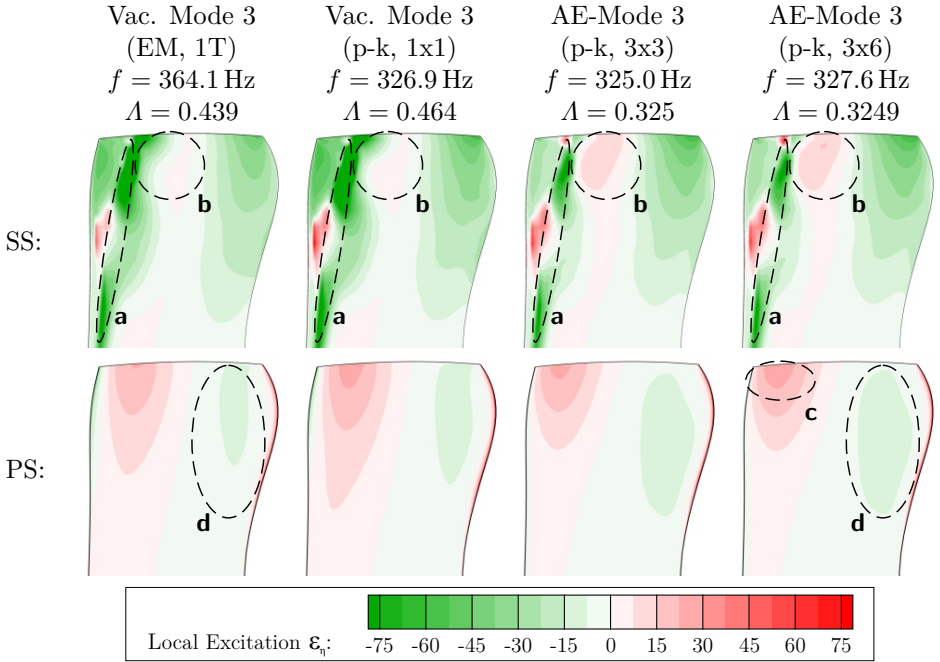


**Figure 7.19.:** OP *n090b*,  $\sigma = 36^\circ$ : Local excitation in the tip region of rotor 1 for different modeshape vibrations

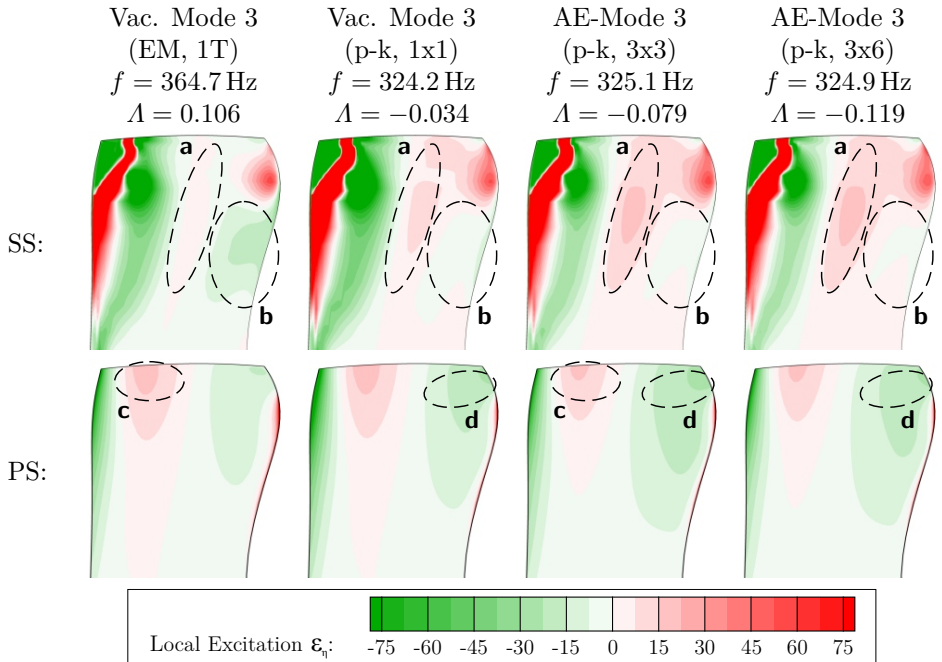


**Figure 7.20.:** OP *n090c*,  $\sigma = 144^\circ$ : Local excitation in the tip region of rotor 1 for different modeshape vibrations

## 7.5. Summary and Outlook

Aerodynamic coupling of modeshapes between the working line and stall mainly leads to a destabilization coming from the third aeroelastic modeshape. It mainly consists of the first torsion of the vacuum modeshapes. Especially in mid-speed operating points, modal coupling is significant when comparing to the conventional work-per-cycle approach. It is shown that mainly the first three fundamental vacuum modeshapes contribute to the coupling behavior of the geometry. Adding so-called higher vacuum modeshapes has only minor influence on the analysis outcome for this geometry. Nevertheless, the trend of including those additional modeshapes leads to a further destabilization, although with a decreasing impact the higher the distance of the respective natural frequencies is.

It shall be mentioned that the presented analysis is only valid for the flutter onset. Based on the results in chapter 5, it can be assumed that aerodynamic nonlinearities will counteract the aerodynamic excitation at higher vibration amplitudes. While those initial coupled CFD-CSM simulations are a strong lead, the current solver environment used at the time of writing this thesis did not allow to investigate those cases in more detail. Furthermore, structural damping is neglected in the flutter onset analysis. The CRISPmulti geometry is manufactured using a CFRP material which may possess a high structural damping. In practical terms, assumptions about structural damping of the CRISPmulti are merely educated guesses as no numerical model or experimental data was available at the time of writing this thesis. Both factors, aerodynamic nonlinearities and structural damping, can lead to limit cycle oscillations which may be tolerated for a certain amount of time in off-design operating points. Currently, different methods for including such factors into the solvers are being worked on [99] and a future combination of those methods is very much achievable as a next step.

# 8

## Conclusion

### 8.1. Aerodynamic Coupling of Modeshapes in Turbomachinery

Aerodynamic coupling between mode shape families cannot be neglected and needs to be included in the analysis process of future lightweight turbomachinery bladings. In the investigated 3D case, the flutter-free regime is significantly reduced when modal coupling is taken into account. The stability boundary is much closer to the working line than predicted by the energy method. Three main conclusions can be drawn [44, 45]:

- The energy method approach yields a non-conservative statement about aeroelastic stability of the blades when the mass ratio is low.
- The p-k method allows a good assessment of the coupled-mode flutter phenomenon. The validation results show good agreement with the time-marching simulations, even in regimes with slight aerodynamic nonlinearities.
- The p-k method, when used with aerodynamic responses from frequency domain solvers, offers a pre-determined effort over time-marching simulations.

Time-marching simulations require a large computational setup with full-wheel configurations, that include several uncertainties. In contrast, with the p-k method only the modeshapes of interest need to be determined. CFD with the already existing infrastructure can be performed at several different frequency sampling points and then be post-processed by an eigenvalue solver. This method allows the assessment of the modal participation factors of the fundamental structural mode shapes, or in other words: the flutter characteristics (what is in line with SRIVASTAVA AND REDDY's proposals [24]). The sensitivity of modal coupling towards mass ratio or frequency separation can be assessed with

a refined sweep of the scaling variable of the GAF matrix in the aeroelastic eigenvalue analysis.

## 8.2. Occurrence of Aerodynamically Coupled-Mode Flutter

There is no general guideline that avoids coupled-mode flutter by design. Flutter is a geometry-specific phenomenon and needs to be treated as such. The only way to avoid coupled-mode flutter is mainly by having a high mass ratio of the component, and secondarily by decreasing the aerodynamic load on the blades. This contradicts the engineering approach and challenge of lightweight design and stage reduction. Generally, flutter cannot be excluded by design and numerical analysis has to be carried out anyway. For a design which is similar to known cases, the previous flutter analysis results may be utilized to get a general idea of how far away from an instability the new design might be. If any of the parameter changes in the new design is considered as critical towards a coupled-mode flutter, the p-k method provides a good numerical tool for the flutter analysis of such cases.

Qualitatively, the main contributors which increase the aerodynamic modal coupling, and as a consequence, might lead to a destabilization, are: a low mass ratio, a low frequency separation and a high solidity (or low blade-to-blade distance respectively low pitch). The influence of the latter design variable is contradicting the findings of CLARK [27, 28], who reported a higher solidity would lead to a stabilizing effect.

If aerodynamic damping of the single mode analysis at a fixed frequency is already low for some IBPAs, flutter with coupled modes is likely to occur at this IBPA range first. A higher modal coupling will widen the list of critical IBPAs. Besides the general observations, in the presence of an aerodynamic or acoustic resonance phenomenon the cascade can be (metaphorically) “pushed over the edge” by the frequency coalescing behavior of the modal coupling.

None of the investigated cases had a subcritical bifurcation (damped at low amplitudes, excited at higher cases). That does not rule out the possibility, but as known from VAN ROOIJ [37], the subcritical bifurcation will be succeeded by a “regular” flutter case at higher loads. Thus, in practical terms, a safety margin in critical cases (large gradient of logarithmic decrement) is advisable.

### 8.3. The P-K Method: Verification vs. Validation

In classical project management or software engineering, the two terms *verification* and *validation* fulfill two different purposes. The first is to check if the requirements of a product are met. The latter checks if the requirements fit to a certain purpose.

Asking the question “*Are you building it right?*” (verification), the clear answer is yes. The p-k method was adapted from fixed-wing to turbomachinery usage and delivers the coupled-mode parameters i.e. vibration frequency, aerodynamic damping, modal participation factors (magnitude/phase) from a precomputed set of frequency domain sampling points in the regime of linear flow responses. Comparison to the time-marching simulations clearly shows this for the subsonic operating conditions. The question is more challenging for the transonic cases: the flutter onset is predicted in accordance with the time-marching simulations, even though there are some minor differences in the coupled-mode parameters. This leads to the second question: “*Are you building the right thing?*” (validation). This question is ambiguous.

First, the p-k method is only valid at the point of flutter onset and requires a linear flow response, as already laid out in the theory section. Nevertheless, it can be used even in areas where typical flow nonlinearities arise, i.e. shockwaves and slight flow separation. Discrepancies will arise from these nonlinearities, but if only small amplitudes are investigated, the overall differences between time-marching and frequency domain simulations is small. If the requirement is “*We need a tool to predict coupled-mode flutter onset.*”, the question of validation is also answered with “yes” as engineering problems are always confronted with uncertainties – the smaller, the better. To perform an uncertainty quantification, more experience and comparison with different geometries is needed, especially experimental comparison will be required.

Another aspect which was excluded from the beginning is amplitude-dependent behavior. The p-k method per se cannot predict the limit-cycle oscillations as shown for higher amplitudes in some of the transonic conditions. But it was never intended to. An interesting approach is the *amplitude-dependent* p-k method as implemented by VAN ROOIJ [37]. This so-called *ADePK* method comes with an even more increased computational effort and its usage will have to be evaluated carefully and weighted against time-marching methods for special selected cases. The “general” p-k method may however be a good indicator where to look for LCOs in a wider parameter range (compressor map, flight levels etc.).

As in many cases, the application of a certain method comes down to an engineering judgment and does not relieve from critical evaluation.





# Bibliography

- [1] M. Vahdati, K.-B. Lee, and P. Sureshkumar. “A Review of Computational Aeroelasticity Of Civil Fan Blades”. In: *International Journal of Gas Turbine, Propulsion and Power Systems* 11.4 (2020), pp. 22–35. DOI: 10.38036/jgpp.11.4\_22.
- [2] H. Zhou, J. Huang, and F. Lu. “Reduced Kernel Recursive Least Squares Algorithm for Aero-Engine Degradation Prediction”. In: *Journal of Mechanical Systems and Signal Processing* 95 (Oct. 2017), pp. 446–467. ISSN: 0888-3270. DOI: 10.1016/j.ymssp.2017.03.046.
- [3] G. Polek. *FutureFlight.aero: NASA Invests in Further R&D For More Efficient Airliner Engines*. <https://www.futureflight.aero/news-article/2021-10-28/nasa-invests-further-rd-more-efficient-airliner-engines>. Accessed: 2021-Nov-02. 2021.
- [4] *Safran Engines Product Website CFM56-5B*. <https://www.safran-aircraft-engines.com/commercial-engines/single-aisle-commercial-jets/cfm56/cfm56-5b>. Accessed: 2021-Jan-20. 2021.
- [5] *Pratt & Whitney Product Website GTF*. <https://prattwhitney.com/products-and-services/products/commercial-engines/pratt-and-whitney-gtf>. Accessed: 2021-Jan-20. 2021.
- [6] T. Wuerfel. “Flying The A321neo: Technology Upgrades Under The Skin”. In: *Aviation Week & Space Technology* (2017).
- [7] A. Geeraert and C. Stephan. “CROR Blade Deformation, Part 1: Experimental Results by Strain Pattern Analysis”. In: *International Forum on Aeroelasticity and Structural Dynamics (IFASD), Saint Petersburg, Russia*. IFASD-2015-023. 2015.
- [8] Y. Mauffrey, A. Geeraert, and S. Verley. “CROR Blade Deformation, Part 2: Aeroelastic Computations and Comparison with Experiments”. In: *International Forum on Aeroelasticity and Structural Dynamics (IFASD), Saint Petersburg, Russia*. IFASD-2015-043. 2015.
- [9] H. Förching. “Aeroelastic Stability of Cascades in Turbomachinery”. In: *Progress in Aerospace Sciences* 30 (1994).
- [10] O. Bendiksen, R. E. Kielb, and K. C. Hall. “Turbomachinery Aeroelasticity”. In: *Encyclopedia of Aerospace Engineering* 3 (2010). Ed. by R. Brockley and W. Shyy, pp. 1625–1639. DOI: 10.1002/9780470686652.eae156.

- [11] F. Eichner and J. Belz. “Application of the Modal Approach for Prediction of Forced Response Amplitudes for Fan Blades”. In: *Journal of Engineering for Gas Turbines and Power* 141.3 (Mar. 2019), p. 031019. DOI: 10.1115/1.4041453.
- [12] R. E. Kielb, K. C. Hall, M. A. Spiker, J. P. Thomas, E. T. Pratt Jr., and R. Jeffries. *Non-Synchronous Vibration of Turbomachinery Blades*. Tech. rep. Final Report. Duke University, Departement of Mechanical Engineering and Materials Science, 2006.
- [13] J. G. Marshall and M. Imregun. “A Review of Aeroelasticity Methods with Emphasis on Turbomachinery Applications”. In: *Journal of Fluid and Structures* 10.3 (Apr. 1996), pp. 237–267. DOI: 10.1006/jfls.1996.0015.
- [14] C. Gao and W. Zhang. “Transonic aeroelasticity: A new perspective from the fluid mode”. In: *Progress in Aerospace Sciences* 113 (2020), p. 100596. ISSN: 0376-0421. DOI: 10.1016/j.paerosci.2019.100596.
- [15] J. Nitzsche, L. M. Ringel, C. Kaiser, and H. Hennings. “Fluid-Mode Flutter in Plane Transonic Flows”. In: *IFASD 2019* (2019). IFASD-2019-006.
- [16] J. R. Kinney. *The power for flight : NASA’s contributions to aircraft propulsion*. Government Printing Office, 2018. ISBN: 9781626830387.
- [17] F. Lane. “System Mode Shapes in the Flutter of Compressor Blade Rows”. In: *Journal of Aeronautical Science* 23.1 (1956), pp. 54–66. DOI: 10.2514/8.3502.
- [18] F. O. Carta. “Coupled Blade-Disk-Shroud Flutter Instabilities in Turbojet Engine Rotors”. In: *Journal of Engineering for Power* 89.3 (July 1967), pp. 419–426. DOI: 10.1115/1.3616708.
- [19] M. May. “Linearized Flutter Investigations of Mistuned Turbomachinery Blading”. PhD thesis. TU Berlin, 2012.
- [20] R. L. Bisplinghoff, H. Ashley, and R. L. Halfman. *Aeroelasticity*. Addison-Wesley Publishing Company, Inc., 1957.
- [21] A. A. Mikolajczak, R. A. Arnoldi, L. E. Snyder, and H. Stargardt. “Advances in Fan and Compressor Blade Flutter Analysis and Predictions”. In: *Journal of Aircraft* 12.4 (1975), pp. 325–332. DOI: 10.2514/3.44451.
- [22] O. Bendiksen and P. Friedmann. “Coupled Bending-Torsion Flutter in Cascades”. In: *AIAA Journal* 18.2 (1980), pp. 194–201. DOI: 10.2514/3.50748.
- [23] O. Bendiksen and P. Friedmann. “The Effect of Bending-Torsion Coupling on Fan and Compressor Blade Flutter”. In: *Journal of Engineering for Power* 104.3 (July 1982), pp. 617–623. DOI: 10.1115/1.3227324.

- [24] R. Srivastava and T. S. R. Reddy. “Comparative Study of Coupled-Mode Flutter-Analysis Methods for Fan Configurations”. In: *Journal of Propulsion and Power* 15.3 (1999), pp. 447–453. DOI: 10.2514/2.5447.
- [25] V. Carstens and J. Belz. “Numerical Investigation of Nonlinear Fluid-Structure Interaction in Vibrating Compressor Blades”. In: *Journal of Turbomachinery* 123.2 (2001), pp. 402–408. DOI: 10.1115/1.1354138.
- [26] M. Sadeghi and F. Liu. “Computation of cascade flutter by uncoupled and coupled methods”. In: *International Journal of Computational Fluid Dynamics* 19.8 (Nov. 2005), pp. 559–569. DOI: 10.1080/10618560500508367.
- [27] S. T. Clark, R. E. Kielb, and K. C. Hall. “The Effect of Mass Ratio, Frequency Separation and Solidity on Multi-Mode Fan Flutter”. In: *Proceedings of the ISUAAAT12, London, UK*. 2009.
- [28] S. T. Clark. “Design for Coupled-Mode Flutter and Non-Synchronous Vibration in Turbomachinery”. PhD thesis. Duke University, 2013.
- [29] D. Korte and D. Peitsch. “An Adaption of the p-Method to Analyse the Aerodynamic Damping in Turbomachinery Considering Modal Coupling”. In: *Proceedings of the 15th International Forum on Aeroelasticity and Structural Dynamics (IFASD), Bristol, UK*. IFASD-2013-05A. 2013.
- [30] P. C. Chen. “Damping Perturbation Method for Flutter Solution: The g-Method”. In: *AIAA Journal* 38.9 (Sept. 2000), pp. 1519–1524. DOI: 10.2514/2.1171.
- [31] J. Schwochow. “Die aeroelastische Stabilitätsanalyse - ein praxisnaher Ansatz zur intervalltheoretischen Betrachtung von Modellierungsunsicherheiten am Flugzeug”. PhD thesis. Universität Kassel, 2013.
- [32] R. Corral, J. M. Gallardo, and C. Martel. “A Conceptual Flutter Analysis of a Packet of Vanes Using a Mass-Spring Model”. In: *Journal of Turbomachinery* 131.2 (Apr. 2009), p. 021016. DOI: 10.1115/1.2952364.
- [33] C. Chahine, T. Verstraete, and L. He. “On the Validity of Decoupled Flutter Prediction Methods For Composite Fan Blades”. In: *Proceedings of the ISUAAAT14, Stockholm, Sweden*. I14-S5-1. 2015.
- [34] C. Chahine, T. Verstraete, and L. He. “A Comparative Study of Coupled and Decoupled Fan Flutter Prediction Methods under Variation of Mass Ratio and Blade Stiffness”. In: *Journal of Fluid and Structures* (2019).
- [35] J. D. Jeffers and C. E. Meece. “F100 Fan Stall Flutter Problem Review and Solution”. In: *Journal of Aircraft* 12.4 (1975), pp. 350–357. DOI: 10.2514/3.44454.

- [36] H. J. Hassig. “An Approximate True Damping Solution of the Flutter Equation by Determinant Iteration”. In: *Journal of Aircraft* 8.11 (Nov. 1971), pp. 885–889. DOI: 10.2514/3.44311.
- [37] A. C. L. M. van Rooij. “Aeroelastic Limit-Cycle Oscillations resulting from Aerodynamic Non-Linearities”. PhD thesis. TU Delft, 2017.
- [38] M. Fehrs. “Boundary Layer Transition in External Aerodynamics and Dynamic Aeroelastic Stability”. PhD thesis. TU Braunschweig, 2017.
- [39] M. Sadeghi, M.-T. Yang, H.-M. Shang, and E. Grover. “On the Effect and Analysis of Fluid-Structural Mode Coupling”. In: *Proceedings of the ASME Turbo Expo 2020, Virtual, Online*. 2020. DOI: 10.1115/GT2020-15083.
- [40] R. Kemme. “Numerische Untersuchungen zum aeroelastischen Verhalten eines hochbelasteten Verdichterrisors”. PhD thesis. Universität Hannover, 2004.
- [41] M. F. Platzer and F. O. Carta. *AGARD Manual on Aeroelasticity in Axial-Flow Turbomachines. Volume 1. Unsteady Turbomachinery Aerodynamics*. Tech. rep. Advisory Group for Aerospace Research and Development Neuilly-sur-Seine (France), 1987.
- [42] M. F. Platzer and F. O. Carta. *AGARD Manual on Aeroelasticity in Axial-Flow Turbomachines. Volume 2. Structural Dynamics and Aeroelasticity*. Tech. rep. Advisory Group for Aerospace Research and Development Neuilly-sur-Seine (France), 1988.
- [43] M. Schuff. *Evaluation of Numerical Modal Analysis with Cyclic Symmetry Boundaries and Complex Mode Shapes due to Structural Coupling in Turbomachinery*. Tech. rep. DLR-IB-AE-GO-2018-142. DLR, 2018.
- [44] M. Schuff and V. A. Chenaux. “Coupled Mode Flutter Analysis of Turbomachinery Blades Using An Adaptation of the P-K Method”. In: *Proceedings of the ASME Turbo Expo 2020, Virtual, Online*. 2020. DOI: 10.1115/GT2020-14105.
- [45] M. Schuff and V. A. Chenaux. “Coupled Mode Flutter Analysis of Turbomachinery Blades Using An Adaptation of the P-K Method”. In: *Journal of Engineering for Gas Turbines and Power* 143.2 (Feb. 2021). GTP-20-1533, p. 021017. DOI: 10.1115/1.4048986.
- [46] J. G. Leishman. *Principles of Helicopter Aerodynamics*. Cambridge University Press, 2006.
- [47] G. Merziger and T. Wirth. *Repetitorium der höheren Mathematik*. 6. Auflage. Binomi Verlag, 2006.
- [48] D. H. Hodges and G. A. Pierce. *Introduction to Structural Dynamics and Aeroelasticity*. Cambridge University Press, 2002.

- [49] E. Dowell. *A Modern Course in Aeroelasticity*. Kluwer Academic Publishers, 2004.
- [50] M. Ritter, J. Hilger, and M. Zimmer. “Static and Dynamic Simulations of the Pazy Wing Aeroelastic Benchmark by Nonlinear Potential Aerodynamics and detailed FE Model”. In: *AIAA Scitech 2021 Forum*. 2021. DOI: 10.2514/6.2021-1713.
- [51] J. Hilger and M. R. Ritter. “Nonlinear Aeroelastic Simulations and Stability Analysis of the Pazy Wing Aeroelastic Benchmark”. In: *Aerospace* 8.10 (2021), p. 308. DOI: 10.3390/aerospace8100308.
- [52] H. Hönlinger. *Einführung in die Aeroelastik I, Vorlesung von Dr.-Ing. H. Hönlinger and der Technischen Universität Braunschweig nach dem Scriptum von Professor Dr.-Ing. H. Försching*. Date unknown.
- [53] M. Pastor, M. Binda, and T. Harčarik. “Modal Assurance Criterion”. In: *Procedia Engineering* 48 (2012), pp. 543–548. DOI: 1.
- [54] P. Vacher, B. Jacquier, and A. Bucharles. “Extensions of the MAC Criterion to Complex Modes”. In: *Proceedings of the ISMA 2010, Leuven, Belgium*. 2010.
- [55] D. Nürnberger, F. Eulitz, S. Schmitt, and A. Zachcial. “Recent Progress in the Numerical Simulation of Unsteady Viscous Multistage Turbomachinery Flow”. In: *Proceedings of the 15th International Symposium on Air Breathing Engines (ISABE), Bangalore, India*. 2001-1081. 2001.
- [56] *TRACE User Guide*. <http://www.trace-portal.de/userguide/trace/index.html>. Accessed: 2021-Jan-18. 2021.
- [57] S. Schmitt. “Simulation von Flattern und aerodynamischer Zwangserregung in Turbomaschinenbeschaufelungen”. PhD thesis. Ruhr-Universität Bochum, 2003.
- [58] V. Carstens, R. Kemme, and S. Schmitt. “Coupled Simulation of Flow-Structure Interaction in Turbomachinery”. In: *Journal of Aerospace Science and Technology* 7.4 (2003), pp. 298–306. ISSN: 1270-9638. DOI: 10.1016/S1270-9638(03)00016-6.
- [59] C. Berthold, C. Frey, and H. Schönenborn. “Coupled Fluid Structure Simulation Method in the Frequency Domain for Turbomachinery Applications”. In: *Proceedings of ASME Turbo Expo 2018, Oslo, Norway*. 2018. DOI: 10.1115/GT2018-76220.
- [60] H.-P. Kersken, C. Frey, C. Voigt, and G. Ashcroft. “Time-Linearized and Time-Accurate 3D RANS Methods for Aeroelastic Analysis in Turbomachinery”. In: *Journal of Turbomachinery* 134.5 (Sept. 2012), p. 051024. DOI: 10.1115/1.4004749.

- [61] G. Ashcroft, C. Frey, and H.-P. Kersken. “On the Development of a Harmonic Balance Method for Aeroelastic Analysis”. In: *Proceedings of the 6th European Conference on Computational Fluid Dynamics, Barcelona, Spain*. 2014.
- [62] H. Schoenenborn and G. Ashcroft. “Comparison of Non-Linear and Linearized CFD Analysis of the Stator-Rotor Interaction of a Compressor Stage”. In: *Proceedings of the ASME Turbo Expo 2014, Düsseldorf, Germany*. 2014. DOI: 10.1115/GT2014-25256.
- [63] R. Thormann and M. Widhalm. “Linear-Frequency-Domain Predictions of Dynamic-Response Data for Viscous Transonic Flows”. In: *AIAA Journal* 51.11 (2013), pp. 2540–2557. DOI: 10.2514/1.j051896.
- [64] R. Thormann. “Accurate and Efficient, Time-Linearized Flutter Analysis of Transport Aircraft”. PhD thesis. TU Braunschweig, 2015.
- [65] D. C. Wilcox. “Reassessment of the Scale-Determining Equation for Advanced Turbulence Models”. In: *AIAA Journal* 26.11 (Nov. 1988), pp. 1299–1310. DOI: 10.2514/3.10041.
- [66] D. C. Wilcox. *Turbulence Modeling for CFD*. 3rd ed. DCW Industries, La Cañada, USA, 2006.
- [67] M. B. Giles. “Nonreflecting boundary conditions for Euler equation calculations”. In: *AIAA Journal* 28.12 (1990), pp. 2050–2058. DOI: 10.2514/3.10521.
- [68] H.-P. Kersken, G. Ashcroft, C. Frey, N. Wolfrum, and D. Korte. “Non-reflecting Boundary Conditions for Aeroelastic Analysis in Time and Frequency Domain 3D RANS Solvers”. In: *Proceedings of ASME Turbo Expo 2014, Düsseldorf, Germany*. 2014. DOI: 10.1115/GT2014-25499.
- [69] D. Schluß, C. Frey, and G. Ashcroft. “Consistent non-reflecting boundary conditions for both steady and unsteady flow simulations in turbomachinery applications”. In: *Proceedings of the 7th VII European Congress on Computational Methods in Applied Sciences and Engineering (EC-COMAS), Crete Island, Greece*. 2016.
- [70] D. Schluß and C. Frey. “Time domain implementation of and a spectral non-reflecting and boundary condition for unsteady and turbomachinery flows”. In: *Proceedings of the 24th International Symposium on Air Breathing Engines (ISABE), Canberra, Australien*. ISABE-2019-24196. 2019.
- [71] C. Frey, D. Schluß, N. Wolfrum, P. Bechlers, and M. Beck. “On the Formulation of Nonreflecting Boundary Conditions for Turbomachinery Configurations: Part I – Theory and Implementation”. In: *Proceedings of the ASME Turbo Expo 2020, Virtual, Online*. 2020. DOI: 10.1115/GT2020-14684.

- [72] N. Wolfrum, P. Bechlars, M. Beck, C. Frey, and D. Schließ. “On the Formulation of Nonreflecting Boundary Conditions for Turbomachinery Configurations: Part II – Application and Analysis”. In: *Proceedings of the ASME Turbo Expo 2020, Virtual, Online*. 2020. DOI: 10.1115/GT2020-15358.
- [73] *MSC Nastran Product Website*. <https://www.mscsoftware.com/product/msc-nastran>. Accessed: 2021-Jan-18. 2021.
- [74] MSC Software. *MSC Nastran Quick Reference Guide*. 2014.
- [75] C. Voigt, C. Frey, and H.-P. Kersken. “Development of a Generic Surface Mapping Algorithm for Fluid-Structure-Interaction Simulations in Turbomachinery”. In: *Proceedings of the V European Conference on Computational Fluid Dynamics ECCOMAS CFD 2010, Lisbon, Portugal*. 2010.
- [76] A. de Boer, M. S. van der Schoot, and H. Bijl. “Mesh Deformation Based on Radial Basis Function Interpolation”. In: *Journal of Computers and Structures* 85.11 (2007), pp. 784–795. ISSN: 0045-7949. DOI: 10.1016/j.compstruc.2007.01.013.
- [77] M. Schuff, P. Kranzinger, M. Keßler, and E. Krämer. “Advanced CFD-CSD Coupling: Generalized, High Performant, Radial Basis Function Based Volume Mesh Deformation Algorithm for Structured, Unstructured, and Overlapping Meshes”. In: *40th European Rotorcraft Forum 2014, Southampton, UK*. 2014.
- [78] M. Schuff, T. Lengyel-Kampmann, and N. Forsthofer. “Influence of the Steady Deformation on Numerical Flutter Prediction for Highly Loaded and Flexible Fan Blades”. In: *Proceedings of ASME Turbo Expo 2017, Charlotte, NC, USA*. 2017. DOI: 10.1115/GT2017-64027.
- [79] M. Schuff. *Automatized turbomachinery map generation and aeroelastic Analysis. Part 1: Steady fluid structure coupling and flutter analysis*. Tech. rep. DLR-IB-AE-GO-2018-129. DLR, 2018.
- [80] N. Forsthofer and C. Reiber. “Structural Mechanic and Aeroelastic Approach for Design and Simulation of CFRP Fan Blades”. In: *Deutscher Luft- und Raumfahrtkongress 2016, Braunschweig, Germany*. 2016.
- [81] V. A. Chenaux, M. Blocher, and P. Ott. “Numerical and Experimental Investigations of an Annular Transonic Compressor Cascade Considering Leakage Flows”. In: *Proceedings of the ISROMAC15, Honolulu, HI, USA*. 2014.
- [82] V. A. Chenaux and B. Grüber. “Aeroelastic Investigation of an Annular Transonic Compressor Cascade: Numerical Sensitivity Study for Validation Purposes”. In: *Proceedings of the ASME Turbo Expo 2015, Montreal, Canada*. 2015. DOI: 10.1115/GT2015-43297.



- [83] V. A. Chenaux and B. Grüber. “Aeroelastic Investigation of an Annular Transonic Compressor Cascade: Experimental Results”. In: *Proceedings of the ASME Turbo Expo 2015, Montreal, Canada*. 2015. DOI: 10.1115/GT2015-43317.
- [84] V. A. Chenaux. “Experimental Investigation of the Aeroelastic Stability of an Annular Compressor Cascade at Reverse Flow Conditions”. PhD thesis. EPFL Lausanne, 2012.
- [85] M. Schuff and V. A. Chenaux. “Nonlinear Aerodynamic Damping in a Highly Loaded Vibrating Compressor Cascade”. In: *Proceedings of ASME Turbo Expo 2019, Phoenix, AZ, USA*. 2019. DOI: 10.1115/GT2019-91550.
- [86] M. Schuff and V. A. Chenaux. “Coupled Mode Flutter of a Linear Compressor Cascade in Subsonic and Transonic Flow Conditions”. In: *Journal of Physics: Conference Series* 1909.1 (May 2021). Proceedings of the ISROMAC18, Online Conference, p. 012033. DOI: 10.1088/1742-6596/1909/1/012033.
- [87] P. Schimming, L. Enghardt, W. Neise, G. Schewe, S. Schmitt, R. Schnell, L. Wallscheid, and Y. Zhang. *Experimentelle Untersuchungen zur Aeroakustik, -elastik und -dynamik am CRISP-1m-Modell*. Tech. rep. Abschlussbericht 1996-1999, BMBF Förderkennzeichen LFT 9601. DLR, 2000.
- [88] D. Görke, A.-L. Le Denmat, T. Schmidt, F. Kocian, and E. Nicke. “Aerodynamic and Mechanical Optimization of CF/PEEK Blades of a Counter Rotating Fan”. In: *Proceedings of ASME Turbo Expo 2012, Copenhagen, Denmark*. 2012. DOI: 10.1115/GT2012-68797.
- [89] A.-L. Aulich, D. Görke, M. Blocher, A. Moreau, T. Otten, and E. Nicke. *Projekt CRISP II: DLR-Projekt zur Multi-Disziplinären Entwicklung und Erprobung einer hocheffizienten, gegenläufigen Fan-Stufe für die nächste Triebwerksgeneration mit sehr hohem Bypassverhältnis, Aerodynamisches, -elastisches, -akustisches und mechanisches Verhalten eines gegenläufigen Fans*. Tech. rep. DLR-IB-325-13-13. DLR, 2013.
- [90] A.-L. Aulich, D. Görke, M. Blocher, E. Nicke, and F. Kocian. “Multi-disciplinary Automated Optimization strategy on a Counter Rotating Fan”. In: *Proceedings of ASME Turbo Expo 2013, San Antonio, TX, USA*. 2013. DOI: 10.1115/GT2013-94259.
- [91] M. Schuff and J. Reisberg. “Flutter Analysis of a Flexible UHBR Fan at Different Flight Conditions”. In: *Proceedings of ASME Turbo Expo 2018, Oslo, Norway*. 2018. DOI: 10.1115/GT2018-76930.
- [92] Project Management Institute. *A Guide to the Project Management Body of Knowledge (PMBOK Guide)*. 5th ed. 2013.

- [93] M. Schuff and V. A. Chenaux. “On the Effect of Frequency Separation, Mass Ratio, Solidity and Aerodynamic Resonances in Coupled Mode Flutter of a Linear Compressor Cascade”. In: *Proceedings of ASME Turbo Expo 2022, Rotterdam, The Netherlands*. GT2022-82160. 2022. DOI: 10.1115/GT2022-82160.
- [94] V. A. Chenaux, M. Schuff, and D. Quero. “Applicability of Harmonic Balance for the Determination Of Blade Stability within the Prescribed Motion Approach”. In: *Proceedings of the ASME Turbo Expo 2020, Virtual, Online*. 2020. DOI: 10.1115/GT2020-14132.
- [95] C. Gao, W. Zhang, X. Li, Y. Liu, J. Quan, Z. Ye, and Y. Jiang. “Mechanism of frequency lock-in in transonic buffeting flow”. In: *Journal of Fluid Mechanics* 818 (2017), pp. 528–561. DOI: 10.1017/jfm.2017.120.
- [96] C. Gao, W. Zhang, and Z. Ye. “Reduction of transonic buffet onset for a wing with activated elasticity”. In: *Aerospace Science and Technology* 77 (2018), pp. 670–676. ISSN: 1270-9683. DOI: 10.1016/j.ast.2018.03.047.
- [97] D. Quero, P. Vuillemin, and C. Poussot-Vassal. “A generalized eigenvalue solution to the flutter stability problem with true damping: The p-L method”. In: *Journal of Fluids and Structures* 103 (2021), p. 103266. ISSN: 0889-9746. DOI: 10.1016/j.jfluidstructs.2021.103266.
- [98] Tecplot Inc. *Tecplot 360 EX 2020 R1 User’s Manual*. 2020.
- [99] C. Berthold and et al. “Fully Coupled Analysis of Flutter Induced Limit Cycles: Frequency vs. Time Domain Methods”. In: *Proceedings of ASME Turbo Expo 2022, Rotterdam, The Netherlands*. 2022. DOI: 10.1115/GT2022-77999.
- [100] M. Vahdati and N. Cumpsty. “Aeroelastic Instability in Transonic Fans”. In: *Journal of Engineering for Gas Turbines and Power* 138.2 (2016). GTP-15-1257, p. 022604. DOI: 10.1115/1.4031225.





# Appendix

## A.1. IBPA Patterns

Table A.1 gives an overview of different IBPA patterns of periodic geometry with 20 identical segments. For a 20 blade cascade, the individual phase shift of each blade is listed according to a certain IBPA. Thus, to achieve the IBPA pattern without phase-lag boundary conditions, the number of passages needed are summed at the bottom of the table. A periodic setup is restricted to a certain selection of IBPAs, e.g. a four passage cascade allows  $\sigma$  to be  $0^\circ$ ,  $\pm 90^\circ$ , or  $180^\circ$  and five blades allow  $\sigma$  to be  $0^\circ$ ,  $\pm 72^\circ$ , or  $\pm 144^\circ$ . For a geometry with 10 identical segments (10 blades), only every second column is applicable (starting at  $0^\circ$ ).

**Table A.1.:** Phase shift<sup>†</sup> of each blade depending on the IBPA\*  $\sigma$ 

$\sigma$ bl.	0°	18°	36°	54°	72°	90°	108°	126°	144°	162°	180°
1	0°	0°	0°	0°	0°	0°	0°	0°	0°	0°	0°
2		18°	36°	54°	72°	90°	108°	126°	144°	162°	180°
3		36°	72°	108°	144°	180°	216°	252°	288°	324°	
4		54°	108°	162°	216°	270°	324°	18°	72°	126°	
5		72°	144°	216°	288°		72°	144°	216°	288°	
6		90°	180°	270°			180°	270°		90°	
7		108°	216°	324°			288°	36°		252°	
8		126°	252°	18°			36°	162°		54°	
9		144°	288°	72°			144°	288°		216°	
10		162°	324°	126°			252°	54°		18°	
11		180°		180°				180°		180°	
12		198°		234°				306°		342°	
13		216°		288°				72°		144°	
14		234°		342°				198°		306°	
15		252°		36°				324°		108°	
16		270°		90°				90°		270°	
17		288°		144°				216°		72°	
18		306°		198°				342°		234°	
19		324°		252°				108°		36°	
20		342°		306°				234°		198°	
M <sup>‡</sup>	1	20	10	20	5	4	10	20	5	20	2

<sup>†</sup> Blank lines mean the pattern from above is repeated.

\* Negative IBPAs would have negative signs in each row.

<sup>‡</sup> A multiple of this number of passages is required to allow for this IBPA to be simulated without phase-lag boundary conditions.

## A.2. Additional Validation for FUTURE-2D-LC Case Transonic I

The case study was already introduced in section 5.2. For the operating point “Transonic I”, the mass ratios  $\mu_1 = 47.5$ ,  $\mu_2 = 45.9$ ,  $\mu = 44.4$ , and  $\mu_4 = 42.9$  were used for the validation of the p-k method against the time domain fluid-structure-coupled simulations. For the setup using four blade passages, the excitation occurred in the IBPA  $\sigma = 180^\circ$ . This behavior was in line with the p-k method results. When extending the validation for even lower mass ratios, a switch of the IBPA with the highest excitation will occur. This behavior is also captured by the p-k method.

For two IBPAs,  $\sigma = -90^\circ$  and  $\sigma = 180^\circ$ , the generalized aerodynamic forces are plotted in fig. A.1. Although there are larger gradients in the GAFs, they are not as characteristic as the aerodynamic resonance in chapter 6. Figure A.2 plots the p-k history for these two IBPAs, where  $\sigma = 180^\circ$  is already known from section 5.2. At a high values of  $q_{\text{scale}}$ , the pitch branch of  $\sigma = -90^\circ$  performs a sudden drop in aeroelastic frequency and aerodamping that comes with a sudden change of the aeroelastic modeshape. The time-marching simulations establish the IBPA  $\sigma = 180^\circ$  at the various mass ratios already known from section 5.2. At the lowest mass ratio of  $\mu = 39.3$ , the aerodamping solution of the IBPA  $\sigma = -90^\circ$ , according to the p-k method, falls below the solution of the IBPA  $\sigma = 180^\circ$ . At this point, the time-marching solution with four blades establish the more unstable pattern of the changed IBPA (aeroelastic frequency, damping and aeroelastic modeshape). As mentioned in the main chapters, the behavior of the time-marching simulations is to ultimately establish the vibration pattern with the highest excitation.

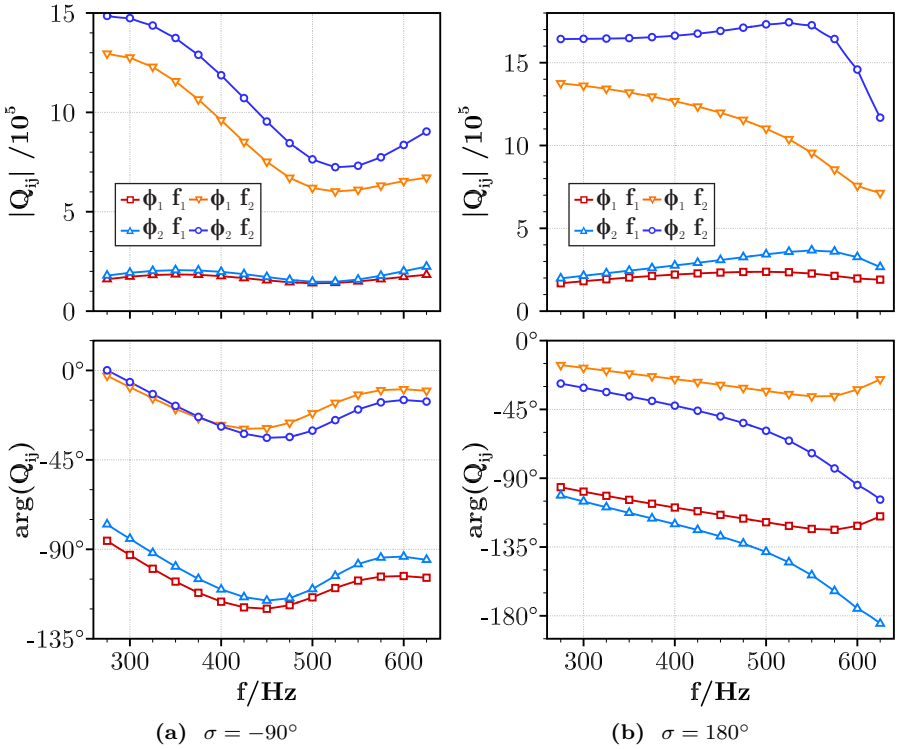


**Figure A.1.:** FUTURE-2D-LC, case “subsonic”: Generalized aerodynamic forces for selected IBPAs

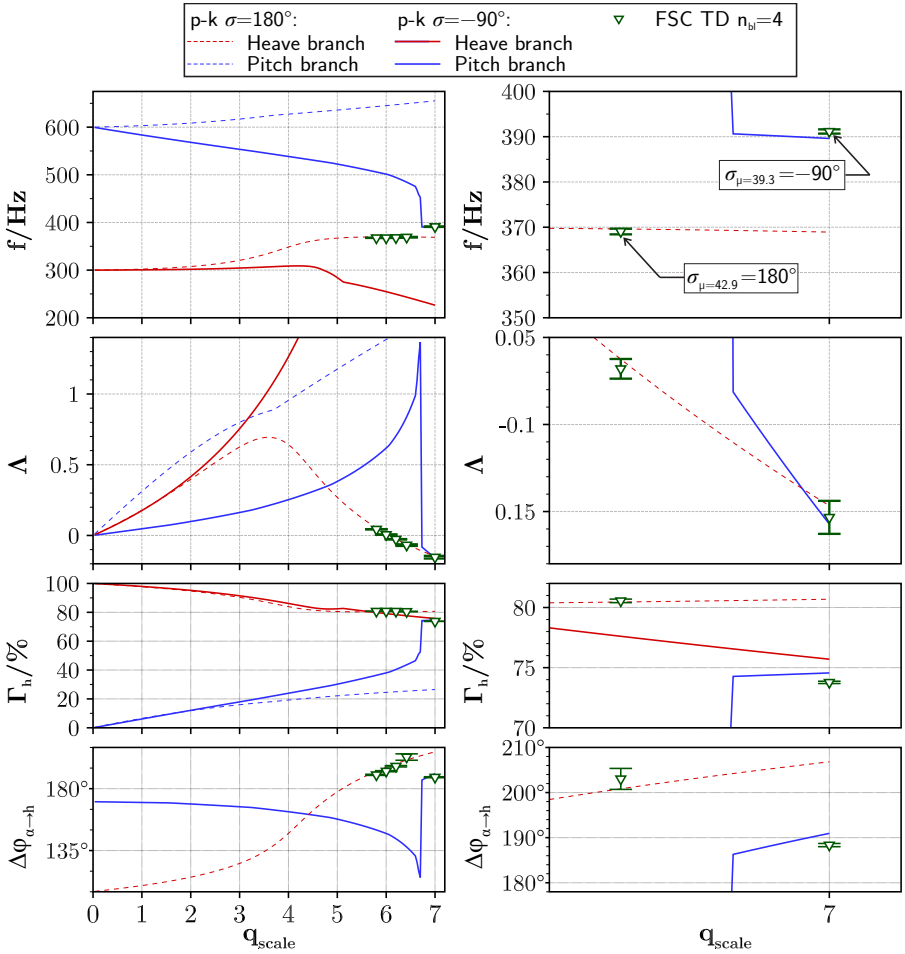


**Figure A.2.:** FUTURE-2D-LC, case “transonic I”: p-k solution history for two IBPA (left: full view, right: detailed view)





### A.3. Computational Efficiency: Time-Marching Simulation vs. P-K Method Analysis

The advantage of time-marching simulations with fluid/structure coupling is that each interaction or coupling mechanism is respected in the simulation (given that the “right” spatial and time resolution are adequately high enough).

In a favorable condition, i.e. when flutter onset is checked and the initial vibration pattern is close to the flutter vibration pattern, the result might be quite rapidly available. But the usage of time-marching methods comes also with a great disadvantage: if the coupling mechanism, frequency and final vibration pattern is not known initially, the user may decide for a very unfavorable starting condition.

Figure A.3 shows a case, where the simulation with time-marching simulations takes a very long time. The mass ratio of this case is quite high, which causes a long delay until the aerodynamic forces can change the vibration pattern. The walltime of this case is multiple weeks. In fig. A.4, the initial starting conditions are changed to the known final vibration pattern and the vibration amplitude rises almost immediately. The walltime is now a few days. Although the behavior of the individual blades between  $t = 1.5$  s and  $t = 2.0$  s in fig. A.3, where the structural energies drift apart, may be an indicator that the blade vibration is not final, it is not necessary an indicator the blade becomes unstable. At a higher natural frequency, the system is stable but still a similar behavior can be observed in fig. A.5.

The energy method (EM) and p-k analysis of this case is shown in fig. A.6. Both methods are very close together, so that the EM might be sufficient. No major stability change is induced when the p-k analysis is applied, but the frequency changes are already quite distinct and could influence the stability analysis in unfavorable cases of GAF-over-frequency distribution.

The EM and the p-k method require many “smaller” computations in the frequency domain (FD) which have much less walltime than the time-marching simulation. To make a comparison of the computational effort, the CPU hours need to be compared.

The required CPU time  $t_{\text{FD,total}}$  can be estimated via

$$t_{\text{FD,total}} = n_{ae} n_{vac} n_{\sigma} n_f n_{cpu} t_{fd} \quad (\text{A.1})$$

with the number of investigated aeroelastic branches  $n_{ae}$ , the number of considered vacuum modeshapes  $n_{vac}$ , the number of IBPAs  $n_{\sigma}$ , the number of frequency samples  $n_f$ , the required number of CPUs  $n_{cpu}$  and the average walltime of a single frequency domain computation  $t_{fd}$ .

Considering only the four blade passage setup, there are four possible IBPAs. For each IBPA, at least three different frequencies ( $n_f = 3$ ) around the vacuum frequency should be simulated to get a good approximation of the GAF behavior over the frequency.

Each simulation took an average of  $t_{fd} = 40$  min on 64 CPUs<sup>8</sup>. Thus, the total CPU time is approx. 500 CPU hours for the p-k analysis. The time-marching simulations were carried out on 256 CPUs<sup>9</sup> and took several weeks to finish, what comes down to an order of 130 000 CPU hours. Even in the *best case* scenario, a walltime of under 2 hours is required so that the time-marching simulations would in the same order of magnitude of computational costs.

For the full 20 blades setup, the CPU time for the p-k analysis is approx. 2600 CPU hours. The time-marching simulation with 1280 CPUs (assuming a linear scale-up of required CPUs to the four passage setup, and a similar walltime) would be about 700 000 CPU hours.

Only one modeshape was considered in this case. For more considered modeshapes, the CPU hours increase linear for each investigated aeroelastic branch. As more aeroelastic branches are investigated, the number increases linear by each branch. As a consequence, the total amount increases exponentially. A p-k analysis with a 3x3 system for all 20 IBPAs results in approx. 23 000 CPU hours, with a 3x6 system approx. 46 000 CPU hours.

---

<sup>8</sup>This does not result in an “optimal” number of cells per CPU as per hand-rules in various textbooks. The applied splitting is merely a result of a simple distribution of “one computation per cluster node”, which consists of 64 CPUs.

<sup>9</sup>Also not the “optimal” distribution, but to match the FD computations, the same CPU load was applied.

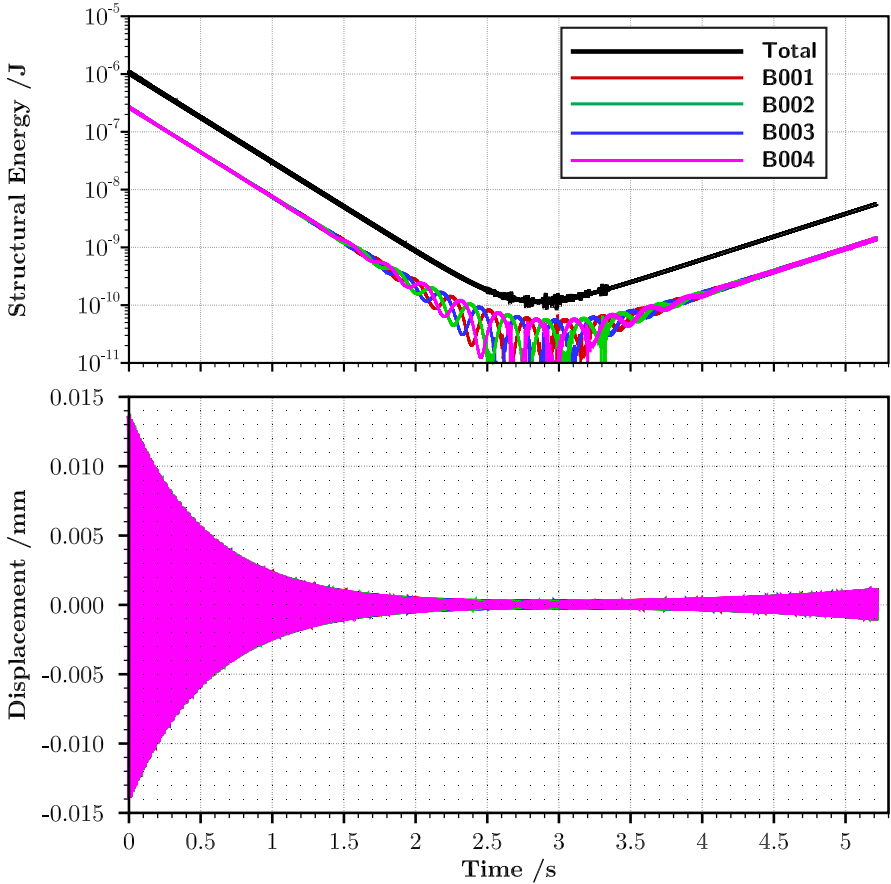


**Figure A.3.:** NACA3506-2D-LC, case “subsonic”,  $n_{bl} = 4$ ,  $\mu = 2803$ , only the pitch mode is allowed with natural frequency  $f_{vac} = 115$  Hz: Total and individual blade structural energy, and individual blade displacements, unfavorable initial conditions

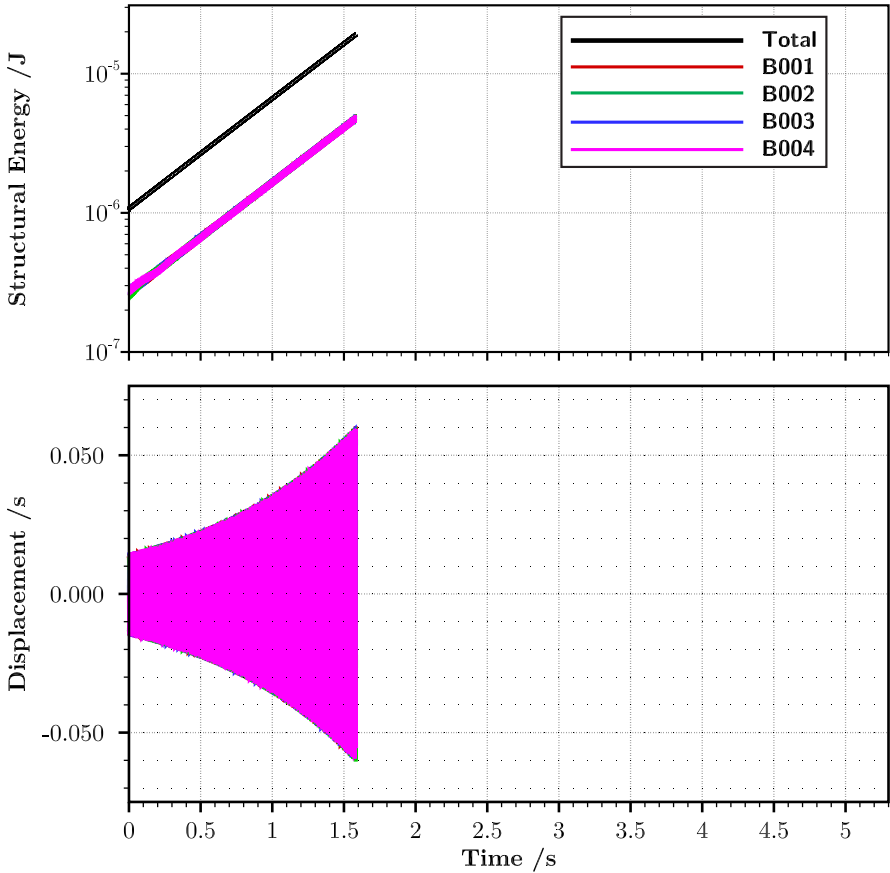


**Figure A.4.:** NACA3506-2D-LC, case “subsonic”,  $n_{bl} = 4$ ,  $\mu = 2803$ , only the pitch mode is allowed with natural frequency  $f_{vac} = 115$  Hz: Total and individual blade structural energy, and individual blade displacements, initial conditions close to final vibration pattern

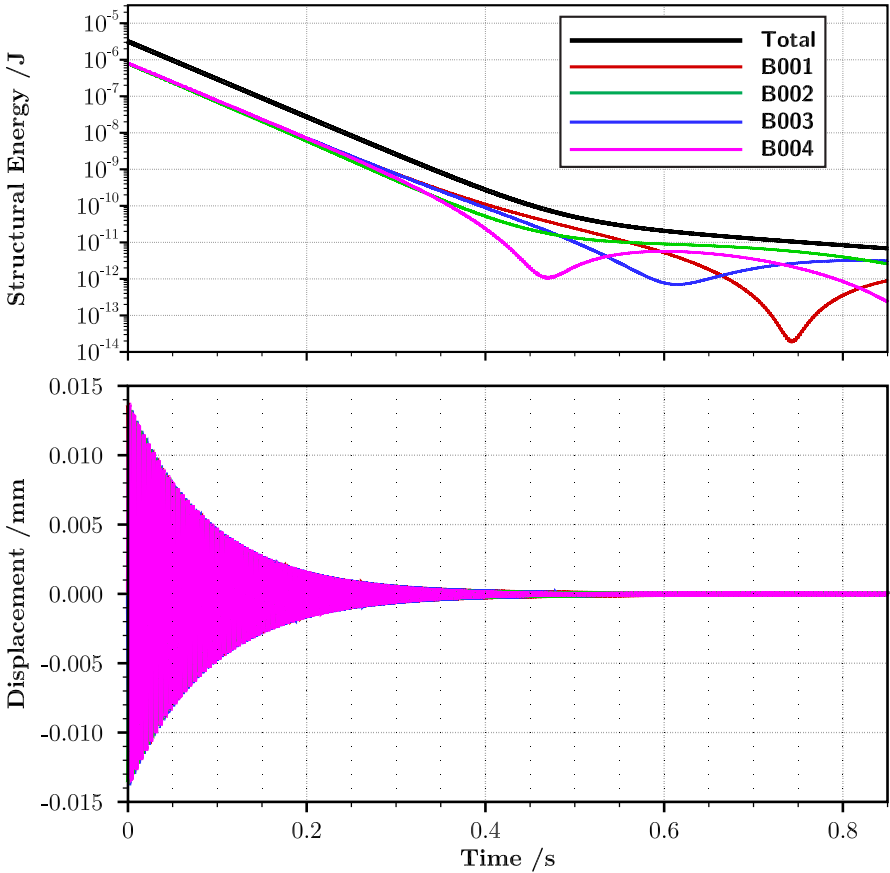


**Figure A.5.:** NACA3506-2D-LC, case “subsonic”,  $n_{bl} = 4$ ,  $\mu = 2803$ , only the pitch mode is allowed with natural frequency  $f_{vac} = 200$  Hz: Total and individual blade structural energy, and individual blade displacements

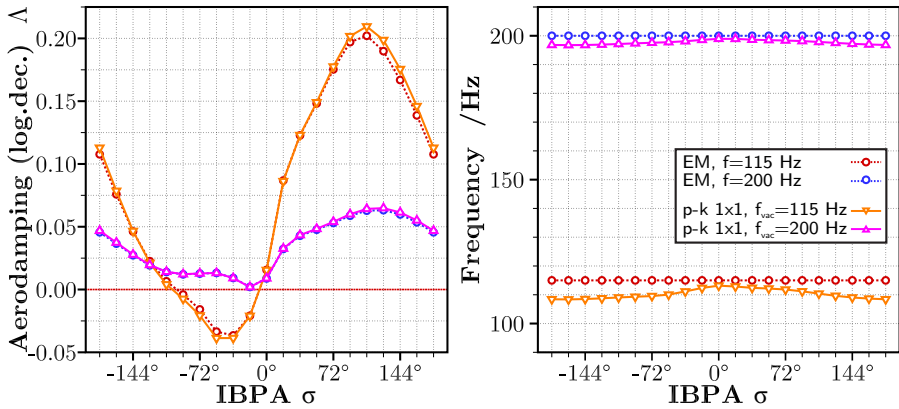


**Figure A.6.:** Traveling wave damping diagram for pitch mode with different vacuum frequencies, compared between energy method (EM) and as 1x1 system in the p-k analysis (NACA3506-2D-LC, case “subsonic”) at a high mass ratio of  $\mu = 2803$

### A.3.1. Natural Frequencies of Modeshapes

Due to rotational and aerodynamic loads, the eigenmode frequencies in the structural dynamics change for each operating point. As depicted in figs. A.7 and A.8 for the CRISPMulti geometry, the major change comes from the change in rotational speed, but also the influences of the different aerodynamic loading of different throttling states is visible.

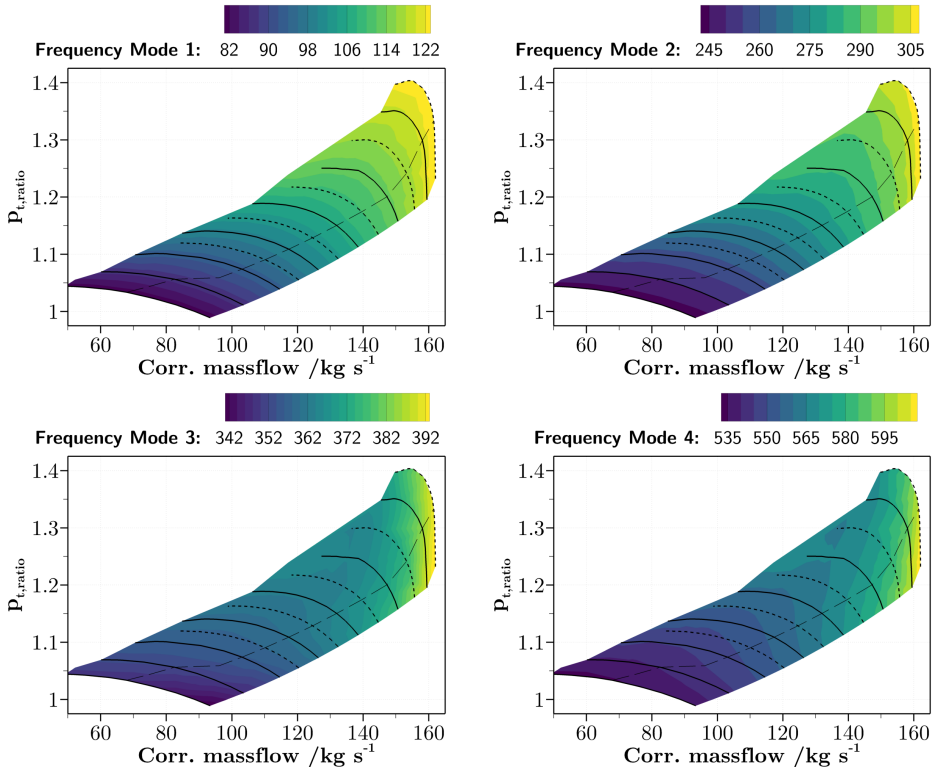


**Figure A.7.:** CRISPMulti, rotor 1: Modal frequencies of modes 1 to 4 throughout compressor map



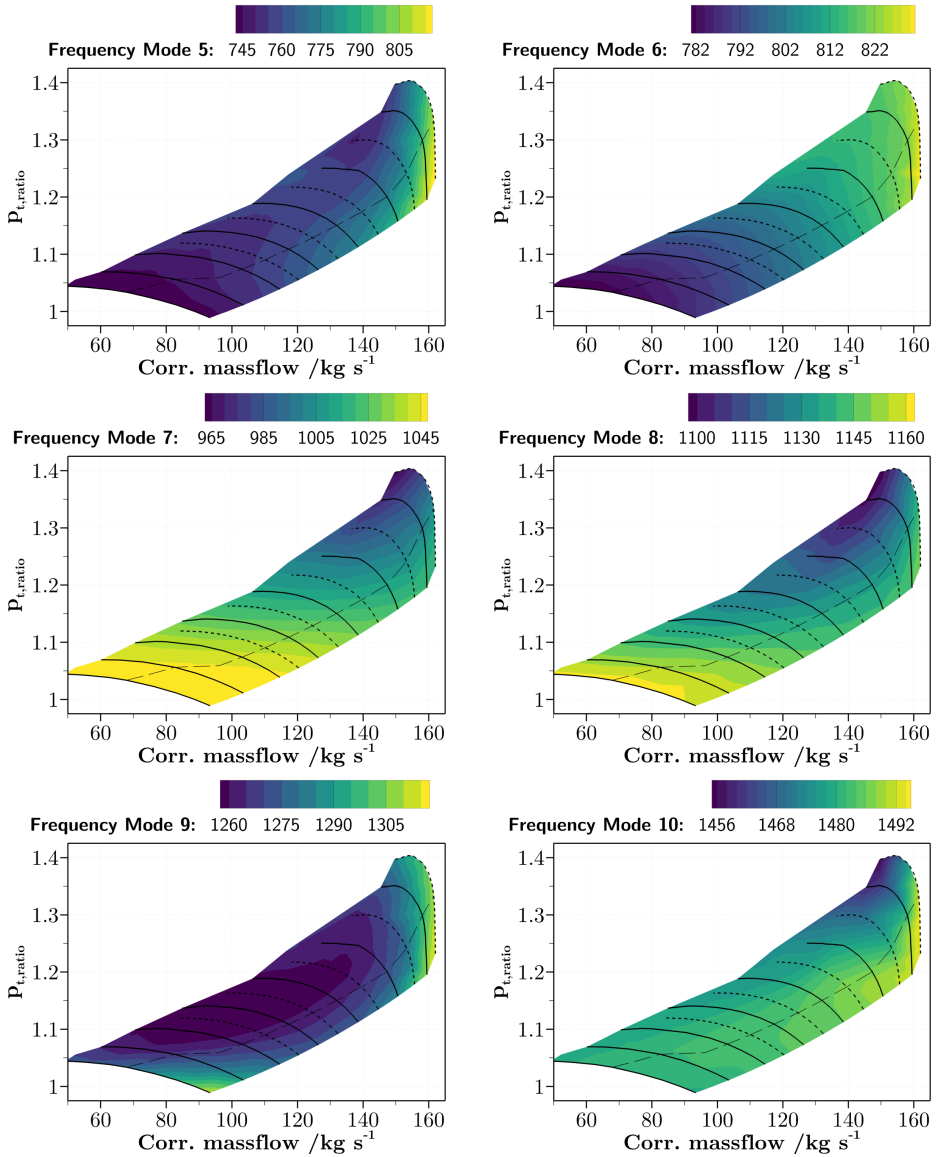


**Figure A.8.:** CRISPMulti, rotor 1: Modal frequencies of modes 5 to 10 throughout compressor map

## A.4. CRISPmulti: Parameter Changes Throughout the Compressor Map

### A.4.1. Twist-to-Plunge Ratio of Modeshapes

As stated by VAHDATI [100], the twist-to-plunge ratio parameter  $\alpha$  is defined as the product of the twist angle amplitude (in radians) times the semichord of the blade at the tip divided by the plunging amplitude at the tip of the blade and can be calculated from

$$\alpha = \frac{2 (z_{LE} - z_{TE})}{z_{LE} + z_{TE}} \quad (\text{A.2})$$

where  $z_{LE}$  and  $z_{TE}$  are the magnitudes of the displacements and the leading edge and at the trailing edge, respectively. To gain the magnitude, the displacement vector is projected onto a normal vector that is perpendicular to the chordline. From this projected vector, the vector length is taken as the magnitude. As a rule, the positive normal vector points towards the suction side. Therefore, magnitudes pointing to the suction side have a positive sign, vectors pointing to the pressure side have a negative sign.

The higher the twist-to-plunge ratio, the more twisting component is included in the modeshape. This ratio is measured at the tip of the blade, and being an integral value of the whole blade, it is only meaningful for the fundamental modeshapes, i.e. first or second bending and first torsion.

For the CRISPmulti geometry, the twist-to-plunge ratios of the first rotor are plotted for the three fundamental modeshapes “1. bending” (Mode 1), “2. bending” (Mode 2), and “1. torsion” (Mode 3) in fig. A.9.

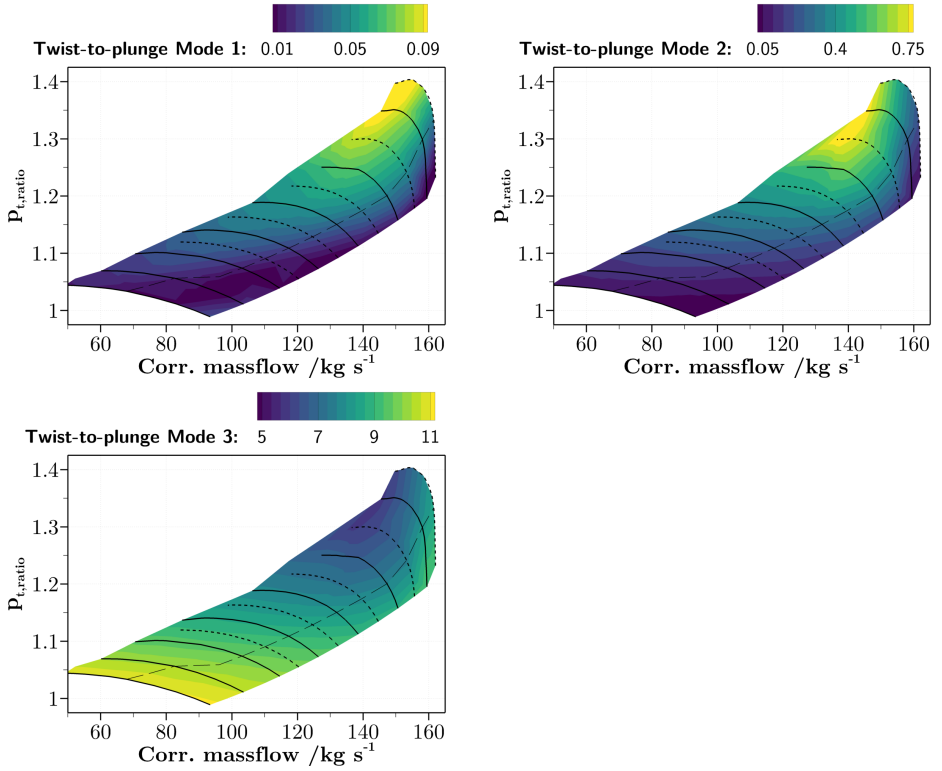


**Figure A.9.:** CRISPMulti, rotor 1: Changes of twist-to-plunge ratio throughout the compressor map

## CURRICULUM VITAE

# Matthias Schuff

Born April, 8th, 1988 in Kaiserslautern, Germany

### EDUCATION

---

- 10/19 – 07/22 **Technical University of Berlin**, Berlin, Germany  
Doctoral Thesis, Advisor: Prof. Dr.-Ing. Dieter Peitsch
- 10/08 – 08/15 **University of Stuttgart**, Stuttgart, Germany  
Studies: Aerospace Engineering  
Qualification: Diplom-Ingenieur  
Specialization: Aerodynamics and Gas Dynamics,  
Aeromechanics of Helicopters, Space Transportation Systems,  
Plasma Flows
- 08/98 – 03/07 **High School Hohenstaufen-Gymnasium**, Kaiserslautern,  
Germany

### PROFESSIONAL EXPERIENCE

---

- since 07/22 **German Aerospace Center DLR**, Augsburg, Germany  
Research Associate at the Institute of Test and Simulation for  
Gas Turbines, *Research Group Virtual Engine Platform*
- 11/15 – 06/22 **German Aerospace Center DLR**, Göttingen, Germany  
Research Assistant at the Institute of Aeroelasticity, *Research  
Group Aeroelasticity of Turbomachinery*
- 04/14 – 12/14 **Baylor University**, Waco, TX, USA  
Visiting Research Scholar at the Center for Astrophysics, Space  
Physics and Engineering Research, *Space Science Lab*
- 01/12 – 01/14 **University of Stuttgart**, Stuttgart, Germany  
Student Research Assistant at the Institute of Aerodynamics  
and Gas Dynamics, *Team Helicopters and Aeroacoustics*
- 10/10 – 02/11 **Air Berlin Technik**, Düsseldorf, Germany  
Internship in Line and Base Maintenance, *Airframe & Systems  
Engineering for Airbus A320/A330*
- 05/07 – 01/08 **German Red Cross**, Kaiserslautern, Germany  
Alternative Service as Emergency Medical Technician

